HETEROTOPIC OSSIFICATION: PHYSICOCHEMICAL ANALYSIS AND DEVELOPMENT OF A NOVEL TREATMENT STRATEGY

By

NEIL MICHAEL EISENSTEIN

A thesis submitted to the University of Birmingham for the degree of DOCTOR OF PHILOSOPHY

Biochemical Engineering
School of Chemical Engineering
College of Engineering and Physical Science
University of Birmingham
May 2017

ABSTRACT

Heterotopic ossification (HO) is the pathological formation of ectopic bone and can be a devastating complication of military injuries. It causes multiple problems, including prosthetic limb fitting difficulties and ankylosis, ultimately causing loss of mobility, independence, and dignity. There is no effective prophylaxis and the only treatment is surgery, which causes rehabilitation delays and risks of bleeding and nerve injury. This work aimed to develop a new therapy for HO. A review of mineralised tissue analytical methods was performed and used to guide the study of human HO samples using X-ray micro computed-tomography, X-ray fluorescence, synchrotron X-ray diffraction / nano-tomography, Raman spectroscopy, and scanning electron microscopy. Screening of therapies demonstrated that hexametaphosphate (HMP) could dissolve hydroxyapatite (the mineral component of bone) under physiological conditions. Formulation engineering principles were applied to control this effect temporally and anatomically. A murine HO model was developed and used for feasibility testing of injected HMP as an HO therapy, showing that it had no adverse effect on normal bone. In summary, this project revealed the physicochemical structure of HO in unprecedented detail, discovered and developed a novel therapy, set up an animal model of HO, and showed that injected HMP is feasible in this model.

DEDICATION

This thesis is dedicated to the British military servicemen and women who have developed heterotopic ossification as a consequence of injuries received in the course of their duties. My hope is that this work will make some progress towards a new treatment that can provide these, and future, patients with improved function, independence, and human dignity.

I would also like to dedicate this thesis to my wife, Dr Emily Kingham, and my parents, Professor Stephen Eisenstein and Mrs Helen Rooney, without whose support, encouragement, and proof reading skills, this would not have been possible.

ACKNOWLEDGEMENTS

Professor Liam Grover and Surgeon Captain Sarah Stapley are foremost in a long line of people to whom I owe a huge personal debt of gratitude. Their dedication and enthusiasm has been an inspiration. This project is their brainchild and it has been a privilege to work on it with them. I am also very grateful to Professor Ann Logan and Professor Owen Addison who have played a crucial role in mentoring me throughout. Thanks also to Surgeon Captain Mark Midwinter and the surgeons of the Queen Elizabeth Hospital who had the foresight to save the HO tissue used in this study. Dr Sophie Cox, Dr Richard Williams, Dr Zubair Ahmed, Mr Tom Robinson, Miss Emma Jones, Mr Slobodan Sirovica, Mr Adam Thompson, and Dr Alexandra Pacureanu have all contributed to this work and deserve my deep gratitude. Their contributions are described within the manuscript.

No academic work exists in a vacuum and I am grateful to those researchers whose work has been cited in this thesis and whose ideas have laid the foundation upon which I have built this project.

None of this work would have been possible without funding and I am profoundly grateful to the following for their support: Orthopaedic Research UK, The Drummond Foundation, UK Joint Medical Command, The Birmingham Human Biomaterials Resource Centre, The European Synchrotron Radiation Facility, Diamond Light Source, The University of Birmingham, and the Army Medical Directorate.

SELECTED ACADEMIC OUTPUT FROM THIS WORK

Peer-Reviewed Publications

Eisenstein N, Williams R, Cox S, Stapley S, Grover L. Enzymatically regulated demineralisation of pathological bone using sodium hexametaphosphate. *Journal of Materials Chemistry B* 2016;4(21):3815-22. doi: 10.1039/c6tb00461j

Eisenstein N, Cox S, Williams R, Stapley S, Grover L. Bedside, Benchtop, and Bioengineering: Physicochemical Imaging Techniques in Biomineralization. *Advanced Healthcare Materials* 2016;5(5):507-28. doi: 10.1002/adhm.201500617

Podium Presentations

"Heterotopic Ossification: A novel way to treat and prevent this military epidemic", *Military Healthcare Systems Research Symposium.* 16th August 2016, Orlando, Florida, USA. **Won Young Investigator of the Year 1st Prize**

"Multimodal physicochemical analysis of human trauma-related heterotopic ossification", *Colt Military Medicine Research Meeting.* 8th December 2016, Royal Society of Medicine, London, UK. **Shortlisted finalist for best presentation**

"Polyphosphate Dissolution of Hydroxyapatite – A Potential Treatment for Pathological Biomineralisation", *Royal Society of Chemistry – Biomaterials Chemistry Conference.* 7th January 2016, University of Birmingham, UK.

"Heterotopic Ossification – A Novel Approach to Prevention and Treatment", *Colt Military Medicine Research Meeting.* 10th December 2015, Royal Society of Medicine, London, UK. **Won 1st prize for best presentation**

"Heterotopic Ossification – A Novel Approach to Prevention and Treatment", *British Orthopaedic Association Annual Congress.* 16th September 2015, Liverpool, UK **"Best of the Best" plenary session finalist**

"Heterotopic Ossification – A Novel Approach to Prevention and Treatment – Preliminary Results", *Combined Services Orthopaedic Society Meeting*. 8th May 2015, Newcastle, UK. **Won the Philip Fulford Prize for best presentation**

Invited Podium Presentations

"Physicochemical Characteristics of Heterotopic Ossification", *Centre for Blast Injuries Studies Networking Event.* 15th November 2016, Imperial College, London, UK.

"Heterotopic Ossification: A novel approach to prevention and treatment", *National Institute for Health Research Dissemination Event.* 11th March 2016, Queen Elizabeth Hospital, Birmingham, UK.

Poster Presentations

"Heterotopic Ossification: From Physical Chemistry to Future Treatments", *Association of Military Surgeons of the United States Annual Meeting*. 1st December 2016, Maryland, USA.

"A Novel Treatment Strategy for Preventing and Treating Heterotopic Ossification", *World Biomaterials Congress.* 18th May 2016, Montreal, Canada.

"A Novel Treatment Strategy In Preventing And Treating Heterotopic Ossification", *United Kingdom Society for Biomaterials Annual Meeting.* 25th June 2015, Belfast, Northern Ireland, UK. **Won 1st prize for best poster presentation**

TABLE OF CONTENTS

LIST OF FIGURES

LIST OF TABLES

LIST OF ABBREVIATIONS

ACVR	Activin A Receptor
ALP	Alkaline Phosphatase
BMD	Bone Mineral Density
BMP	Bone Morphogenic Protein
CNS	Central Nervous System
CT	Computed Tomography
CTMP	Cyclical Trimetaphosphate
diH_2O	Deionised water
EDTA	Ethylenediaminetetraacetic acid
ESRF	European Synchrotron Radiation Facility
FOP	Fibrodysplasia Ossificans Progressiva
HA	Hydroxyapatite
HMP	Hexametaphosphate
HO	Heterotopic Ossification
LTPP	Linear Tripolyphosphate
NSAIDs	Non Steroidal Anti-inflammatory Drugs
OCP	Octacalcium Phosphate
OCT	Optimal Cutting Temperature Compound
Pi	Orthophosphate
PPi	Pyrophosphate
SAED	Selected Area Electron Diffraction
SD	Standard Deviation
SEM	Scanning Electron Microscope
SEM	Standard Error of the Mean
SXRD	Synchrotron X-Ray Diffraction
TMD	Tissue mineral density
VOI	Volume of Interest
XRD	X-Ray Diffraction
XRF	X-Ray Fluorescence

1 UNDERSTANDING HETEROTOPIC OSSIFICATION

1.1 Clinical Considerations

1.1.1 Historical and Contemporary Context

Heterotopic ossification (HO) is the pathological formation of bone in soft tissues. Despite being first described in very early medical literature[1,2] approximately 1000 years ago, this condition still poses significant problems in modern times, most notably amongst military combat casualties (Figure 1-1).

The relationship between military injuries and HO was first discussed in the medical literature of the American civil war.[3] Writing about experience gained in the First World War, Colonel E G Brackett wrote a description of the macroscopic appearance and development of HO that would be familiar to those in the field today:

"*Excessive terminal bone production in… stumps was the rule. The most common form was an irregular mushrooming with a tendency to spurs on the inner aspect of the femur. Occasionally sharp exostoses were seen. These often were sharp enough and long enough to cause sufficient pain to warrant their removal.*"[4]

The recent conflicts in Iraq and Afghanistan have provided further examples of how HO can present a significant challenge as a consequence of combat injury. The burden of HO has been so great that Alfieri *et al* have described it as an "epidemic" and argue that it is the single biggest barrier to functional recovery for combat-injured patients.[5]

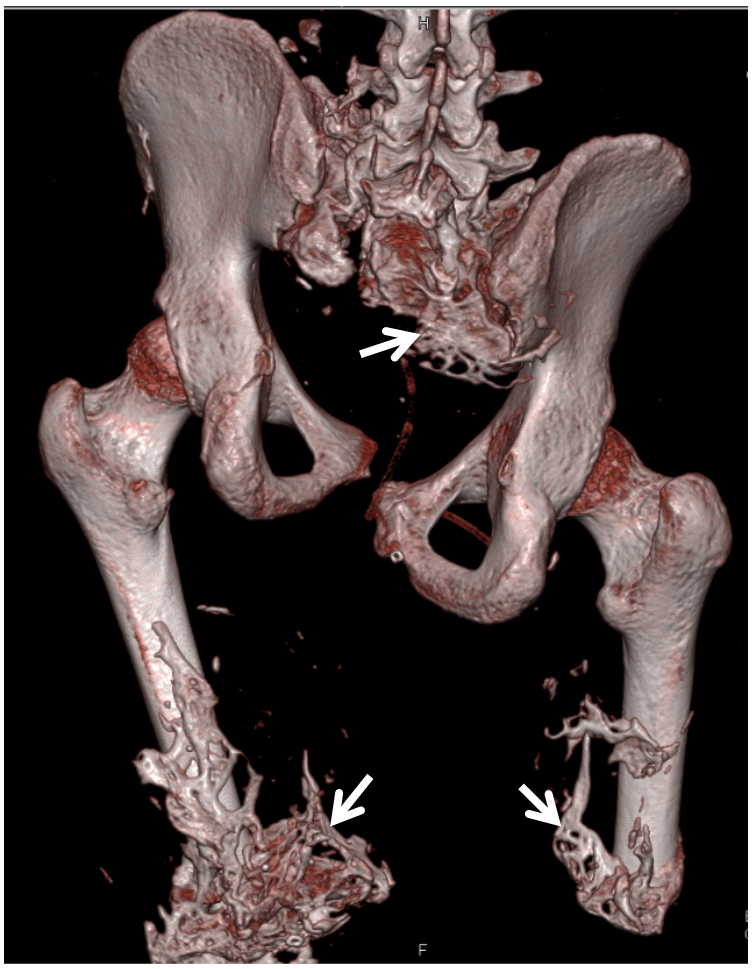

Figure 1-1: 3D computed tomographic reconstruction of the pelvis and residual femora of a combat-injured patient. White arrows = heterotopic ossification.

1.1.2 Aetiology

HO is not the only form of pathological mineralisation. Many disease processes drive aberrant mineralisation and a wide variety of tissues can be affected: blood vessels, heart valves, eyes (band keratopathy), spinal ligaments (ankylosing spondylitis), peripheral nerves (neuritis ossificans), dermis (osteoma cutis), and subcutaneous tissue (panniculitis ossificans traumatica).[6-14] In these conditions, the calcium phosphate mineral deposition does not usually demonstrate significant short or long-

range organisation, nor is it associated with collagen. In contrast, and despite demonstrating a disordered arrangement of these features, HO demonstrates many of the defining characteristics of bone such as lamellae, osteons, marrow cavities, bone forming and maintaining cells, and collagen. Thus, HO is uniquely similar to bone compared with other disorders of pathological mineralisation. Chapter 3 contains a detailed analysis of the current understanding the structure of HO in addition to new results collected in the course of this project.

HO may be caused by genetic or acquired factors. The genetic forms of HO are not the focus of this research project but have relevance due to historical attempts to treat them with polyphosphates and the insights that they provide into pathological bone formation.

1.1.2.1 Genetic HO

The pathological mechanism that causes the genetic form of HO known as fibrodysplasia ossificans progressiva (FOP) (Figure 1-2A) has been studied extensively and is well characterised: a heterozygous single nucleotide substitution of arginine to histidine (R206H) in the activin A type I receptor (ACVR1) gene.[15,16] This gene encodes for the protein activin-like kinase 2 (ALK2), which is a receptor for bone morphogenic proteins (BMPs). $ALK2^{R206H}$ has greater sensitivity to the ligand, BMP-2, leading to increased phosphorylation and nuclear localisation of SMAD proteins, and increased *Id1* promoter activity.[17] Increased ALK2 activity subsequently leads to increased chondrogenic and osteogenic differentiation and the formation of bone in ectopic sites through endochondral ossification.

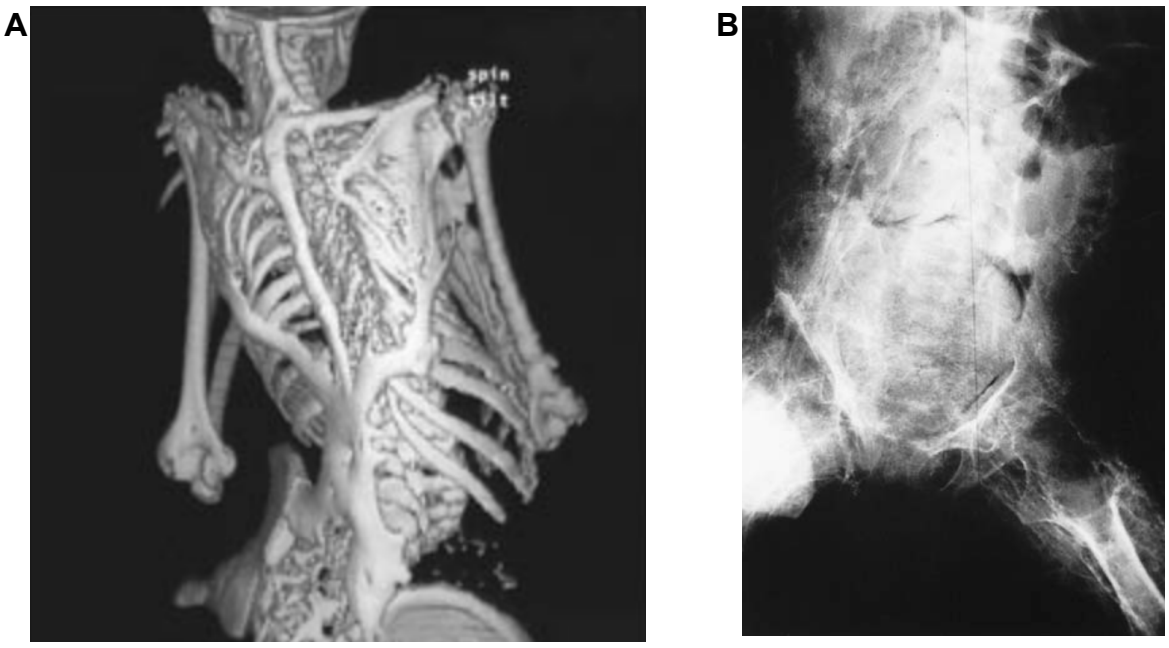

Figure 1-2: A) 3D computed tomographic reconstruction of the thorax, spine, and upper limbs of a 12 year old child with familial ossificans progressiva. Reproduced from Shore *et al.*[16] B) Plain radiograph of the trunk and pelvis of a 20 month old child with progressive osseous heteroplasia. Reproduced with permission from Urtizberea *et al.*[18]

In contrast to FOP, progressive osseous heteroplasia (POH) (Figure 1-2B) occurs through intramembranous ossification and its genetic basis is less well characterised but is thought to involve heterozygous mutations in the GNAS1 (guanine nucleotide binding protein alpha stimulating) gene.[19] The mutation inactivates the GNAS1 gene, which encodes for the alpha subunit of Gsα, and it is thought that this leads to dysregulation of cell lineage switching, resulting in excessive osteogenic differentiation of mesenchymal stem cells (MSCs).[20]

1.1.2.2 Acquired HO

HO may develop after almost any significant injury but is particularly common after blast injury, high-energy transfer gunshot wounds, central nervous system injury,

burns, hip and knee replacement surgery, and elbow injuries. It is not clear whether a single common cellular and biochemical mechanism is responsible for the development of HO secondary to each of these causative events. The rest of this chapter will discuss acquired HO in more detail.

1.1.3 Epidemiology

Radiological evidence of HO was found in 64.6% of a cohort of combat injured patients.[21] A similar figure of 62.9% is reported in a series of combat-injured patients who had undergone amputations.[22] In the blast injury subset of these cases, where amputation was performed through the zone of injury, the rate of radiographically moderate or severe HO rose to 79.6%. It is worth noting that in the Afghanistan conflict, from 2003 to 2014, British service personnel suffered 416 combat amputations from 265 patients (giving the mean limbs lost per patient as 1.6).[23]

A retrospective observational study of civilian amputations demonstrated that 22.8% of patients developed symptomatic HO.[24] HO is also common amongst patients with traumatic brain injury (radiological evidence in 37% of patients),[25] spinal cord injury (5 to 60%),[26] hip arthroplasty (5%),[27] distal humerus fractures (8.6%),[28] and burns (0.15%).[29]

Leading researchers in the field have commented that the incidence of HO has been much higher in the cohort of injured combatants from the Iraq and Afghanistan conflicts compared to historical data. Potter *et al* propose that the reasons for this increase in HO include a high incidence of blast injury (due to increased use of explosive weaponry) and increased survival amongst seriously injured combatants

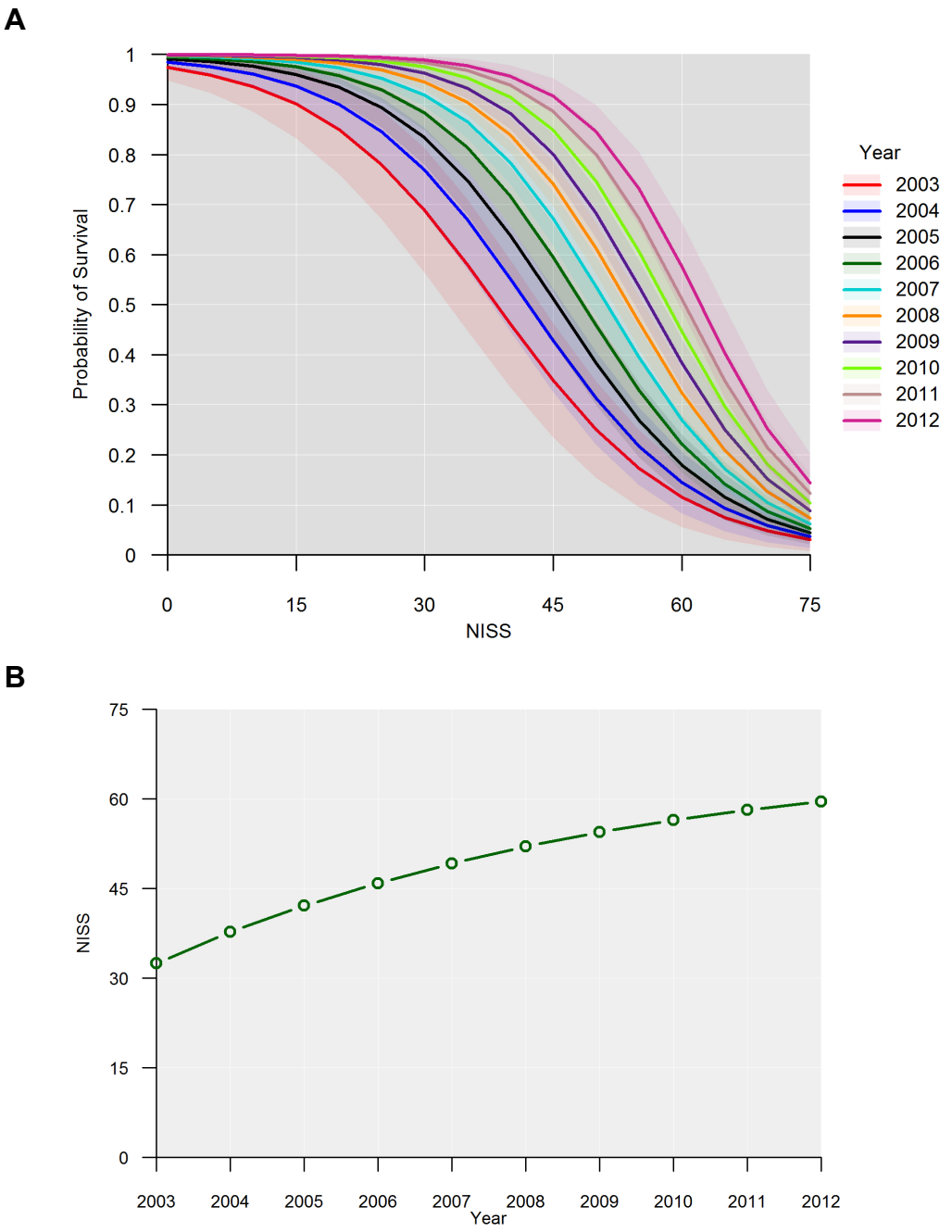

Figure 1-3: A) Plot of predicted probability of survival by New Injury Severity Score (NISS) value for each year of the conflict (Iraq and Afghanistan, 2003-2012). Shaded regions indicate the 95% confidence intervals. B) NISS values associated with a predicted 50% or greater probability of survival. These data demonstrate a year-on-year improvement in survival during these armed conflicts. By the later stages, a significant proportion of the most seriously injured patients (NISS = 75) survived. Thus, the increased incidence of HO may be explained, at least in part, by these very seriously injured survivors. Reproduced (creative commons) from Penn-Barwell *et al.*[30]

(due to improvements in body armour, medical care, forward surgical treatment, and rapid evacuation).[31]

Thus the combination of exposure to blast,[5] extremity amputation,[32,33] and improved survival[30] (Figure 1-3) is thought to have generated an extent and severity of HO not seen before. Historically, patients with these injuries would not have survived long enough to develop symptomatic HO after combat trauma.

1.1.4 Clinical Problems Caused By HO

Patients with HO experience a wide range of problems due to the mechanical effects of hard tissue in extra-skeletal sites. These include pain, loss of joint range of motion, joint ankylosis, skin ulceration, overlying skin graft failure, muscle entrapment, neurovascular entrapment, and prosthetic limb fitting difficulties (Figure 1-4).[34] Evriviades *et al* described the clinical impact of HO on patients eloquently as follows:

"The development of HO can occur in the soft tissues very early and is sometimes found even before primary healing occurs. However, in the majority, it occurs after a number of months. The patient will typically have had an [improvised explosive device] *injury and sustained bilateral traumatic above-knee amputations (often with other significant injuries), and will have initially done well with limb fitting and mobilization. They may develop increasing pain in their stumps and can often feel a hard lump or spike within the stump. In severe cases, the bone has actually eroded through the soft tissues. This may prevent them from mobilizing and poses a significant challenge to the prosthetics team."*[35]

A  B 

Figure 1-4: A) Clinical photograph of HO ulcerating through the distal aspect of a long transfemoral amputation. Note the skin graft over the terminal portion of the residual limb. Reproduced (creative commons) from Alfieri *et al.*[5] B) Preoperative clinical photograph of an above-knee amputee with severe heterotopic ossification beneath a split-thickness skin-grafted site. Reproduced with permission from Potter *et al.*[31]

Given the high prevalence of HO after civilian and combat-related limb amputations, it is worth noting the problems that these patients have with limb fitting. In the civilian setting, 50% of patients with HO require prosthetic modifications such as selective padding, hard socket reshaping, or new socket fabrication.[24] Also, microbiological contamination is a key feature of the kind of high-energy military wounds that are predisposed to the formation of HO.[35] One author reported that 100% of peri-operative HO samples were positive for infection.[22]

1.1.5 Financial Cost of HO

There are no published data on the direct financial costs of HO. However, some indication may be gained from a paper by Masini *et al* who estimate that the direct cost of disability benefits for US service personnel with extremity injury sustained during the campaigns in Iraq and Afghanistan between October 2001 and 2005 to be

$1.2 billion.[36] Given that more than 10 years of conflict continued after the publication of that report, the true figure is likely to be vastly more than this estimation. If 64% of combat extremity injuries develop HO (see above), the proportion of this cost estimate that relates to HO prevention, treatment, and rehabilitation is likely to be significant.

Another analysis, looking at the long term financial cost associated with UK military amputees has identified that approximately £288 million will be required over the next 40 years.[23] Again, this analysis does not specifically estimate the contribution that HO will make to this total figure but it illustrates that the magnitude of the financial cost in addition to the clinical and personal burden to the individuals.

1.1.6 Current Prophylaxis

There are currently no methods of primary prophylaxis that are entirely appropriate for the military population who are likely to be catabolic, at risk of gastric ulceration and renal injury, have open wounds and fractures, and are often in austere environments.

1.1.6.1 Non-Steroidal Anti Inflammatory Drugs (NSAIDs)

NSAIDs are used widely in civilian practice to cover a variety of situations where patients are at high risk of developing HO.[37] An example is revision total hip replacement surgery where the patient has demonstrable HO secondary to the initial operation. However, there is evidence that, in addition to their normal side effect profile, NSAIDs increase the risk of non-union in the setting of HO prophylaxis after acetabular fixation.[38] Impairment of fracture healing would be a particularly

problematic side-effect in major trauma patients as they are highly likely to have sustained at least one fracture as part of their pattern of injuries. Further, these patients are likely to have high risk of kidney injury, which is a major contraindication to NSAID use.[39]

1.1.6.2 Radiotherapy

Radiotherapy is also used in the elective civilian setting and has been shown to be effective but there is lack of consensus on timing and dose.[40] Radiotherapy and NSAIDs may be given in combination for high-risk patients.[41] There is a paucity of data to guide the use of radiotherapy in the traumatic injury cohort. Even if there was good evidence, the logistical challenges to delivering radiotherapy in austere environments are considerable. Further, there are multiple adverse effects of radiotherapy such as impaired wound and bone healing, which mean that it would be contraindicated in military patients who often have co-synchronous fractures and extremely challenging soft tissue wounds.

1.1.6.3 Bisphosphonates

Bisphosphonates are a class of drugs whose primary use is to prevent and treat osteoporosis. They have also been prescribed as prophylaxis against HO. However, their use remains controversial after a Cochrane review[42] and other studies[43] failed to find conclusive evidence of efficacy. There have been no studies looking at their role after major trauma.

1.1.6.4 Passive Movement Therapy

Another Cochrane review[44] investigating the use of passive movement physiotherapy in a heterogeneous group of patients (including traumatic brain injury and spinal cord injury patients at risk of HO) concluded that there is insufficient evidence show whether or not this therapy is effective.

1.1.6.5 Experimental Prophylaxis

One strategy that has shown immense promise is retinoic acid receptor gamma (RARγ) agonism to inhibit chondrogenesis.[45] Without a cartilage scaffold, the endochondral processes that form HO are blocked and no mineral can be deposited. It is worth noting that, in the rodent model, there was a transient prolongation of fracture healing associated with RARγ agonism. Despite this concern, the treatment was so effective that the RARγ agonist palovarotene has been taken forward into clinical trials (NCT02279095) as a treatment for the genetic form of HO known as fibrodysplasia ossificans progressiva (FOP).[46]

Another novel strategy has been demonstrated in a burn-tenotomy rodent HO model[47] whereby hydrolysis of adenosine triphosphate (ATP) at the burn site led to reduced HO formation at a distant site. In addition to revealing a potential therapeutic strategy, this “remote ATP hydrolysis” method provides a further mechanistic insight into the role of phosphorylated SMAD proteins in the development of HO.

In another rodent tenotomy model (without burn injury), treatment with the antibiotic echinomycin inhibited HO formation.[48] The proposed mechanism is that echinomycin inhibits hypoxia-induced factor 1-α (HIF-1-α), a signalling molecule thought to be

crucial to the process of chondrogenic differentiation of mesenchymal stem cells in HO.

It is important to note that all of the experimental and extant prophylaxes work by attempting to inhibit the cellular and/or biochemical pathways that are thought to cause HO. There are no published data on experimental or clinical treatments that have been designed to directly inhibit or disperse the mineral component of heterotopic ossification.

1.1.7 Current Treatment

1.1.7.1 Non-Operative Management

Rest, analgesia, nerve blocks, and nerve ablations form the mainstay of non-surgical treatments.[5] However, once HO has formed and matured, it has not been shown to regress or remodel significantly, so patients who remain symptomatic after optimisation of non-surgical management options will often require surgery.

1.1.7.2 Operative Management

In a civilian amputation study, 25% of patients were treated with NSAIDS, 8% with bisphosphonates, and 11% underwent surgery to resect the ectopic bone.[24] In a series of military patients, 19% required surgical excision, with a mean interval between injury and excision of 8.2 months.[22] Excision had a significant effect on the analgesic requirements of the patients: 63% were able to cease opioid analgesia completely. There is debate about the exact timing of surgery. If HO is excised too early then it may recur but waiting too long may delay the patient's rehabilitation and return to function. A systematic review of studies of HO excision after brain injury did

not find evidence to support the view that early surgery predisposes to recurrence.[49] With appropriate timing of surgery and secondary prophylaxis with NSAIDS and/or radiotherapy, recurrence of HO rarely requires further surgery. In a large series of patients who had undergone primary HO excision secondary to acquired brain or spinal cord injury, only 5.8% required further surgery due to recurrence.[26]

Despite the success of operative interventions in controlling HO, it must be stressed that these operations are technically extremely challenging and come with significant risks of adverse events such as bleeding and damage to remaining soft tissues.[35] Standard practice at the UK Defence Medical Rehabilitation Centre, Headley Court, is that amputee patients are non-weight bearing for 6 weeks after surgery to their stumps (personal communication). Given that these patients can have multiple operations for soft tissue reconstruction, any additional requirement for surgery due to HO excision can add to their already significant period of non-weight bearing and this can have lasting effects on their rehabilitation potential.

1.2 Pathophysiology

1.2.1 Signalling and Cellular Factors

There is significant controversy in the literature about the fundamental cellular and molecular mechanisms involved in acquired HO formation.[50-52] Candidate cell populations of mesodermal, ectodermal, and endodermal origin have all been proposed.[53,54] One of the key problems is that while there are many cell types that may be influenced to produce mineralisation *in vitro* or *in vivo*, this does not mean that they are responsible for HO in patients. Davies *et al*[55] reviewed the evidence for and against all of these candidates and concluded that it is most likely that HO

results from complex signalling networks involving multiple cell types (Figure 1-5). However, consensus is building to favour the direct role of multipotent cells of mesenchymal origin.[56]

One example of how intercellular signalling is important in the formation of HO comes from the work of Olmsted-Davis *et al.*[57] They used a mouse bone morphogenic protein (BMP-2) model to demonstrate that hypoxic adipocytes were required for the differentiation of stem cells to chondrocytes, which is a key early step in the formation of ectopic bone. In addition to illustrating the role of multiple cell populations in the formation of HO, this work demonstrates that local physicochemical environment may play a role. Tissue hypoxia may not only stimulate intercellular signalling but will also lead to reduced pH through cellular anaerobic respiration. Low pH will, in turn, have an effect on the chemical phases that are stable in that environment and may even be exploited for the purposes of preventing and treating HO (see Chapter 4).

Recent work has provided evidence that different cell types may even generate phenotypically distinct HO subtypes. In an $Acvr1^{R206H}$ knock in mouse model that phenotypically resembles the genetic from of HO (FOP), $Mx1^{+}$ cells produced injury-dependent intramuscular HO whereas Scx^{+} cells lead to injury-independent ossification of ligaments and tendons.[58]

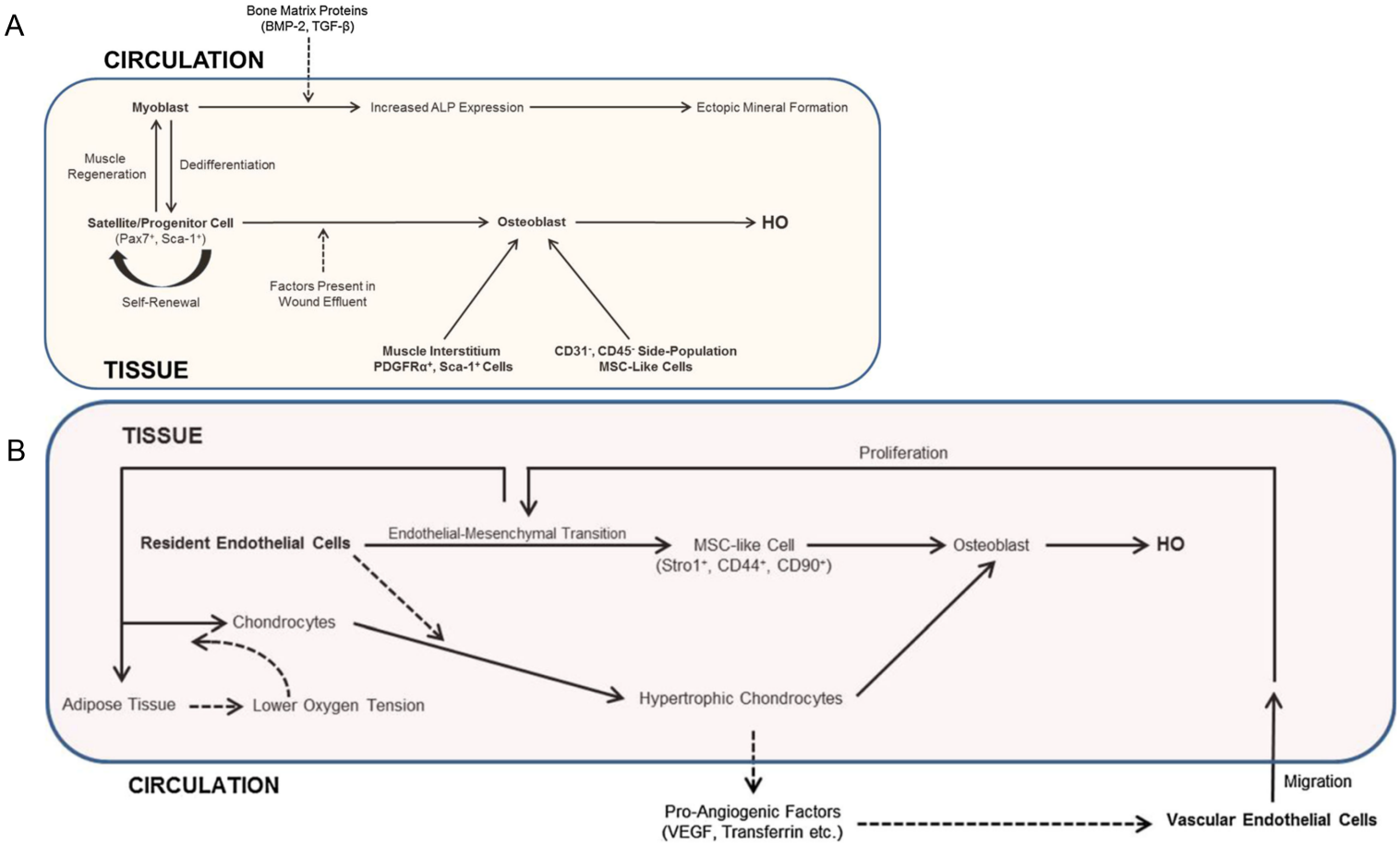

Figure 1-5: A) The potential direct and indirect contribution of well-characterised cells such as myoblasts and satellite/progenitor cells and the potential involvement of under-characterised resident cells such as muscle interstitium cells and side population MSC-like cells. B) The paracrine roles of endothelial cells, as well as the potential direct contribution of these cells through endothelial–mesenchymal transition (EMT). Reproduced with permission from Davies et al.[55]

The findings that HO may be caused by interacting networks of cells and that different cell populations can form distinct forms of HO raise several questions: Could the different distribution patterns of HO seen after different triggering events be due to different cell populations? Is HO seen after different causes even the same condition? Also, if more than one cell type can generate HO then is therapeutic blockade of one signalling pathway sufficient to prevent the condition clinically? Could the pathophysiological processes use alternative signalling pathways and cell populations to drive HO formation in spite of blockade at a single point? One way to overcome these concerns is to ignore the upstream signalling and cellular process and attempt to prevent or treat HO by inhibiting the formation of a key component of the final product of the process: hydroxyapatite. This is the fundamental principle that has been used to develop the novel treatment discussed later in this manuscript.

1.2.2 Inflammation and HO

There is significant support in the clinical[59,60] and basic science[61] literature for the central role of an exaggerated inflammatory response in the pathogenesis of HO. It is well recognised that patients who have suffered major trauma demonstrate multiphasic inflammatory dysregulation after injury with both acute and chronic components.[62,63] This seems to fit with the observed clinical experience of HO in a number of interesting ways. It might explain why HO develops after weeks to months and then progresses for months to years, after which time it stabilises and becomes quiescent.[50] It may also explain why the timing of excision surgery is important if recurrence is to be avoided.[64] Finally, this may suggest an alternative mechanism of action for NSAID prophylaxis in HO.

1.2.3 Ossification Mechanism in HO

It has been shown that there is upregulation in key osteogenic and chondrogenic gene transcripts (BMP2, BMP3, ALPL, COLL2A1, COLL10A1, COLL11A1, COMP, CSF2, CSF3, MMP8, MMP9, SMAD1, and VEGFA) in the soft tissues of high-energy combat wounds.[65] The upregulation of these gene transcripts suggests an endochondral (as opposed to an intramembranous) model of development of acquired HO, something that has been confirmed separately in an animal model.[66,67]

1.2.4 Early Detection

Currently, HO is diagnosed using imaging techniques (see Chapter 2). However, significant benefits may be gained by earlier identification and better risk stratification of those patients who will go on to develop HO. Reliable risk stratification and prediction allows clinicians to target prophylactic therapies at the right patients thus reducing the risk of harmful side effects in those who would never have developed HO anyway. The increasing knowledge of cellular and biochemical pathophysiology of this condition has allowed the development of several techniques that set out to achieve this goal. For example, one group has shown that serum levels of interleukin (IL) 3 and 12p70 and wound effluent levels of IL-3 and 13 at the time of first debridement predicted those would go on to develop HO.[59,60] However, it must be noted that these studies have not been validated in a civilian population and the authors stress that the complex interrelationship between the inflammatory markers remains incompletely understood.

The same gene expression data that was used to demonstrate that HO forms through endochondral ossification could also be used as a predictor of HO in combat

wounds.[65] There was a significant difference in the transcriptional activity of key osteogenesis-related genes between patients that developed HO and those who did not. This study may, however, be confounded by the finding that the HO group had a significantly higher injury burden, more bacterial colonisation, bigger wounds, and more amputations than the non-HO group.

1.3 Discussion

HO is a fascinating and debilitating condition (or perhaps group of conditions) that has been known about for a very long time. For many years it has been regarded as a rare complication of central nervous system injury or an inconvenient adverse effect of major surgery and so a handful of prophylactic approaches were discovered and developed to attempt to prevent it in those settings. However, since 2003, with the beginning of the conflicts in Iraq and Afghanistan and the subsequent on-going unrest in the region, our experience of this condition has changed completely. This is due to the alignment of a unique set of circumstances: increased incidence of blast injuries, increased incidence of combat-related amputations, and vast improvement in survival of even the most seriously injured patients. The result of this is that we have seen a significant increase in both the incidence and severity of this disease. The few prophylaxes that had been developed to prevent HO in the civilian setting have been shown to be either ineffective or inappropriate for the complex and often multiply injured military casualties, who are thus left at high risk of developing HO. Despite their severe injuries, these patients have been shown to have a high potential for good functional outcome with appropriate rehabilitation.[68,69] However, it has been claimed that the single biggest barrier to achieving this potential is HO. This

is because not only does it prevent patients from using the highly advanced prosthetics that are made available to them but also because the surgery required to excise HO introduces multiple long delays into their rehabilitation, which have a cumulative deleterious effect on their final functional outcome. This challenging problem has generated a large amount of research activity recently. This activity is almost exclusively focussed on understanding and inhibiting the signalling and cellular processes involved. What has become clear is that these processes are not only extremely complicated but that different processes may be involved in different cases or at different times. The lack of clinical effectiveness of the experimental treatments developed as a result of this approach may be evidence of the ability of the HO-generating process to “work around” a prophylactic blockade. It is also clear that there has been little or no exploration of the concept of targeting the key component of the final product of these processes, the bone mineral hydroxyapatite. It is the hypothesis of the author that direct inhibition or dispersion of the bone mineral itself could be developed into a treatment or prophylaxis for HO. This manuscript details the steps taken to explore this hypothesis. These steps include exploring the methods available for analysing bone mineral (Chapter 2), using the most appropriate of these methods to analyse samples of human HO (Chapter 3), discovering a means of inhibiting and dispersing hydroxyapatite *in vitro* (Chapter 4), developing this into a deliverable treatment (Chapter 5), and testing this in an animal model of HO (Chapter 6). The primary goal of this work is to provide the proof of concept for this novel method of preventing and treating HO in order to lay the foundations for human trials in the future. Ultimately, the author and collaborators

hope that this treatment will go some way towards fulfilling the unmet clinical need of this cohort of severely injured survivors.

2 ANALYSING HETEROTOPIC OSSIFICATION

2.1 Introduction

In order to disperse the end product of the pathological bone formation process, we first need to understand its physical and chemical structure. Additionally, this knowledge may be used to help develop a directed treatment such that pathological tissue may be targeted rather than normal bone. Given the importance of understanding the structural and chemical features of pathological bone, this chapter outlines the methods used to evaluate bone structure and chemistry (summarised in Table 2-1). A version of this review has been published in Advanced Healthcare Materials.[70]

Not all of the techniques discussed below have been used to analyse HO but all have been used to investigate biological mineralisation or mineralised tissue and were included because they have the potential to be used to study HO. Techniques have been divided into those that provide structural information and those that provide chemical information. This division is slightly artificial as many modalities can provide both types of information about mineralised tissue.

Table 2-1: Summary of analytical techniques discussed in this chapter

	Resolution	Information	In Vitro, In Vivo, Ex Vivo	Destructive?	Advantages	Disadvantages	Preparation Required	References
Histology	~10μm	Structure	In Vitro Ex Vivo	✓	Cost, widely used, minimal specialist equipment	Expertise required to interpret images	Sectioning, fixing, and staining	34,48,56,61,71-81
Fluorochrome Labelling	~10μm	Structure	Ex Vivo	✓	Gives temporal information about new bone formation. Can be used for longitudinal analysis if multiple administrations	Need to wait for fluorochrome label to be incorporated into newly formed bone	Fluorochrome administration, sectioning, and fixing	80,81
Transmission Electron Microscopy	Angstroms	Structure	Ex Vivo In Vitro	✓	Resolution	Two-dimensional projection of three-dimensional structure	Embedding and sectioning	82-85
Scanning Electron Microscopy	~1nm	Structure	Ex Vivo In Vitro	✓	Depth of field Resolution	Technically demanding at very high magnification	Coating of sample	76,78,86-88
Plain Radiography	~1mm	Structure	In Vivo	X	Cost Availability Simplicity	Ionising Delay to diagnosis	Nil	59,60,89,90
Microradiography	~10μm	Structure	In Vitro Ex Vivo	✓	Cost	Limited information	Embedding, sectioning	78,91
Micro CT	~1μm	Structure	In Vitro Ex Vivo In Vivo	X	Rapid Allows longitudinal analysis in vivo 3-dimensional dataset	Ionising Highest resolution not safe in vivo	Nil	48,57,61,75,87,92,93
Isotope Bone Scan	~1cm	Structure	In Vivo	X	Early In Vivo detection	Non-specific Ionising	Radioisotope administration	94
Near Infra-Red Fluorescence	~1mm	Structure	In Vivo	X	Gives information on process of mineralisation	Relatively poor spatial resolution	Administration of IR dye	81,95,96
MRI	~100μm	Structure Elastography	In Vivo In Vitro	X	Provides multimodal data	Requires highly specialised equipment	Nil for structural information Mechanical vibration for elastography	97-109
Ultrasound	~25μm	Structure Composition Elastography	In Vivo In Vitro	X	Cheap, safe, real-time, multimodal information	User dependent	Nil for structural information	110-118
Energy Dispersive X-ray Spectrometry	~1μm^3	Composition	In Vitro	X	Elemental analysis	Low efficiency at exciting x-ray fluorescence	Slow scan speeds	79,119
X-Ray Fluorescence Spectrometry	10μm	Composition	In Vitro Ex Vivo	✓/X	Femtogram quantities of elements detectable	Requires access to synchrotron for highest resolution data	Pellet formation for bulk XRF, embedding for mapping	120,121
Fourier Transform Infrared Spectroscopy (FT-IS)	~10μm (1.3μm using synchrotron)	Composition	Ex Vivo In Vitro	X	Chemical bond analysis	Requires access to synchrotron for highest resolution data	Nil	92,122-125
Raman Spectroscopy	~1μm	Composition	Ex Vivo In Vivo In Vitro	X	Non destructive No sample preparation Safe in vivo	Very large datasets when imaging volumes	Nil	34,61,126-129
X-Ray Diffraction (XRD)	Atomic (WAXS)	Composition	Ex Vivo In Vivo	✓/X	Can identify mineral species present	Not suitable for live cells/tissue Ionising radiation Destructive at higher beam energies	Grind sample to powder	79,130-133
Multi-photon	~0.1μm^3	Structure Composition	Ex Vivo In Vitro In Vivo	X	Tissue penetration Resolution High signal to noise ratio	Technically challenging Photodamage	Fluorescent labelling if needed Untreated samples can be used	134-139

2.1.1 Structural Analysis of Mineralised Tissue

2.1.1.1 Light Microscopy

Light microscopy covers a broad range of well-established techniques, most of which utilise visible light reflected from or transmitted through a sample (Figure 2-1). This enables direct visualisation of tissue and cells as a result of differences in their optical properties. While the theoretical resolution of light microscopy is less than 1μm, this is limited by the wavelength of light and the poor structural contrast of biological samples in their unprocessed form.[71] Light absorption contrast may be increased by selectively staining components of interest with chemical dyes.[72]

Histology remains a very popular modality for investigating mineralisation both in HO and bone tissue engineering due to its relatively low cost and ability to provide insight into the biological response of the surrounding tissue. A significant disadvantage is that histological techniques are destructive, as they require the samples to be embedded in plastic or paraffin and then to be processed using chemical fixatives and dyes. Furthermore, processing of mineralised samples requires either specialised cutting techniques or a demineralising step, which is to be avoided if the researcher is interested in the mineral content. Histological techniques may be combined to provide counterstaining to reveal more than one component of interest.

While standard hematoxylin and eosin staining may be used, there are many specialist histological techniques for imaging mineralisation.[140] One of the oldest is the Von Kossa method, which uses a silver nitrate-based treatment that selectively

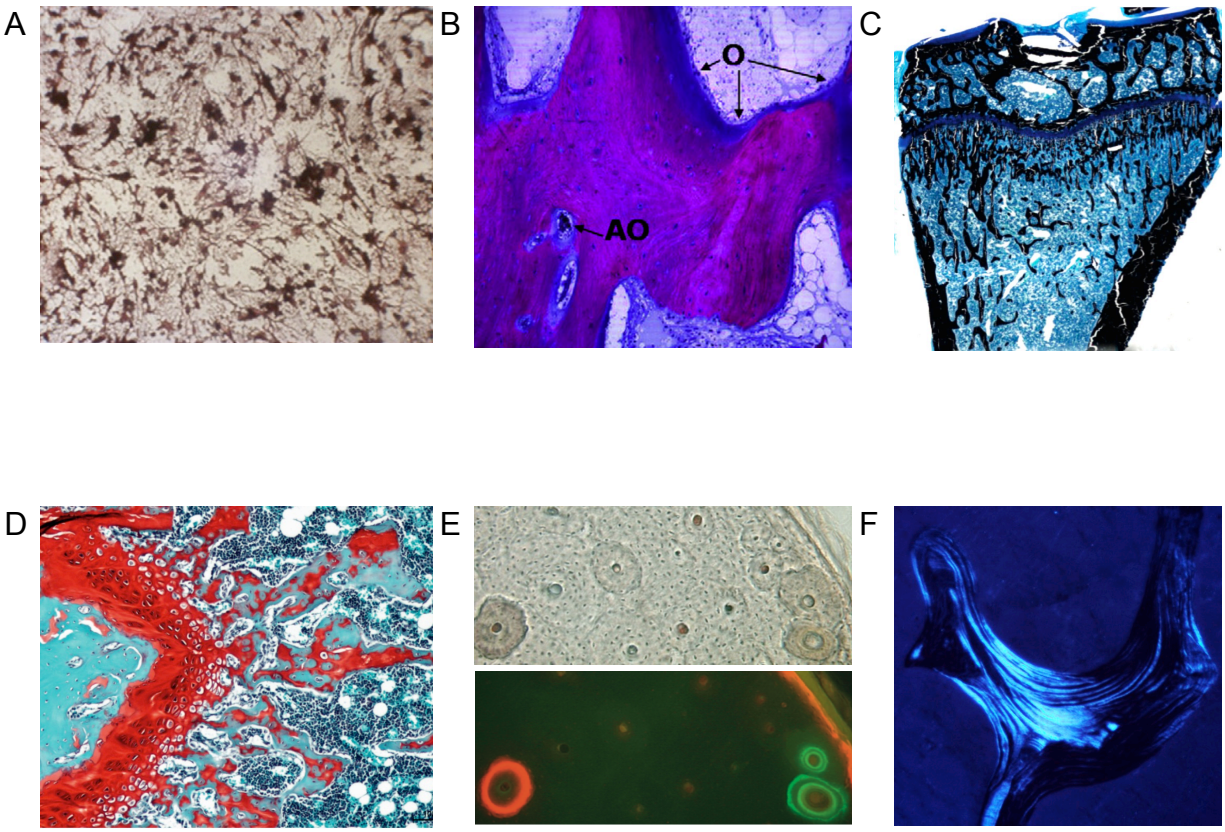

Figure 2-1: Examples of light microscope techniques used to visualise mineralised tissues. A) Von Kossa staining of a mineralising culture of rat calvarial osteoblasts. Black = mineralisation. Reproduced with permission from Zhang *et al.*[133] B) Sanderson bone stain of a sample of human combat-related HO. O = osteoid. AO = arteriole. Purple = mature bone. Blue = osteoid. White = unmineralised tissue. Reproduced with permission from Isaacson *et al.*[78] C) Von Kossa and MacNeal tetrachrome staining of a rat proximal tibia. Black = mineralisation. Light blue = marrow contents. Dark blue / purple = cartilage. D) Safranin O with alizarin red counterstain of the growth plate. Green = mineralisation. Orange = cartilage. Black = cell nuclei. E) White light (upper image) and ultraviolet light (lower image) of cortical bone after fluorochrome labelling with calcein (green) and alizarin (red) demonstrating osteon formation during the period of administration. F) Polarised light microscopy of lamellar bone demonstrating varying layers of collagen alignment in the lamellae. Subfigures C-F reproduced with permission from Allen and Burr.[72]

stains the mineralised tissue in a sample.[73] In a modification of this staining process, von Kossa tetrachrome, osteoid is also visualised in blue as compared to the black colour of mineral. More recent examples are: Alizarin red staining of mineralisation in mesenchymal stem cell (MSC) cultures treated with HO wound effluent, *ex-vivo* samples of HO from rodent burn model using Safranin O, Picrosirius Red, and aniline blue, Picrosirius red dye used in mouse Achilles tenotomy model, Masson's trichrome staining in examining *ex vivo* ectopic bone and osteoid formation in dog HO model (ceramic implantation), Masson's trichrome in human combat-related HO samples, and Sanderson's bone stain used to analyse bone and osteoid formation in combat-related HO.[34,61,75-78]

Immunohistochemical staining is a refinement of standard histological processing that allows identification of proteins relating to the cell biology of tissues. The principle of this technique is the conjugation of a dye molecule to an antibody that will bind to a specific target protein of interest. Fluorescence microscopy is then exploited to image the distribution of the labelled antibody without any interference from unlabelled background tissue components, and hence a large increase in image contrast can be achieved. The protein target could, for example, be a tissue matrix component such as collagen or cell surface markers. Cell markers can indicate cell phenotype and stages of cellular processes such as proliferation and apoptosis. This offers the possibility to correlate changes in the hard tissue matrix to changes in cellular function, which may aid mechanistic understanding of different types of mineralisation. A common refinement of this technique is to use one antibody to bind to the target and a second, labelled, antibody to bind to the first. In mineralisation research, immunohistochemical staining has been used to highlight hypoxia-inducible

factor 1-alpha (HIF-1-α) in a mouse tenotomy HO model and in an *in vitro* 3D MSC mineralisation model.[48,79]

Examination of the particular cell types within HO or mineralising tissue can also be undertaken using selective staining techniques. Osteoclasts can be highlighted by tartrate-resistant acid phosphatase (TRAP).[93] Immunohistochemical analysis of alkaline phosphatase will highlight osteoblast activity.[56,74] Staining for lactate dehydrogenase can identify osteocytes and indicate viability.[141]

Fluorochrome labelling is a technique that provides information on the process of mineralisation. A fluorescent dye is injected into a live animal or human and acts as a substrate for mineralisation or binds to calcium as it is deposited into soft tissue. The tissue/bone sample is retrieved after an appropriate interval and analysed under ultraviolet light to reveal the labelled newly deposited mineral. The key information to be gained from this technique is the rate and location of new mineral deposition. In humans, the antibiotics tetracycline or doxycycline are commonly used as fluorochromes. In an animal study on ectopic mineralisation using BMP-loaded HA scaffolds, calcein, xylenol orange, and alizarin red have been used to demonstrate the rate of mineralisation at different time points.[80]

2.1.1.2 Plain Radiography

Plain radiographs are commonly used in clinical practice for diagnosis and surveillance of pathological mineralisation (Figure 2-2B). The sample or patient is illuminated with a short pulse of X-rays. The detector collects transmitted X-rays, which are attenuated to different extents depending on the elemental composition of

the sample. Regional density and thickness of the sample or structures within the sample can be inferred. Highly radio-dense matter, such as calcium in mineralized tissue, absorbs or scatters the X-rays more than less radio-dense components leading to the formation of a “shadow” image on the detector. X-radiation is ionizing and therefore potentially damaging to live tissue but controlled and sparing use can mitigate the risk to acceptable levels. *Ex vivo* and *in vitro* samples of mineralising tissue are not adversely affected by the low doses of radiation required to form a routine image. Advantages of radiography are its relative low cost, rapid acquisition, and suitability for use *in vivo*. One significant disadvantage is the delay between the start of mineralisation and the time that it becomes detectable. For example, after head injury, it takes approximately 4-5 weeks for HO to be detected by this method.[89] There is a similar time delay in surveillance of combat-related HO in humans and blast-related HO in a rat model.[59,60,90] Another disadvantage of plain radiography is that the images produced are not spatially resolved in three dimensions making it less suitable for quantification of volume of HO or for pre-operative planning.

Microradiography is used for monitoring calcification *ex vivo*. The macroscopic technique is modified by sectioning the sample, embedding it in a radiolucent material, and placing the sample in direct contact with the detector. Isaacson *et al* used this technique to highlight the hypervascularity of HO samples excised from civilian trauma patients (Figure 2-2A).[78] Despite its relative simplicity, microradiography can provide information on calcification with a spatial resolution of approximately 10 μm.[91]

A

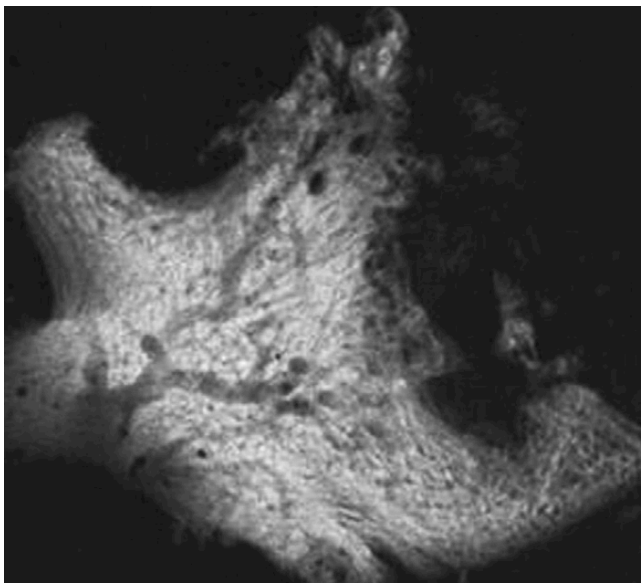

B

Figure 2-2: Radiographic imaging of human HO. A) Contact microradiograph demonstrating an extensive vascular network. Reproduced with permission from Isaacson *et al.*[78] B) Macroscopic clinical plain radiograph of a left femur with extensive terminal and medial HO. Reproduced with permission from Potter *et al.*[34]

2.1.1.3 Electron Microscopy

Electron microscopy relies upon the short (de Broglie) wavelength of electrons to provide higher resolution images than is possible using visible light. Scanning and transmission electron microscopy are able to produce structural and chemical information relevant to mineralisation research. The structural information is discussed here. For the chemical techniques, see sections 2.1.2.1 and 2.1.2.2 below.

2.1.1.3.1 Scanning Electron Microscopy (SEM)

SEM is used to provide information on the topography of a sample surface through the back-scattering of electrons or the generation of secondary electrons. Secondary electron mode is the most common imaging mode found on SEM systems and

involves the production of high energy electrons ejected from the surface atoms of the sample upon excitation by the incident electron beam. The intensity of the secondary electrons reaching the detector is strongly dependent on the angle of the sample plane probed by the incoming beam relative to the plane of the detector and therefore samples with large changes in topography will produce large changes in image contrast. The fine lateral resolution of this technique (around 1 nm) and a large depth of field make SEM particularly suited to imaging three-dimensional engineered constructs or trabecular structures within bone. As an example, SEM has shown utility in evaluating calcium phosphate coating and biomineralisation of an electrospun polycaprolactone model in an *in vitro* study of ectopic mineralisation.[87] It has also been used recently to analyse the microarchitecture of calcium phosphate ceramics before implantation into rats, rabbits, and dogs as part of an ectopic ossification model.[76] In addition to the insights gained through transmission electron microscopy (TEM), Scaglione *et al* used SEM to define microarchitecture, and pore size and shape of their scaffolds before seeding with MSCs.[142] Once the scaffolds had been seeded with MSCs but before they were implanted into the murine model, they were able to demonstrate that a certain scaffold architecture caused polarisation of the cells with subsequent alteration in their bone extracellular matrix deposition behaviour.

Backscattered electron imaging modes detect the reflection of beam electrons scattered elastically after interaction with atoms in the specimen interaction volume. The image contrast is strongly dependent on the atomic number of the elements present within the sample. This relationship enables good contrast to be obtained of sample with very small changes in topography (of the order of tens to hundreds of

nm) and biological samples, which typically consist of light elements or elements close together in terms of their atomic number. This imaging mode is often used to identify chemical elements within the sample by analysing the characteristic X-ray emission from the elements when irradiated by the incident electron beam.

Backscattered SEM of *ex vivo* samples of combat related HO has provided data on the maturity of the trabecular structure.[78] Surface details over several orders of magnitude down to the nanometre scale can be detected which makes it particularly suited to studying the lamellar organisation of bone (Figure 2-3A).

One of the key advantages of SEM is its versatility in terms of rapid image acquisition over a huge range of magnifications and choice of systems available to accommodate biological samples. Traditionally, SEM samples require sputter coating of a thin layer of conductive metal in order to electrically ground the sample during imaging and prevent artefacts due to charge build up on the surface. Biological samples usually require chemical fixation prior to surface coating. Sputter coating processes may physically alter delicate and/or thin biological samples such as muscle sections but can be avoided by using a low voltage mode in some SEM instruments while maintaining a good lateral resolution and contrast. Alternatively, samples can be infused with substances such as osmium tetroxide, which improves the bulk conductivity of the sample. Environmental SEM (ESEM) enables characterisation of wet uncoated samples by maintaining a suitable pressure around the sample. The risk of sample damage from chemical fixation or coating is thus avoided but this comes at the penalty of restricted field of view as the electron beam becomes increasingly attenuated the further away the sample is. While electron

induced damage or chemical changes to samples may be a risk in any form of electron microscopy, the use of a gaseous sample environment in ESEM adds a further factor to the issue. To date, the precise impact of electron-gas-sample interactions are largely unknown, but should be taken into consideration when analysing imaging or spectral data.

For the analysis of samples relevant to bone engineering and bone disease, the choice of technique and whether the use of extensive chemical processing methods is acceptable depends largely on the nature of the sample and what information one wishes to extract from that sample. Samples consisting largely of hard matter such as excised bone or bone substitute are likely to be more robust against dehydration compared to soft tissues and hence the full range of SEM techniques are available to gain high-resolution images of sample microstructure. On the other hand, the impact of sample preparation techniques on samples containing a mix of hard and soft tissues/materials is likely to be varied. Some reports suggest that chemical fixation of cells and soft tissues may induce precipitation within the sample, which is obviously a concern if investigating the presence and composition of small mineral or amorphous deposits in the soft tissue components of samples.[143]

Despite these considerations, SEM offers a powerful tool for studying samples' physical structure and the most promising frontier in this field is the development of systems capable of acquiring and co-registering SEM data with optical fluorescence and X-ray imaging data. Although, to the best of our knowledge, such an approach has been untested on mineralisation samples under discussion in this review, the

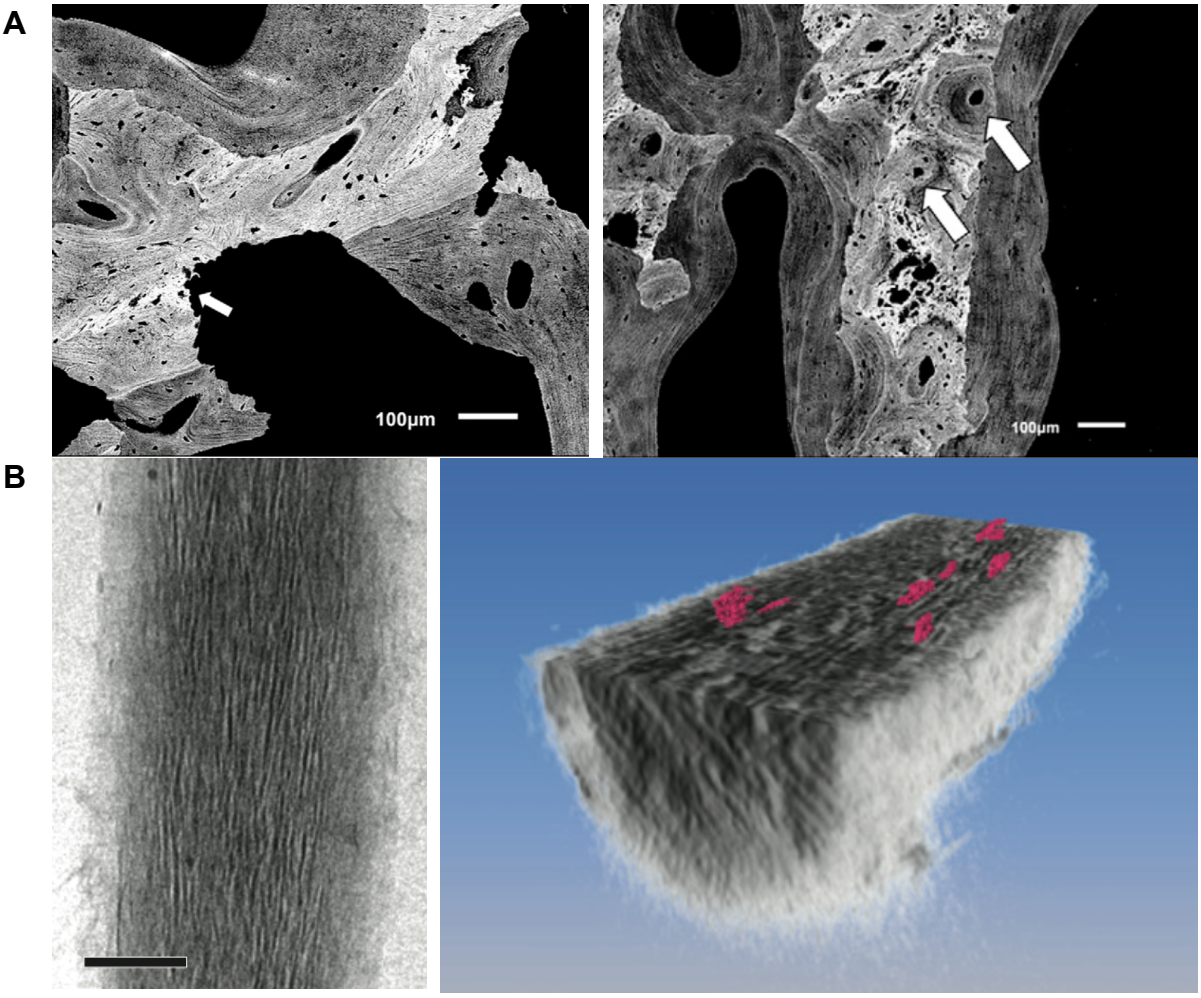

Figure 2-3: A) Scanning electron microscopy back scattered electron image of a sample of blast-related HO demonstrating osteoclast resorption pits (white arrows in left image) and osteons (white arrows in right image). Reproduced with permission from Isaacson *et al.*[144] B) Left: 2-D transmission electron microscope image of a cryosection of a collagen fibril from a mineralising horse tendon. Scale bar = 100 nm. Right: computer-generated 3-D reconstruction of the tendon with plate-like mineral crystals highlighted in pink. Reproduced with permission from Nudelman et al.[84]

concept has the potential to remove the number of sample preparation and handling steps between imaging with different modalities and hence aid the preservation of such samples.

2.1.1.3.2 Transmission Electron Microscopy (TEM)

TEM is an imaging technique used to determine the shape and surface structure of thin samples with Angstrom-scale lateral resolution. The physical principle behind image contrast in TEM depends on the mode of operation, but the most common mode (and the mode used to observe the shape of HA crystals) is called 'bright-field' mode. In this mode, the electrons can be treated under classical physics principles as being occluded or absorbed by the sample. Image contrast is then obtained because fewer electrons are transmitted through thicker regions (or regions containing elements of higher atomic number) compared to thinner regions, (or regions containing elements of low atomic number) which appear as dark and bright regions in the image respectively. The image formed at the detector can then be regarded as a 2D projection of the volume of the sample irradiated by the electron beam. The power of TEM resides in its ability to overcome the diffraction limits imposed on light microscopy systems. A generalised approximation of the Abbe diffraction limit states that the size of the smallest sample feature resolvable using an optical system is approximately equal to half the wavelength of the light. The De Broglie wavelength of electrons accelerated by the typical kV voltages used in TEM instruments would be under 1nm, which is several hundred times smaller than the wavelengths typically used in light microscopy (e.g. 532nm green laser line). It then becomes clear that TEM can resolve features in the pm-nm range and achieve atomic scale resolution, which cannot currently be achieved with light microscopy techniques. Consequently, TEM is suited to elucidating the mechanism of mineralisation at the nano-scale due to its ability to resolve individual mineral crystals (Figure 2-3B).[83,145] The utility of this technique is enhanced by the use of uranyl

nitrate staining to reveal the repeating structure of collagen fibrils thus allowing direct imaging of the interaction between the mineral and organic components of ectopic bone. Scaglione *et al* used TEM to define the deposition and orientation of collagen into HA scaffolds that had been loaded with MSCs and implanted ectopically in a murine model.[142] This insight allowed them to infer the mechanisms behind the observed differences in the bone produced by each scaffold.

The main drawback to using TEM techniques in general is the extensive sample preparation required to produce sectioned samples thin enough to be electron transparent and obtain good image contrast. As with any chemical or physical sample preparation process, there is the risk of altering the natural physical structure of the sample. Although this can be mitigated to an extent by cryofreezing samples, this process also requires a specialist TEM setup with a cryostage and the appropriate sample preparation equipment close to hand. Given the level of sample preparation required and low sample throughput, TEM may lend itself best as an end stage nanoscale structural analysis tool for samples known to contain evidence of early mineral formation rather than act as a 'screening process' to detect mineral in bulk samples.

2.1.1.4 Computed Tomography

The principle of computed X-ray tomography (CT) involves the use of X-rays to illuminate the target and a detector to measure the intensity of the transmitted X-rays. The key is that there is relative rotational movement between the sample and axis of the radiation such that an image-processing computer can build up a 3D dataset of radiodensity within the sample. Calcium phosphate in bone is relatively radiodense

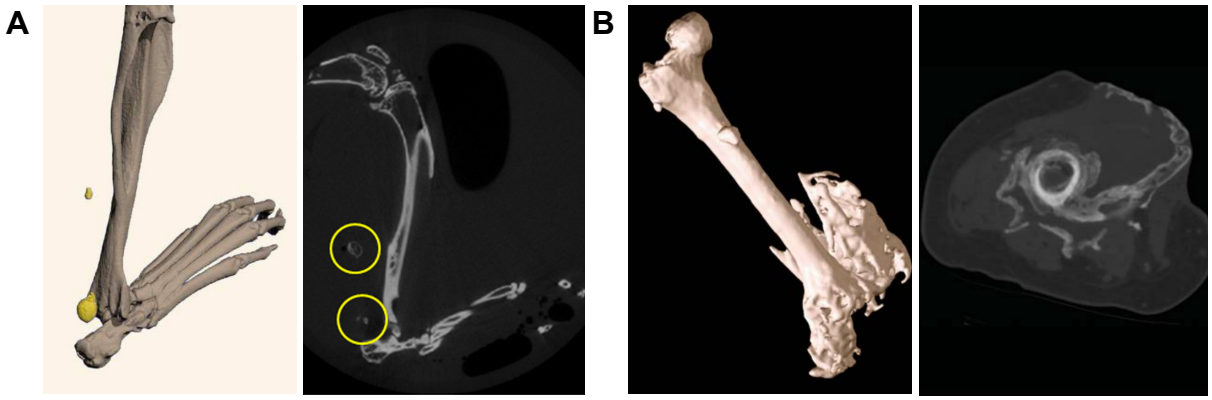

Figure 2-4: Examples of computed tomography in HO research. A) Micro CT 3-D reconstruction (left) and axial slice (right) of HO in a mouse Achilles tenotomy model. Yellow shading / circles indicates the HO tissue. Reproduced in a modified form under Creative Commons Attribution Licence from Zimmermann *et al.*[146] B) Clinical CT 3-D reconstruction (left) and axial slice (right) of a human femur after an above-knee amputation. These images demonstrate severe heterotopic ossification extending from the distal femur into the soft tissues of the thigh including the skin. Reproduced with permission from Potter *et al.*[31]

compared with surrounding soft tissue so this technique is well suited to detecting mineralisation in *in vivo*, *ex vivo*, and tissue engineering applications. A potential problem with CT is that the dose of ionising radiation received by the sample is much higher than with plain radiography due to the need to illuminate from many directions. However this does not prevent this technique from being used in clinical practice, *in vitro* culture, or *in vivo* models. Clinically, CT remains a common modality for the classification and diagnosis of HO and pre-operative planning for its removal.[147] Micro CT utilises exactly the same physical principles as clinical CT but at much higher resolution (less than 10 μm^3).[148] Resolution can be optimised by minimising the size of the sample so that the source-to-sample distance can be kept as short as possible while still keeping the entire sample in the field of view. Porter *et al* used micro CT to monitor cell-mediated mineralisation in a perfusion bioreactor and demonstrated that this modality could be used in a tissue engineering application

without detrimental effects to the cell culture under study.[92] One particular advantage of CT is that the dataset can be used to quantify the volume of bone formation in all types of mineralising construct including *in vitro* scaffolds, *in vivo* lesions, and *ex vivo* samples.[48,57,87,93,140] This is because CT can generate high contrast between hard and soft tissues meaning that relatively simple image thresholding-based methods can be used to segment the mineralised regions for analysis. Ultimately, being able to quantify exactly how much bone has been formed or inhibited is the single most important question to answer in most translational biomineralisation studies. Another major advantage of CT is that it can be used to monitor ossification serially over time. This has clear beneficial implications for the numbers of animals or samples required for experiments in this field. Two recent studies by Peterson *et al* demonstrated this longitudinal monitoring of HO in mouse *in vivo* implantation models.[61,75] CT is also able to demonstrate both surface and cross-sectional detail (Figure 2-4). The versatility of this technique in being able to generate striking visual images in addition to quantitative information, such as histomorphometric or bone mineral density data makes it a very powerful tool in mineralisation research.

Nano-scale computed tomography has become possible through the use of synchrotron beamlines due to the high flux and tight collimation of X-radiation possible in such systems.[149] However, technical differences in the beam geometry between traditional CT systems and synchrotron systems means that the latter use phase contrast, rather than beam attenuation, as their underlying physical principle.[131] This requires an additional step of phase retrieval when converting the raw datasets into images. Additionally, synchrotron systems may require additional X-ray focussing systems such as Kirkpatrick-Baez optics. The added complexity of

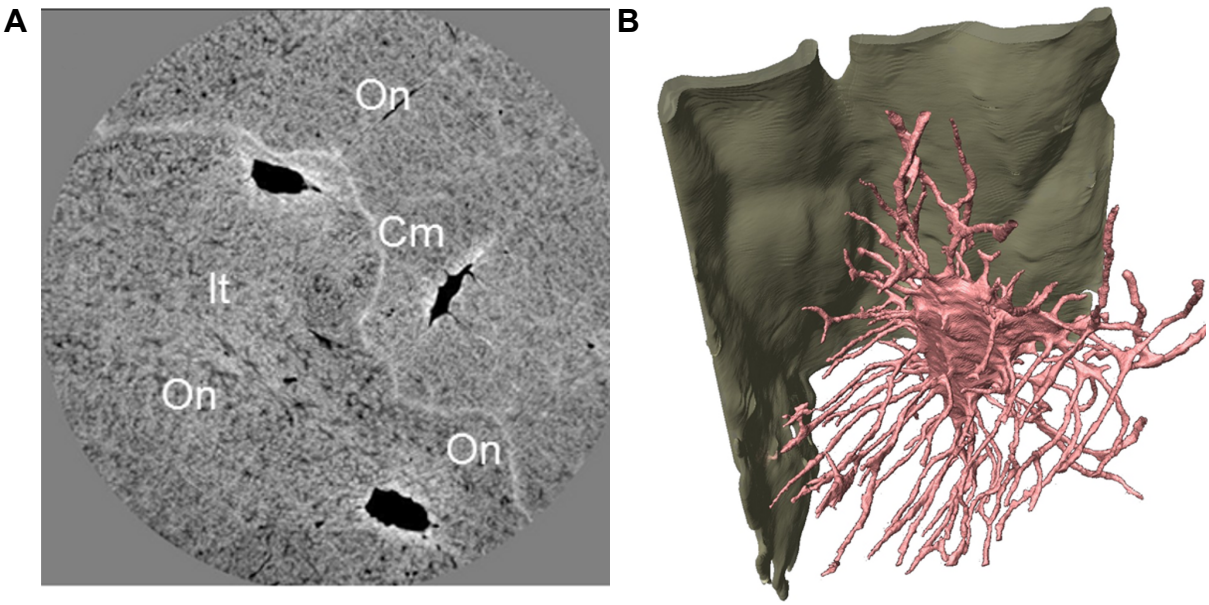

Figure 2-5: A) Transverse slice through a synchrotron x-ray nanotomography dataset. Empty spaces such as osteocyte lacunae and canaliculi are black. High density mineral is white. On = osteonal bone. It = interstitial bone. Cm = cement line. Field of view is approximately 100 μm. B) Computer generated 3-D rendering of a single osteocyte lacuna with associated canaliculi (pink) adjacent to a cement line (green) taken from the dataset in A). Images reproduced under Creative Commons Attribution Licence from Langer *et al.*[150]

synchrotron systems pose challenges but the advantages are also significant, including a volumetric resolution in the nanometre range and excellent compositional contrast in mineralized tissue (Figure 2-5).[150] The high resolution is particularly well suited to demonstrate the canalicular network in detail.[151] A recent application of synchrotron nanotomography has been to define the relationship between canalicular network morphology and the spatial distribution of mass density in human bone.[152] This study demonstrated that mineral density is highest near to canaliculi and lacunae. This supports the hypothesis that the raw materials for mineralisation are supplied from the extracellular fluid via the lacunar canalicular network. Synchrotron nanotomography has not previously been used to study samples of HO.

2.1.1.5 Isotope Bone Scanning

Isotope bone scanning is mentioned here for completeness as it has become less commonly used in clinical practice since the advent of other modalities, such as CT. It has not been used extensively in recent research literature for analysis of ectopic ossification or bone tissue engineering. The principle of this technique involves the administration of a radioisotope (usually technetium-99m conjugated to a bisphosphonate) that will localise to areas of metabolic bone activity. The radioisotope produces gamma radiation that is detected by a "gamma-camera" (Figure 2-6A). This technique is able to detect HO as soon as 2.5 weeks post injury but with the caveat that it is highly non-specific. Infection, tumour, thrombosis, and fracture can all provide false positive results.[94,153]

2.1.1.6 Near Infrared Fluorescence

Near infrared (NIR) light covers the wavelength range of 700 – 1000 nm and has two key properties of relevance to *in vivo* imaging: i) these wavelengths induce little to no auto-fluorescence in biological samples and, ii) tissues generally have a low molar attenuation coefficient in the NIR range.[95] Good tissue penetration depth and high signal to noise ratio can be achieved when transmitting NIR through tissue and NIR-emitting dyes are therefore excellent reporter molecules for tissue structures for *in vivo* or *intra vital* imaging. Generally, NIR imaging systems consist of a NIR source in transmission or reflection geometry with a sensitive CCD camera or an InGaAs detector (for less sensitive measurements but over the full NIR range). NIR dyes can be conjugated to chemical species that will highlight sites of mineralisation in a manner similar to fluorochrome labelling. Pamidronate has been conjugated with an

infrared fluorophore to demonstrate development of ossification in a nude mouse model.[96] A particular benefit of this technique in the context of monitoring ectopic mineralisation is that is it able to demonstrate mineralisation in its very early stages (Figure 2-6C).[81] The probe in this case was a calcium-chelating agent conjugated to an infrared fluorescent dye and this system was able to detect HO five days post injury, compared with five weeks for micro CT in the same model. This sensitivity to very early ossification could be extremely useful in *in vivo* experimentation as the ability to quantify mineralisation at much earlier time points would have a beneficial effect on animal welfare. However, while this technique may be able to detect mineralisation much earlier than micro CT, its spatial resolution is much lower and it does not produce a three-dimensional dataset.

2.1.1.7 Magnetic Resonance Imaging

MRI is a technique widely used in clinical practice and also, to a limited extent, in biomaterials science. This technique utilises a constant, strong magnetic field (0.5-1.5 Tesla in clinical settings) to align the spin axis of hydrogen nuclei parallel to the direction of the applied magnetic field.[97] A radio-frequency pulse is applied perpendicular to the magnetic field, causing the spin axis of the nuclei to tilt away from the direction of the magnetic field. Upon cessation of the pulse, the spin axis of the hydrogen nuclei realigns to the magnetic field, in a process called relaxation. This causes emission of radio frequency energy that is detected by receiver coils. Spatial encoding of the data is achieved by employing a secondary gradient coil, which manipulates the strength of the magnetic field across the subject such that only nuclei within a given ‘slice’ are forced to align with the magnetic field and respond to

the radio-frequency pulses. Sequential movement of the slice under analysis along the length of the subject then permits the building of a three-dimensional data set. Altering the timing, frequency, and intensity of the radio frequency pulses, allows encoding of different structural information.

One of the main benefits of this technique is that it is non-destructive and requires no sample preparation. It has the further advantage that it does not expose the sample to ionising radiation. These attributes would seem to make it ideal for monitoring progression of mineralisation in animal models but the cost, complexity, and long scan times have been inhibitory to its routine use.

Sites of developing HO in humans have been shown to have the following characteristic features on MRI: diffuse muscle hyperintensity on T2 weighted images (which enhances with contrast), enhancing hyperintense surrounding fascia, and non-enhancing foci within the muscles that were later shown to indicate the origin of mature HO.[98] As HO matures, T1 imaging shows areas within the lesion that have low signal intensity (relative to muscle) diminishing while areas isointense to muscle increased.[99] Signals indicating fat and cortical bone within the lesion become more intense. On T2 images, the intensity of the signal, which is initially high, decreases with maturity. However, some authors have questioned the specificity of MRI in the early stages as it can mimic infection (abscess, osteomyelitis), fat, and tumour.[100] Several groups have published further evidence of the heterogeneity of HO as seen on MRI with the only common characteristic linking their cases being a low-intensity rim around the lesion, which is contradictory to previous reports.[101,102] Further, there is evidence that MRI grossly underestimates the presence and extent of ossification

with only 10% of bony lesions being detected in one study.[99] MRI has been shown to be useful in the initial stages of analysis of mineralisation in implanted tissue-engineered structures but the signal becomes less intense as the mineralisation progresses and no additional data is provided that could be generated by simpler means.[103,104] One method for improving the specificity of MRI for bone mineral is to conjugate gadolinium, an MRI contrast agent, to a bisphosphonate.[105] The bisphosphonate adsorbs onto the surface of HA co-locating the gadolinium. In explanted polymeric scaffolds seeded with osteoblasts, MRI sensitivity was improved by using a gadolinium-alendronate conjugate marker.[106] One of the benefits of this technique is that it counteracts the image-degrading effects of ingrowing blood vessels in implanted bone constructs in animal models. MRI is also safe and effective for use in animal models. Several studies have used MRI to quantify mineralisation in bone graft substitute implanted ectopically in a rat model.[108,109] Further, MRI microscopy has been used to evaluate the mineralisation of tissue-engineered phalange constructs implanted into athymic mice (Figure 2-6B).[154]

MRI elastography is an experimental technique demonstrating how modalities that have previously generated only structural data may be modified to allow analysis of material properties of mineralising constructs. As an example, micro MRI elastography has been used to infer the tensile strength and elasticity of a mineralising tissue engineered osteogenic cell culture.[107] The possibility of using a non-invasive technique to infer mechanical properties has major implications for studying mineralisation in bone graft substitutes that have been populated with cell cultures. This is because traditional mechanical testing is incredibly challenging to carry out in the sterile environment required for cell culture techniques. Another

advantage is that this methodology of mechanical testing is non-destructive and may be more appropriate for immature cell-infiltrated scaffolds.

2.1.1.8 Ultrasound

Ultrasound is an established imaging modality in clinical practice and provides structural information based on tissue transduction and reflection of high frequency sound waves. This modality is based on electrically driven high-frequency (>20 kHz) oscillation of a piezoelectric crystal in the transducer probe. These oscillations are conducted via a coupling gel to the tissue of interest. Inside the tissue they are transmitted, refracted, diffracted, or reflected depending on the sound conducting properties of the tissue and the interfaces between tissues with differing conductive properties. The reflected sound wave is received by the probe and interacts with the piezoelectric crystal to generate an electrical signal pulse. The magnitude of this pulse and the time taken to travel back to the transducer is recorded and correspond to the impedance mismatch at the reflecting boundary between two tissue types and the depth of that boundary within the body respectively. In practice, the probe consists of an array of piezoelectric crystals, enabling processing of data from a two-dimensional plane or three-dimensional volume and conversion into an image.[110] Ultrasound has the advantages of being relatively cheap, safe, non-destructive to samples, and can provide real-time information. One disadvantage is that it is highly user dependent meaning that there is often poor correlation between results obtained by different operators.[116] In clinical practice, ultrasound has been used to diagnose HO before calcification becomes appreciable on plain radiographs or CT.[111-115] This is possibly due to the change in stiffness of soft tissues observed in what has been

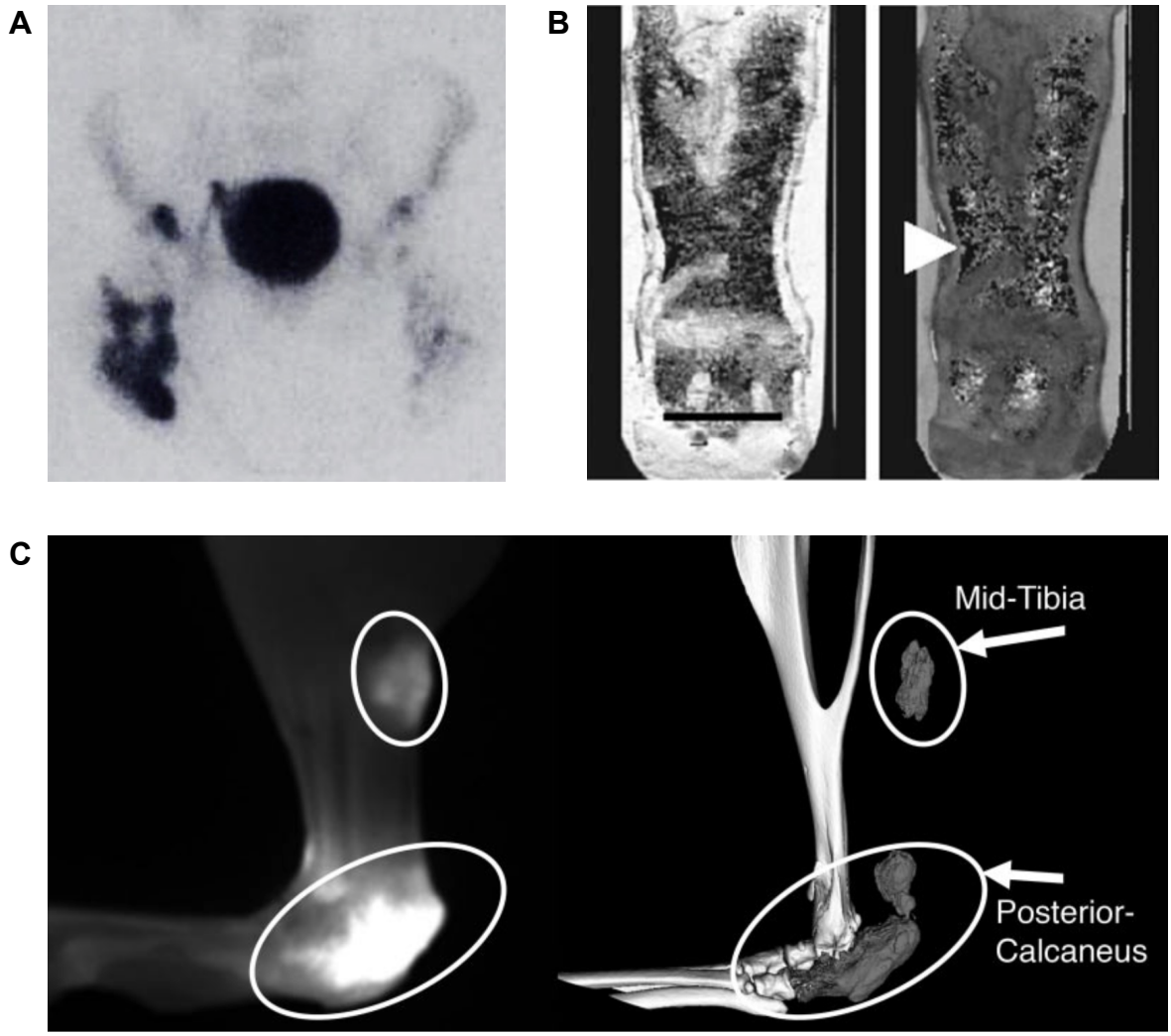

Figure 2-6: A) Radionucleotide bone imaging study taken three hours after injection of Technitium-99 into a patient with HO around the hip joint after CNS injury. The normal outline of the pelvis and lumbar spine can be visualised. Darker areas demonstrate high uptake in the developing HO and pooling within the bladder. Reproduced with permission from Orzel *et al.*[89] B) Quantitative proton density (left) and T2-weighted (right) magnetic resonance images of mineralisation within an engineered phalangeal scaffold. Scale bar = 5mm. White arrowhead = dense bone formation. Reproduced with permission from Potter *et al.*[154] C) *Ex vivo* near infrared (left) and microCT (right) images of HO formation in a mouse Achilles tenotomy model. The high signal in the near-infrared image is generated by a calcium-chelating infrared dye. White ovals = HO. Reproduced with permission from Perosky *et al.*[81]

termed "pre-HO".[128] HO is recognised using ultrasound by characteristic "zone phenomenon": outer sonolucent muscle zone, highly sound-reflective middle zone of mineralisation, and hypoechoic central zone.[113] Clinically, the use of Doppler

ultrasound has a secondary advantage in that as well as being able to diagnose HO, it may be used to rule out venous thromboembolism, which is a dangerous and common differential diagnosis of early HO in its inflammatory phase. Ultrasound has been used to monitor the progression of HO in patients with central nervous system injury, showing strong correlation with histological findings.[114] This study also used the Doppler shift of reflected sound energy to demonstrate vascular ingrowth into the new area of ossification. This may be of use in animal models of HO formation and in tissue engineering applications when researchers want to monitor scaffold implantation.

Ultrasound also has a role in *in vitro* mineralisation research. A novel ultrasound technique for analysis of mineralisation within a 3D scaffold has been developed.[117] In addition to high-resolution structural information (25 μm), this technique provides data on concentration, distribution, and particle size of the mineral phase. Mineralisation can be monitored in an animal model using ultrasound.[118] Researchers implanted mesenchymal stem cell-seeded 3D matrices into rats and were able to follow the osteogenesis, degradation, and calcification of these constructs over time. Ultrasound is relatively uncommon in mineralised tissue research but given that it does not rely upon ionising radiation, and requires no sample preparation, it may become more common in future.

2.1.2 Chemical Analysis of Mineralised Tissue

2.1.2.1 Selected Area Electron Diffraction (SAED)

This technique is an adjunct to TEM which exploits the fact that de Broglie wavelength of a high energy electron beam is within the same order of magnitude as

the typical atomic spacing in a crystalline material, leading to electron diffraction by the crystal structure.[155] A fraction of the incident electrons are scattered at a particular angle, which relates to the spacing between atoms in a particular plane of the sample, and shows as a series of ordered bright spots in an image. Rotation of the sample relative to the incident electron beam enables diffracted electrons from a range of angles to be detected sequentially to build a diffraction pattern covering a range of crystal planes. This pattern is unique to the composition and structural phase of the crystalline material within the sample. A 'selected area' of the sample is analysed simply by placing a thin metal strip with a small aperture underneath the sample to block all electrons except those coming from the region of the sample directly above the aperture. A significant advantage of this technique over x-ray diffraction is that it can be used to analyse a several hundred nm portion of a sample (microns) in contrast to bulk sampling. This is ideal for tissue samples containing small amounts of mineral whereas X-ray diffraction usually requires large (mg-1g) amounts of the material of interest to generate adequate diffraction patterns. This modality can provide information on the identity and spatial distribution of crystalline species present in a sample. For example, Hong *et al* used it to confirm the identity of crystals in murine bone as HA (Figure 2-7A).[83] Nudelman *et al* used SAED to demonstrate that the initial infiltration of calcium phosphate into mineralising collagen fibres is amorphous and that the characteristic diffraction pattern of HA develops later.[85] In the field of tissue engineering, SAED can be used to investigate the interface between implanted bone graft substitutes and host bone. De Aza *et al* implanted bioactive glass/ceramic composites into a murine model and used SAED

to demonstrate the presence and crystal orientation of HA in newly deposited collagen at the interface region.[156]

2.1.2.2 Energy Dispersive X-ray Spectroscopy (EDX)

This modality is another adjunct to electron microscopy whereby high-energy electrons strike a sample causing the ejection of electrons in lower energy shells. X-ray radiation is emitted as an electron in an outer shell moves to fill the gap. Each different element produces a unique series of peaks on an X-ray emission spectrum (Figure 2-7B). A major advantage of this technique is that it provides semi-quantitative evidence to corroborate qualitative interpretation of electron microscopic images. For example, this technique has been used to confirm the pattern of calcium and phosphorus deposition in mineralising horse-tendon collagen fibrils and the distribution of mineralisation on a synthetic collagen sponge.[85,157] Data processing techniques even allow two-dimensional mapping using this technique. For example, Koburger *et al* used it for phosphate mapping of mineralisation of the engineered hard-soft interface and Sasaki *et al* used it to confirm the distribution of calcium and phosphorus in a MSC populated cell scaffold.[79,158] Finally, as an example of the complementary use of SEM, SAED, and EDX to provide structural and chemical information in a mouse model of ectopic mineral deposition, see Kikkawa *et al.*[88] This group were able to determine the location of mineral deposition within muscle bundles, confirm its identity as a calcium phosphate, and compare the diffraction pattern to pure HA.

Limitations of EDX relate to how the nature of the sample can influence the detected emission spectrum. X-ray fluorescence will be emitted in all directions, with a portion

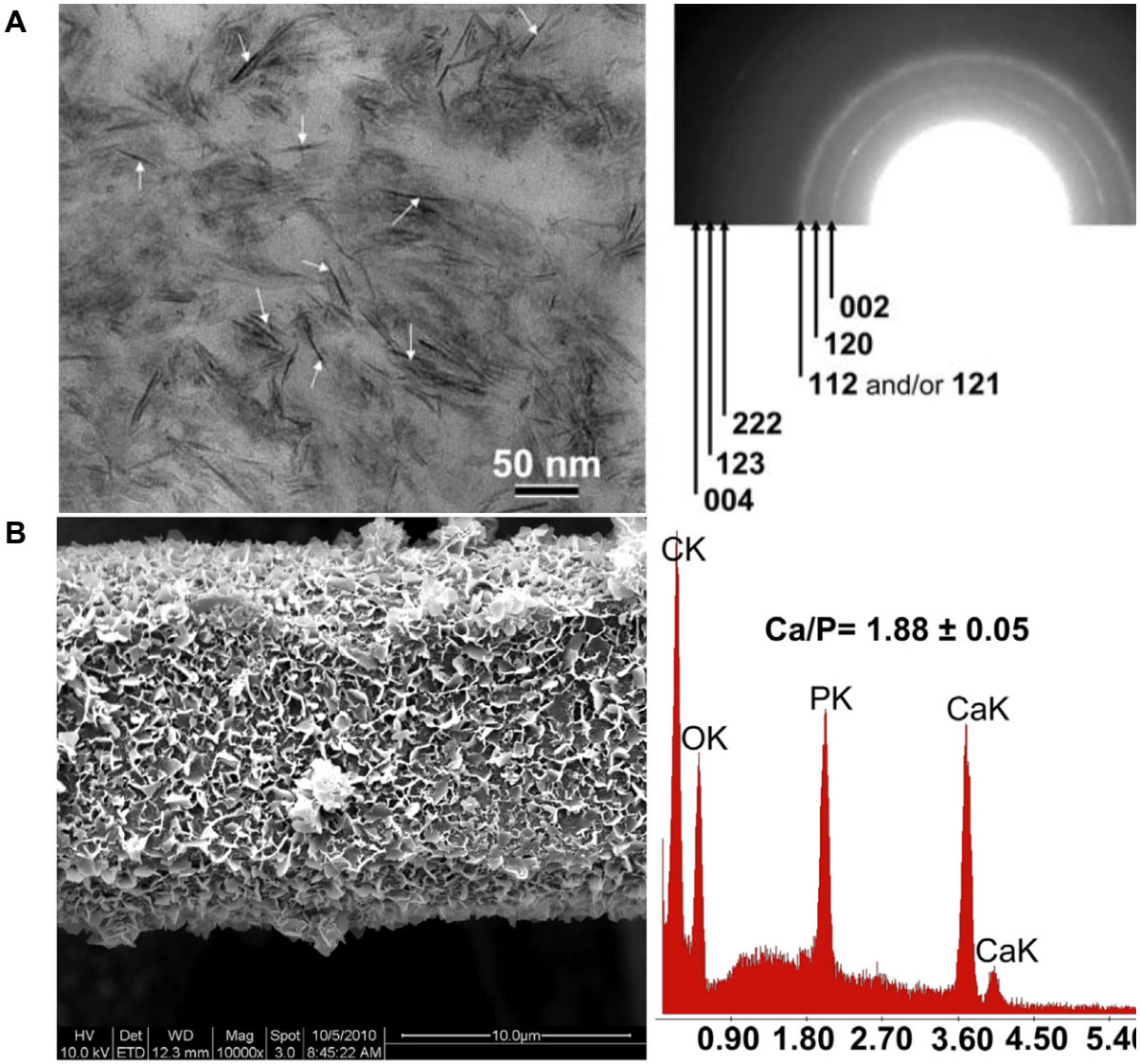

Figure 2-7: A) Left: Transmission electron micrograph of collagen fibrils containing crystals (white arrows). Right: selected area electron diffraction (SAED) pattern of the same image field. The EDX diffraction pattern confirms the identity of the crystals as apatite and demonstrates a continuous pattern, confirming that the crystals have no preferred orientation. Reproduced with permission from Hong *et al.*[83] B) Left: Scanning electron micrograph of a filament of mineral-coated electrospun polycaprolactone scaffold. Right: Energy dispersive X-ray (EDX) spectrum and calcium/phosphate ratio of the coating. Reproduced with permission from Vaquette *et al.*[87]

of this reaching the detector. A proportion of these X-rays will not leave the sample due to scattering events or attenuation and the influence of these effects on the

detected signal depends on the energy of fluorescent X-ray and the density and thickness of the material the X-ray must pass through. This can be a particular problem in rough samples where thicker regions are likely to attenuate the X-ray fluorescence signal more, reducing the signal-to-noise ratio and hence compromise accuracy of element identification. With respect to bone mineral research, this could pose a particular issue when attempting to characterise ion substitutions.

2.1.2.3 X-Ray Fluorescence Spectrometry (XRF)

Similar in principle to energy dispersive x-ray spectrometry (above), XRF can identify elements in a sample through the generation of X-ray spectra. However X-rays, rather than electrons, are used to excite the sample and such measurements are performed in a lab/benchtop scale instrument, often operated under ambient conditions. Much finer chemical sensitivity (femtogram quantities) can be achieved with this technique compared with energy dispersive X-ray spectrometry, particularly if the beam is synchrotron generated.[120] Relatively recent advances of this technique have included the ability to focus the incident X-rays to a microscale spot and raster over the sample surface, enabling elemental mapping with lab/benchtop grade XRF instruments. XRF analysis in this manner requires little to no sample preparation and fresh tissue samples can be analysed without any noticeable drying due to heating from X-ray exposure. Stahler *et al* used micro-XRF to map abnormal mineralisation by demonstrating low calcium and phosphorus signals in chick embryo tibiotarsi.[121]

Synchrotron-based XRF measurements and mapping utilise X-ray sources orders of magnitude brighter than the X-ray sources typically used in lab grade instruments, which further enhances the lower limit of detection of elements. The ability to

continuously control the incident X-ray beam energy and spectral resolution opens up a more refined subdivision of techniques known collectively under the term of X-ray Absorption Spectroscopy. A detailed discussion of such methods is beyond the remit of this thesis, but they essentially probe electron scattering effects at energies around the X-ray absorption edge of elements as a means of investigating the covalency, electronic structure, oxidation state and site symmetry of elements and compounds within a sample. Thus such methods go beyond identification of elements and into reaction dynamics of elements within their sample environment.

The application of XRF to bone tissue engineering and HO research has so far been limited in scope. Typically, its use has been bulk measurement of calcium phosphate ratios in pre-implantation ceramic materials.[159,160] However, an example of a more advanced application is the use of synchrotron XRF to produce elemental mapping of zinc and calcium in a rabbit zinc-doped HA implantation model.[161] XRF provided data to demonstrate the post-implantation distribution of this element. Thus elemental mapping using XRF is demonstrated to be an excellent technique for mapping the fate of the constituents of doped or substituted calcium phosphates being used as bone grafts. There are currently no published studies using mapped XRF to investigate elemental distribution in samples of HO.

In terms of limitations, care must be taken to consider how the sample topography and thickness may influence the XRF spectrum/elemental map in much the same way as EDX, albeit to a lesser extent. Some signal will still be lost within the sample but this can be partly offset by using the more intense X-ray based sources associated with XRF to create more excitation events in the sample per unit time.

The depth penetration of XRF depends on the elements under investigation and the intensity of the incident beam with general penetration ranging from tens to hundreds of μm. As a result, this is still largely a surface based technique in the context of bone samples and does not afford depth-resolved chemical mapping. Micro-XRF instruments have a very small depth of field and hence only regions of a sample surface within a few hundred micron window range of the detector will mapped accurately. For samples with large undulations (mm), this could simply be overcome by bringing the sample closer or further away from the detector.

2.1.2.4 Fourier Transform Infrared Spectroscopy (FTIR)

Infrared (IR) light can be absorbed by molecules within samples to cause stretching, twisting and rocking modes of their chemical bonds. The frequencies of light required to resonate with such modes are highly dependent on the constituent elements of a molecule and, unlike X-ray fluorescence spectrometry, the nature of the bonding between those elements. A broadband IR beam incident on a sample may resonate with multiple modes of several different chemical bonds creating a spectrum of well-defined absorption bands unique to the molecule. FT-IR is most commonly used to produce spectra for bulk samples but recent advances have meant that it can produce two-dimensional mapped data (Figure 2-8A) and even, using the confocal principle, a three-dimensional data-set in a non-destructive manner. Using a standard IR emission source, spatial resolution is in the region of 10 μm, but this may be reduced to 1.3 μm by illuminating the sample with a synchrotron unit.[122] FT-IR data can provide the following spatially-resolved information for mineralized tissue samples: mineral content, carbonate/phosphate content, crystallinity, the type of

carbonate substitution, the relative acid phosphate content, and collagen maturity.[122] In bone graft substitute bioengineering, FT-IR has been used to map the spatial distribution of HA and poly(D,L-lactide) in a bioglass-loaded composite foam.[162] FT-IR has also been used to demonstrate the evolution of calcium phosphate crystal phases in sites of heterotopic ossification in a mouse model.[125] This technique has yet to be used to analyse the chemical bonds present in human HO but given how valuable it has been in providing insights into physiological mineralisation, much may be gained by doing so.

2.1.2.5 Raman Spectroscopy

Raman spectroscopy has revolutionised the compositional analysis of samples in ossification research. Monochromatic laser light is used to illuminate the sample and is scattered inelastically by the chemical bonds within molecular species present, resulting in a shift in the wavelength of the light.[126] A chemical bond between two elements produces a unique wavelength shift of the incident light, which is detected as peak on a plot of Raman intensity against wavenumber, and hence mineral and collagen have distinct patterns of Raman peaks (Figure 2-8B). Depending on the species present, Raman spectroscopy is also sensitive to the chemical coordination around the bond of interest and orientation of the molecule within the sample matrix. Raman mapping can be performed by rastering a diffraction-limited laser spot over the sample surface and collecting a Raman spectrum at each point. The integrated intensity under a peak relating to a molecule of interest produces a grey level pixel value and hence changes in the image intensity representing differences in the abundance of that particular molecule across the sample. Lateral resolutions are

defined by the Abbe diffraction limits and hence have a theoretical resolution of the order of half the wavelength of light used. However, in practice, 1 μm is the limit of resolution of this technique and analyte sensitivity is in the nanogram range.[127] Three-dimensional chemical maps can be obtained by raising or lowering the sample with respect to the objective lens after rastering each plane in the same way as confocal fluorescence microscopy. One major advantage of Raman spectroscopy for analysis of biological samples is that there is minimal interfering signal from water, in contrast to FT-IR. Additionally, Raman spectroscopy can be considered a complementary technique to FT-IR in that it can analyse transitions such as those exhibited by centrosymmetric molecules.

The spectra generated by Raman spectroscopy show peaks specific for molecular bond bending, vibration, and rotation. In bone, the ν_1 phosphate vibration at 961cm^{-1} is the predominant peak with others at 438cm^{-1} (ν_2 phosphate), 589cm^{-1} (ν_4 phosphate), 1075cm^{-1} (carbonate substitution), 1256cm^{-1} (amide III in collagen), and 1677cm^{-1} (amide I in collagen).[126] Raman spectroscopy has been used to demonstrate that ectopic bone in a mouse burn model is compositionally identical to normal cortical bone.[61] Potter *et al* used Raman spectroscopy to detect "pre-heterotopic ossification" in combat-injured muscle by the appearance of mineral bands at 961 cm^{-1}.[34] The same group undertook a more detailed analysis of combat-injured tissue using this technique to demonstrate the early deposition of type I collagen followed by the appearance of mineralisation.[128] The maturation of mineralisation was then monitored spectroscopically by the reduction in the ratio of amorphous calcium phosphate to HA. This suggests that Raman spectroscopy may

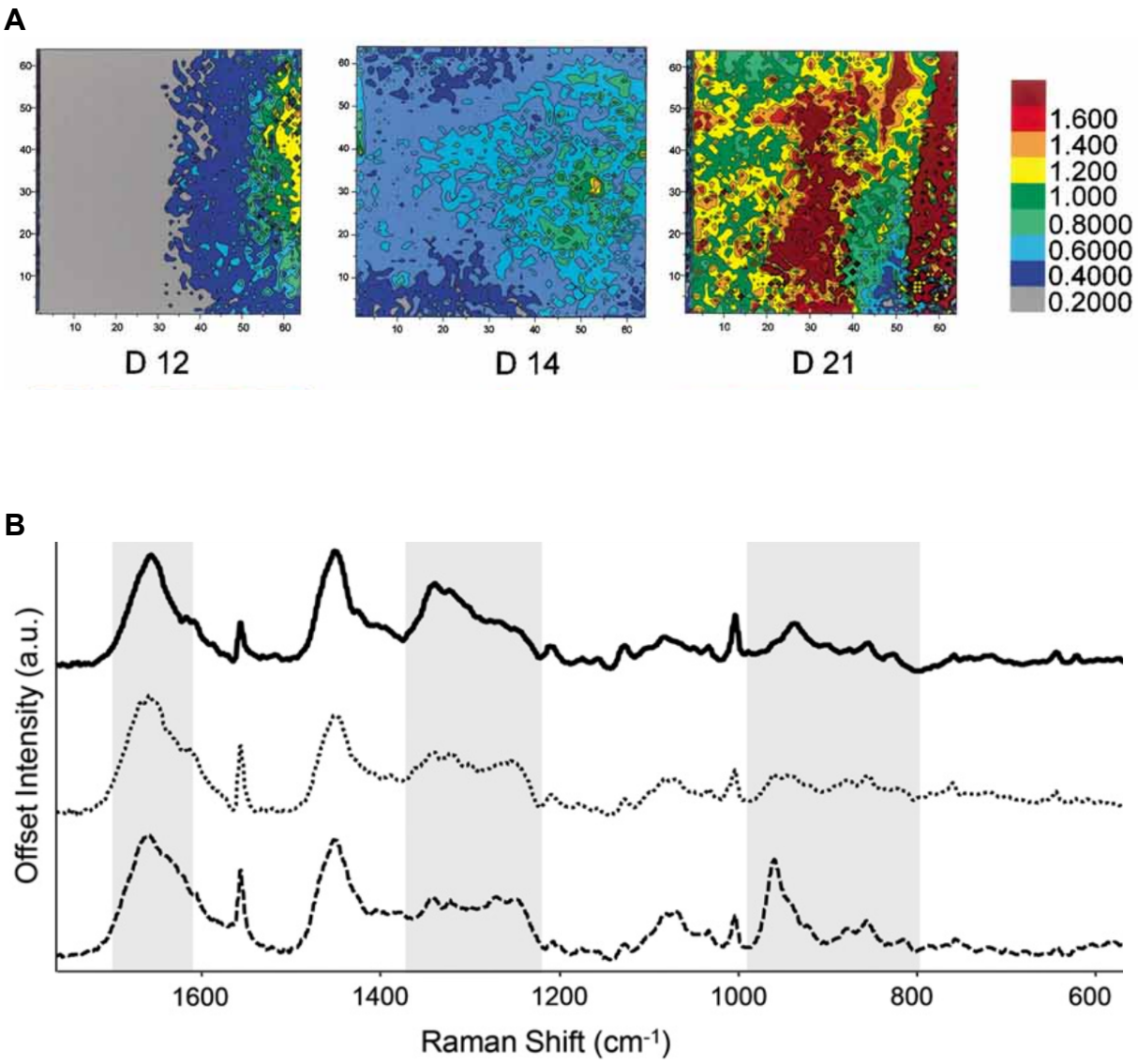

Figure 2-8: A) A sequence of Fourier Transform Infrared Spectroscopy mapped datasets of mineralising chick limb-bud mesenchymal cells taken at 12, 14, and 21 days of culture. The colours represent the ratio of mineral to matrix in the cultures. The field of view is 400 x 400 μm. Reproduced with permission from Boskey *et al.*[124] B) Raman spectra of normal muscle (solid line), immature HO tissue (dotted line), and mature HO tissue (dashed line) taken from human subjects. Shaded regions indicated regions where vibrational bands differ significantly. The most prominent feature of the mature HO spectrum is the peak at 960 cm^{-1}, which indicates a v_1 P-O stretching mode due to the presence of mineral in the soft tissue. Reproduced with permission from Crane *et al.*[128]

have a clinical role in the minimally-invasive detection and monitoring of HO, a concept supported by a recent pilot study by Harris *et al*.[163] Evidence that this concept is viable in living tissue is provided by Peterson *et al* who used

Raman spectroscopy to detect HO progression in a live mouse model.[75] This paper reports that HO may be detected as early as 5 days post injury using *in vivo* Raman. Ghita *et al* have shown that Raman spectroscopy is also a viable technique for prolonged *in vitro* monitoring of mineralising cell culture.[129] Over 28 days of culture they demonstrated the conversion of amorphous calcium phosphate into HA.

In terms of future prospects for Raman mapping and spectroscopy in the field of bone mineral research and engineering, developments are occurring across the field from lab-based research to remote diagnostic use. The development of advanced polarisation resolvable systems and cheaper commercially available longer wavelength lasers are enabling the orientation of bone matrix components such as collagen to be resolved at larger tissue depths. Raman micro-needle based spectroscopic methods have been developed by researchers for clinical applications to differentiate between healthy and diseased tissues. While the driving force for this has been early detection of cancer in a minimally invasive manner, the identification of a series of characteristic peaks specific to early HO or normal or sub-optimal bone healing may form the basis of utilising such technology in the clinic in time.

2.1.2.6 X-Ray Diffraction (XRD)

XRD is a technique that provides information on the crystal structure of a sample through the illumination of a sample with of a beam of monochromatic X-rays and the analysis of the unique pattern of intensity of X-rays scattered over an angular range. Elastic scattering of incident X-rays by a crystalline sample occurs because the wavelength of X-rays is comparable to the chemical bond lengths and because the atomic arrangement exhibits long range periodic order.[130] Importantly, the reflection

of X-rays from a crystal plane only occurs when the incident beam is at a precise angle to that plane. The detector is moved relative to the axis of the beam to detect the summation of radiation diffracted by various magnitudes. The degree of crystallinity, size and orientation of crystals, and crystalline chemical composition can all be determined by the resulting diffraction pattern. This is of particular interest in ossification research as it allows the mineral component of bioengineered or native tissue to be analysed. XRD is divided into wide-angle x-ray scattering (WAXS) and small-angle X-ray scattering (SAXS), which provide data on atomic and colloidal scale structural regularity respectively. The beam of X-rays may be generated by conventional means or by a synchrotron facility, which can deliver higher intensity radiation with controlled wavelength distribution, lower signal to noise ratio, and ultimately greater analytical sensitivity.[131] In addition to information on the identity of crystalline phases within a sample, the Scherrer method may be applied to XRD data to allow calculation of fundamental crystallite size and shape.[155,164] The most common use for XRD in mineralisation research is simply to compare the diffraction pattern of bulk samples of ectopic bone or engineered mineralised tissue to reference samples of pure HA or normal bone. For example, Sabou *et al* used conventional XRD to compare the mineral phase of *ex vivo* human HO with that of normal bone and found a high degree of similarity.[132] Similarly, Saito *et al* used XRD to confirm the presence of hydroxyapatite after ectopic implantation of a BMP2-derived peptide into a murine model.[93] Synchrotron XRD has been used recently to demonstrate the presence of octacalcium phosphate and dicalcium phosphate dihydrate in an osteoblast cell culture model with phase evolution into HA.[133] Synchrotron beamline XRD is able to detect smaller quantities of crystalline phases in a sample,

differentiate more components of mixed samples, and detect biological macromolecules. However, for the vast majority of biomineralisation research, laboratory XRD is sufficient.

2.1.2.7 Multi-photon Spectroscopy

The underlying principles of multiphoton microscopy (MPM) have been understood for decades but it is only recently that it has become a commonly used technique in the characterisation of biomaterials. The mechanism is that two (or more) long wavelength photons can interact simultaneously with electrons in the target sample to elevate them to a higher energy level than either could achieve alone.[134] As the electron returns to its resting state, it emits a photon with a shorter wavelength (higher energy) than the excitation photons. This is known as the anti-Stokes effect. The difference between coherent anti-Stokes Raman spectroscopy (CARS) and standard multiphoton imaging is that in CARS, the excitation photons are generated by two different lasers and have different wavelengths. By using longer wavelength excitation photons in the near infrared spectrum, it is possible to achieve greater fresh tissue penetration (up to 1mm) without any preparation or staining.[135,136] This is due in part to the reduction in autofluorescence of biological tissues at these wavelengths. Omelon *et al* have used MPM to demonstrate the presence of polyphosphates in areas of mouse vertebral bone remodelling.[165] This study used a fluorescent dye, DAPI, to improve detection of polyphosphates. The differentiation of human adipose-derived stem cells into HA-producing osteoblasts has been studied using CARS.[137] Liu *et al* used MPM to characterise their engineered polycarbonate scaffolds and analyse osteoblastic seeding.[138] This study demonstrated how MPM

provides greater sample penetration, less photobleaching, and higher signal-to-noise ratio than conventional single photon imaging. Villa *et al* have shown that *in vivo* MPM is possible, by using it to monitor integration and ossification of donor-cell impregnated scaffold constructs in mouse calvarial defects.[139] MPM in this study provided three-dimensional structural information highlighting the spatial relationships of osteoblasts, scaffold, and deposited mineral. Furthermore, this study highlights another feature of MPM, second harmonic generation, which can be used to image collagen in situ without any staining or preparation. This means that MPM can provide a full picture of the hard and soft components in an in vivo or in vitro mineralisation system.

2.2 Discussion and Future Directions In Imaging

2.2.1 Discussion

Pathological mineralisation in tissues can cause dysfunction in a broad array of organ systems. Its effects are dependent upon the anatomical location and can lead to significant problems as varied and serious as heart failure, loss of mobility, and blindness. HO is an outlier in this spectrum of disease due to the speed, volume, and degree of hierarchical organisation it displays. This fascinating problem is currently the subject of intense research activity relating to the biological stimuli and processes that cause it. However, the chemical and physical processes occurring at tissue level remain comparatively under-investigated. This is surprising given that tissue mechanics and chemistry are known be able to drive biological processes and cell differentiation. For example, work by Engler and Discher has demonstrated clearly that mesenchymal stem cells can be made to follow an osteoblastic lineage purely

through the stimulus of a stiff culture substrate.[166,167] The recent rapid advancement of techniques has allowed materials scientists to analyse the physical and chemical changes within pathologically mineralised tissue in an unprecedented level of detail. Critically, it is through an improved understanding of these material properties that new approaches to treating and preventing these conditions will be discovered and refined.

Despite all of the potential benefits that physicochemical analysis of HO tissue might bring, the limitations of this approach must be acknowledged. The modalities described in this paper are unlikely ever to be able to advance our understanding of the upstream biology involved. Meaningful elucidation of the complex interplay between tissue damage, inflammation, signalling pathways, and stem cell recruitment and differentiation cannot be achieved through observation of the mineral product, no matter how careful that observation may be.

2.2.2 Future Clinical Directions

One particularly promising experimental technique that could be used in the clinical setting in future is percutaneous Raman spectroscopy to diagnose HO earlier and with more certainty than is currently possible. The Raman laser light and return signal could be delivered transcutaneously via optical fibre within a needle to “interrogate” a region suspected of developing the disease. If the signal came back showing characteristics of mineral where there should only be soft tissue then this would be a strong indicator of HO rather than one of the differential diagnoses such as venous thromboembolism or infection. The possibility of using Raman in this way to provide an early and highly reliable diagnosis would enable clinicians to target prophylactic

therapies to those who needed it rather than exposing entire cohorts of patients to the adverse effects of these treatments.

Another potential use for Raman spectroscopy in this field may be during surgical excision. Once HO has matured into fully mineralised bone-like tissue, it is relatively easy to identify intraoperatively. In this case the surgeon can be sure that all of the tissue has been excised. However, waiting several months for the tissue to reach this level of maturity will adversely impact upon the rehabilitation of the patient. One of the reasons why surgical excision is not undertaken earlier is that, in its immature and only partially mineralised state, HO tissue is challenging to identify with certainty and the surgeon has to risk either excessive resection of healthy tissue or inadequate resection leading to recurrence. This situation is highly analogous to the dilemma faced by surgeons excising tumours. However, intraoperative Raman spectroscopy could be used to analyse the resection margins for residual immature mineralisation. The surgeon would then be able to operate earlier on in the progression of the disease and resect only tissue with developing mineralisation. This in turn would enable the patient to start their rehabilitation at an earlier stage with all the attendant benefits that this would bring. Given that Raman spectroscopy has already been used intraoperatively to confirm resection margins in neurosurgery, there is no conceptual reason why this could not be used during HO excision surgery.[168]

2.3 Conclusion

This chapter has demonstrated that there is a wide variety of techniques for analysing mineralisation and mineralised tissue. The length scale available for physical analysis ranges from a few nanometres to greater than one metre while the

chemical analytical techniques can demonstrate elemental composition, bond identities, crystallite characteristics, and macromolecular interactions. Also the applications are as numerous and diverse as the techniques themselves and include identifying the calcium phosphate phase within a single mineralising fibril of collagen, quantifying the degree of mineralisation within a cell culture or bioreactor or animal model, diagnosing HO in a patient, and visualising the true structure of the lacunar / canalicular network *inter alia.* The challenge for this project, therefore, is in selecting the techniques that can provide insights into the structure and formation of HO. In part, the nature of the samples will provide a practical limitation on the choice of techniques. For example, the samples of HO have already been collected and frozen, which means that it is not possible to administer fluorochrome dyes to the patients to determine the rate of mineral apposition. Also, cell culture forms no part of this work so those techniques adapted to this application will not be used. Nor will clinical diagnostic techniques because this is a basic science and *in vivo* proof of concept study. This still leaves many techniques available however, so the two questions that will help make the decision as to which to use are: 1) could this help to understand the structure of HO in a way that has not been done before and, 2) could this demonstrate a chemical property of HO that could be exploited for the purposes of prevention or treatment. The first question is based on the fundamental principle that bone is an active tissue that remodels according to the forces acting upon it. The physical history of the tissue is “written” in its structure. As such, understanding the physical structure of HO will provide evidence of the physical forces that have shaped it and possibly caused it. The second question is fundamental to the development of a chemical means of prevention or treatment of HO. If the identity of

the hard mineral component of HO is understood then a therapeutic agent can be tailored to attack it preferentially to normal bone. Also, it is not clear whether the mineral component of HO forms in the same way as normal bone. Chemical mapping of HO mineral and its soft-tissue envelope together may provide clues as to the mechanism of formation.

In summary, this review of mineralised tissue analytical techniques (along with their underlying principles, applications, and limitations) has provided the understanding required for the physicochemical analysis of HO samples detailed in Chapter 3.

3 PHYSICOCHEMICAL ANALYSIS OF HUMAN POST-TRAUMATIC HETEROTOPIC OSSIFICATION

3.1 Introduction

3.1.1 Structure and Function of Normal Bone

Before one can consider the structure of pathological bone, it is important to understand the structure of normal bone. Bone is a hierarchically-ordered composite material with levels of organisation from the molecular to the macroscopic scale.[120] By mass, bone is 65% inorganic mineral, 25% organic (cells and proteins), and 10% water. The inorganic mineral phase is almost entirely composed of nanocrystalline non-stoichiometric (calcium deficient) hydroxyapatite (HA) with various lattice substitutions and trace element inclusions.[169-171] This so-called “biological apatite” is relatively poorly crystalline compared to mineral apatite.[172]

The protein content of bone is 90% type I collagen, which provides a matrix into which the mineral phase is deposited.[173] The direction and arrangement of collagen fibres in bone varies according to bone type and anatomical location and is one of the causes of anisotropy.[174] Non-collagenous proteins make up the remaining 10% of the protein content of bone and are grouped into one of the following categories: proteoglycans, glycoproteins, small integrin-binding ligand N-linked glycoproteins (osteopontin, matrix extracellular phosphoglycoprotein, bone sialoprotein, dentin matrix protein-1, dentin sialophosphoprotein, and dentin phosphoprotein), osteocalcin, and osteonectin.[175,176]

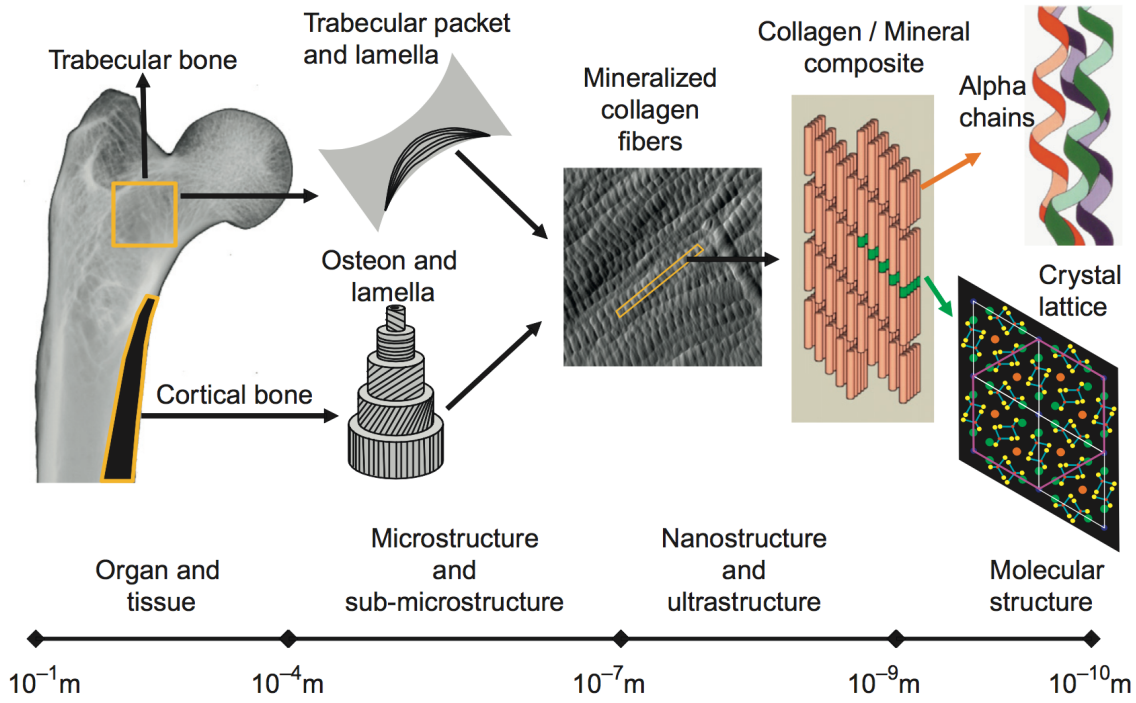

Figure 3-1: Hierarchical structure of bone from whole bone to crystal lattice structure. At the macroscopic level, a whole bone is composed of mesh-like trabecular bone surrounded by a shell of dense cortex. At the sub-millimetre scale, both trabecular and cortical bone have a lamellar sub-structure where the mineralised collagen fibrils are arranged in layers. The identity and distribution of bone cells relate closely to lamellar organisation at this length scale. At the sub micron scale, hydroxyapatite is seen to coat and infiltrate collagen. At the nanometre scale there is structuring of the hydroxyapatite crystal orientation and crystal lattice composition. Reproduced with permission from Burr and Akkus.[176]

There are three specialised cell populations in bone.[177] Osteoblasts are the product of mesenchymal stem cell differentiation and their function is to form bone through the production and mineralisation of extracellular matrix. Osteoclasts are multinuclear bone-resorbing cells descended from a monocyte/macrophage lineage. They resorb bone through the formation of a sealed microenvironment into which they actively secrete protons, chloride ions, and cathepsin K. Together, osteoblasts and osteoclasts form multicellular units to facilitate coupled bone remodelling, which is a process controlled by local and systemic signalling systems.[178] During the process of bone formation, some of the osteoblasts become trapped in lacunae and change

morphology to become osteocytes. These specialised cells form an interconnected network throughout the bony tissue and are thought to have multiple roles including calcium sensing, remodelling control, and strain detection.[179]

Vertebrates form normal bone through two main mechanisms: intramembranous ossification (disorganised woven bone is remodelled into the mature lamellar version) and endochondral ossification (mineralisation of a cartilage template by osteoblasts).[180] Multicellular functional units consisting of coupled osteoblasts and osteoclasts constantly remodel developing and mature bone in response to local strain.[181,182] This is known as Wolff's law, which plays a crucial role in driving the observed organisation of bone at multiple length scales.[14] Bone functions as a mechanical scaffold for weight bearing and is an effector mechanism for muscle contraction.[183] It also acts as an endocrine organ, storing calcium and phosphorus, and a haematopoietic organ generating blood components.[184] Finally, bone has a protective function to prevent damage to crucial organs such as the brain and heart.

3.1.2 Current Understanding of the Structure of Human HO

3.1.2.1 Macroscopic

On the whole organism length scale, one important feature of HO is that some anatomical sites are more prone to HO development than others. As described in Chapter 1, HO forms most commonly around the hips and, in the context of traumatic amputations, the distal end of the residual femur.

At the macroscopic level, HO has a highly variable morphology (Figure 3-2).[185] This makes it challenging to make generalisations about, but there are some common

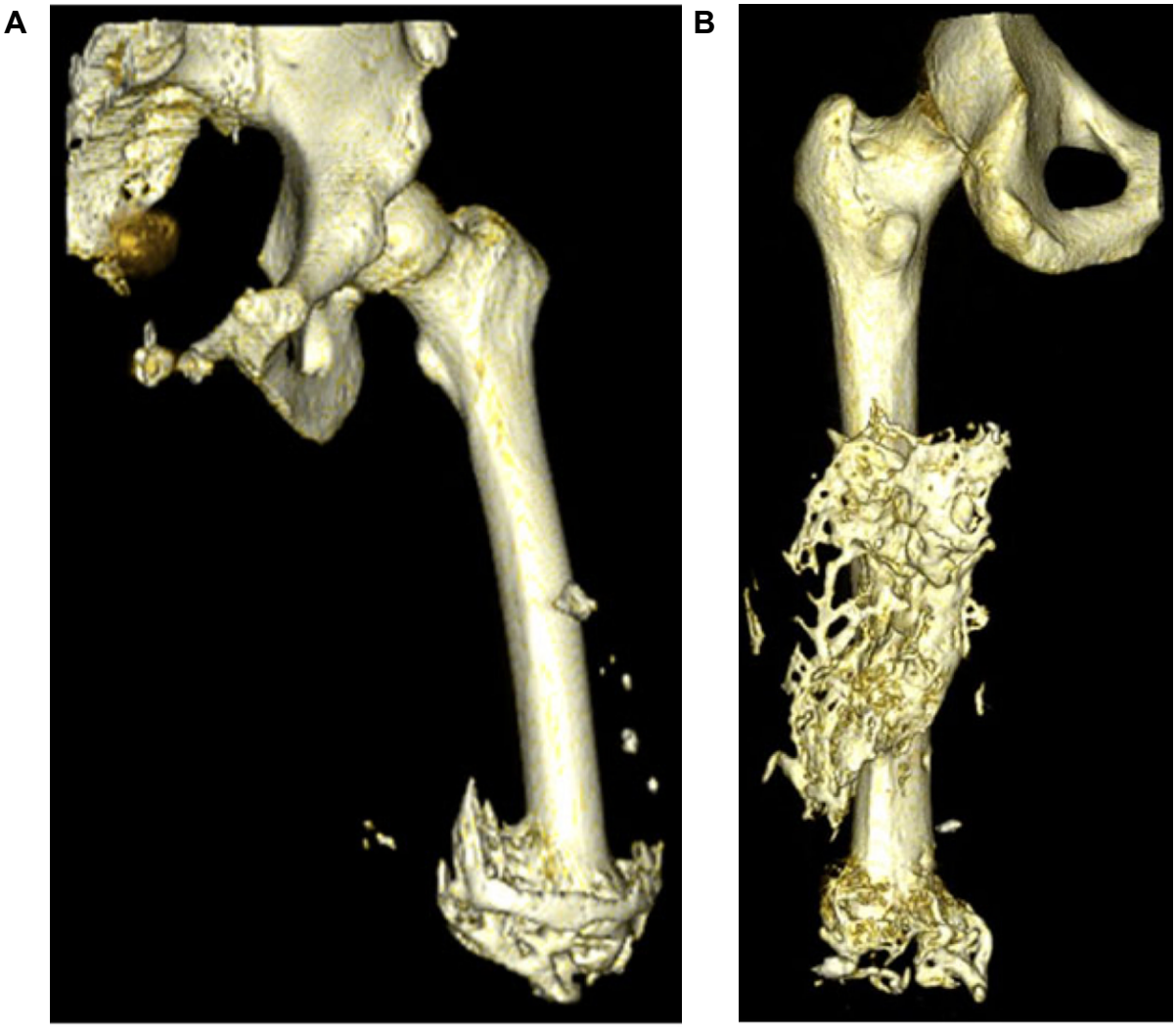

Figure 3-2: 3-D computed tomography reconstructions of the residual femora of patients with combat-related amputations and HO. These images illustrate the variable morphology and disordered architecture of HO on a macroscopic scale. A: inverted dome (convex side pointing downwards) shape of HO extending from the distal femoral residuum. Also, note the islands of HO not attached to the orthotopic bone. Characteristically, the growth of HO on the medial side is more extensive than that on the lateral side. B: There is HO developing from the end of the residual femur in this case but the morphology is different, with extensions growing distally rather than proximally and no preference for the medial side. There is also a large volume of HO at the level of the mid-portion of the residual femur in the posterior compartment. There are also small islands of HO. Reproduced with permission from Isaacson *et al.*[186]

patterns described in the literature. For example, in the simplest of terms, HO may be attached to, or separate from, normal bone. This forms the basis of a classification system that was derived from MRI scans of a non-blast trauma series of patients and describes HO as intramuscular (separate from normal bone), periosteal (attached to normal bone), or intermediate (associated with the insertion site of muscles into bone). Another morphological description in paraplegic patients divided cases into those with HO “needles “ or “blades”.[187] In post-surgical cases of HO around the hip, the most commonly used morphological classification system was derived by Brooker, who used the degree of bony bridging across the joint as the key indicator of severity.[188] CT scanning has allowed a more nuanced appreciation of the morphology of HO around the hip but the classification system that results is still very simple and merely describes which side of the joint is affected.[147] Similarly, HO in the residual stumps of blast amputees can form a wide variety of shapes but the classification system that has been developed is simply a description of the amount of HO as a proportion of the width of the residuum.[22]

A common theme of these classification systems is simplicity. Highly complex structures are reduced to a handful of categories based on simple parameters such as location or size. This is possibly due to the fact that these are clinical classification systems and so only a few parameters have clinical importance. Also, different morphological parameters are clinically relevant at different sites. Near a joint, the extent to which the HO interferes with movement is most important whereas in a residual limb stump, the relative diameter of HO is most important as it will guide prosthetics management. However, while these systems do have clinical utility, they do not provide fundamental insights into the condition. In the literature there are no

studies that quantify morphology more completely than these simple classification systems or compare morphology over time or between aetiologies.

3.1.2.2 Micro to Nano Scale

In the millimetre to micron length scale, HO also displays a disordered architecture. All of the structures found in normal bone are present but their spatial arrangement is abnormal. This was demonstrated by Isaacson *et al,* who used microradiography, SEM, and histology to demonstrate vascular channels, Haversian systems, mixed cancellous and cortical morphology, active remodelling, bone marrow, and adipose cells.[78] They also noted highly variable distribution of mineralisation within samples. In fact, the same group discovered such a significant variation in the degree of mineralisation within their samples that they hypothesised that the HO had been seeded by chips of normal bone displaced into the soft tissue during the injury.[144] As with their previous study, they describe HO as displaying a hybrid of cortical and cancellous morphology but they do not characterise it any further.

Crane *et al.* used histological techniques to assess human HO bone and described it as hypercellular and disorganised.[128] They also report identifying cement lines and marrow elements but reported that they saw no evidence of osteoclasts or remodelling activity. Histological data presented by Rangnathan *et al.*[50] have been interpreted as evidence that maturation of HO bone is more advanced at the periphery of the lesion compared to the centre but the rationale for this conclusion is not explored. It could equally be concluded from the published images that the peripheral portions of the lesion were tending towards a cortical morphology while the

central portions were predominantly trabecular; which would be more in keeping with other data.

Beyond these qualitative descriptions, there has been no attempt to quantify the structure of human HO at this length scale. Also, notably, there has been no published work using micro or nano tomographic techniques to examine the 3-D structure.

3.1.2.3 Molecular Scale

Chantraine *et al.*[189] excised HO from patients with spinal cord injuries and used atomic absorption spectroscopy on processed and finely ground samples to determine the calcium and phosphorous content as 40-236 mg/cm^3 and 28-113 mg/cm^3 respectively. They did not provide any data on how the calcium and phosphorous were chemically bound. Sabou *et al.*[132] also analysed processed and finely ground HO samples and used X-ray diffraction to confirm that the mineral component was crystalline hydroxyapatite. They used manual peak matching to confirm the presence of hydroxyapatite but did not provide any data on the presence of any secondary phases. There was no data on the crystal lattice parameters or, due to the sample preparation, on crystallite orientation.

In addition to their histological data described in 3.1.2.2 above, Crane *et al.*[128] used Raman microscopy to investigate the chemical species present in HO and confirmed that the predominant mineral phase was the same carbonated hydroxyapatite ("biological apatite") as found in normal bone. They were also able to provide information on different mineral species present such as amorphous calcium

phosphate (through deconvolution of the 960 cm^{-1} v_1 phosphate band) and the degree of carbonation of the hydroxyapatite (1070 cm^{-1} v_1 carbonate band). This work does not provide any quantification of the absolute amounts of amorphous calcium phosphate or carbonate, nor does it provide any spatial distribution data for the chemical species. Indeed, there are currently no published data on the spatial distribution of chemical species in HO.

3.2 Methods

3.2.1 Samples

Samples of heterotopic ossification were harvested from patients undergoing excision surgery at the Queen Elizabeth Hospital, Birmingham, United Kingdom. All patients gave their full consent for their tissue and data to be used for research purposes. All of the patients developed HO secondary to major traumatic injuries. The demographic details of the patients are included in Table 3-1.

All tissue transfer and handling was done with reference to the Human Tissue Act 2004 and local regulations. Ethical approval was acquired from the North West 5 Research Ethics Committee. The samples were frozen immediately after removal and transferred to the Human Biomaterials Resource Centre (HBRC) at the University of Birmingham. After release from the HBRC, the samples were kept at minus 80°C until required for sectioning or analysis. Sample preparation varied according to the individual techniques and is described in greater detail below. Throughout this chapter, sample numbers and patient numbers will be synonymous; i.e. sample 1 is from patient 1 and so on. Where there is more than one sample per patient, this is indicated by a suffix letter.

Table 3-1: Samples of heterotopic ossification excised from these patients were stored in the Human Biomaterials Resource Centre before being used in this study. IED = Improvised explosive device. This is an abbreviated version of the clinical data to ensure confidentiality.

Patient No.	Age at Injury	Sex	Mechanism	Anatomical Site	Limb Amputation	Interval Between Injury and Excision
1	23	Male	IED Blast	Right lower abdomen	Bilateral above knee amputation	28 months
2	30	Male	IED Blast	Right lower limb residuum	Right though knee amputation, Left above knee amputation	23 months
3	25	Male	IED Blast	Left lower limb residuum	Left above knee amputation, Right below knee amputation	No data
4	36	Male	Fall from height	Not recorded	No amputations. But multiple fractures and wounds.	No data
5	30	Male	Fall from height	Right lower limb residuum	Right below knee amputation	12 months
6	42	Male	IED Blast	Left lower limb residuum	Left above knee amputation	36 months
7	37	Male	IED Blast	Right thigh	Left above knee amputation	24 months

3.2.2 Plain Radiograph Methods

Upon receipt of the samples from the HBRC biobank, contact radiographs were performed as a screening investigation to establish the degree of mineralisation. These were taken using a Faxitron LX-60 (Faxitron X-ray LLC, Lincolnshire, USA) with exposure time of 10 s and beam voltage 25 kV. Contact radiograph images were digitised using the Agfa CR-30X radiography imaging system. Photographs of the samples were taken at the same time for comparison.

3.2.3 Micro Computed Tomography (MicroCT) Methods

Samples from patients 3 - 6 were thawed at room temperature for 1 hour and each was then cut into 3 smaller samples using hand tools. These were sealed in radiolucent cellulose tubes with wet tissue paper to prevent drying during scanning. Scanning was performed using a Bruker Skyscan 1172 microCT scanner (Bruker, Coventry, United Kingdom). The scan settings used were as follows: near camera position, tube voltage 70 kV, tube current 100 μA, 180^{o} rotation, rotation step 0.4^{o}, frame averaging 3, exposure time 950 ms, pixel size 3.51 μm, camera size 2000 x 1332 pixels, 0.5 mm aluminium filter. Each sample scan lasted for approximately 43 minutes. Scans were reconstructed using NRecon (software version 1.6.10.2, Bruker microCT) with the following settings: beam hardening correction 30, smoothing 3, ring artefact reduction 10. Reconstructed datasets were processed using CTan (version 1.15.4.0, Bruker microCT) as follows: 3-D automatic Otsu adaptive thresholding, 2-D black despeckling with 9 pixel limit, 3-D black despeckling with 100 voxel limit, and 3-D white despeckling with 100 voxel limit. The data were analysed using the 3D object tool in the same programme. Details of the algorithms used to

generate the quantitative data may be found at: http://bruker-microct.com/next/CTAn03.pdf. Tissue mineral density (TMD) calibration was performed with proprietary hydroxyapatite phantoms (Bruker) using the same scanning and reconstruction parameters as for the samples. Once calibration had been completed, TMD was calculated by binarising the dataset and then producing a VOI mask with which to selectively measure the greyscale values of the mineralised parts of the sample. 3-D reconstructions were created using CTvox (version 3.0.0 r1114 (64 bit), Bruker microCT).

3.2.4 Scanning Electron Microscopy (SEM) Methods

A different subset of samples was used for SEM. Samples designated for surface topographical investigation were incubated in hypochlorite solution overnight to remove any non-mineralised tissue. They were then mounted directly onto aluminium conductive stubs using adhesive conductive carbon discs, and sputter coated with a 50 nm coating of gold. These were studied using a Hitachi TM3030Plus (Hitachi High-Technologies Europe GmbH) in secondary electron (SE) mode with a beam voltage of 10 kV. Samples designated for cross-sectional analysis were treated in hypochlorite solution for 1 hour and then embedded in epoxy (EpoFix Low Viscosity Resin, Struars Ltd, Rotherham) under vacuum. They were then ground and polished before being mounted on conductive aluminium stubs as above. Conductive copper tape was used to prevent charging of the samples but no gold sputter coating was applied. They were studied using the same electron microscope in backscattered electron (BSE) mode with a beam voltage of 15kV.

3.2.5 Synchrotron X-Ray Diffraction (SXRD) Methods

Samples were thawed at room temperature for 1 hour and then embedded in optimal cutting temperature (OCT) compound (VWR Chemicals, Leuven, Belgium) under vacuum (20 kPa) using a Struers CitoVac (Struers Ltd, Rotheram, United Kingdom). After refreezing at -80°C overnight, the samples were equilibrated to -18°C and then cut into 100 μm sections using a Leica cryotome fitted with a tungsten carbide blade. Sections were mounted on glass microscope slides and allowed to dry in ambient conditions for 72 hours.

SXRD measurements were carried out on the I22 beamline at the Diamond Light Source (Oxford Harwell Campus, Didcot, UK). An incident X-ray energy of 14 keV was used (equivalent to a wavelength (λ) of 0.8856 Å) with a beam size of 10 μm^2 defined using vacuum tube collimation slits. Tissue samples were mounted normal to the impinging X-rays in transmission geometry onto a travelling sample stage to allow movement in two orthogonal directions perpendicular to the X-ray beam for SXRD mapping.

A wide angle X-ray scattering (WAXS) geometry was used to study the hydroxyapatite phase, by placing a 2D area detector (Pilatus P3-2M, Dectris, Baden-Daettwill, Switzerland) with a 1475 x 1679 pixel resolution (172 μm^2 optical pixel size) 270 mm behind the sample to give a q range of 0.1 - 4.7 $Å^{-1}$. SXRD maps were collected in high and low resolution modes corresponding to measurement increments (along each row of a mapped area) of 12.5 and 50 μm respectively, by moving the sample relative to the beam in an x and y direction, with each measurement having an exposure time of 15 s. A photo-diode was mounted on to the

beam stop to simultaneously record the attenuation of the direct beam to correct the data for varying transmission.

To aid data analysis, further measurements were taken for the direct beam, empty sample containers and water to allow diffraction patterns to be corrected for background and normalisation effects. Instrument parameters such as the X-ray wavelength, sample to detector distance and the peak shape profile were accurately determined using a lanthanum hexaboride (LaB_6) standard sample (Sigma Aldrich, Dorset, UK).

Diffraction data were normalised and background corrected using the DAWN software package (version 2.1, DAWN science).[190] Texture parameters, such as the direction and magnitude of the preferred orientation were obtained by integrating the intensity around the Debye ring of the (002) Bragg reflection over 360° and plotted against the azimuthal angle. Preferred orientation was determined as this reflection is perpendicular to the C axis of the hydroxyapatite unit cell. Peaks were fitted with a Gaussian shape to calculate the deviation angle φ of the crystallite axis with respect to the vertical axis.[191]

Note that scanning and data processing were undertaken with the assistance of Mr Slobodan Sirovica (PhD Researcher, Aston University, Birmingham) and Professor Owen Addison (School of Dentistry, University of Birmingham).

3.2.6 X-Ray Fluorescence (XRF) Methods

An initial attempt to investigate HO using XRF was performed on a single subsample of tissue from patient 2. This sample was defrosted for 1 hour from -80 to room

temperature and underwent no further preparation. More detailed XRF examination was performed on subsamples from patients 2, 3, 4, and 6. These samples were defrosted and vacuum embedded in OCT before being sectioned to 100 μm thickness in a cryostat using a tungsten carbide blade. Sections were air-dried on glass slides.

Elemental maps of the HO samples were generated using a Tornado M4 micro-XRF system (Bruker Nano Gmbh, Berlin, Germany) fitted with a Rhodium micro focus X-Ray tube and a polycapillary lens. The X-ray tube voltage was set to 50 kV and a tube current set to 300 μA. XRF spectra were collected pixel by pixel while the microfocus beam was rastered over the sample. Elemental maps were generated progressively in real time by gating around the phosphorous $K_{\alpha 1}$ (2.0137 keV), calcium $K_{\alpha 1}$ (3.692 keV) and sulphur $K_{\alpha 1}$ (2.30784 keV) X-ray emission lines in the spectra, creating an image where pixel intensity represented X-ray detector pulses integrated under an elemental peak at each measurement point on the sample. Maximum pixel intensity for each element was normalised to the peak pulses/eV value for that element across the whole sample. The instrument was set to map the selected area twice to generate a single averaged map for each element.

Maps were generated with a pixel resolution of 15 x 15 μm and a measurement time of 60 ms per pixel. The chamber pressure was lowered to 50 mbar in order to maximise sensitivity to the phosphorus signal, which can be attenuated by air. In a preliminary experiment, brightfield images of test samples (at x10 and x100 magnification) subjected to incremental vacuum pressures of 1000 mbar, 500 mbar, 200 mbar, 100 mbar, and 50 mbar did not reveal evidence of vacuum distortion.

Note that scanning and data processing for the XRF and Raman spectroscopy investigations were done with the assistance of Dr Richard Williams (School of Chemical Engineering, University of Birmingham, UK).

3.2.7 Raman Spectroscopy Methods

The sample from patient 4 (Figure 3-17C) that had undergone XRF analysis was reinvestigated using mapped Raman spectroscopy. Raman maps of the samples were collected with a confocal Raman microscope (Alpha300r, Witec, Ulm Germany), with a 785nm 250 mw diode laser (XTRA II, Toptica photonics, Munich, Germany) and a spectrograph (Acton SP2300, Princeton instruments, Trenton, NJ, USA) fitted with a 300 g/mm 750 nm blaze grating.

Raman maps were generated by rastering the beam over the samples via a 20x (numerical aperture = 0.45) objective lens with a 50μm step size and accumulating 3 spectra with an integration time of 1 second at each point. The laser power was measured at 60 mW (standard deviation 0.06 mW) at the back aperture of the objective lens. The data were collected and saved using the WITec control version 1.6 software (WITec, Ulm, Germany).

Spectral data cubes were pre-processed to remove cosmic rays using the instrument associated software (Witec Project v2.10, Witec, Ulm, Germany), exported in .SPC format. The .SPC files were imported into MATLAB (MATLAB 2016b. Mathworks, Natick, Massachusetts, USA), baseline corrected using an adaptive iteratively reweighted penalised least squares method,[192] and vector normalised. Least squares regression was used for fitting of individual Gaussian curves to each peak.

Octacalcium phosphate (OCP) was represented by the P−O stretching mode (ν_1) of the PO_4 group between 953-956cm^{-1}. Hydroxyapatite was represented by the symmetric stretching mode (ν_1) of the PO_4 group (P−O bond) between 958-961cm^{-1}. Collagen was represented across all maps by the amide I peak spanning 1620-1650 cm^{-1}. To best visualise the relative amounts, distribution of, and association between, mineral and collagen throughout the samples RGB image maps were produced by integrating over the sum of peaks of interest.

3.2.8 Nano Computed Tomography (NanoCT) Methods

Samples from patients 3, 4, and 6 were thawed, embedded in OCT, and sectioned as described in 3.2.5 (above). 100 x 100 x 4000 μm batons were cut from these sections by hand using a scalpel with visualisation via an optical microscope. These were then mounted onto aluminium sample-holding stubs. NanoCT was performed under vacuum at the ID16A beamline at the European Synchrotron Radiation Facility (ESRF) in Grenoble, France according to standard protocols.[150] This beamline uses Kirkpatrick-Baez X-ray optics to produce a moderately monochromatic focused beam (ΔE/E ~1%). Beam energy was set to 17.05 keV. The detector was the FReLoN HD E230-84, which is an ESRF-developed charge couple device. Sample areas of interest were scanned at multiple spatial resolutions to allow an overview followed by a closer interrogation of sub volumes of interest. Overview scanning generated a voxel size of 120 nm (giving a cylindrical volume of interest with diameter and height 245.76 μm). High resolution scanning generated a voxel size of 50 nm (cylindrical volume of interest diameter and height of 102.40 μm). Raw image data was collected at four different focus-to-sample distances for each rotation step (20.13, 20.99,

24.45, and 31.62 mm). Focus to detector distance remained constant at 1208 mm. Image reconstruction was performed as described previously.[150] Briefly, the raw data generated during scanning were in the form of magnified Fresnel diffraction patterns. These data underwent alignment, phase retrieval, and tomographic reconstruction to obtain the 3D distribution of the real part of the complex refraction index decrement, which is proportional to the electron density.[193] From this information, 3-dimensional mass density distribution may be ascertained. As the raw data were generated using hard synchrotron radiation, propagation and dynamical effects within the sample are negligible. Retrieved phase maps were converted to tomographic reconstructions using a filtered back projection algorithm (PyHST, ESRF). All reconstructed output images were 2048 x 2048 pixels in size. The output images were in the form of a stack of 2048 2-D greyscale cross sections. These data were thresholded and processed using CTan (version 1.15.4.0, Bruker microCT) to remove the canaliculi and any other features (such as Haversian canals etc.) apart form the osteocyte lacunae themselves (see Figure 3-19 C and D).

Note that scanning and data retrieval were undertaken with assistance from Dr Alexandra Pacureanu (ESRF, Grenoble, France) and Professor Owen Addison (School Of Dentistry, University of Birmingham, UK).

3.3 Results

3.3.1 Plain Radiograph Results

Radiographs show the marked heterogeneity of the samples in terms of the quantity and distribution of the radio-dense mineral phase (Figure 3-3). Samples 1, 5A, and 7 have no areas of high X-ray attenuation and are comprised of soft tissue only.

Sample 2 is predominantly composed of soft-tissue X-ray density with small islands of high attenuation material distributed in bands throughout. Sample 3 has a central area with cortical morphology surrounded by soft tissue containing islands of mineral similar to those seen in sample 2. Samples 4A-C are the most abundant and are relatively homogeneously trabecular in morphology at this macroscopic scale. These samples are comprised of multiple smaller fragments, which would be consistent with piecemeal removal during surgery. Sample 5B is entirely cortical and appears to be a piece of orthotopic rather than heterotopic bone. Sample 6 has mixed cortical and trabecular morphology with little soft tissue envelope.

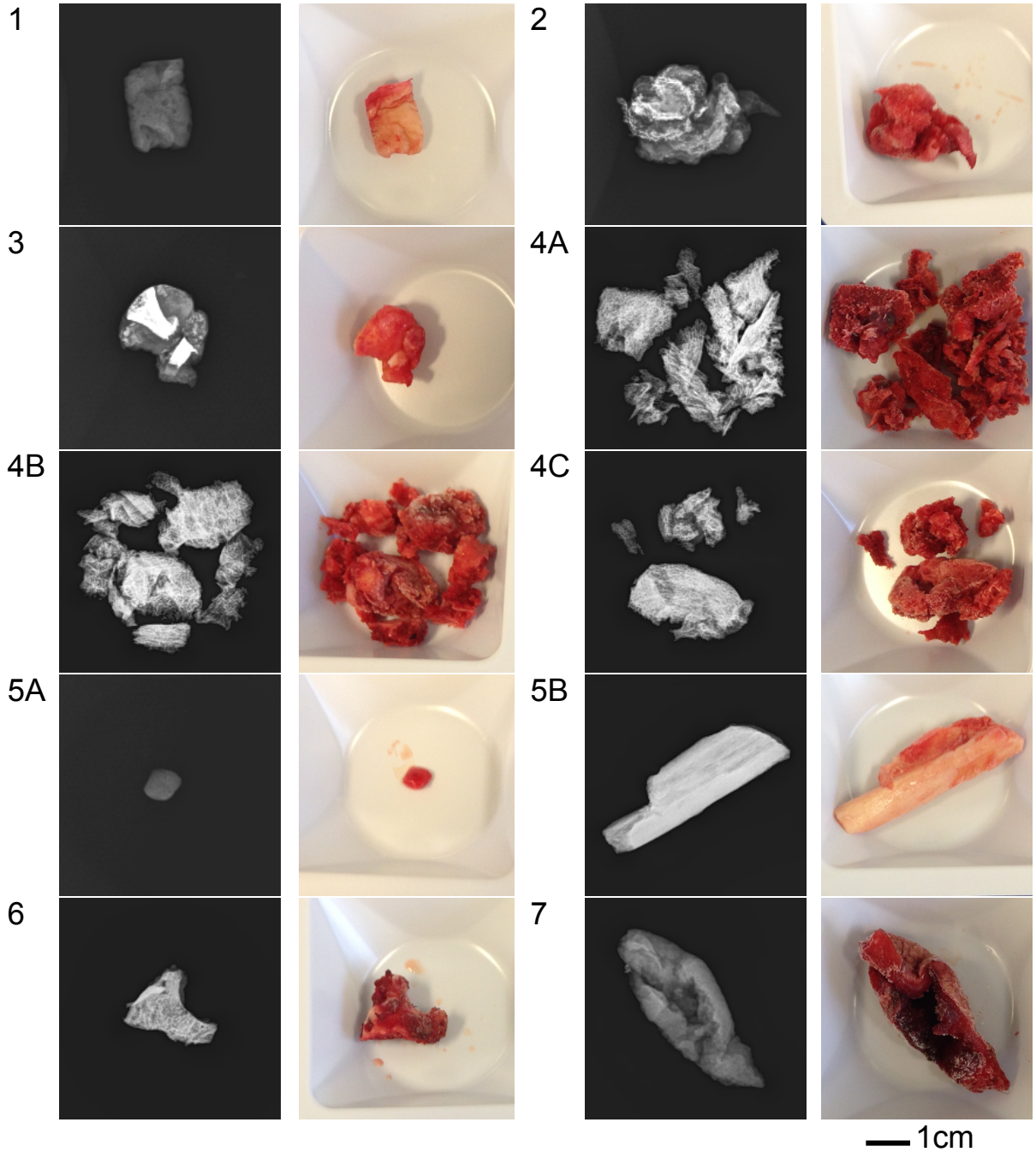

Figure 3-3: Contact radiographs and photographs of all of the samples of human HO. It is clear that there is a great deal of variability with cortical, cancellous, and hybrid morphologies demonstrated to different degrees within and between samples. Scale: each radiograph / photograph is 5cm across.

3.3.2 MicroCT Results

MicroCT 3-D reconstructions of samples 3 to 6 are shown in Figure 3-4 and Figure 3-5. Samples 3A-C are neither classically cancellous nor cortical in morphology but are a hybrid of both. Channels approximately 50 μm in diameter can be seen opening onto the surface of the samples in an irregular distribution. The surfaces of the samples are textured with pits and depressions of approximately 500 μm diameter. Channels of 1 mm diameter are seen to perforate the samples. Sample 4A is almost entirely trabecular. There is a clear graduation in trabecular size from left to right across the sample ranging from a few tens of microns to a few hundred microns. Sample 4B demonstrates a predominantly plate-like morphology with plate thickness of 150-300 μm separated by unmineralised gaps of similar width. Sample 4C has a trabecular central volume bounded by a perforated cortical shell of 80-300 μm thickness and, as seen in sample 4A, the trabeculae demonstrate variable size in a graduated pattern with thickest trabeculae adjacent to the cortical shell and thinnest trabeculae further towards the central volume. Samples 5A-C appear to be normal cortical bone. They demonstrate regularly arranged osteons and larger channels, presumably vascular in nature. Samples 6A-C have cortical shells of 200-1500 μm thickness adjacent to trabeculae. The trabeculae in sample 6A appear similar to those in normal bone whereas those in 6B and 6C are more disordered and even plate-like. A 500 μm diameter perforating channel is visible in 6B, which is consistent with a vascular structure. The tissue mineral density (TMD) and quantitative morphometric parameters of these datasets are shown in Figure 3-6 and Figure 3-7 respectively.

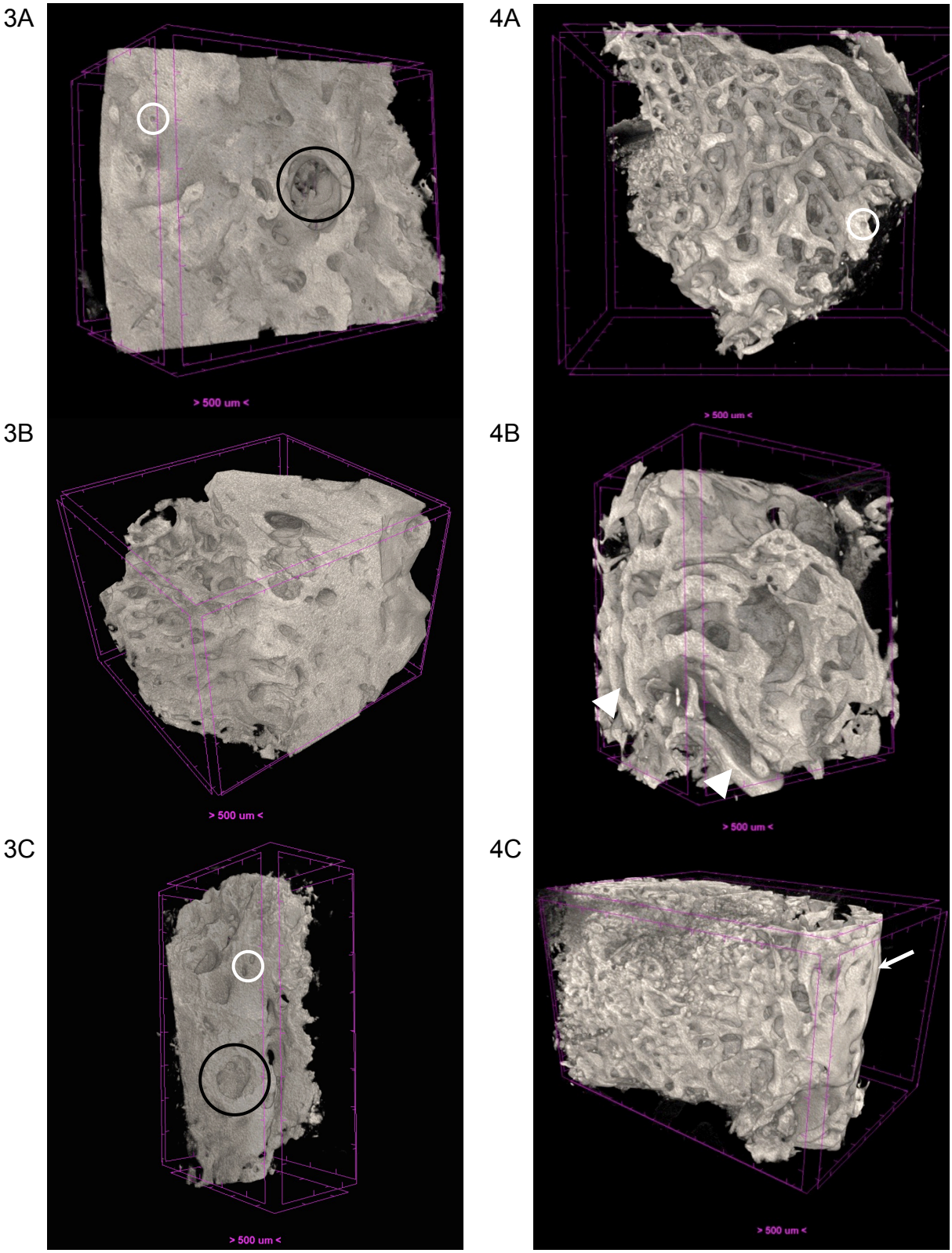

Figure 3-4: MicroCT 3-D reconstructions of HO samples from patients 3 and 4. 3A-C: cancellous and cortical hybrid morphology. 4A: variation of trabecular size. 4B: plate-like morphology. 4C: trabecular volume bounded by cortical shell.
Arrowheads = plate-like morphology. White circles = osteons. Black circles = vascular channels. Distance between "ticks" on the bounding cuboid = 500 μm in all images.

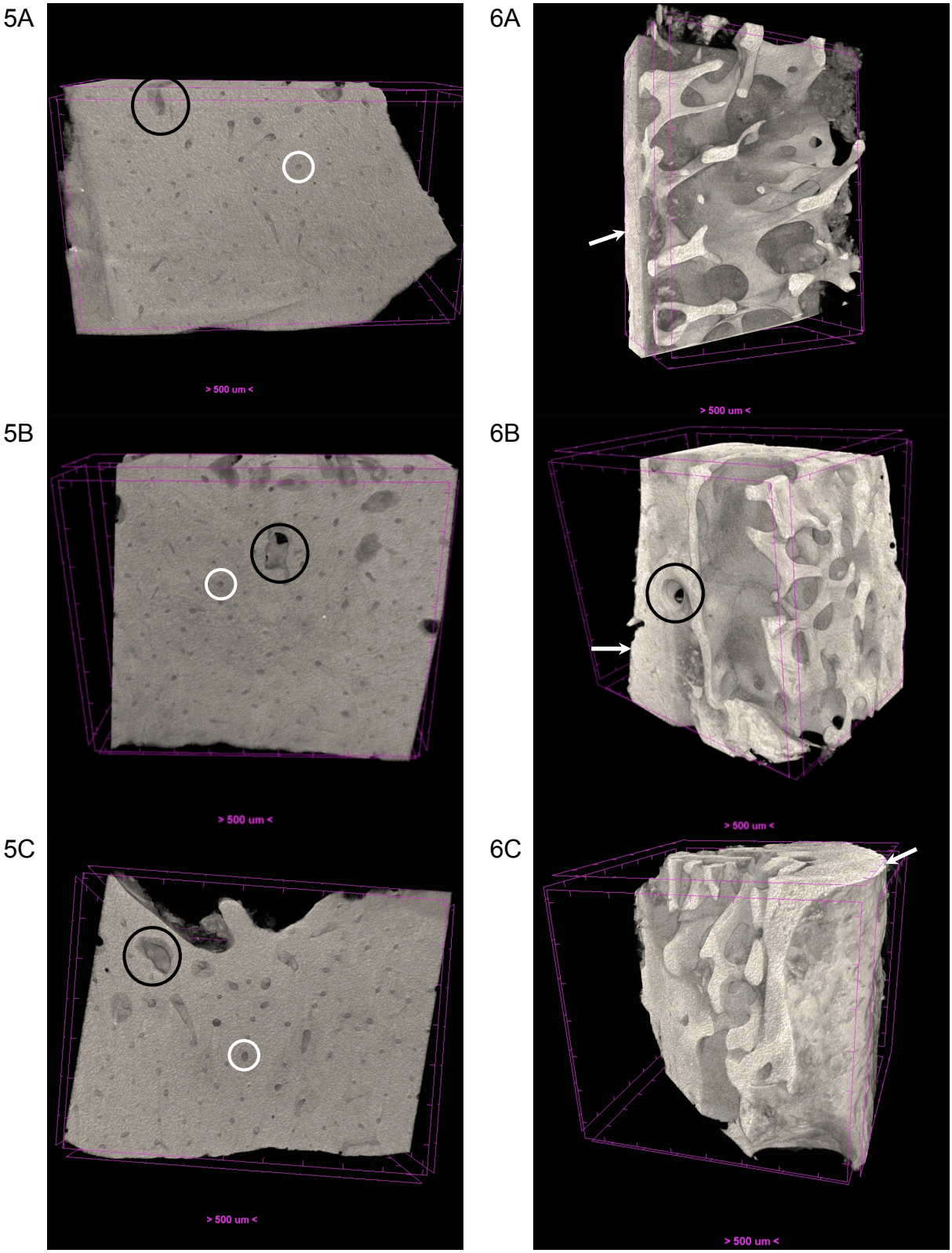

Figure 3-5: MicroCT 3-D reconstructions of HO samples from patients 5 and 6. 5A-C: normal cortical bone appearance with osteons and vascular channels. 6A-C: coarsely trabecular volume bounded by cortical morphology of variable thickness.
White arrows = cortical morphology. White circles = osteons. Black circles = vascular channels. Distance between "ticks" on the bounding cuboid = 500 μm in all images.

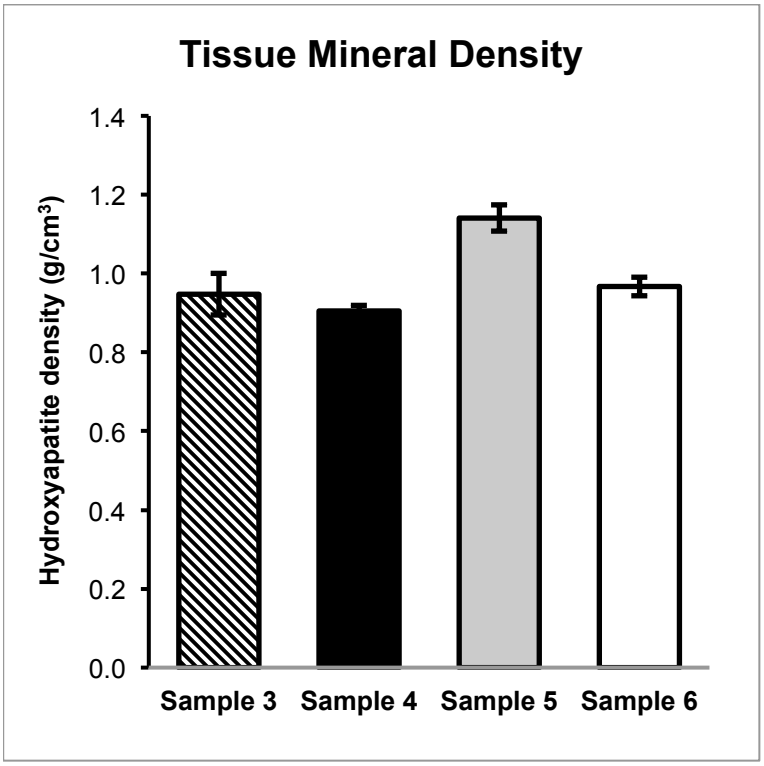

Figure 3-6: Tissue mineral density (grams of hydroxyapatite / cm^3) for samples of human HO. This measure is insensitive to morphology. Error bars = SD.

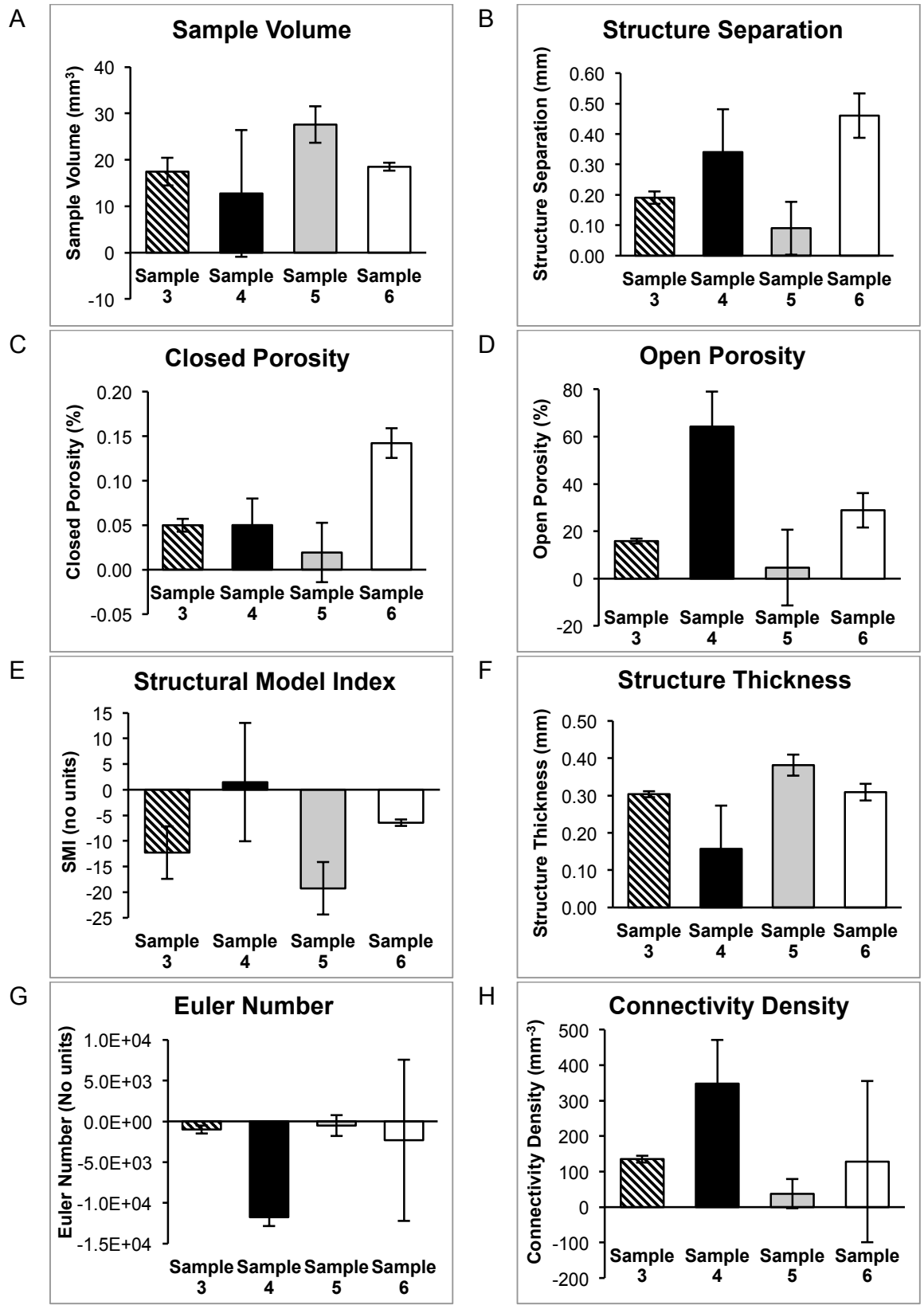

Figure 3-7: Quantitative morphological analysis of the microCT datasets shown in Figure 3-5.

3.3.3 SEM Results

SE SEM topographic images of HO from patient 4 are shown Figure 3-8 and Figure 3-9. The images show the mineralised portion of the HO sample after soft tissue removal using sodium hypochlorite. The low magnification images demonstrate a predominantly hybrid morphology that is neither truly cortical nor trabecular. There are multiple channels opening onto the surface of the sample (Figure 3-8 A and B). These range in diameter from 30-80 μm. There is also extensive scalloping of the surface. These depressions are approximately 10-20 μm across and are consistent with osteoclast resorption pits. They form confluent patches on the surface of the HO but are not seen in all areas. In certain areas of the sample, the fractured surface can be seen (Figure 3-8 A and C). Higher magnification images show the osteoclast resorption pits in more detail. In a number of areas near these resorption pits, there are deeper depressions in the surface that contain multiple roughly spherical forms, which are approximately 1 μm in diameter. In the highest magnification view, these spherical objects can be seen to be formed from plate-like subunits that are approximately 0.5 μm in their longest dimension (Figure 3-9D).

BSE SEM images of samples of HO from patients 3, 4, and 6 are shown in Figure 3-10, Figure 3-11, Figure 3-12, Figure 3-13, and Figure 3-14. At low magnification, disordered trabecular (Figure 3-10A), hybrid (Figure 3-13A), and disordered cortical Figure 3-11A) morphology can be seen. There is also a region that has a plexiform appearance (Figure 3-11B). Across all the samples, there is a common appearance of disordered core regions containing a high density of osteocyte lacunae with little or no obvious organisation. These core regions are bounded by highly organised

lamellar bone, which is more sparsely populated with osteocyte lacunae. There is a sharp delineation between the ordered and disordered regions. The lacunae in the lamellar regions demonstrate a high degree of alignment with the lamellae and each other. Another finding is that the lacunae in the core regions appear larger and more rounded than those in the lamellar regions, which have a flatter and more elongated appearance in the direction of the lamellae. The lamellar regions are distributed both circumferentially around the Haversian canals and linearly at the surface of the samples. The lamellar regions are also darker than the disordered core regions. This darker appearance corresponds to a lower mean atomic number (Z) of the atoms in the lamellar regions compared to the disordered core regions.

Like in the SE images, shallow pits can be seen on the surface of the HO (Figure 3-10C). These are approximately 20 μm across and are found in a confluent group.

At high magnification, osteocyte canaliculi can be visualised. These appear more numerous in the organised lamellar regions and are arranged at right angles to the orientation of the lamellae. The repeating wave-like pattern in Figure 3-14D is consistent with the previously described “twisted-plywood” orientation of collagen fibres.[194]

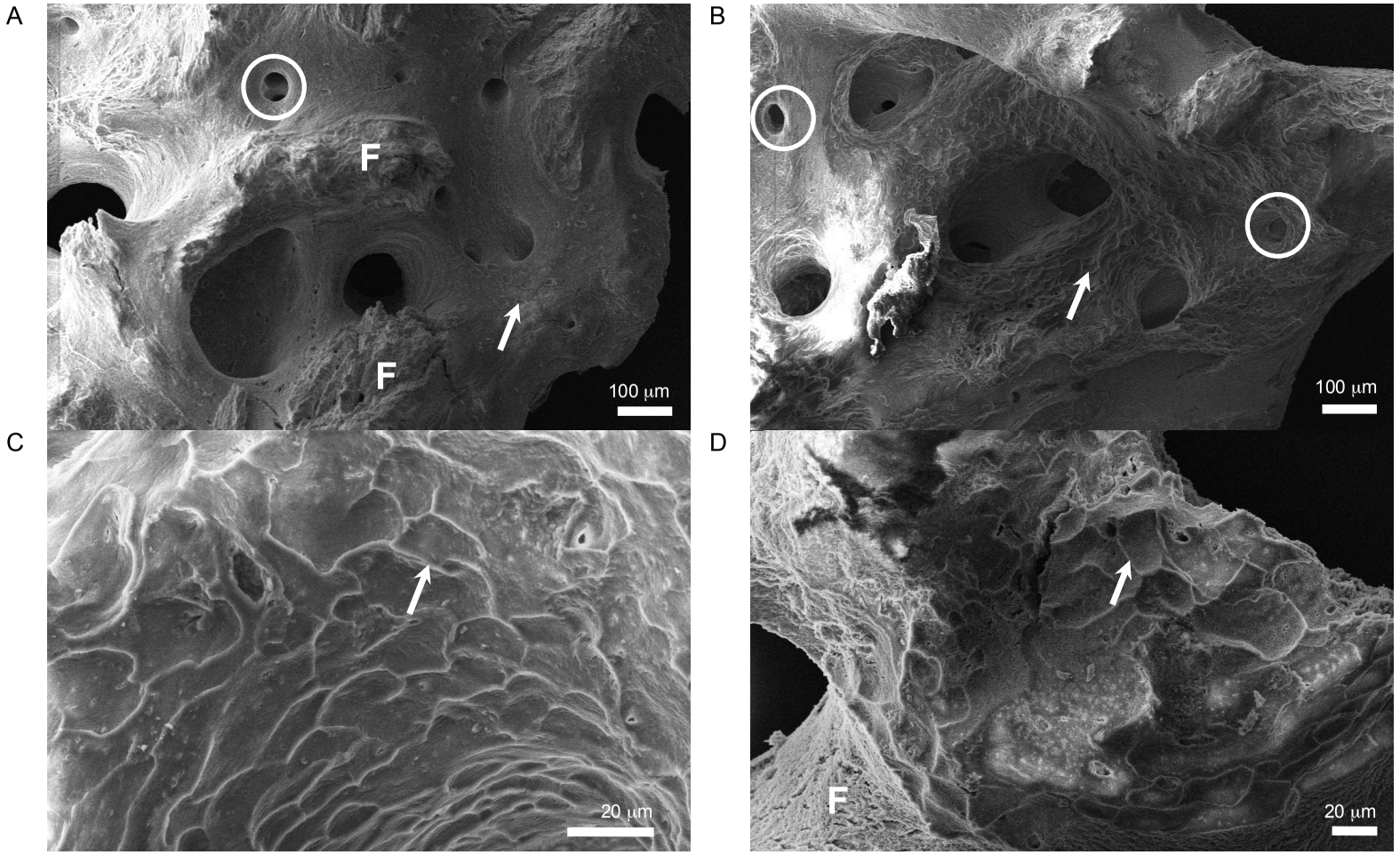

Figure 3-8: Secondary electron (SE) scanning electron microscopy (SEM) images of human HO from patient 4. Arrows = osteoclast resorption pits. Circles = Haversian canals opening onto surface. F = fracture surfaces caused during sample preparation.

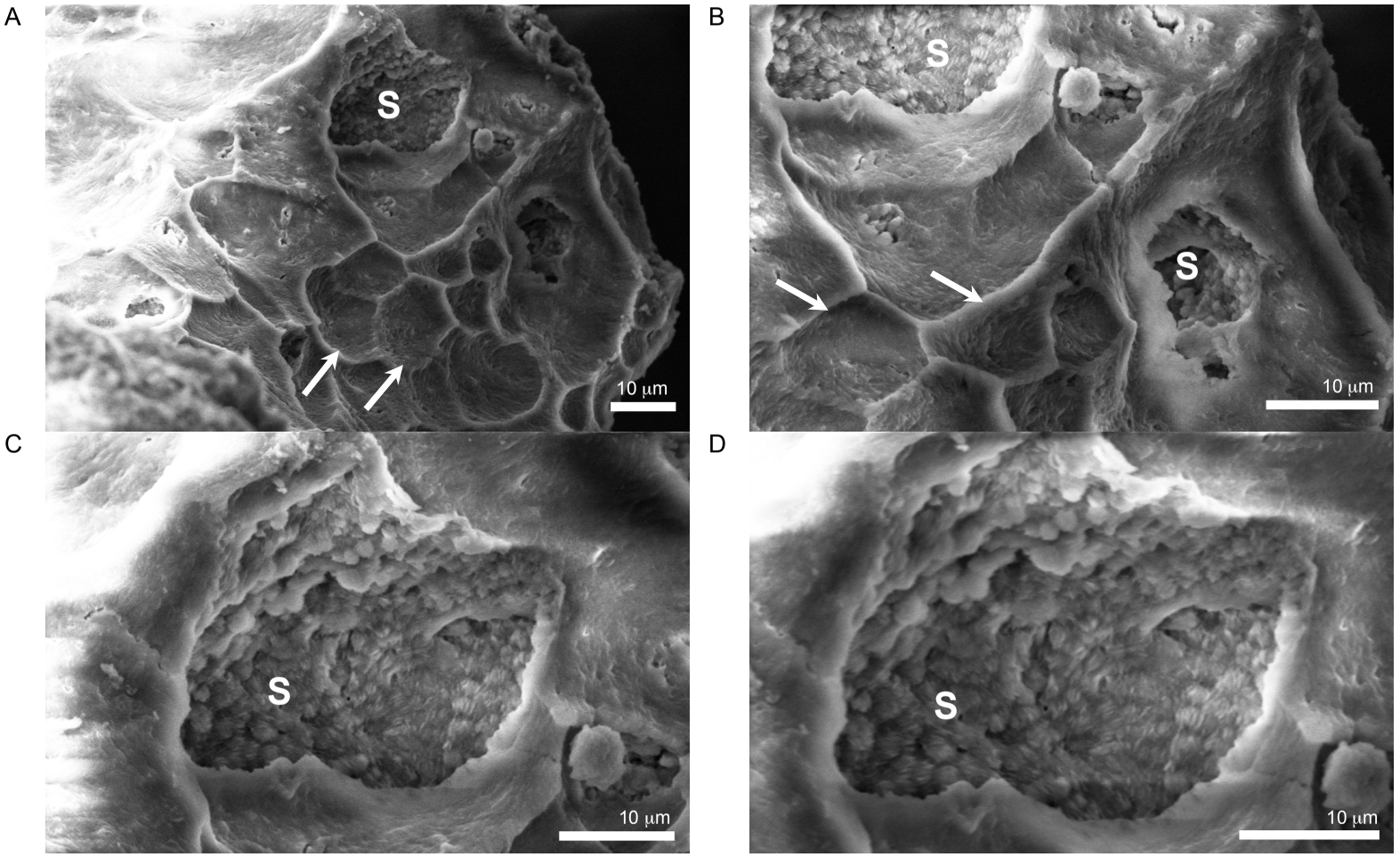

Figure 3-9: SE SEM images of human HO from patient 4.
Arrows = osteoclast resorption pits. S = 1 μm diameter spherical structures in groups.

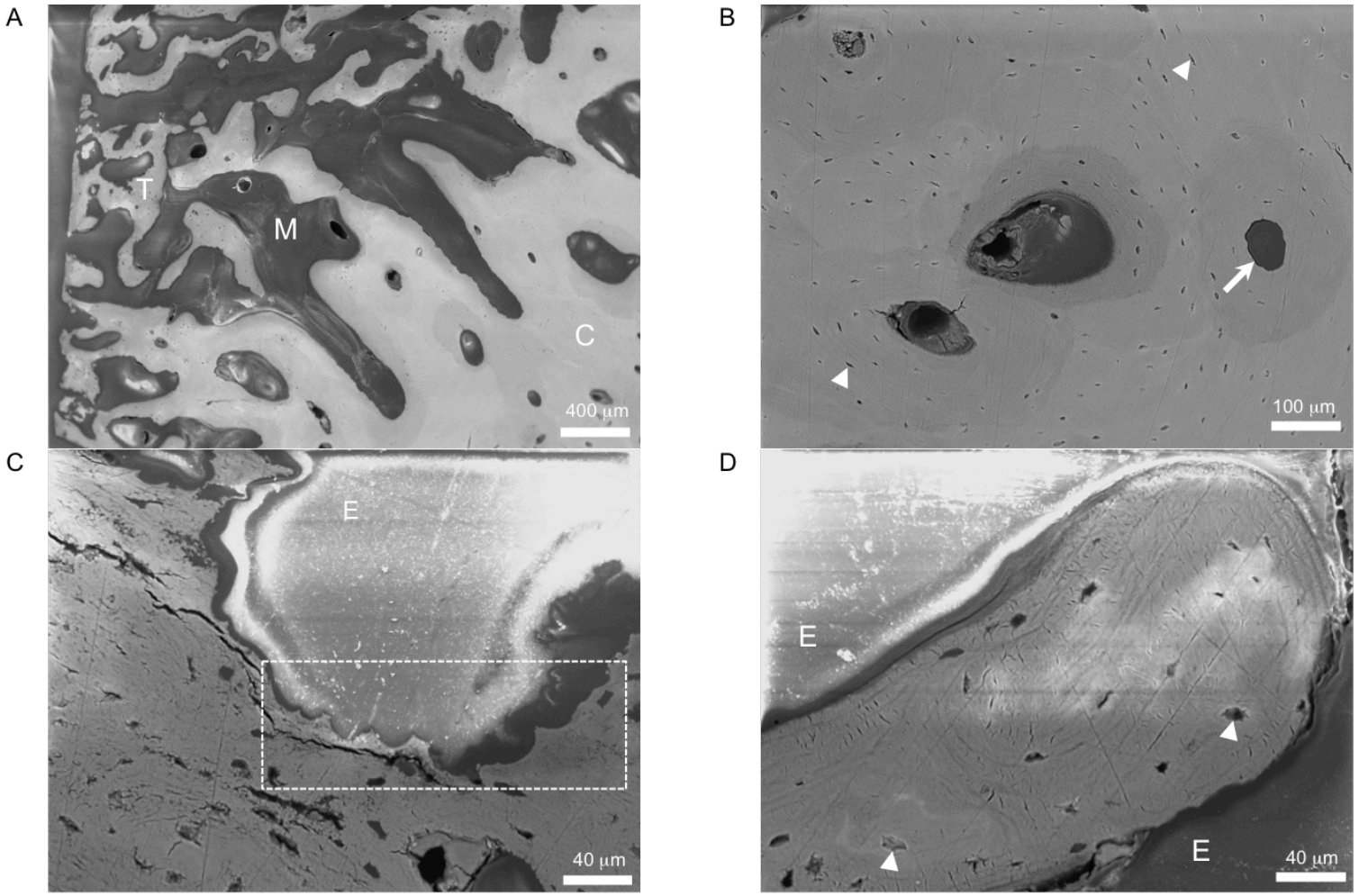

Figure 3-10: Backscattered electron (BSE) microscopy images of HO (Patient 3). A: Disordered morphology. B: Osteocyte lacunae (arrow heads) aligned with lamellae around Haversian canals (arrow). C: Osteoclast resorption pits (dashed box). D: Osteocytes within a single trabeculum.
E = epoxy. T = trabecular morphology. C = cortical morphology. M = marrow space. Straight dark lines = polishing artefacts.

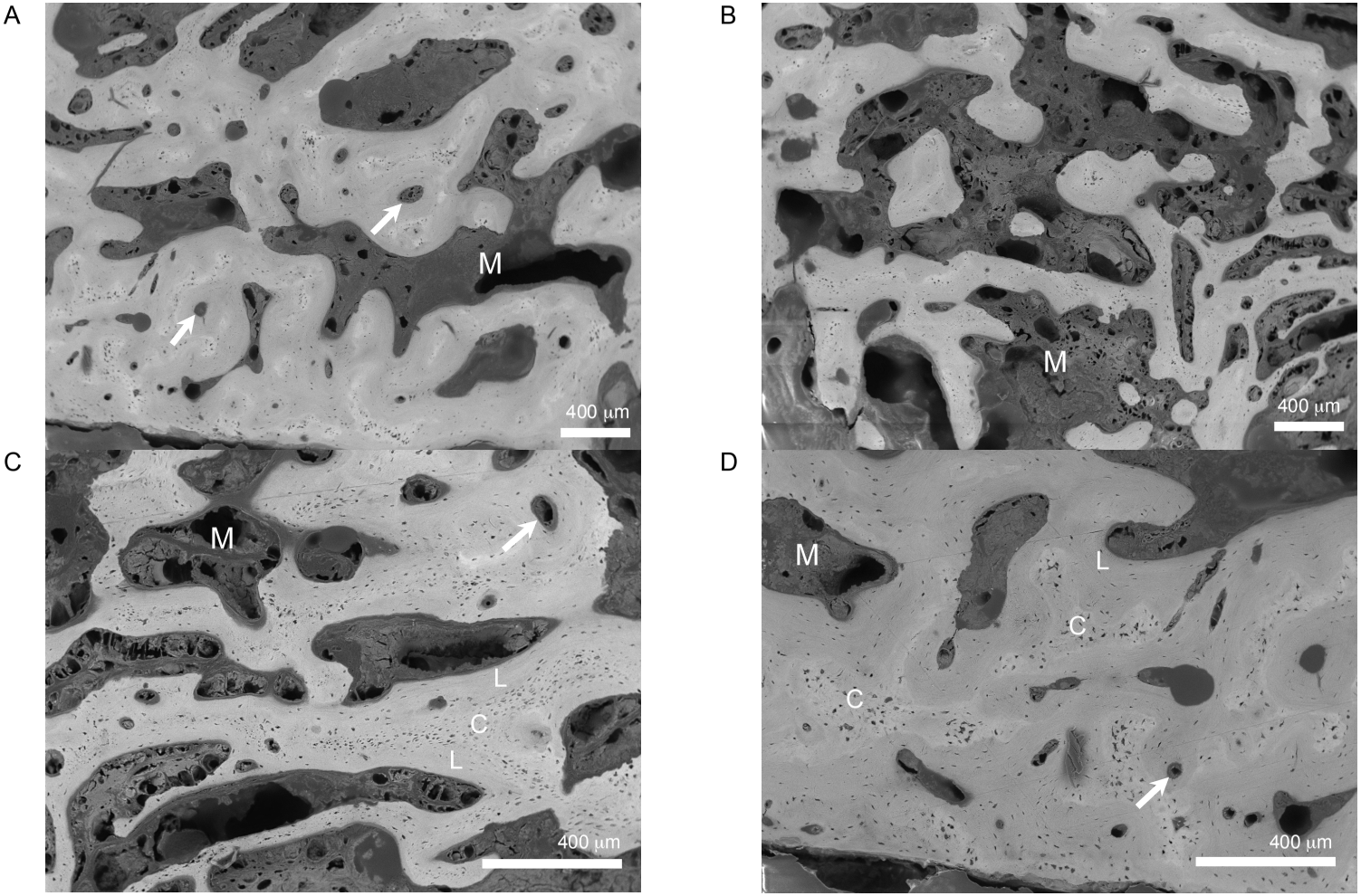

Figure 3-11: BSE SEM images of HO (Patient 4). A: Hybrid morphology. B: Trabecular morphology tending towards plexiform morphology in bottom right of image. C: Trabeculae with disordered highly cellular central regions bounded by ordered laminae. D: Disordered highly cellular regions adjacent to sparsely cellular ordered osteons.
C = highly cellular core region. L = sparsely cellular laminar region. M = marrow space.

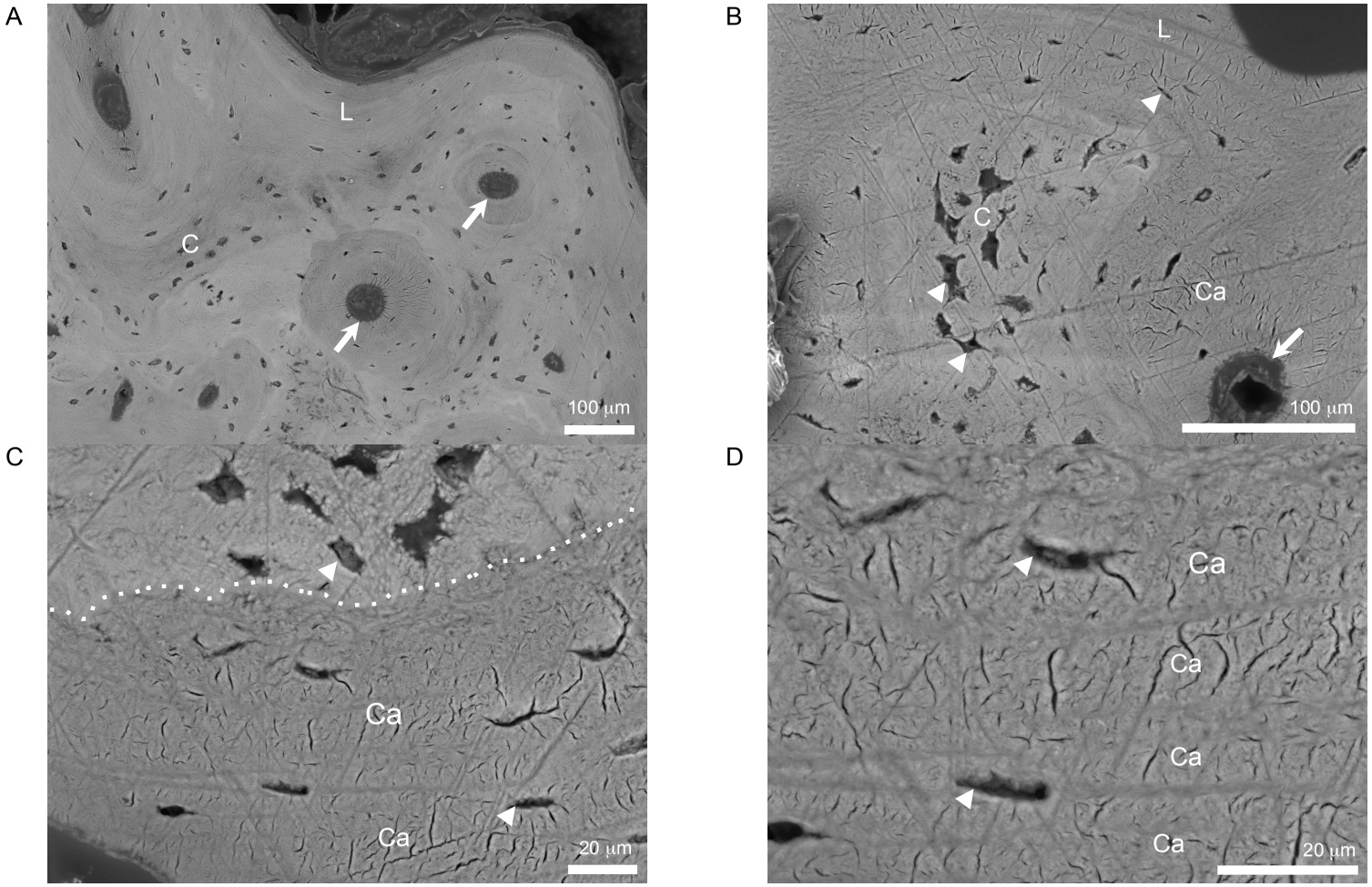

Figure 3-12: BSE SEM images of HO (Patient 4). A: Ordered osteons surrounded by disordered highly cellular regions. B: Unaligned and aligned osteocytes in adjacent domains. C: Border between order and disorder (dotted line). D: Canaliculi visible in lamellae.
Ca = canaliculi. C = highly cellular core region. L = sparsely cellular laminar region. Arrows = Haversian canals. Arrowheads = osteocyte lacunae. Straight dark lines = polishing artefacts.

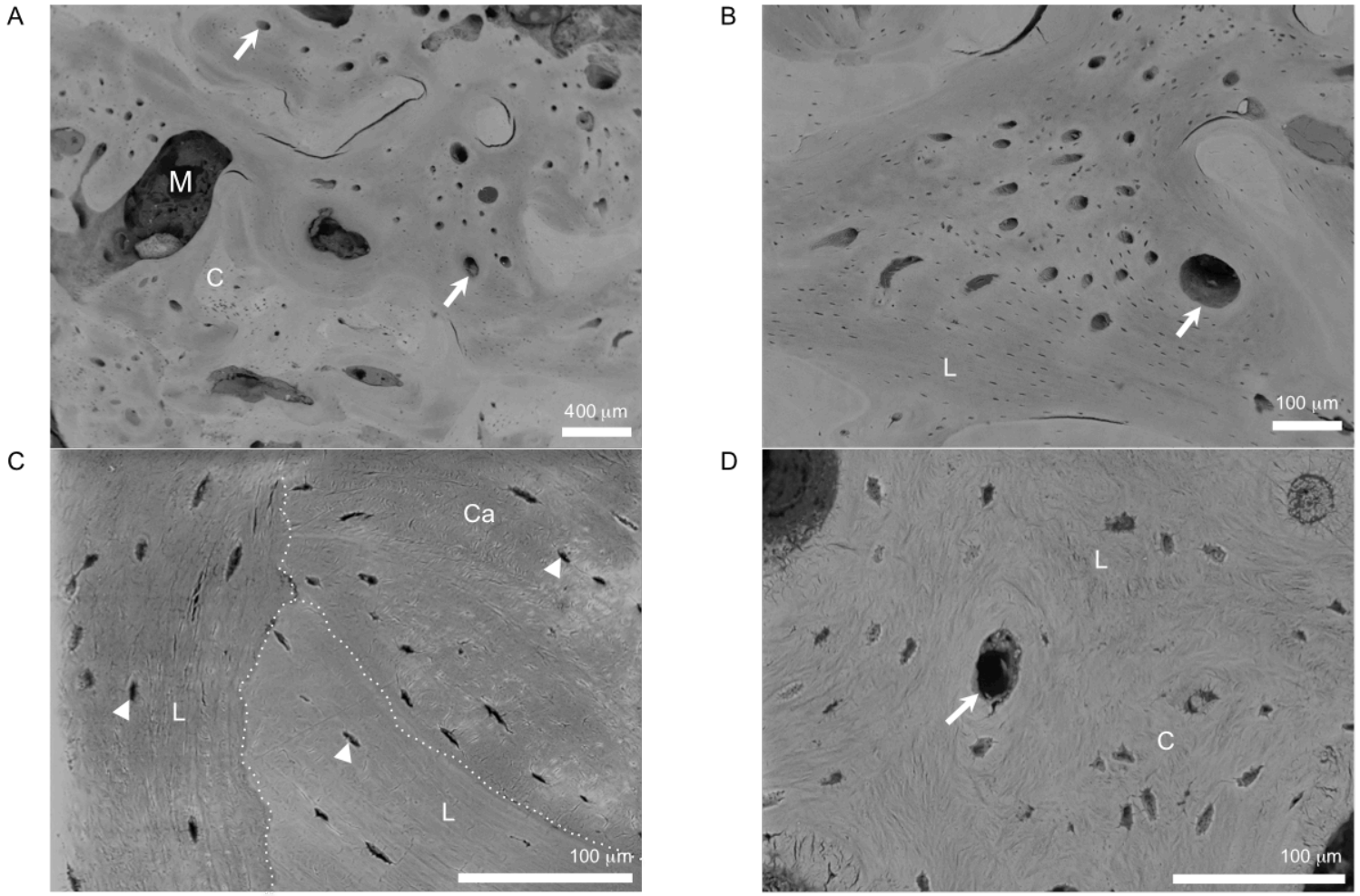

Figure 3-13: BSE SEM images of HO (Patient 6). A: Mainly cortical morphology. B: Unusually high density of small channels grouped together near a Haversian canal. C: Discontinuous lamellae as evidence of remodelling. D: Haversian canal with poorly organised surrounding bone.
Ca = canaliculi. C = highly cellular core region. L = sparsely cellular laminar region. M = Marrow space. Arrows = Haversian canals. Arrowheads = osteocyte lacunae.

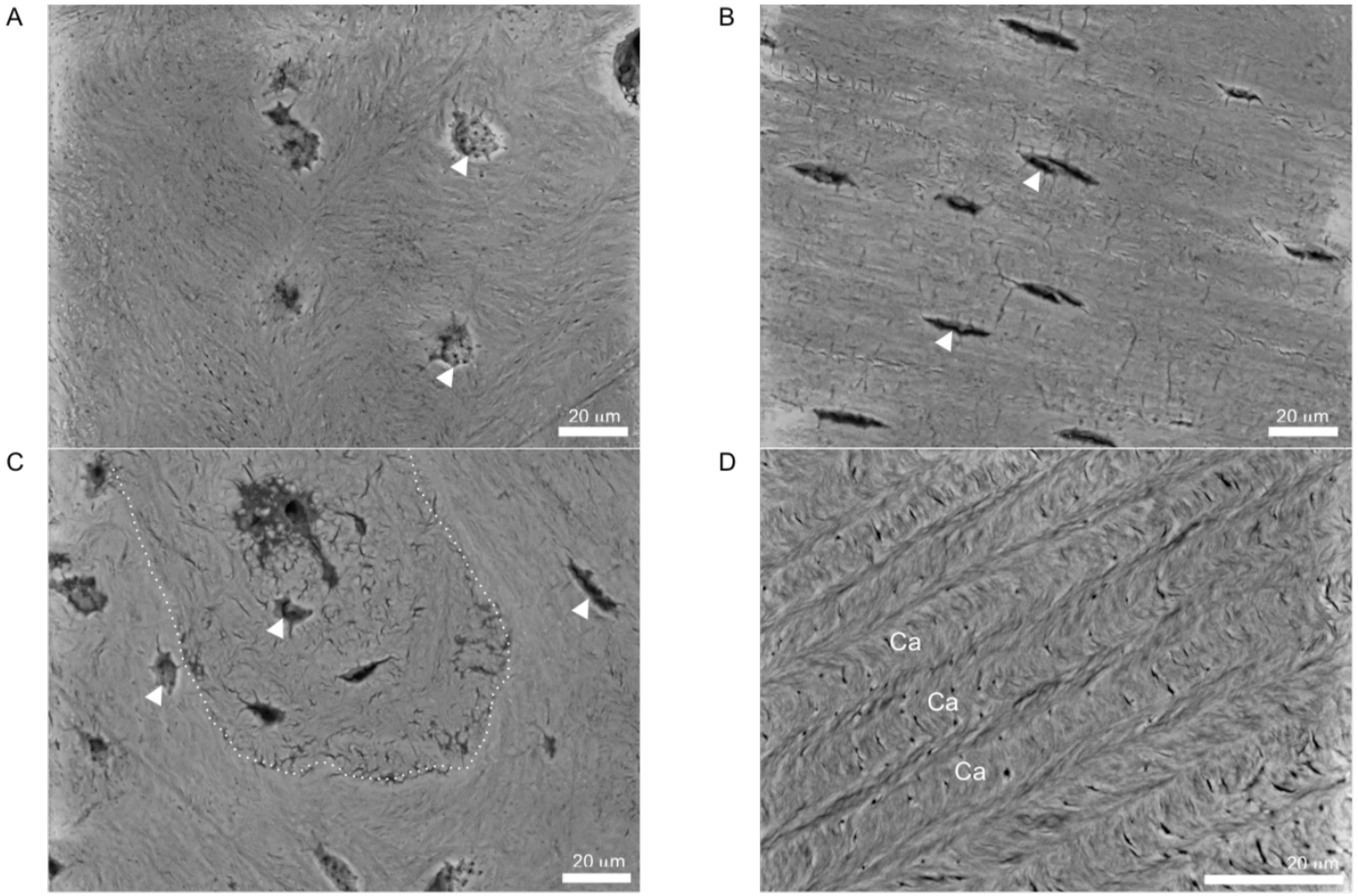

Figure 3-14: BSE SEM images of HO (Patient 6). A: Osteocyte lacunae with canaliculi opening visible in the far wall. B: Flattened osteocyte lacunae with connecting canaliculi. C: Possible remodelling via cutting cone. D: Highly ordered arrangement of canaliculi in lamellae.
Ca = canaliculi. Arrowheads = osteocyte lacunae.

This lends weight to a central conclusion of this chapter; that while HO appears to be macroscopically disordered, below a certain length scale it is highly ordered. In other words, the fundamental constituents of and processes within HO are normal but lack coordination and direction above the micron to millimetre length scale. One hypothesis may be that the lack of insertion of muscles into HO, and the subsequent atypical loading that the tissue is therefore subjected to, could be the cause of the observed disorder. A clear demonstration of just how ordered and normal HO bone can be on a small length scale is shown in Figure 3-14D. This demonstrates the highly ordered arrangement of collagen fibres in a “twisted plywood” configuration, which has been described at length in the normal bone literature.[194]

3.3.4 SXRD Results

C-axis length for the HA component of each sample was determined to be follows: sample 3: 6.86 Å (SD 0.0047), sample 4: 6.86 Å (SD 0.0047), sample 6: 6.87 Å (SD 0.0035). Spatially resolved data for beam transmission, hydroxyapatite c-axis length, and orientation / texture are presented in Figure 3-15. Crystal orientation in each sample has the appearance of a dominant orientation with individual regions of variability. There is a correlation between areas with low transmission and areas of high pixel-by-pixel variation in orientation.

Hydroxyapatite was the only crystalline calcium phosphate phase detected in the samples.

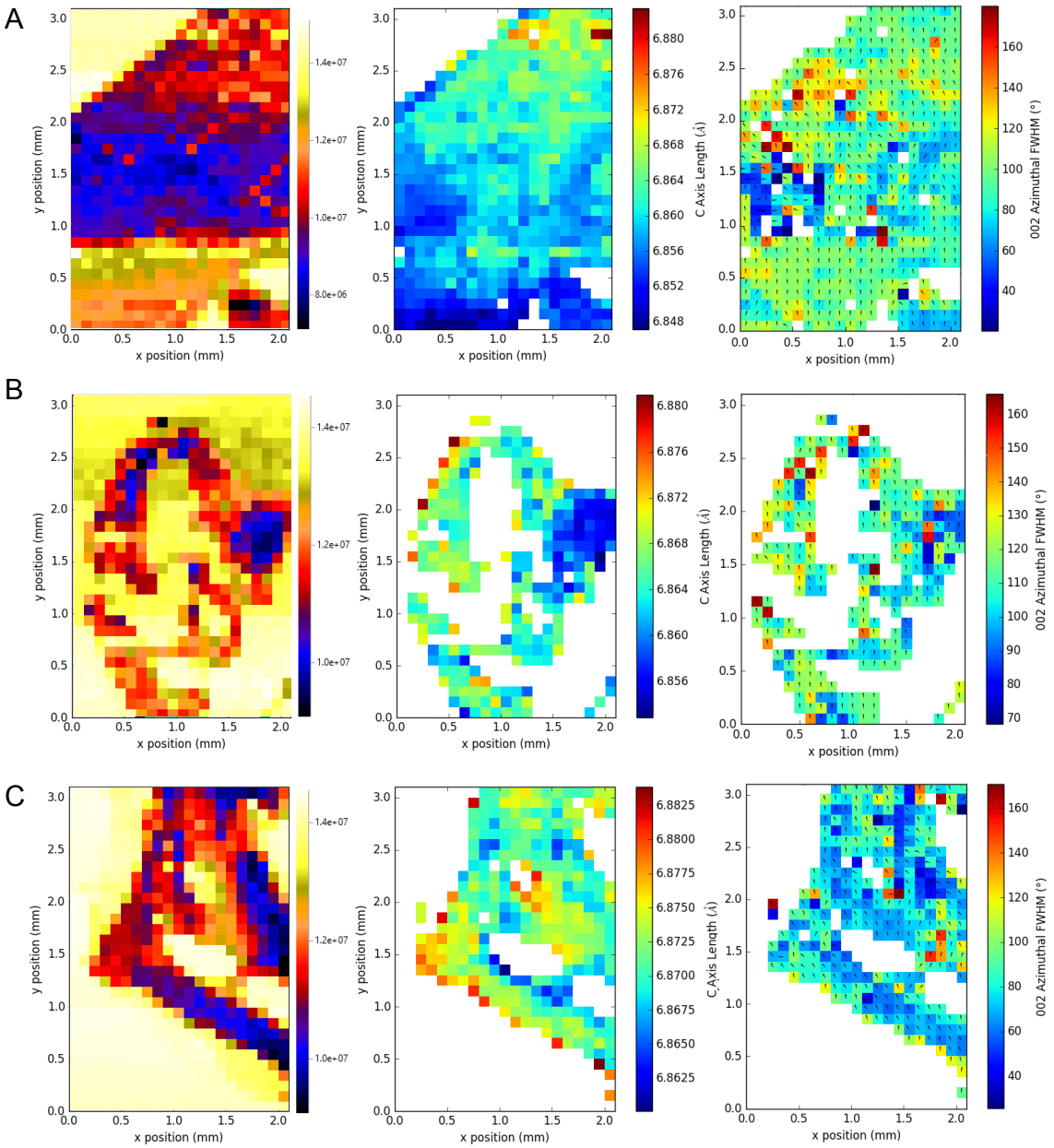

Figure 3-15: Synchrotron X-ray diffraction mapping of samples of HO from patients 3 (row A), 4 (row B), and 6 (row C). Representative beam transmission maps (left), hydroxyapatite c-axis length maps (middle), and texture / orientation maps (right) for each sample. Transmission intensity is inversely related to tissue mineral density and is represented by an arbitrary scale.

3.3.5 XRF Results

The image generated from the sample of HO from patient 2 shows several trabeculae with co-localised calcium and phosphate signals (Figure 3-16). Additionally, there are several areas of calcium signal without any appreciable phosphorus signal. In some cases, these calcium-rich areas are not connected to the trabeculae and thus form islands.

Figure 3-17 shows XRF maps from patients 2, 3, 4, and 6. Sample 3 (subfigure A) is largely unmineralised as demonstrated by a high sulphur signal from proteins in the soft-tissue extracellular matrix. There are several islands of co-localised phosphorus and calcium. There are also islands of high calcium signal without phosphorus. In samples 2 and 4 (subfigures B and C) the co-localised calcium and phosphorus signals form a recognisable, albeit disordered, trabecular pattern that is to be expected in HO. In several places, a calcium signal can be seen extending into the surrounding soft tissues.

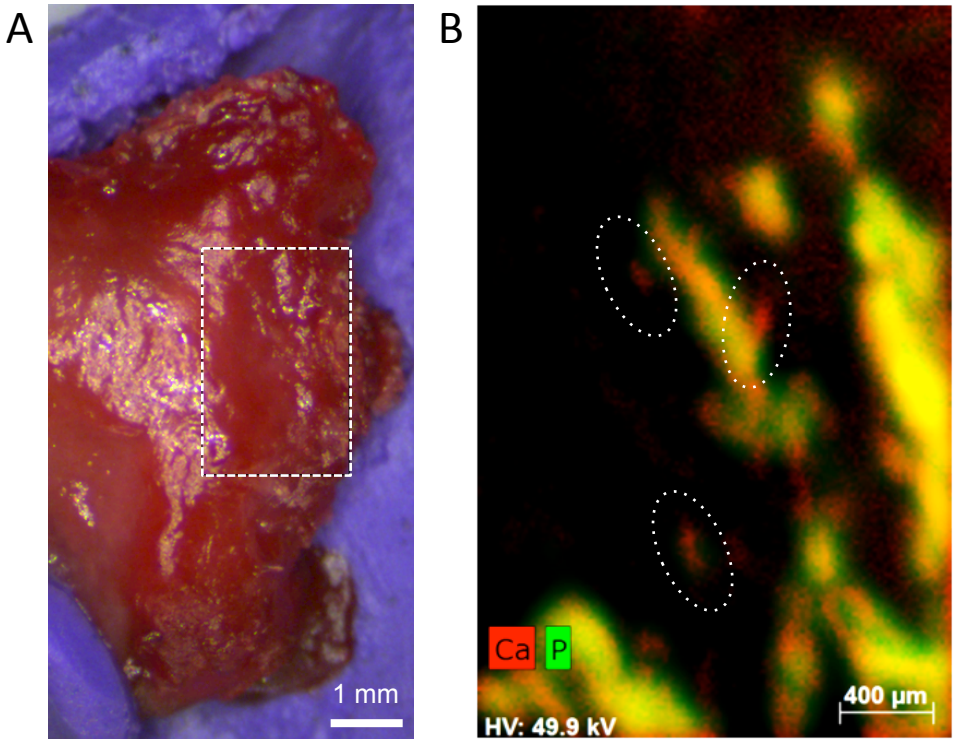

Figure 3-16: Sample of HO from patient 2. A: photograph of the sample taken using the optical microscope in the XRF scanner. The sample has undergone no preparation since removal from the patient. B: XRF image of the area within the dashed white box in A. Calcium rich islands are indicated by dotted white ellipses. Two of these calcium rich islands do not appear to be connected to the mineralising projections. Red = calcium. Green = phosphorus. Yellow = co-localised calcium and phosphorus.

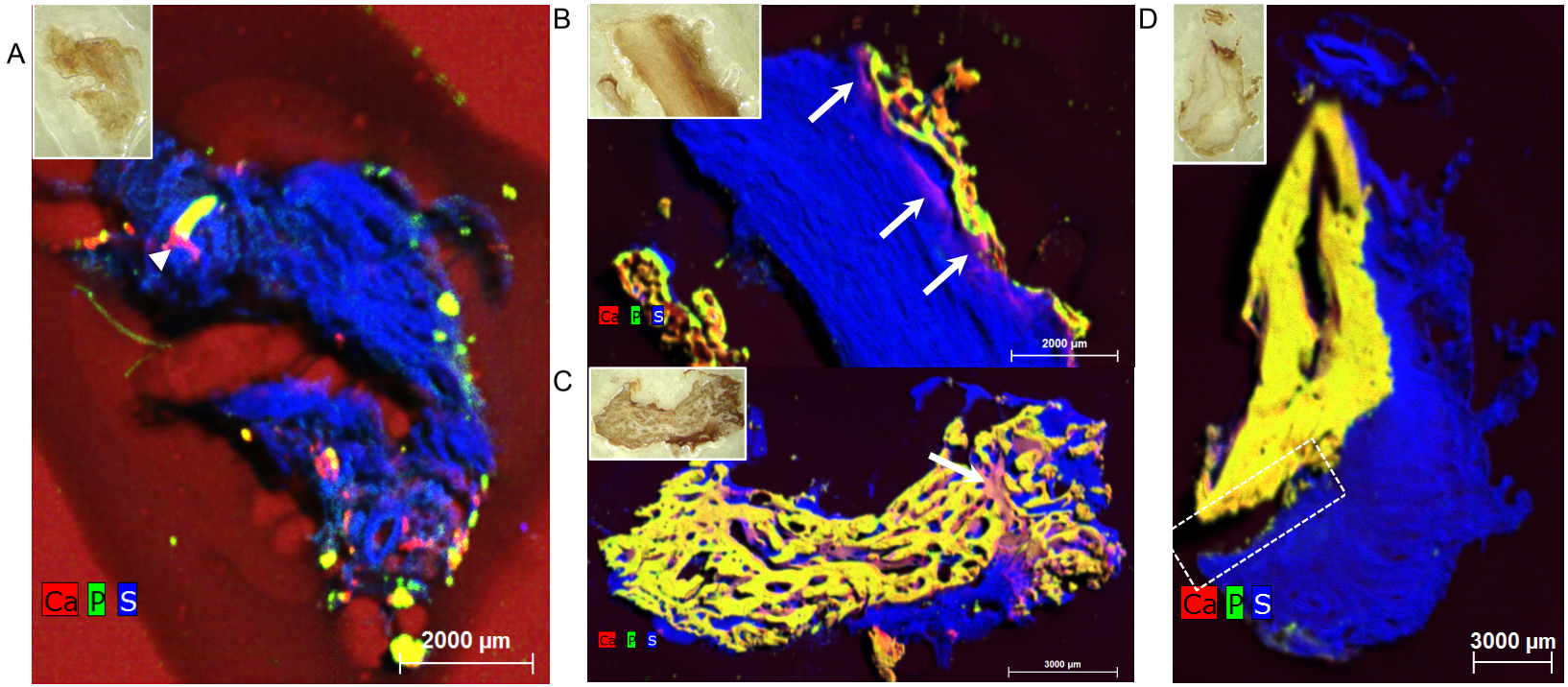

Figure 3-17: XRF images of samples of HO from patient 3 (A), 2 (B), 4 (C), and 6 (D). These images illustrate a hypothesised aging / maturation sequence for HO from A to D. Initially, calcium-rich islands (arrowheads in A) develop with partial colocalisation of phosphorus. Subsequently, there is coalescence of the islands to form disordered micro and macro-scale bone tissue (B and C). Note that there is still a calcium rich mineralisation front at the edges of the maturing bone (arrows in B and C). The final sample (D) shows complete homogeneity of calcium and phosphorus with no active calcium-rich mineralisation front extending into the surrounding collagen. This is hypothesised to be the final, quiescent, fate of the tissue. In the lower left of the image the unmineralised tissue has pulled away from the mineralised area (white box). Red = calcium. Green = phosphorus. Blue = sulphur (representing collagen). Yellow = colocalisation of calcium and phosphorus. Insets are corresponding visible light micrographs of these samples.

3.3.6 Raman Spectroscopy Results

Raman maps for hydroxyapatite (HA), octacalcium phosphate (OCP), and collagen in a sample of HO from patient 4 can be seen in Figure 3-18. OCP is shown to be highly co-localised with HA (subfigures B and C). These maps also correlate well with the distribution of colocalised calcium and phosphate (yellow areas in subfigure A) in the XRF map except in the lower right quadrant of the map. In this quadrant, there is a diffuse HA/OCP signal that does not correspond well to the structured calcium and phosphorus seen in a trabecular pattern in the XRF image.

Subfigure D shows that collagen occupies the sample outline as the HA/OCP signal but that within this boundary, there is an inverse relationship in signal. Areas rich in HA/OCP show lack of collagen and *vice versa*. This is confirmed in the composite image where the map is either dominantly yellow (indicating colocalisation of HA and OCP) or blue (indicating predominance of collagen) with no areas of white, which would indicate the co-localisation of all three molecules.

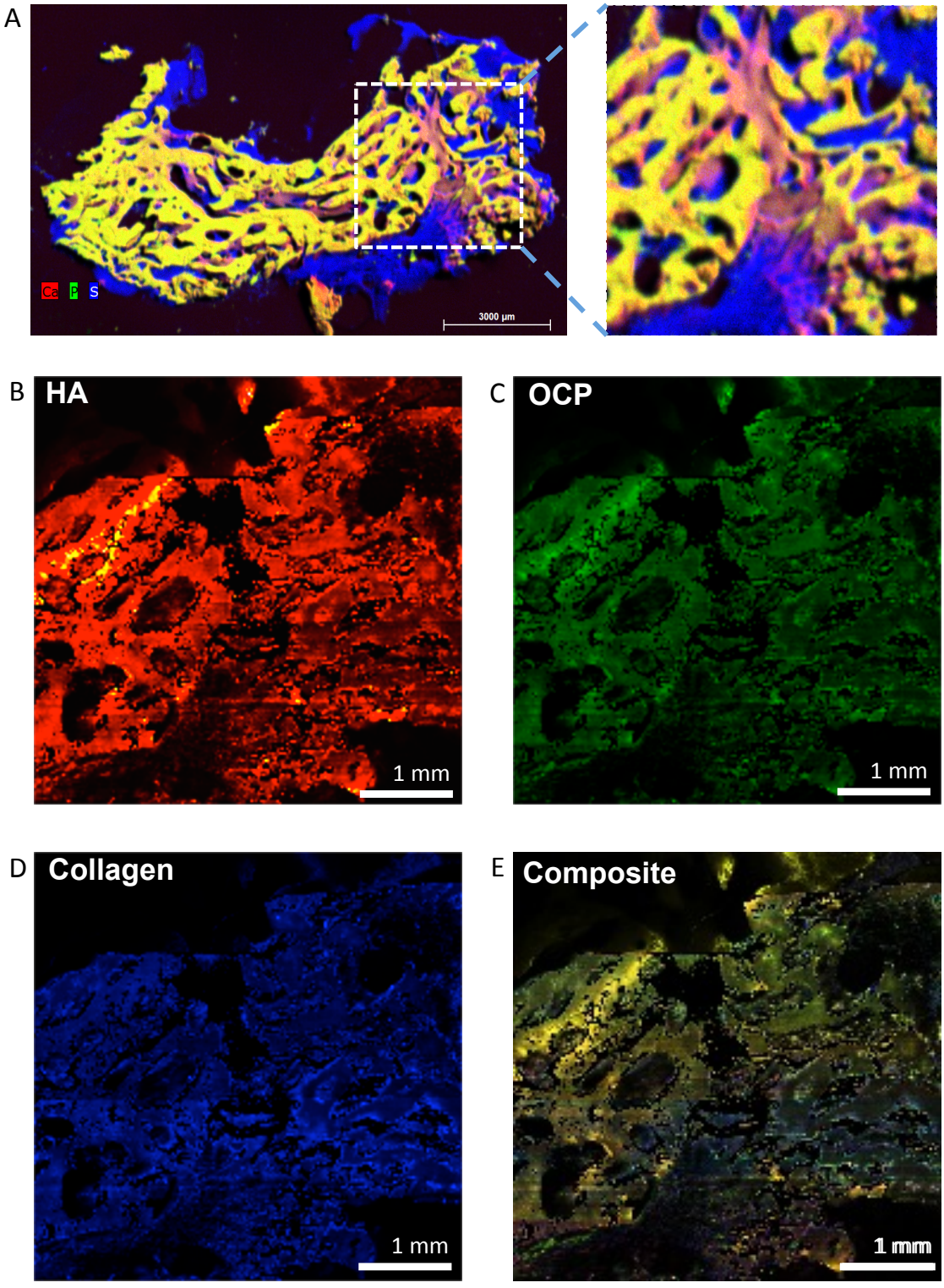

Figure 3-18: A: XRF map of a sample of HO from patient 4, indicating the region of interest for Raman mapping. B-D: Maps showing the relative distribution Hydroxyapatite (HA), Octacalcium Phosphate (OCP), and Collagen within the region of interest. Brighter pixels indicate higher concentration. E: composite of subfigures B-D. Yellow area indicates colocalisation of HA and OCP. Blue area indicates mineral-poor soft tissue matrix.

3.3.7 NanoCT Results

Figure 3-19A and B were formed by summing information from 200 slices of the datasets. These cross-sectional images show that the osteocyte lacunae are highly aligned with each other and with the lamellar structure within which they reside. They have a typically flattened lozenge shape, which can be approximated to an ellipsoid. There are abundant canaliculi emerging from each osteocyte lacuna and these branch multiple times and form a densely connected network with canaliculi from other osteocytes. The canaliculi are also highly aligned with each other, with their primary axis of alignment being at right angles to the axis of alignment of the long axis of the lacunae.

Striations within the inter-lacunar tissue are also visible. These match the orientation of the long axis of the lacunae. Within and between these striations are bright flecks, which represent lower density material or porosity.

Three-dimensional reconstruction of processed data reveals the 3-dimensional morphology of the osteocyte lacunae and their alignment with the lamellar structure of the samples. In Figure 3-19C, the long axes of the lacunae align themselves along lamellae around a Haversian canal (digitally removed from the image). In Figure 3-19D these same lacunae are viewed along an orthogonal plane to reveal that their intermediate and short axes also demonstrate a high degree of alignment.

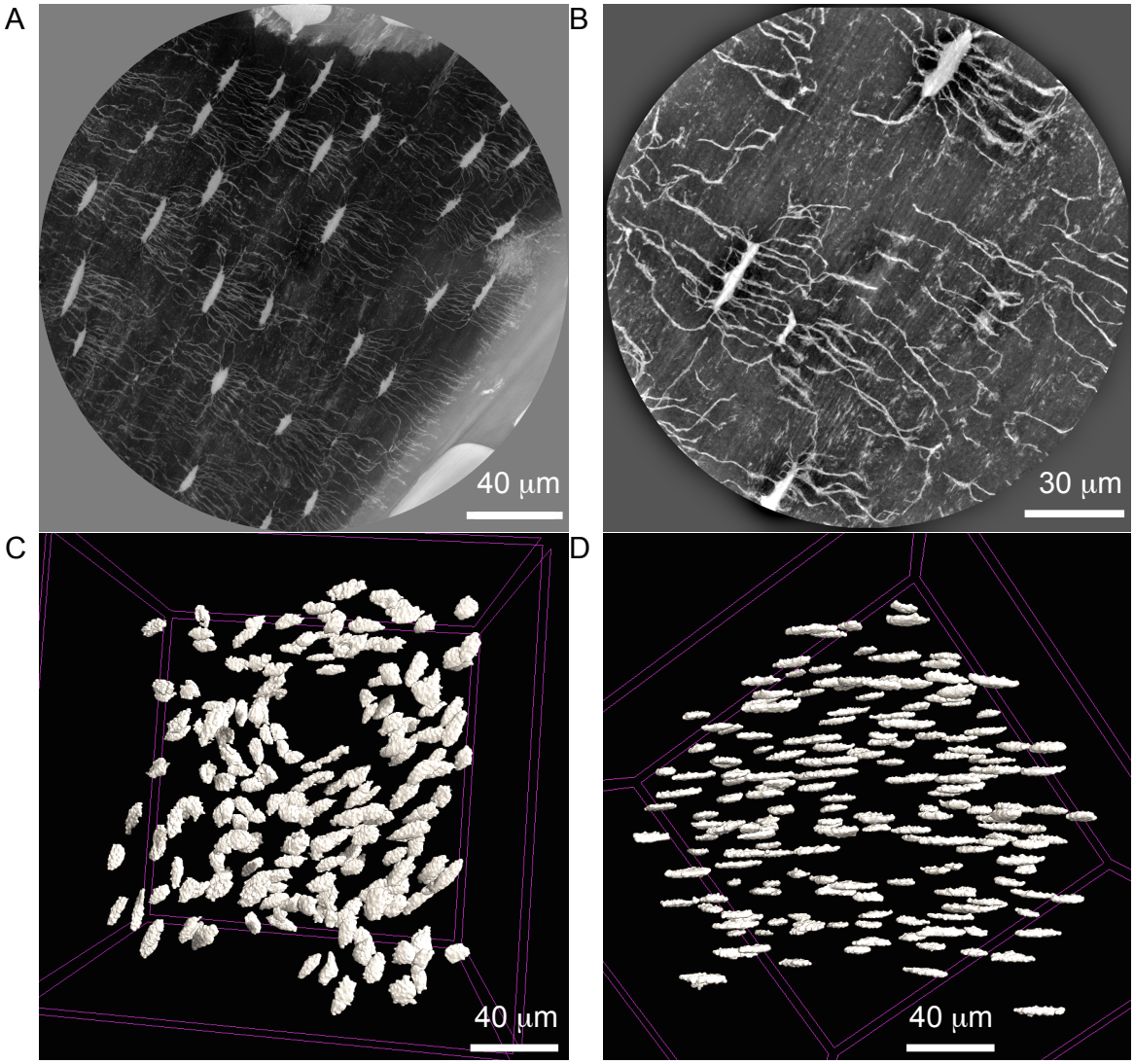

Figure 3-19: Processed nanoCT images of HO from patient 6. A: 200-slice (24 μm) maximum intensity image at 120 nm per pixel resolution. The elongated osteocyte lacunae are highly aligned with each other. Canaliculi are visible extending at right angles to the axis of orientation of the lacunae. Haversian systems are partially visible at the bottom right and top of the image. B: 200-slice (10 μm) maximum intensity image at 50 nm per pixel resolution. In addition to the osteocyte lacunae and canaliculi, alignment of the extracellular matrix can be seen as alternating dark and lighter striations running from the top right to the bottom left of the image. Within and aligned to these striations, there are low-density (bright) features, which could represent collagen fibres. C: 3-D reconstruction of processed dataset after removal of all features except osteocyte lacunae. Note how the lacunae are arranged around a Haversian canal (removed) D: Orthogonal view of same dataset as in C. Note the high degree of alignment of the osteocytes with each other. In all of these images, bright pixels/voxels represent low density regions (porosity) and dark pixels/voxels represent high density regions (mineralised tissue).

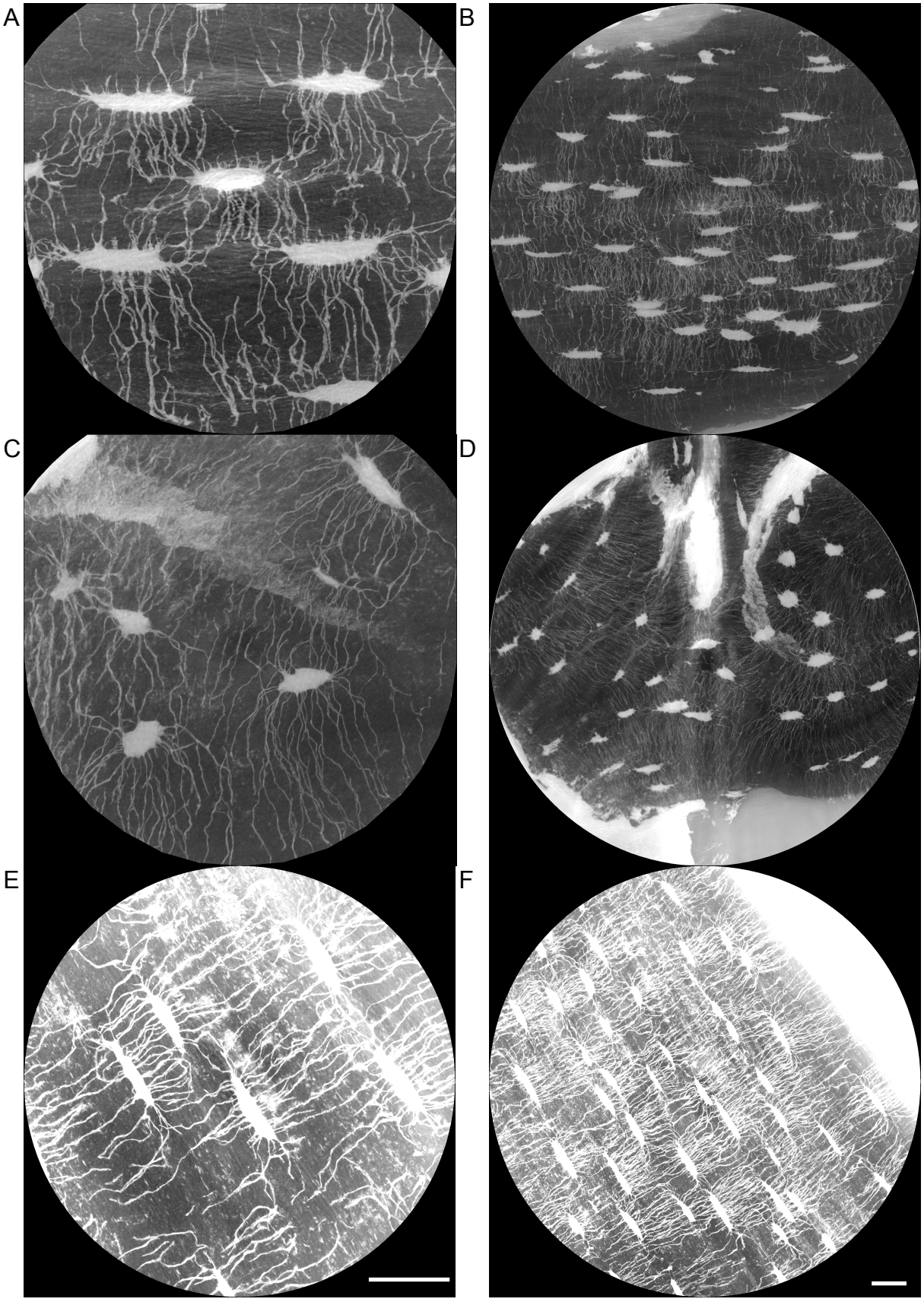

Figure 3-20: 200-slice Z projections of maximum greyscale values from nanoCT datasets. A & B = patient 3. C & D = patient 4. E & F = Patient 6. Scale bar = 10 μm.

The bright flecks in the inter-lacunar tissue are also of interest. As they are brighter than the mineralised background they must have a lower mean Z value. They may possibly represent collagen-rich regions or nano-scale porosity. Unfortunately, these data do not contain any compositional information (other than mean Z) so it is not possible to determine the nature of these observed structures any further.

3.4 Discussion

3.4.1 Plain Radiograph Discussion

All 7 of the patients from whom the HO was excised were male and had been exposed to major trauma. The mechanism of injury was blast in 5/7 and blunt force trauma in 2/7. All except one patient had an amputation; either caused by their mechanism of injury or performed surgically in the course of their treatment.

Looking at the macroscopic radiographic appearance of the samples, it is striking how variable the morphology is. Within the subset of samples containing obvious mineralisation, regions of cortical, trabecular, and hybrid morphology are clearly visible.

Samples 1 and 7 do not contain any mineralised tissue detectable by contact radiographs. It is unclear why these samples were included in the cohort. It is possible that they were suspected of being “pre-HO” but these data are not available. Also, sample 5 may not be HO at all. Its macroscopic appearance is that of a portion of the distal fibula, which may have been removed during a stump refashioning operation. This is consistent with the clinical information that the patient had a below-

knee amputation. Despite the hypothesis that this sample was not HO, it was still subject to microCT scanning as detailed in 3.2.3.

The heterogeneity and small number of samples means that any statistical analysis or quantitative comparison of the samples with each other or even with normal bone is unlikely to be of value. Also, the variable morphology and quantity of the samples means that they are not all suitable for all the various analytical modalities available.

3.4.2 MicroCT Discussion

MicroCT investigation of HO has revealed a wide variety of morphological features. As in normal bone, osteons, vascular channels, cortical volumes, and trabecular volumes are all present. However, the disordered arrangement of these anatomical elements in relation to each other sets this tissue apart from normal bone. Additionally, these features demonstrate variability over short length scales, which is unlike normal bone. For example, there is a distinct graded increase in size of trabeculae in samples 4A and 4C over a few mm and a similarly variable cortical shell thickness in samples 6B and 6C.

Another interesting feature is the hybrid morphology seen in samples 3A and 3C. This is neither typically cortical nor trabecular but contains elements of both. The samples are largely solid but contain channels (300-500 μm in diameter) and extensive surface texturing including depression and ridges with approximately 300-500 μm feature size. There is also evidence of osteons opening onto the surface of this hybrid tissue, as seen inside the white circles in Figure 3-4 A and C.

Sample 4B demonstrates an entirely novel architecture that has not previously been described in the context of HO. This sample is dominantly plate-like in its morphology with mineralised and unmineralised layers approximately 150-300 μm in depth. This structuring is reminiscent of distorted fibrolamellar or plexiform bone, which is not usually present in adult humans except in response to injury or inflammation, and even then only rarely.[195]

Samples 5A-C are clearly different to the other samples. They are almost entirely cortical, with highly regular Haversian canals of 40-80 μm in diameter. This provides support to the hypothesis that this sample is normal bone. It may be tempting to use this as a form of control tissue but there are two significant reasons not to do so. First, the macro and micro scale morphology look normal but this cannot be definitively proven one way or another. Second, the very idea of control tissue is problematic in the context of HO. It has been demonstrated (above) that HO bone can be morphologically similar to normal bone (cortical and cancellous), to at least one type of pathological bone (plexiform bone), and to a hybrid of any of these put together. So it would be hard to justify what type of normal bone one would choose as a control. Additionally, bone morphological parameters vary between different bones, making it even more challenging to justify what could be considered a valid control. The lack of consensus on this issue has led to the decision not to use sample 5, or any other tissue, as a control for any of the physicochemical techniques. Further, given the strong suspicion that sample 5 is normal bone, its quantitative morphological results will not be discussed below.

It is important to note that the aim of this work is not to compare the samples against one another, merely to observe what morphology is available to be observed. Therefore, no statistical significance testing has been performed on these data. Mean values and standard deviations for each patient have been derived from the subsample data.

Tissue mineral density was notably constant within and between samples (Figure 3-6). This may be partly explained because, unlike bone mineral density (BMD), TMD is insensitive to morphology of the samples because it is calculated from the mineralised portion of the dataset only (as defined by the binarisation process). In contrast, BMD is highly sensitive to the morphology of the samples because it averages the density values for the entire volume, including any soft tissue, vascular network, marrow elements, and other porosity. BMD has merit when one is interested in bone that conforms to normal trabecular morphology because it provides a clinically meaningful result but is of highly questionable relevance to HO. In contrast, TMD is particularly suitable for samples that do not fit standard morphological models and gives a clearer indication of the density of the mineral component only. What is surprising is how similar the TMD results are across the patients: 0.95 g/cm^3 (SD 0.05), 0.91 g/cm^3 (SD 0.01), and 0.97 g/cm^3 (SD 0.02) for patients 3, 4, and 6 respectively.

In contrast to the quantitative TMD data, the rest of the quantitative morphological data must be interpreted with extreme caution. The sample volumes used in this experiment were necessarily small due to the nature of the samples themselves. Figure 3-7A shows that the samples were only a few cubic millimetres in volume. The

relevance of this is that any calculated parameter will be highly influenced by small variations in the samples and may therefore provide information that is more to do with random sampling effects than being truly reflective of the tissue itself. In normal bone, it is important that a large sampling volume is used in order to improve the signal to noise ratio in the data. This is a reasonable approach when the architecture of the tissue being sampled is relatively homogeneous, such as orthotopic trabecular or cortical bone. However, given the highly variable morphology of the HO samples, even over short length scales, it is not clear that sampling larger volumes would be meaningful.

An additional limitation of these quantitative data is that many of the algorithms used to generate them rely upon models developed for bone that is clearly trabecular or cortical. It is not clear how meaningful the data generated by these algorithms will be. There are plans to develop new methods of quantifying the morphology of HO bone (personal communication) but, until that time, the current tools are all that are available. The quantitative data are included despite the sampling and quantification challenges because there are currently no published data whatsoever about the microCT-derived histomorphometric parameters of HO. Providing this information will be a starting point from which a greater understanding of the structure can be built over time.

Drawing conclusions from the quantitative results is challenging as there is such variation between (heights of bars) and within (magnitude of error bars) samples. Thus, perhaps the key conclusion to draw from these data is that there is not yet a satisfactory method for quantifying morphology of HO on this scale. This conclusion

supports a shift away from using current bone histomorphometric parameters and supports the development of new tools for quantifying the morphology of HO.

3.4.3 SEM Discussion

The topographical images generated by SE SEM confirm the qualitative findings of the microCT investigation, which are that HO can be morphologically similar to cortical bone, trabecular bone, a hybrid between the two, and even plexiform bone. Additionally, these images reveal extensive surface pitting, which is interpreted as evidence of osteoclast remodelling.

BSE SEM images reveal a wealth of detail that is not available from the SE SEM or microCT investigations. The most striking finding is that the internal structure is sharply divided into two types of tissue and that this appears to be independent of the external morphology. There is a core tissue that is densely populated with large, unaligned osteocyte lacunae. This is surrounded by a more organised tissue that has a classically lamellar structure with fewer, more highly aligned, osteocytes. The delineation between these two tissue types is clearly defined with no evidence of intermediate tissue types. Not only is this subdivision of internal structure constant across the samples, but the spatial distribution of the tissue types is also constant. Ordered lamellar bone is present around Haversian canals and on the surface of the samples. Taken with abundant evidence of osteoclast remodelling of the surface of HO, this finding provides a key insight into how HO forms: the primary structure is likely to be the disordered core tissue, which is replaced through remodelling by the ordered lamellar bone.

Another finding that is common to all samples is that the lamellar regions appear darker than the intervening disordered regions. In BSE SEM, the higher the mean atomic number (Z) in a region, the more electrons are scattered and the brighter it appears. Thus Z must be higher in the disordered regions than the lamellar regions. It is unclear why this is the case and would certainly be of interest for a potential future examination of these samples.

The clusters of approximately 1 μm diameter spheres visible in the SE SEM images (Figure 3-9) are also of interest. These appear similar to what has been described in the literature as calcospherites or mineralisation clusters.[196] It is significant that these calcospherites are seen close to sites of resorption but nowhere else. This is strong evidence that local resorption and mineralisation are coupled, as in normal bone remodelling. Thus the disordered macroscopic and millimetre-scale architecture is not driven by uncoupled remodelling. Instead, the remodelling process is working normally but is being directed in a disordered manner.

3.4.4 SXRD Discussion

In general, the maps in Figure 3-15 show a correlation between areas with low transmission, shorter c-axis length, narrowness of the full-width half maximum (FWHM) 002 value, and variability in the lattice orientation. One interpretation of the correlation between areas with low transmission and areas of variable orientation is that these areas represent the disordered core regions seen in cross-sectional SEM imaging. Their central distribution in the sample fits this interpretation. Also, they were seen to be brighter on BSE SEM, indicating a higher mean Z value, which would account for lower X-ray transmission seen in the synchrotron data. What is

less clear, however, is why these areas demonstrate low FWHM values and shorter c-axis values. The FWHM value is an indicator of the magnitude of crystalline alignment and c-axis values are dependent on a number of values including lattice substitutions and local conditions at the time of formation. It seems paradoxical at first that there should be a high magnitude of crystallite alignment (low FWHM) in areas demonstrating disorder. However, if one examines the direction of alignment in these areas, one can see that there is a high degree of variation between pixels. So the picture is more nuanced than first appears: there is disordered alignment at longer length scales, but a high degree of order at shorter length scales. With respect to the c-axis parameter, the maps show shorter lengths in the core regions and a rim of longer lengths at the peripheries (although an exception is that there is a region of the rim of sample 3 that has a shorter than average c-axis). Without further data, this finding is challenging to explain. However, the strength of this effect is not great, with less than 1% difference between the longest and shortest c-axis lengths in any map.

Put together, the conclusion from these data is that core regions have high mineral density, locally (<50 μm length scale) highly aligned crystals with short c-axis lengths, and poor alignment on longer length scales (>50 μm).

3.4.5 XRF Discussion

There is currently no published mechanistic data on mineralisation in HO so the finding of calcium-rich islands in developing HO is highly significant. This suggests that rather than synchronous deposition of calcium and phosphorus species to make hydroxyapatite, some other mechanism is occurring. It is conceivable that a calcium salt is deposited with a counter ion that is not detectable using XRF. Possibilities

could include organic acids such as lactate, oxalate, or carbonate. It is possible that this salt then transforms into an orthophosphate phase. This hypothesis is supported by the presence of a calcium-rich leading edge in the more mature samples of HO, suggesting that the tissue grows through a “calcium first” mechanism. Also, in the most mature specimen (3 years between injury and excision) there is no calcium-rich leading edge, suggesting that the growth of the mineralised tissue has ceased and it has become quiescent. This fits the clinical picture where HO grows rapidly over the course of months to years and then stabilises and stops progressing. It might be argued that embedding the samples in OCT could have caused some kind of soluble calcium phase to be washed out of the mineralised portion of the samples into the soft tissue giving the observed calcium-rich regions. However, these regions were also seen in Figure 3-16, in which the sample had undergone no preparation or manipulation of any kind so it makes this explanation much less likely and supports the calcium-first hypothesis.

Another finding that fits with the clinical experience is that there is separation between the mineralised and unmineralised portions in the most mature specimen (Figure 3-17D). While this may be a processing and sectioning artefact, it illustrates that the interface between mature HO and soft-tissue is weak, a fact that is confirmed by excising surgeons who report that mature HO simply peels out of its soft-tissue envelope. Quantitative measurement of the sulphur signal (a surrogate measure of protein) shows that there is progressive loss of organic content within the mineralised portion of the samples as they mature.

In summary, the XRF studies have generated novel hypothesis relating to the mechanism of mineralisation in HO and the maturation process, including an explanation for clinically observed phenomena.

3.4.6 Raman Spectroscopy Discussion

The extensive OCP signal is the most interesting finding from the Raman mapping experiment. Raman spectroscopic evidence of OCP in bone formation has only ever been shown in animal studies, and then only as a point spectrum rather than as spatially resolved data.[197] Its colocalisation with HA is important because it is thought to occur as a preliminary phase in mineralisation.[198] Thus, if HA forms from an OCP precursor phase, it is unsurprising that areas rich in OCP will also be rich in HA. These data support the hypothesis that OCP is a significant precursor to HA formation in HO. This is relevant because OCP is much more soluble than HA and would therefore make developing HO bone more amenable to chemical dissolution than formed bone.

3.4.7 NanoCT Discussion

These are the first nanotomography datasets of HO bone ever recorded. At this scale, what is most remarkable about the tissue is how ordered it is. The long axes of the lacunae are predominantly determined by the lamellar orientation while the short and intermediate axes are determined by another factor that is not obvious from these data. For example, in Figure 3-19C, the long axes of the lacunae are seen to follow the lamellae around a Haversian canal (not shown in this image). In Figure 3-19D, which is an orthogonal view of the same dataset, there is a striking degree of alignment of the short axis of the lacunae, which all lie on the same plane. It would

be of great value to know what the orientation of the samples was in the body so that the factors determining the alignment of these axes could be understood in greater detail. One hypothesis is that while the lamellar structure of the bone determines the long axis alignment of the lacunae, gravity or a chemotactic gradient may determine the alignment of the short and intermediate axes.

3.5 Discussion and Conclusions

This study is the first time that human HO has been analysed by nano tomography or any of the spatially-resolved chemical modalities (XRD, XRF, and Raman). It is also the first time that microCT has been used to quantify the histomorphometric parameters or mineral density of human HO.

One of the most striking findings of this study is that HO demonstrates different degrees of order depending on length scale. For example the SEM and microCT data support previous reports of disordered hybrid cortical-cancellous morphology on the millimetre-micron length scale and there is further evidence of disorder when interpreting the crystallite orientation data from the SXRD. However, in contrast to this disorder, the nano-tomography demonstrates that the osteocyte lacunae are highly aligned in planes with canaliculi oriented at 90^{o}, forming ordered connections between these planes. This finding generates a question that cannot be answered with these data: what processes contribute to order or disorder at each length scale?

Another feature that we have detected (using SEM) that has been noted before[144] is the presence of osteoclast resorption pits, indicating that HO is continuously being remodelled. Further evidence for this remodelling is demonstrated by the presence of

discontinuous osteons, showing that existing structures were not simply enlarged but partially reabsorbed and new Haversian systems laid down in their place.

Previous reports have suggested that HO may have a mature leading edge of well-corticated bone with an inner core of immature bone.[78,199] However, we have shown using XRF elemental mapping that there are islands of calcium within the soft tissue surrounding the edge of the main HO mass. This would suggest that rather than enlarging through pure remodelling, there is some *de novo* mineralisation process acting around the HO mass with eventual consolidation of this new bone as the mass enlarges. Looking at this process more closely, our XRF data has provided evidence that the mechanism of mineralisation in HO may be a unique “calcium first” process. The mineral islands forming at the periphery are initially highly calcium-rich and only approach a more normal calcium/phosphate stoichiometry as the HO tissue matures. This is highly unusual and contrary to the accepted mechanism of mineralisation whereby calcium and phosphate are deposited together from the outset.

Due to the heterogeneity of the samples, small sample number, and the nature of the analytical modalities, this work was designed to be predominantly descriptive rather than quantitative in its approach. Few statistical analyses were appropriate. Also, it is important to note that this work is not designed to be a quantitative comparison with normal bone and therefore no “control” tissue has been examined. Given that HO is not a disease of physiological bone but a new and separate entity, it would be challenging to justify which type of normal bone and from what anatomical location one should choose to compare HO against.

It is also important to note that all of our samples and the focus of this work relate to HO secondary to high-energy trauma. It is uncertain whether or not these findings may be generalisable to HO caused by other aetiologies. Indeed, it has not been demonstrated that HO generated as a consequence of different aetiologies has a common pathophysiology, structure, or physicochemistry.

4 DEVELOPMENT OF A NOVEL HETEROTOPIC OSSIFICATION THERAPY

4.1 Introduction

Many of the clinical problems caused by HO are due to the mechanical effects of bone forming in abnormal anatomical locations. If it were possible to prevent this formation, or disperse it once it had formed, then it may be possible to reduce the clinical impact on the patient. However, as discussed in Chapter 1, a fundamental problem with attempting to inhibit the biological processes involved in HO formation is that the signalling network involved may allow more than one way for the pathological end result to occur. This is particularly true when attempting to inhibit a disease such as HO where the mechanism, signalling networks, and cell populations are so poorly understood. The central aim of this work was to overcome this challenge by developing a novel treatment capable of targeting the mineralised component of bone. It was hypothesised that a non-toxic agent could be developed that was able to dissolve hydroxyapatite and / or directly inhibit its formation. This agent would also require a means of delivery to the site of formation of HO. The desired properties of such a treatment would be as follows: ability to dissolve hydroxyapatite under physiological conditions, specificity for HO without affecting normal bone, non-toxic, temporally controllable action, and ability to be delivered percutaneously.

This chapter details the search for, and development of, a polyphosphate treatment for HO. In this study, the demineralising effects of polyphosphate on hydroxyapatite monoliths and pathological bone samples were determined. The mechanism of this

process was investigated using micro X-ray fluorescence (micro-XRF). The potential to regulate the demineralising activity was evaluated through controlling local pH and through the exposure of polyphosphate to alkaline phosphatase (ALP). Finally, the effect on samples of human post-traumatic HO was evaluated using microCT to determine the change in mineralised volume.

A modified version of this chapter was published in the Journal of Materials Chemistry B.[200]

4.1.1 Polyphosphates as Potential HO Therapy

During the 1960s, there was great research interest in the potential role of polyphosphates in regulating biomineralisation. Fleisch *et al.*[201] found that the addition of minute (10^{-6} to 10^{-7} M) concentrations of polyphosphates were able to inhibit calcium phosphate crystallisation. Fleisch *et al* took this work further in 1966 by investigating the *ex vivo* biological effect of polyphosphates on chick femur mineralisation.[202] Incubation in the presence of polyphosphates for 6 days inhibited mineralisation as analysed histomorphometrically and by using X-ray diffraction.

Despite being shown to be effective inhibitors of calcium phosphate crystal formation, polyphosphates subsequently received little attention as inhibitors of biomineralisation. Ultimately, this body of research led to the development of bisphosphonates, which are chemically similar to pyrophosphate except that the central oxygen atom is replaced by a carbon atom with two side chains. Rather than inhibiting mineralisation in the manner of polyphosphates, bisphosphonates have the opposite effect and reduce demineralisation through inhibition of osteoclast activity.

In the dental research literature, polyphosphates have been investigated due to their anti-caries effect, which occurs through increasing the resistance of hydroxyapatite (HA) to acid dissolution and the chelation of calcium ions in order to prevent tartar formation.[203] In 1983, McGaughey undertook detailed mechanistic work to attempt to understand the interaction between HA and a range of polyphosphates.[204] This work showed that hexametaphosphate (HMP) is an effective agent for the dissolution of HA. The author's conclusions about the molecular mechanisms are, however, debatable. Given the size and mass:charge ratio of the polyphosphate molecules, their direct incorporation into the hydroxyapatite lattice is improbable. More recently, Rao and Kannan demonstrated the efficacy of HMP in dispersing HA in aqueous solution.[205] Whatever the mechanism, these papers provide evidence that HMP can dissolve HA, a mineral that is normally incredibly insoluble.

In 2001, Cini *et al.*[206] investigated the use of polyphosphates to dissolve calcium pyrophosphate, a mineral that causes the condition pseudogout. They demonstrated that hexametaphosphate could dissolve this mineral in *in vitro* and *ex vivo* samples of pathologically calcified human meniscal tissue. Although this work related to the effect of HMP on calcium pyrophosphate rather than HA, the results are encouraging. This work demonstrates that hexametaphosphate can accelerate the dissolution of a biologically formed calcium phosphate from within a collagenous matrix (the meniscus) and that this reagent is relatively benign to both chondrocytes and the biological component of the menisci. This gives real weight to the idea that this agent might be used to disperse hydroxyapatite from the collagen template found in heterotopic ossification.

Put together, the data from the 1960's studies into mineralisation control, the dental literature, and the more recent experiments on calcium pyrophosphate, suggested the hypothesis that a polyphosphate may be the agent required for treating and dissolving HO.

4.2 Methods

4.2.1 Experimental Outline and Rationale

The first step in developing an HA-dissolving treatment was to compare the relative effectiveness of a variety of polyphosphates in order to identify the most promising candidate to take forward for further development. A simple screening experiment was undertaken whereby pellets of HA were incubated in a range of polyphosphates and their mass was monitored over time to determine the degree of dissolution. In order to gain a greater understanding of the interaction between the reagents and HA, the residual pellets at the end if this experiment were examined with XRF.

Using the mass-loss of pellets of HA over time was found to be an effective but slow method of determining the HA-dissolving ability of the polyphosphates. In order to be able to determine the HA-dissolving ability of HMP under a variety of conditions, a more rapid experimental technique needed to be developed. HA sol was chosen as the target for dissolution to achieve this faster turn-around time. HA sol is chemically identical to solid HA but is physically dispersed as a nanoparticular solid phase in a continuous liquid water phase. This makes dissolution much more rapid as the surface-to-volume ratio is vastly increased compared to sintered monoliths. A novel method was developed whereby light transmission through HA sol was used to

determine the degree of dissolution. This method was then used to determine the effect of pH and alkaline phosphatase (ALP) on the ability of HMP to dissolve HA.

In order to determine whether or not HMP was able to dissolve HA in a biological setting, post-mortem rat femora were used as a target material and mechanical testing was used to measure the effect.

As a final test of efficacy, samples of human HO were incubated in HMP or control media and the effect on the mineralised volume was assessed using microCT.

In order to investigate the potential of polyphosphates to act as a prophylaxis for HO, a further experiment was undertaken. HA synthesis was attempted in the presence of a variety of polyphosphates, and the products were analysed using XRD.

4.2.2 HA Pellets and Dissolution

Disc-shaped pellets of HA were formed by isostatically pressing 400 mg of HA powder (Sigma-Aldrich, Gillingham, UK) with 100 µL of deionised water (diH_2O) at 2 kN for 5 seconds. These were sintered at 600 ^oC for 1 hour. After cooling in ambient conditions, pellets were weighed and incubated at room temperature (20 ^oC) in 50 ml of a 0.1 M solution of each of the following reagents: sodium pyrophosphate decahydrate ($Na_4P_2O_7 \cdot 10H_2O$), sodium tripolyphosphate ($Na_5P_3O_{10}$), trisodium trimetaphosphate ($Na_3P_3O_9$) (all Sigma-Aldrich), and sodium HMP ($Na_6P_6O_{18}$) (Fisher, Loughborough, UK) (Figure 4-1). Ethylenediaminetetraacetic acid (EDTA) ($C_{10}H_{16}N_2O_8$) (Sigma-Aldrich) was used as a positive control. Before incubation, each

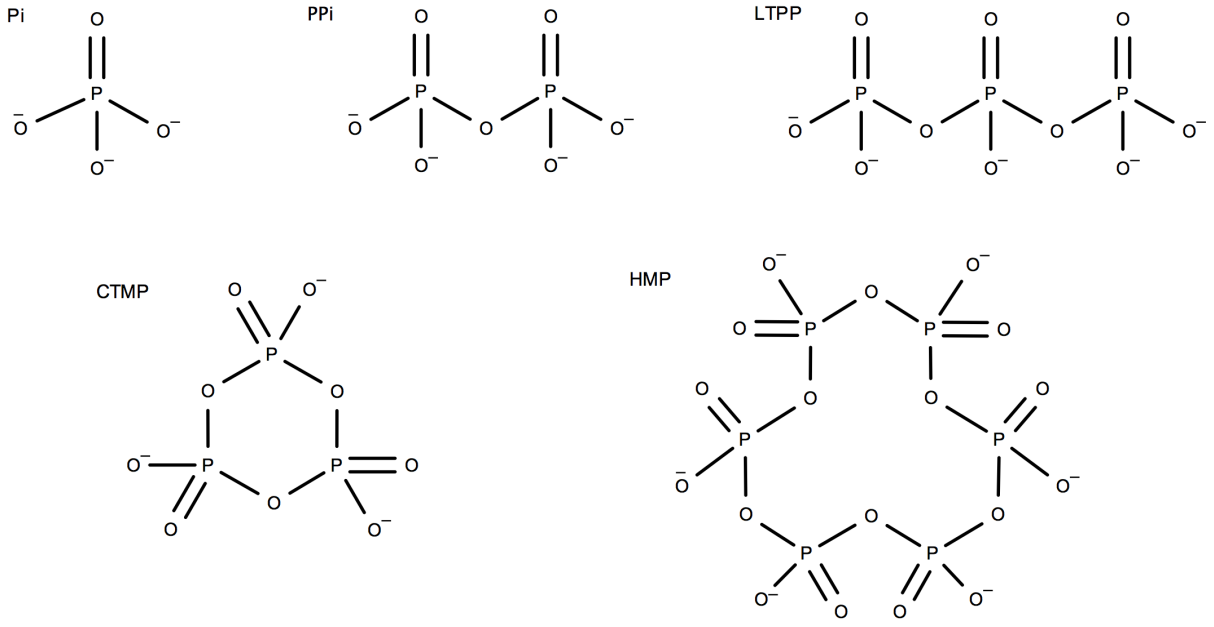

Figure 4-1: Schematic structural diagrams of the ionic forms of the polyphosphates under investigation in this chapter. Pi = orthophosphate. PPi = Pyrophosphate. LTPP = Linear tripolyphosphate. CTMP = Cyclical Trimetaphosphate. HMP = Hexametaphosphate.

reagent was adjusted to pH 7.4 (physiological pH) with 0.1 M NaOH or 0.1 M HCl. There were triplicate repeats of each condition. The pH-adjusted media were replaced every 3.5 days. The pellets were removed from solution every 3.5 days, surface fluid removed with absorbent paper, and weighed. After 21 days the pellets were recovered (except for the EDTA group, which had dissolved completely) and dried overnight at 80 ^{o}C before being analysed by micro XRF to examine the surface chemistry.

4.2.3 XRF

Elemental maps of the recovered and dried HA pellets were generated using a Tornado M4 micro-XRF system (Bruker Nano Gmbh, Berlin, Germany) fitted with a

Rhodium micro focus X-Ray tube and a polycapillary lens. The X-Ray spot size from the polycapillary lens was 25 μm. All samples were analysed under ambient conditions with an X-Ray tube voltage of 50 kV and a tube current of 400 μA. The X-rays were rastered over the sample surface with a step size of 100 μm and an XRF spectrum was collected at each point with an acquisition time per pixel of 2.5 ms. Elemental maps were then generated in real time by gating around the phosphorus $K\alpha_1$ (2.0137 keV) and calcium $K\alpha_1$ (3.692 keV) X-ray fluorescence emission peaks in the XRF spectra, creating an image where pixel intensity represented detected X-ray counts per second per eV from each measurement point on the sample. Pixel intensity increased monotonically with X-ray counts with maximum pixel intensity normalised to the highest count rate per eV for a given element across the whole sample. The instrument was set to map samples three times to generate a single averaged map for each element.

4.2.4 Sol Optical Density Method Calibration

In order to demonstrate that the transmission of light through hydroxyapatite (HA) sol may be used to quantify the concentration of available HA in sol form, the following calibration process was performed. HA sol was synthesised as described by Afshar et al.[207] Briefly, this involves adding 0.3 M orthophosphoric acid dropwise to an equal volume of 0.5 M calcium hydroxide under agitation and close pH control, being careful not to let the pH drop below 10. After synthesis, the HA sol was allowed to age overnight at 40^{o}C.

The concentration of HA per ml of sol was determined as follows. Triplicate volumes of 3ml of pure sol were centrifuged at 3900 rpm for 10 minutes, the supernatant

decanted, and the tubes containing the residual centrifuge pellets dried at 80^{o}C overnight. The mean dried pellet mass was 79.3 g (standard deviation 0.265 g). Thus each ml of pure HA sol yielded 26.43 mg of dried HA. Concurrently, a volume of the same batch of HA sol underwent serial dilution with deionised water. Triplicate repeat volumes of 245 μL of each dilution were transferred to a 96-well plate and optical density (OD) was measured at 650 nm using a Glomax 9301-010 plate reading spectrophotometer (Promega, Wisconsin, USA). The resulting calibration curve is shown in Figure 4-2.

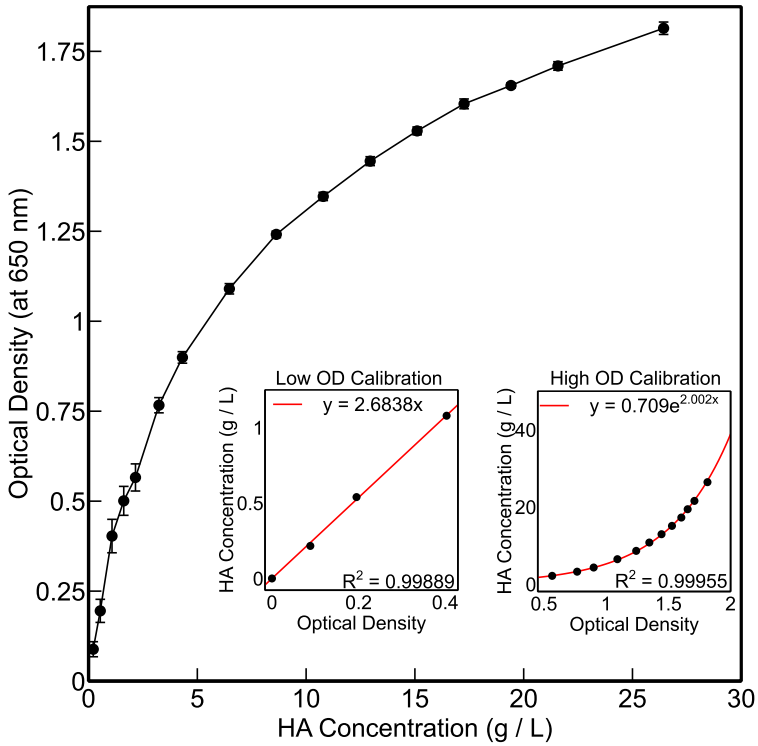

Figure 4-2: Calibration curve showing the relationship between optical density (at 650nm) and the concentration of HA Sol. Error bars are +/- standard deviation. HA = hydroxyapatite. Insets: Reversing the axes and dividing the data into points greater than or less than an OD value of 0.5 allows best-fit lines to be drawn and equations formulated to describe the relationship between optical density and HA concentration. Note the exceptionally high R^2 values. HA = hydroxyapatite. OD = Optical Density.

By using the chart trend line fitting function on Microsoft Excel (Microsoft Corporation, Redmond, Washington, United States), equations relating high (>0.5) and low (<0.5) OD values to HA concentrations were generated (see insets in Figure 4-2). These equations were used to convert OD data to g / L values on the Y-axes of Figure 4-5 and Figure 4-6.

4.2.5 pH Control of HA Dissolution by HMP

HA sol was prepared as described above and was added to serial dilutions of HMP in a 96-well plate. Each concentration was conducted in triplicate. diH_2O was added to each well to give a constant final well volume of 245 μL. A Glomax 9301-010 plate reading spectrophotometer (Promega, Wisconsin, USA) was used to measure light transmission through the sample at 650 nm as a quantitative determination of the degree of dissolution. Results were normalised to a diH_2O blank. This experimental method was repeated with adjustment of the pH to 6.2, 7.4, and 9.6 using 0.1 M HCl or 0.1 M NaOH as required.

4.2.6 Alkaline Phosphatase Control of HA Dissolution By HMP

3.6 mL of undiluted HA sol was dissolved completely in 25 mL 0.1 M HMP (adjusted to pH 7.4 using 0.1 M NaOH). The resulting solution was optically clear on macroscopic examination. 2 mL aliquots of this stock solution were incubated at 37 ^oC for 9 days with addition of either 400 units (in 200 μL) of bovine ALP (Sigma-Aldrich) for the experimental samples or 200 μL diH_2O for the control samples. The optical density of the solution was measured at day zero and day nine using a plate-reading spectrophotometer (see above). Each condition was conducted in triplicate and the results compared using a two-tailed Student's t-test.

4.2.7 Residual Mass Method

The OD method of assaying the concentration of HA sol is novel and, as such, needed to be validated to ensure it is reliable. The calibration data presented above provided reassurance that this methodology was robust but this was not sufficient in itself to prove reliability. Therefore, to support the conclusions drawn from the data,

these experiments were repeated. Instead of determining the concentration of HA sol through light transmission, direct determination of the HA concentration was performed. For the pH experiment, 1.5 ml aliquots of HA sol were added to 10 ml HMP at varying concentrations and the pH was adjusted to 6.2, 7.4, or 9.6. These samples were agitated for 4 hours, centrifuged at 3900 rpm, residual pellets dried overnight at 80^{o}C, and then weighed to determine the HA pellet mass. All conditions were carried out in triplicate. The ALP experiment was repeated exactly as outlined previously, but instead of measuring the OD of the samples, the residual mass method was used to measure the amount of undissolved HA per sample. Triplicate repeats were performed.

4.2.8 Post-Mortem Rat Tibiae

Three pairs of tibiae were harvested immediately post mortem from male Lister hooded rats of 275-325 g bodyweight. The left-sided tibiae were incubated in 50 mL 1% w/v gellan (Gelzan CM, Kelco, Atlanta, USA) loaded with 0.1 M HMP. Right-sided tibiae were incubated in 50 mL 1% w/v gellan only. The gellan was used as an inert delivery vehicle in this experiment (Figure 4-8A). All samples were incubated at room temperature (20 ^{o}C) for 6 days. Destructive 4-point bending was performed on all of the samples using a Bose Electroforce 5500 mechanical tester (Bose / TA Instruments, Minnesota, USA). Testing parameters were as follows: upper points 4.0 mm apart, lower points 10.4 mm apart, displacement ramp 0.02 mm/s, non-destructive displacement limit 0.2 mm, destructive displacement limit 2.0 mm (see Figure 4-8B for details of the test set-up). Data from the mechanical testing were analysed using WinTest 7 software (Bose). Stiffness was calculated as the gradient

of the linear elastic region of the force-displacement curves. Yield force was identified as the force corresponding to the upper limit of the elastic region of the force-displacement curves. Maximum force was taken as the maximum recorded force during destructive testing. A two-tailed paired t-test was used to compare the stiffness, yield force, and maximum load to failure for each pair of tibiae.

4.2.9 Human HO

Samples of human HO excised from a single patient who had suffered civilian poly-trauma were retrieved from the Human Biomaterials Resource Centre at the University of Birmingham. These were incubated in 5 mL of either 0.1 M HMP (adjusted to pH 7.4 with 0.1 M NaOH) or diH_2O as a control for 7 days. Before and after incubation, these samples were wrapped in parafilm and placed inside a polystyrene sample tube. These were scanned using a Bruker SkyScan 1172 X-ray micro computed tomography (microCT) scanner (Bruker, Coventry, UK) with the following settings: no filter, camera position near, pixel size 4.96 μm (voxel size 120.32 μm^3), rotation step 0.2^o, camera resolution 4000 x 2664 pixels, exposure time 400 ms, frame averaging 6, current 70 μA, voltage 70 kV. The scans were reconstructed using NRecon software (version 1.6.10.2, Bruker microCT) and analysed using CTAn (version 1.15.4.0, Bruker microCT). Three-dimensional models were generated using a double time cubes algorithm. Models were visualised with CTvol (version 2.3.1.0, Bruker microCT). The same scanning, reconstruction, and post reconstruction processing settings were used for the samples before and after incubation.

4.2.10 Inhibition of HA Synthesis

HA synthesis (as above)[207] was undertaken in the presence of 10^{-3} M of each of the potential inhibiting reagents: pyrophosphate, linear tripolyphosphate, cyclic trimetaphosphate, EDTA, and HMP. The reaction products were aged for 1 hour then centrifuged (4000 rpm for 10 minutes) and washed with diH_2O three times. The product was dried overnight at 80 ^oC and finely ground. X-ray diffraction patterns were generated using a Bruker D8 diffractometer (2θ 5-80^o) and analysed using Bruker EVA *diffrac.suite* software (version 3.1). The raw diffraction data was baseline corrected but not smoothed. Reference data for HA (PDF 00-009-0432) and calcium hydroxide ($Ca(OH)_2$) (PDF 00-044-1481) were obtained using the software program PDF-4+ with database version 4.4103 (International Centre for Diffraction Data).

4.3 Results and Discussion

4.3.1 HA Pellet Mass Loss

Incubation in HMP reduced the mean mass of HA pellets by 30.2% over 504 hours (Figure 4-3). The EDTA positive control reduced the mass of pellets by 95.0% in the same time period. diH_2O water control, cyclical trimetaphosphate, linear tripolyphosphate, and pyrophosphate had no effect on HA pellet mass over the same time period.

HMP was clearly the most effective polyphosphate at dissolving HA. As such, the other reagents were excluded from further dissolution experiments. They were, however, included in the synthesis-inhibition experiment (below).

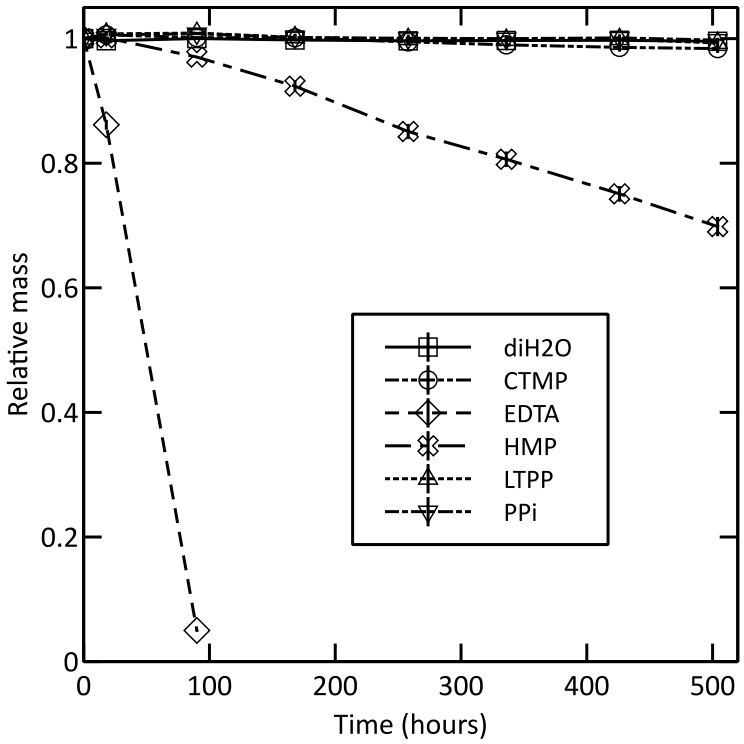

Figure 4-3: Mass loss of hydroxyapatite pellets over time incubated in various potential dissolving agents. This demonstrates the potent dissolving ability of hexametaphosphate. Ethylenediaminetetraacetic acid (EDTA) was used as a positive control. diH_2O = deionised water, CTMP = cyclic trimetaphosphate, LTPP = linear tripolyphosphate, PPi = pyrophosphate, HMP = hexametaphosphate HMP. Error bars are +/-SEM.

4.3.2 HA Pellet XRF Maps

Element maps illustrating the resulting changes in surface chemistry as a result of incubation in the polyphosphates for 21 days are shown in Figure 4-4. diH_2O, HMP, linear tripolyphosphate, and cyclical trimetaphosphate all showed no change in Ca:P ratio over the period of the study.

The pellets incubated in pyrophosphate, however, showed an increased phosphorus signal distributed heterogeneously across the surface of the pellet. This suggests that there is adsorption of pyrophosphate ions onto the surface of the samples. There are no images for the pellets incubated in EDTA as these were dissolved completely. The finding that the HMP group did not cause any change in the Ca:P ratio compared with deionised water controls is significant. This is because an increase in phosphorus signal relative to calcium signal would be expected if the mechanism of dissolution was initial incorporation of the terminal phosphate group of HMP into the HA matrix (as McGaughey proposed).[204]

The lack of change in Ca:P ratio, coupled with the monotonic rate of dissolution was more consistent with a solution-mediated rather than surface-mediated mechanism. Certainly, HMP has a very strong affinity for Ca^{2+} ions, forming a 1:1 complex with a high thermodynamic stability constant.[208] Thus it is possible that HMP is complexing any available Ca^{2+} ions from the hydroxyapatite matrix and forming a highly stable Ca-HMP complex in solution. Indeed, HMP has such a high affinity for cations that it has been demonstrated to dissolve kaolin and kaolinite by complexing the aluminium cations in these minerals.[209]

The finding that incubation of HA pellets in pyrophosphate caused an increase in the surface phosphorus signal on micro-XRF suggests adsorption to the surface of the pellet, which is consistent with previous reports in the literature.[210]

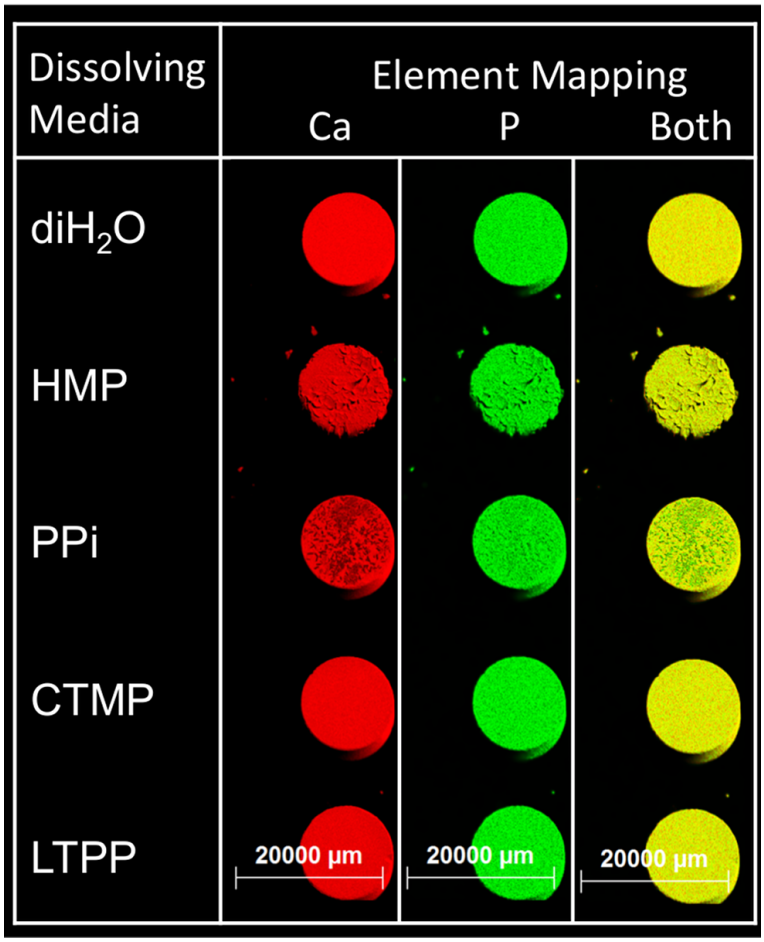

Figure 4-4: Micro X-ray fluorescence mapping of calcium and phosphorus on the surface of pellets of hydroxyapatite after 21 days of incubation in the following potential dissolving agents: deionised water (diH_2O), cyclic trimetaphosphate (CTMP), linear tripolyphosphate (LTPP), pyrophosphate (PPi), hexametaphosphate (HMP). Note that for each dissolving agent, this figure shows the micro-XRF data for different elements on the surface of a single pellet. There were, in fact, triplicate repeats under each condition and the changes shown here were typical for all repeats.

4.3.3 Effect of pH and ALP using the Optical Density Method

At every concentration of HMP, higher pH values reduced the amount of HA sol dissolved (Figure 4-5). For an HMP concentration of 0.1125 M, the available HA in sol form in the samples at pH 6.2, 7.4, and 9.6 was 0.15, 13.3, and 23.4 g/L, respectively (note: control samples of sol had 26.43 g of HA per L). This pH-controlled effect was demonstrated across a range of concentrations of HMP spanning four orders of magnitude. This may prove to be a key mechanism by which the activity of HMP can be targeted towards the sites of pathological bone formation in HO. This is because hypoxia is thought to be a key step in the biological pathway for HO formation, and hypoxia leads to local low pH in tissues through switching toward anaerobic respiration and the generation of lactate.[57,211] Therefore, in sites where pH is low and HO is most likely to develop, HMP will also be most potent at dissolving HA. While these data provide compelling evidence that pH controls the HA-dissolving ability of HMP, they do not provide any mechanistic explanation for the relationship.

Addition of ALP to a solution of HA sol dissolved in HMP caused HA to precipitate out of solution as demonstrated by a change from clear to turbid over 9 days. The mean HA concentration in the ALP group increased from 1.08 to 11.8 g/L ($p = 0.00$) whereas that of the control group fell from 1.13 to 0.94 g/L ($p = 0.007$) (Figure 4-6).

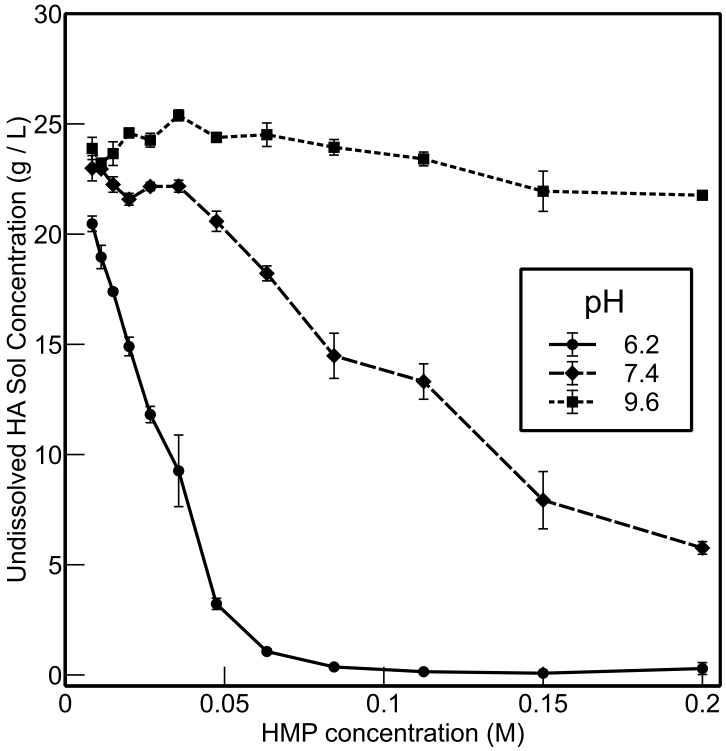

Figure 4-5: Demonstration of the effect of varying the pH and concentration of HMP on the amount of available HA in sol form. Lower amounts (in g/L) of available HA sol indicates higher amounts dissolved by the HMP. Dissolving ability is increased with increasing concentration and decreasing pH. Error bars are +/- SEM.

ALP is an exophosphatase found in many tissues that can cleave the terminal phosphate group from polyphosphates. As demonstrated in Figure 4-3, shorter chain length polyphosphates have little or no HA-dissolving ability. Therefore, the increased turbidity in the presence of ALP is interpreted to be due to HA precipitating out of solution as the solvent (HMP) is cleaved. The importance of this is that it demonstrates that ALP-mediated degradation is a feasible mechanism for the inactivation of HMP over time in the body. It would not be desirable to deliver an

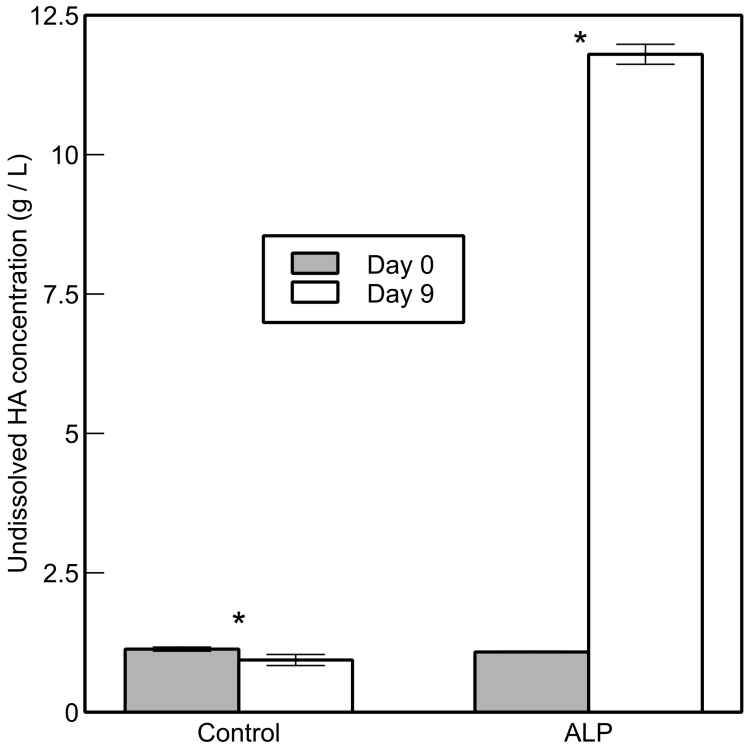

Figure 4-6: Change amount (in g/L) of available HA in sol form in a nearly- saturated solution of HA dissolved in 0.1 M hexametaphosphate after incubation with either alkaline phosphatase (ALP) or control (diH2O) for 9 days. Error bars are +/- SEM. * = p < 0.05.

agent with HA-dissolving activity into the body without the possibility of limiting its duration of action. It is noted that, in contrast to the ALP group, the HA concentration of the control group decreased. This may represent further dissolution of any undissolved HA sol over the incubation period.

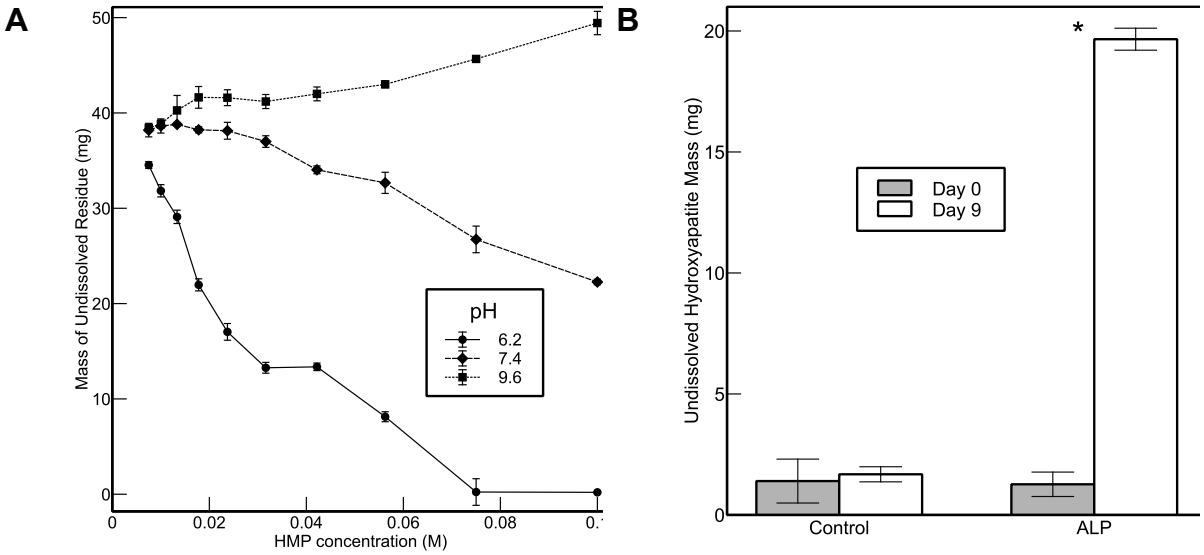

Figure 4-7: Repetition of pH and ALP control experiments using an alternative assay method (residual mass of HA). A: The effect of pH and concentration of HMP on the mass of undissolved HA. Increasing pH is associated with greater mass of undissolved HA suggesting that HMP is less effective at dissolving HA at higher pH. Error bars are +/- SEM. B: Change amount (in g / L) of available HA in sol form in a nearly-saturated solution of HA dissolved in 0.1 M hexametaphosphate after incubation with either alkaline phosphatase (ALP) or control (diH_2O) for 9 days. Error bars are +/- SEM. (* p = 0.00)

4.3.4 Effect of pH and ALP Using the HA Residual Mass Method

The results of these experiments are presented in Figure 4-7. These data are strikingly similar to the OD-derived data and therefore support the conclusions drawn using the optical density methodology.

4.3.5 Post Mortem Rat Tibiae

Incubation of rat tibiae in gellan loaded with HMP caused a reduction in stiffness and maximum load to failure. Stiffness was 49% lower in the HMP/gellan group compared to gellan-only controls ($p = 0.001$). Maximum load to failure was 41% lower in the HMP/gellan group compared to gellan-only controls ($p = 0.03$) (Figure 4-8C). There was no significant difference in the yield force between the two conditions. The reduction in stiffness of the bone is consistent with the dissolution of hydroxyapatite from the bone matrix.[212,213] Interestingly, the yield force was unaffected by incubation in HMP. As the yield force is determined by the collagenous component of bone, this finding suggests that HMP is able to dissolve HA from within the bone composite structure without affecting the collagen component.[174,214] Another notable finding from this experiment was that gellan was able to form a stable gel in the presence of HMP. As discussed below, HMP has unpredictable effects on many hydrogels and prevents gelation in nearly all of them. Thus the finding that 1% gellan will form a set gel in the presence of 0.1 M HMP is significant, particularly given that no cross-linking agent was added.

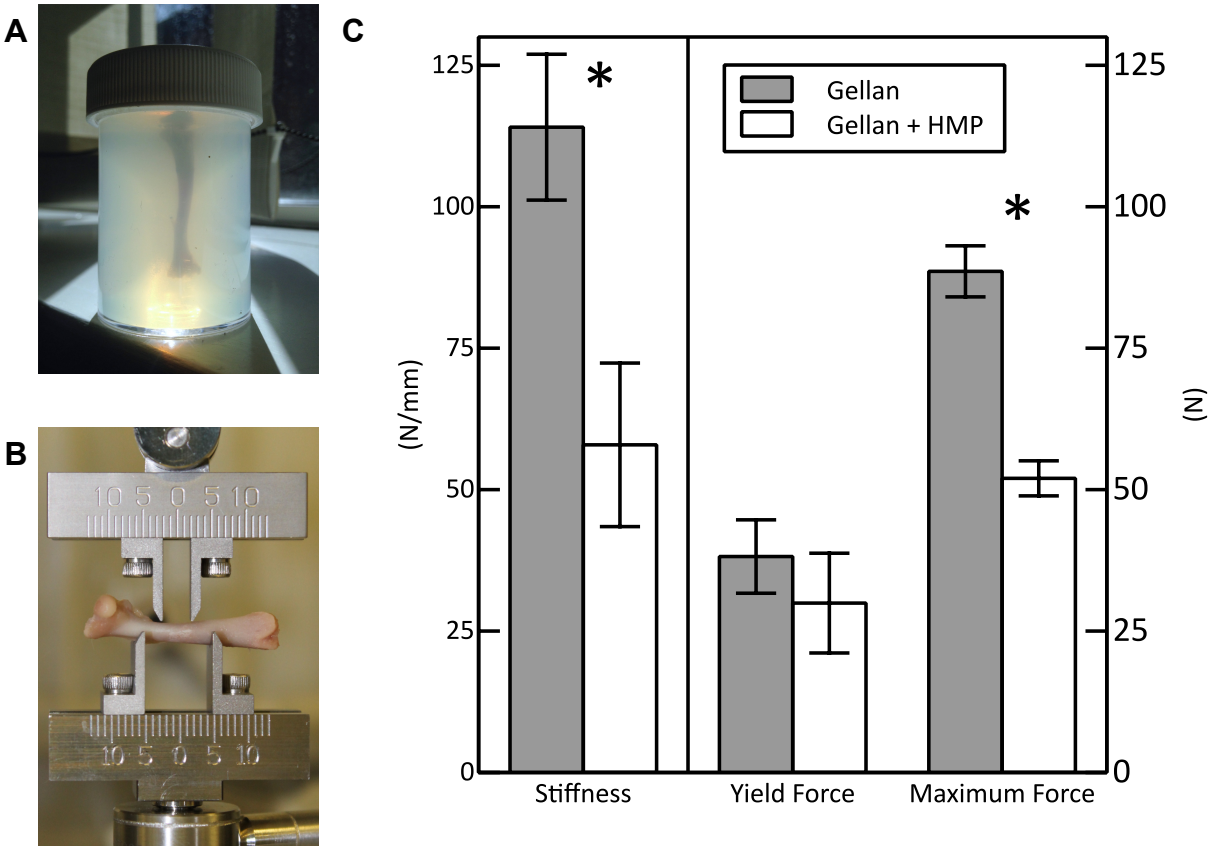

Figure 4-8: A: Rat tibia incubated in 1% gellan containing 0.1 M HMP. B: 4-point mechanical testing of tibia. C: Results of 4-point mechanical testing of rat tibiae after incubation in either 1% gellan alone or 1% gellan loaded with 0.1 M HMP for 6 days. Incubation in HMP caused a significant reduction in the stiffness and maximum load to failure compared to paired controls. Error bars are +/-SEM. * = $p < 0.05$.

4.3.6 Human HO

By using the same scanning, reconstruction, and processing protocols for the samples before and after incubation, micro-CT imaging and volume analysis demonstrated that HMP caused the demineralisation of samples of human HO at physiological pH. The bone volume of the HO sample incubated in 0.1 M HMP at pH 7.4 for 7 days decreased from 11.6 mm^3 to 3.43 mm^3, a reduction of 70.4%. The bone volume of the control sample changed from 9.34 mm^3 to 8.76 mm^3, a reduction of 6.2%. Three-dimensional models of the mineralised component of the HO samples are shown in Figure 4-9. The sample incubated in HMP appears grossly attenuated. In contrast, the sample incubated in diH_2O appears largely unchanged compared with its pre-incubation state. With n = 1 for each experimental condition, these results must be interpreted with caution. However, due to the precious nature of the samples and the encouraging results obtained using other forms of HA, it was decided not to repeat this experiment. The conclusion from this experiment is that HMP is able to dissolve human HO.

4.3.7 Inhibition of Hydroxyapatite Synthesis

X-ray diffraction (XRD) patterns generated from unsintered reaction products are shown in Figure 4-10. The patterns generated in the control sample and in the presence of cyclic trimetaphosphate, EDTA, linear tripolyphosphate, and pyrophosphate match the reference standard of HA with no detectable secondary phases. In contrast, the pattern generated by the sample synthesised in the presence of HMP has additional peaks that match the reference standard for $Ca(OH)_2$, one of the reaction precursors. This suggested that HMP inhibited the formation of HA, as

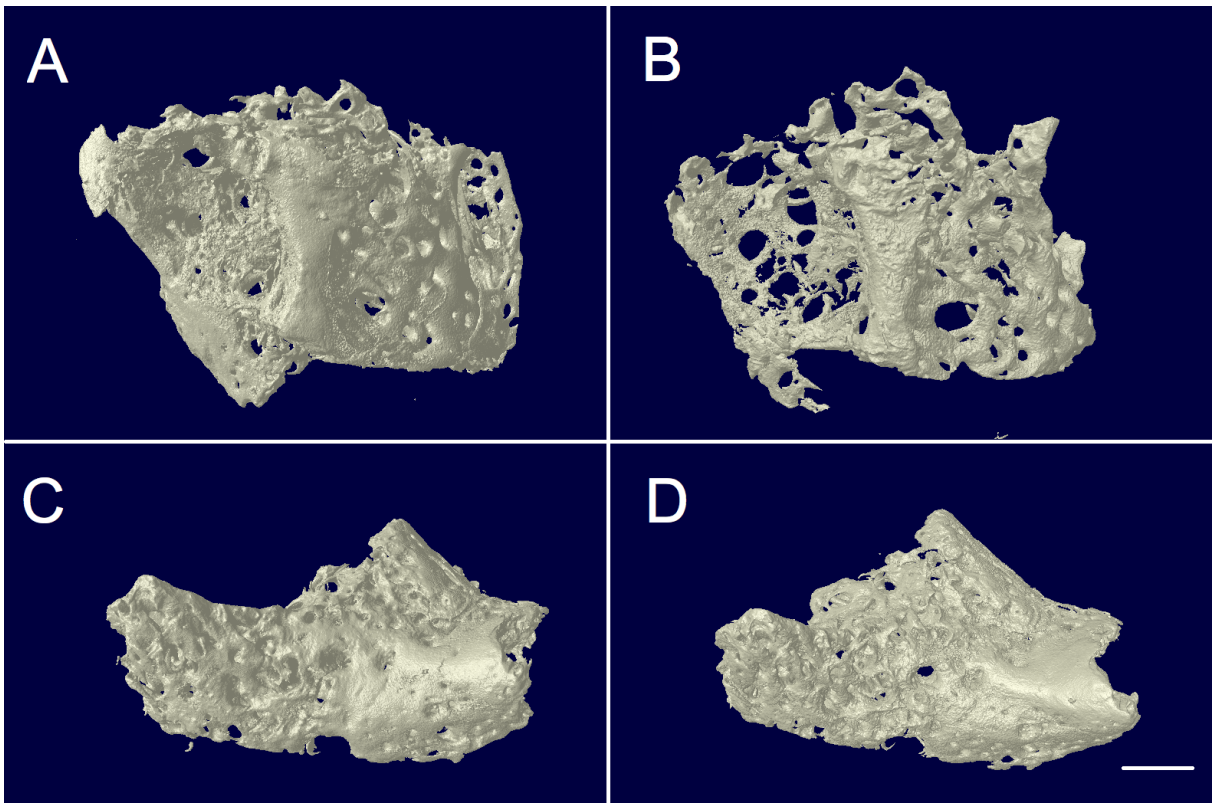

Figure 4-9: Three-dimensional surface-rendered models of the mineralised volumes of samples of heterotopic ossification (from patient 4). Before (A) and after (B) incubation in 0.1 M HMP at pH 7.4 for 7 days. Before (C) and after (D) incubation in diH_2O at pH 7.4 for 7 days. The sample incubated in HMP is clearly attenuated after incubation whereas the control sample shows little change. Scale bar = 1 mm.

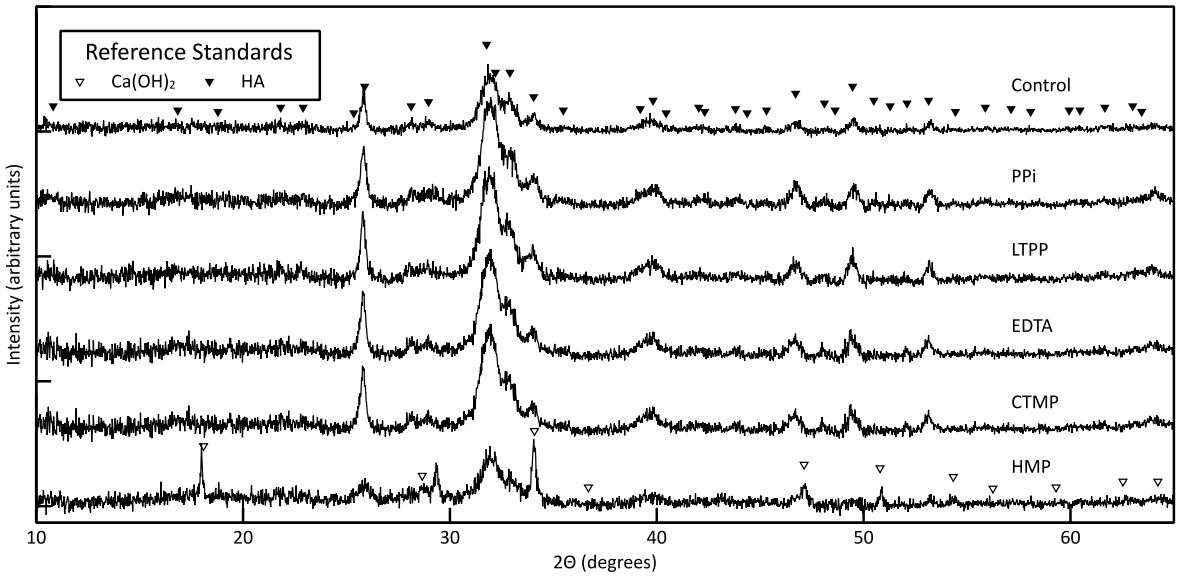

Figure 4-10: X-ray diffraction patterns of the products of HA synthesis. In the presence of hexametaphosphate, the peaks associated with HA are diminished or missing and an increased amount of unreacted calcium hydroxide ($Ca(OH)_2$) precursor is detected, suggesting inhibition of hydroxyapatite crystallisation. The other reagents had no measurable effect compared to control (no added polyphosphates). PPi = pyrophosphate, LTPP = linear tripolyphosphate, EDTA = ethylenediaminetetraacetic acid, CTMP = cyclic trimetaphosphate, HMP = hexametaphosphate.

previously reported elsewhere.[201,202,204] Given that HMP was able to reduce the reaction yield of HA precipitated in a super-saturated solution, it is possible that *in vivo*, it could inhibit the formation of HA in ectopic bone.[169]

4.4 Conclusions

This chapter has detailed the process by which a novel therapy for preventing and treating HO was discovered and developed. Literature review revealed that polyphosphates (hexametaphosphate in particular) had been used experimentally in humans in the 1960s and had shown interesting mineralisation controlling effects *in vitro*. This led to the hypothesis that a polyphosphate may be developed into a therapy by which trauma-induced HO may be inhibited or even dispersed. The results demonstrate that HMP can dissolve HA in inorganic and biological settings, that this effect is controllable through alteration in pH and through the action of ALP, that *ex vivo* human HO is attenuated by its action, and that HA formation can be inhibited in the presence of small concentrations of this simple polyphosphate. Existing clinical prophylaxis and current innovations in this field focus on the upstream biological pathways. However, chemical means of dissolving the final product, hydroxyapatite, could be an effective way of addressing this problem and the data presented here show this to be a possibility. If efficacy is proven in the condition of HO, this opens the possibility of broadening the application to other diseases of extra-skeletal mineral deposition.

5 HYDROGEL FORMULATION ENGINEERING

5.1 Introduction

5.1.1 Requirements of a Delivery Vehicle

The simplest way to deliver a dissolving or inhibiting therapy to the site of HO formation would be to inject an aqueous solution. However, this delivery method would provide little control over the anatomical site of action. This is undesirable because there is a risk that orthotopic bone could be damaged. To prevent this, a delivery vehicle would be required, which could deliver the therapeutic payload to the desired location and deliver a sustained dose. In general, drug delivery systems need to have certain basic properties (Table 5-1).[215] In addition to these general requirements of delivery vehicles, this project demanded additional specific requirements as described in Table 5-2.

In summary, a safe and injectable vehicle was required to carry HMP to the site of HO formation, release it at the correct location in an effective timescale, prevent it's spread to normal bone, and then degrade or disperse safely.

Table 5-1: Basic Properties of Drug Delivery Systems

Biocompatibility	Defined as being non-toxic, non-injurious, and non-immunogenic in a specific application[216]
Stability	Sufficient to allow a reasonable shelf life
Degradability	Ability to be metabolised and / or cleared from the body but still able to maintain its structure and function *in vivo* for an appropriate amount of time.
Cost Effectiveness	It should be reasonably cheap and available.

Table 5-2: Delivery vehicle properties specific to the application of dissolving and inhibiting HO

Injectability (shear-thinning rheological behaviour)	To allow minimally invasive delivery to the site of HO formation.
Compatibility with Polyphosphates	The delivery vehicle must not adversely interact with polyphosphates or require divalent cations in order to function (due to the potent chelating ability of some polyphosphates e.g. hexametaphosphate).
Appropriate Mechanical Properties:	In order to withstand the forces of the surrounding tissues *in vivo* that would act to disperse the delivery vehicle.
Appropriate Drug Release Properties	It would be desirable for the vehicle to be able to control the release of HMP in order to prolong the duration of action.

5.1.2 Hydrogels as Delivery Vehicles

Hydrogels are versatile, safe, and effective materials for a wide range of biomedical applications so they were chosen for the delivery of HMP in this project.[217,218] Hydrogels are hydrophilic polymeric or co-polymeric networks that can absorb thousands of times their own dry mass of water. This gives them a density very close to that of water and viscoelastic mechanical properties close to that of biological soft tissue.[219] These properties make them useful drug delivery agents. Hydrogels are incredibly versatile due the high degree to which their mechanical and chemical properties can be controlled. Manipulation of their mechanical properties allows them to be made into almost any shape or formulation including viscous liquids, microparticles, solid slabs, coatings, and films. Hydrogels have been used as contact lenses, pharmaceutical capsules, implant coatings, and dermal patches *inter alia*.[215]

Gelation in hydrogels occurs due to multiple different types of intermolecular bonding, which are responsible for the ultimate macromolecular structure and mechanical properties. Hydrogels are described as “physical” (or “reversible”) if the polymer network is bound by molecular entanglement, hydrophobic forces, ionic bonding, stereo-complexation, or hydrogen bonding. These bonds can be broken through alteration of the pH, heating, stress, or shear. This causes a return to a liquid state; hence the name “reversible”. One common subgroup of physical hydrogels are known as “ionotropic gels” and these require a multivalent ion of the opposite charge to the polyelectrolyte to form crosslinks; e.g. calcium-alginate. Gelation in these gels can be reversed through the application of an alternative ion that competes with the cross-linker for access to the binding sites.

Hydrogel bonding can also be “chemical” (or “permanent”) when the structure is dependent upon covalent bonds between polymer chains. Chemical bonding may occur directly between polymer chains through functionalisation with reactive groups or may require the addition of small-molecule reactive species.[220,221] Hydrogels formed through intermolecular covalent bonds tend to be more robust and stable over time due to resistance of the chains to diffusing away from one another. Some hydrogels exhibit both types of bonding, with the predominant type being dependant on the physical and chemical conditions.

Hydrogels may be synthetic or derived from natural sources. Natural hydrogels have the advantages of being more degradable, abundant, renewable, non-toxic, and cheaper than synthetic hydrogels.[222] Sources for natural hydrogel polymers include bacteria (gellan[223]), seaweed (alginate[224]), bovine or porcine collagen (gelatin[225]), and crustacean shells (chitosan[226]). Examples of synthetic and natural hydrogels are given in Table 5-3.

5.1.3 Degradability

Hydrogel degradability can occur through enzymatic digestion or hydrolysis. Cross-linked hydrogels may also dissolve when the polyvalent cations holding the network together are replaced by monovalent cations from body fluid.[227] In cases where hydrogel networks disperse in this way, the ultimate fate of the component parts will depend upon whether the host is able to excrete or further degrade them.

Table 5-3: Types of Hydrogel Polymers (modified from Hoffman 2012[215])

Naturally-Derived Hydrogel Polymers	
Anionic Polymers	hyaluronic acid, alginic acid (alginate), pectin, carrageenan, chondroitin sulphate, dextran sulphate, gellan
Amphipathic Polymers	collagen, gelatin, fibrin
Cationic Polymers	chitosan, poly-l-lysine
Neutral Polymers	dextran, agarose, pullulan
Synthetic Hydrogel Polymers	
Polyesters	PEG-PLA-PEG, PEG-PLGA-PEG, PEG-PCL-PEG, PLA-PEG-PLA, PHB
Other Synthetic Polymers	PEG-bis-(PLA-acrylate), PEG±CDs, PEG-g-P(AAm-co-Vamine), PAAm, P(NIPAAm-co-AAc)

Abbreviations: CD, cyclodextrin; PAAc, poly(acrylic acid); PAAm, polyacrylamide; PEG, poly(ethylene glycol); PCL, polycaprolactone; PHB, poly(hydroxy butyrate); PLA, poly(lactic acid); PLGA, poly(lactic-co-glycolic acid); PNIPAAm, poly(N-isopropyl acrylamide); PVamine, poly(vinyl amine).

5.1.4 Formulation Engineering Aims

The aims of the formulation engineering work were to formulate and characterise an injectable hydrogel delivery vehicle for HMP. The objectives required to achieve this aim were as follows: identification of suitable hydrogel polymers through literature review; determination of whether injectable hydrogels can be formed from these polymers with HMP included in their formulation; optimisation of the formulation and processing conditions to give the best product (as defined by homogeneity and injectability); characterisation of the mechanical properties and drug release behaviour of the product; determination of whether the product can be used to dissolve biological apatite (bone).

The work in this chapter was carried out in collaboration with Miss Emma Jones and Mr Tom Robinson, who were undertaking a final-year chemical engineering Masters project under the supervision of the author.

5.2 Methods

5.2.1 Hexametaphosphate Compatibility Screening

Synthetic hydrogels were excluded on the grounds of either cost, complexity of synthesis, or lack of local experience. The literature was then reviewed to provide a selection of naturally derived hydrogels that were then considered for further testing. Table 5-4 summarises the key features of these gels.

Gelatin was excluded because it required chemical cross-linking at body temperature (37^{o}C). Therefore, agarose, alginate, gellan, and pectin were chosen for further screening to establish their suitability as a delivery vehicle for HMP.

A screening experiment was conducted to observe the compatibility of the selected hydrogels with HMP. Divalent cations are commonly used to crosslink these gels but, as HMP has a potent capacity for chelating these ions, it was decided to observe the behaviour of these gels without adding crosslinking agent.

With the exception of pectin, gel concentration and method of synthesis was taken from local laboratory protocols. A concentration of HMP of 0.1 M was chosen as this corresponds to the value used in the HA-dissolving work above. The gels were synthesised as described in Table 5-5 and observed the next day after being left to cool overnight at room temperature (Table 5-6 and Figure 5-3).

Table 5-4: Summary of properties of naturally occurring hydrogels

	Advantages	Disadvantages	
Gelatin	Biocompatible, biodegradable, and non-immunogenic	Weak gelation above 35 °C, must be chemically cross-linked	[228,229]
Gellan	Biocompatible and biodegradable Gelation possible before or after injection	Relatively expensive Few studies investigating gellan for drug delivery	[230-232]
Agarose	Non-toxic, doesn't form damaging by-products, has high gel strength Has significant history of use in tissue engineering	Thermoresponsive – gels with decreasing temperature	[233]
Alginate	Relatively low cost, biocompatible, non-toxic, can be injected Compatible with HMP	Requires purification Partial oxidisation required to speed degradation Cross-linked by calcium (which is sequestered by HMP)	[224,234,235]
Pectin	Non-toxic (widely used in food) Tuneable cross-linking kinetics May be used with polyphosphates	Slow gelation kinetics	[236]
Chitosan	Used as a drug delivery system Non-toxic, biodegradable, sterilisable, easily chemically modified, low cost, and renewable	Poor mechanical properties. Hard to control pore size. May dissolve if physically cross-linked	[237,238]

Table 5-5: Summary of methods of synthesis of hydrogels used in screening experiments

Polymer	w/v	Experimental Method	Reference
Agarose (Fisher Scientific, Loughborough)	1%	Control: Add 0.5 g agarose to 50 ml DiH_2O Test: Add 0.5 g agarose to 50 ml 0.1 M HMP Heat and stir to 80 – 90 °C	Local Laboratory Protocol
Alginate "Alginic Acid, Sodium Salt" (Sigma-Aldrich)	2%	Control: Add 1.0 g alginate to 50 ml DiH_2O Test: Add 1.0 g alginate to 50 ml 0.1M HMP Heat and stir to ≤65 °C	Local Laboratory Protocol
High Acyl Gellan "Kelcogel HA" (CP Kelco, Atlanta, USA)	1%	Control: Add 0.5 g high acyl gellan to 50 ml DiH_2O Test: Ad 0.5 g high acyl gellan to 50 ml 0.1 M HMP Heat and stir (T ≤ 80 °C)	Local Laboratory Protocol
Low Acyl Gellan "Kelcogel LA" (CP Kelco)	1%	Control: Add 0.5 g low acyl gellan to 50 ml DiH_2O Test: Add 0.5 g low acyl gellan to 50 ml 0.1 M HMP Heat and stir (T ≤ 80 °C)	Local Laboratory Protocol
Pectin (Fisher Scientific)	2.4%	Control: Add 1.2 g pectin to 50 ml DiH_2O Test: Add 1.2 g pectin to 50 ml 0.1 M HMP Stir at room temperature	[236]

5.2.2 Varying HMP and Gel Concentration Under Temperature and pH Control

The next step was to test whether the gels would be stable at body temperature (37^{o}C) and at neutral pH (7.0). It has been demonstrated (above) that HMP is more effective at dissolving HA at lower pH levels so the delivery vehicle should be designed to optimise effectiveness. However, if the pH is too low, this may cause pain and inflammation at the site of injection. Thus a balance has to be struck between HA-dissolving potency and safety. A pH value of 7.0 was chosen as it is the lowest pH that is likely to be found in muscle under physiological conditions and therefore represents this optimal balance.[239] Another aim of this stage in testing was to examine the effect of altering the concentrations of HMP and the polymers to see whether there is an upper limit to the amount of HMP that can be loaded into these gels before gelation is compromised. A higher HMP concentration would mean that less volume would needed to be injected to deliver the same molar quantity. Reducing the injected volume is desirable because large volume injections can cause pain and discomfort.

HMP was dissolved in 20 ml aliquots of diH_2O to make concentrations of 0.5, 1.0, or 1.5 M. These were heated to 60 ^{o}C and stirred. High acyl gellan was added to each of these aliquots and allowed to dissolve to give final concentrations of 0.25, 0.50, 0.75, 1.00, or 1.25% w/v. All samples were pH adjusted to 7.0 (+/- 0.1) using 1 M NaOH or HCl. The samples were then left to set for 12 hours at room temperature (20 ^{o}C) before being placed into a 37 ^{o}C incubator for another 12 hours. Gels were observed after this time.

Preliminary testing demonstrated that agarose had a tendency to form inhomogeneous gels if the simple method appropriate for gellan was used. Empirical testing demonstrated that, to produce a homogenous gel in the presence of HMP, the following general method was required. Two 10 ml of aliquots of diH_2O were heated and agitated and made up with twice the desired final concentration of HMP and agarose. These two solutions were then combined in a single vessel under continuous heating and agitation to produce a 20 ml solution with the required final concentrations of agarose (0.5, 1.0, 1.5, 2.0, or 2.5% w/v) and HMP (0.05, 1.0, or 1.5 M). As with the gellan samples, these were then pH adjusted, allowed to set for 12 hours under ambient conditions, and then placed into an incubator at 37 ^{o}C for a further 12 hours before being observed.

5.2.3 Injectability

For the delivery vehicle and HMP to be able to act upon the HO within a patient, it would need to be injected into the site of developing ectopic mineralisation. It would not be suitable to administer the drug systemically (e.g. intravenously) as it might be toxic or damage orthotopic bone. As such, it was desirable to test the injectability of the HMP-loaded gels. This was performed using a combination of needle and syringe sizes that would be typical for this kind of application (as judged by the author, who is a clinician with extensive experience of performing injections into soft tissue). The aim was to attempt to inject the optimised combinations of polymer and HMP and observe the outcome qualitatively. This would provide data on how the materials behaved under the high-shear environment of a syringe and needle and how it felt in the hand of the end user.

Agarose (2.5%) and high acyl gellan (1.25%) gels containing 0.1 M HMP were synthesised as described above, except that they were aspirated into 5ml syringes (BD Discardit II syringe (Becton Dickinson)) while still hot (>60 ^{o}C). These were left to cool under ambient conditions (20^{o}C) overnight. A 19 G (inside diameter 0.686 mm, length 38.1 mm) needle (Terumo, NJ, USA) was attached to each syringe and the contents expelled by compressing the plunger manually. There were triplicate repeats of each experimental condition.

5.2.4 Rheology

In order to provide more quantitative information on the handling properties of the HMP-loaded gels, oscillatory rheological testing was performed. This allows a formal description of the viscoelastic properties of the systems under test. The reason for this is that this application requires the loaded delivery vehicle to be liquid enough to be injectable but then return to a more solid-like state once in situ so that it releases its payload in the desired location. In rheological terms, the material needs to be shear-thinning. This means that it is viscous (able to flow) under high shear conditions but then demonstrate predominantly elastic (solid-like) behaviour in a low shear conditions. Oscillatory rotational rheometry is able to measure the storage modulus (G') and the loss modulus (G") of a soft solid material and use the ratio of these terms to establish the viscoelastic behaviour under different shear conditions.

Before formal rheometry of a material can be undertaken, the linear viscoelastic range (LVR) must be determined. This is the range of strain values over which the internal structure of a material remains intact and determines the range of strain values that can be used to derive the viscoelastic parameters G' and G".

Rheometry was performed on an AR-G2 rheometer (TA Instruments) with a 40 mm, 2° cone and a flat base plate. All experiments were carried out at 37 °C. Parameters were taken from the protocol by Zuidema *et al.*[240]

5 ml of each loaded gel (2.5% agarose or 1.25% high acyl gellan containing 0.1 M HMP) was injected through a 19G needle onto the plate of a rheometer and the normal force was allowed to decay to zero. Strain sweeps were performed at 1 Hz over a strain range of 0.0001 - 0.28, with 3 s conditioning and 3 s sampling duration per strain setting. This was performed in triplicate for each gel. The results (Figure 5-1) demonstrate an upper limit to the LVR of 0.01 strain. 0.005 was chosen as the fixed strain value during the frequency sweep experiments.

Frequency sweeps were performed, in triplicate, using a gap of 1000 μm, zero normal force, 0.005 strain, a range of 1 – 100Hz, 3 s conditioning time, and 3 second sampling per frequency.

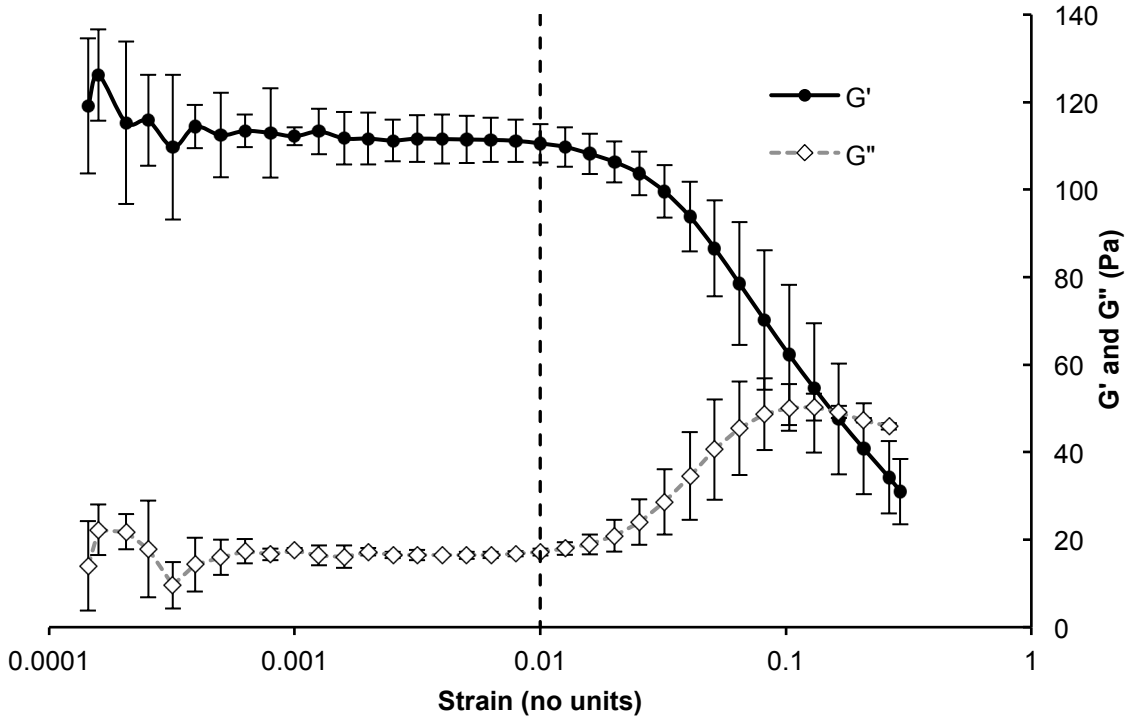

Figure 5-1: Strain sweep for post-injection 1.25% high acyl gellan containing 0.1 M HMP. Above a strain of 0.01 (vertical dashed line), G' and G" deviate significantly from their stable values. Therefore, the upper limit of the linear viscoelastic range of strain is 0.01. Error bars are +/- SD.

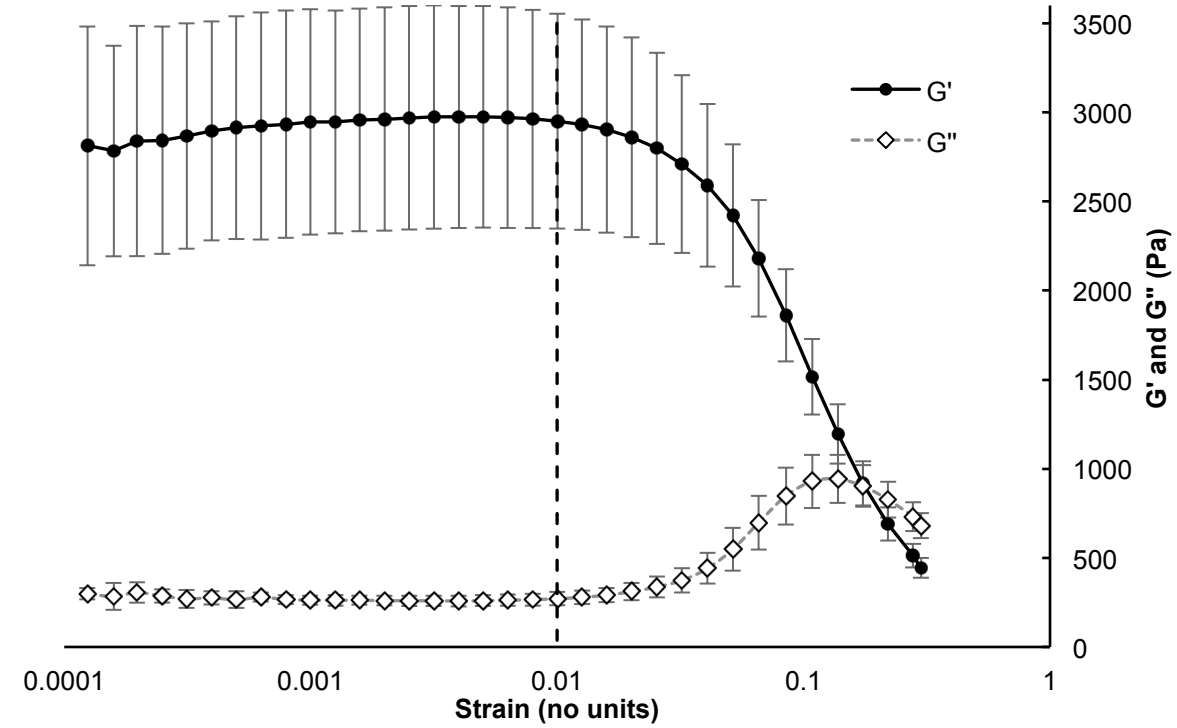

Figure 5-2: Strain sweep for post-injection 2.5% agarose containing 0.1 M HMP. Above a strain of 0.01 (vertical dashed line), G' and G" deviate significantly from their stable values. Therefore, the upper limit of the linear viscoelastic range of strain is 0.01. Error bars are +/- SD

5.2.5 Release Assay

One of the key properties of a delivery vehicle is its ability regulate the release of the active ingredient over time. This allows intermittent administration of the loaded carrier rather than continuous infusion. As such, it was desirable to determine the HMP-release characteristics of these gels. The most significant challenge to performing a release study on vehicles containing HMP is that there is no assay specific for HMP concentration. There is, however, a simple colourimetric assay for orthophosphate concentration. As such, it was decided that the HMP concentration would be determined through hydrolysis of the HMP into orthophosphate followed by assay of orthophosphate. The experimental method was based on the dialysis method described by D'Souza.[241] Briefly, "parcels" of dialysis tubing were loaded with gels and placed in a volume of isotonic phosphate-free buffer at 37^{o}C. The dialysis tubing pore size prevented the gels from dispersing in the buffer but allowed free movement of water and HMP. Aliquots of buffer were taken at intervals, the HMP content hydrolysed to orthophosphate, and the orthophosphate concentration measured using the colourimetric assay. In this manner, HMP release over time could be estimated.

Dialysis tubing (Medicell International) with a permeability range of 12-14 kDa was formed into parcels and filled with 1.5 ml of 1.25% high acyl gellan or 2.5% agarose with and without HMP loading. These were suspended in a vessel containing 50 ml of tris-buffered saline (TBS) and the temperature was controlled at 37^{o}C. The TBS had been prepared by adding 6.05 g of TRIZMA® base (Sigma-Aldrich) and 8.76 g of sodium chloride to 800 ml deionised water. The

pH was adjusted to 7.6 and deionised water was added to give a final volume of 1 litre with a pH of 7.4 and osmolality of 0.2998 Osm/kg. 200 μl aliquots of the TBS media were sampled at timepoints 15, 30, 45, 60, 90, 120, 180, 240, 300, 1440, and 2880 minutes. The vessels were agitated intermittently to ensure adequate mixing and to avoid sampling error. Each experimental condition was carried out in triplicate.

The 200 μl samples were each diluted in 4 ml deionised water. 500 μl aliquots of these diluted solutions were then hydrolysed by addition of 200 μl of 4 M HCl and incubated at 37^{o}C for 72 hours. This HMP hydrolysis method is modified from McGaughey *et al.*[204] After this period, 1 μl of each hydrolysed sample was added to 199 μl of deionised water in the wells of a 96-well plate. 30 μl of a colourimetric phosphate assay dye (Sigma-Aldrich) was added to each well, and the plates were incubated in the dark at room temperature for 30mins. They were subsequently read on a GloMax® Microplate Multimode Reader (Promega) at 650 nm.

5.2.6 Biological Apatite-Dissolving Ability of HMP Loaded Gels

As a final check to ensure that the gel vehicles did not prevent the HA-dissolving effect of the HMP payload, they were tested on samples of rat trabecular bone.

Four tibiae were harvested, post mortem, from adult male Lister rats. The proximal trabecular volume of each tibia was dissected out intact using hand instruments. The samples' mineralised volumes were quantified using microCT before and after incubation in HMP-loaded (0.1 M) and control (no payload) gels (1.25% high acyl gellan and 2.5% agarose). MicroCT scanning was performed using a Bruker SkyScan 1172. Reconstruction was performed using NRecon version 1.6.10.2

(Bruker) and the mineralised volumes determined using CTAn version 1.15.4.0 (Bruker). Scanning, reconstruction, and analytical processing parameters were identical for the pre and post-incubation steps.

5.3 Results

5.3.1 Hexametaphosphate Compatibility Screening

Table 5-6: Observations on compatibility testing of hydrogels with HMP

	Control		With HMP	
	Gelation	**Observations**	**Gelation**	**Observations**
Agarose	Yes	Set gel Cloudy white – translucent	Yes	Less stiff than the control gel Cloudy white – opaque
Alginate	No	Liquid Pale brown - transparent	No	Liquid Very pale brown - transparent
Gellan – high acyl	Yes	Set gel White – opaque	Yes	Set gel - less stiff than control sample White – opaque
Gellan – low acyl	No	Fluid gel Colourless	Yes	Set gel White – opaque Brittle
Pectin	No	Liquid Formed two separate layers: Opaque cream-coloured lower layer. White, foam like upper layer.	No	Liquid Formed two separate layers: Opaque cream-coloured lower layer. White, foam like upper layer.

Agarose | Alginate | High acyl Gellan | Low Acyl Gellan | Pectin

Figure 5-3: Initial results of hydrogel synthesis in the presence of 0.1 M HMP

5.3.2 Varying HMP and Gel Concentration Under Temperature and pH Control

Table 5-7: Summary of results of high acyl gellan and HMP combined in various concentrations at pH 7.0 after 12 hours at 37°C

[HMP] (M)		High Acyl Gellan Concentration (% w/v)				
		0.25	**0.50**	**0.75**	**1.00**	**1.25**
0.05	Gel at 37 °C?	No	No	No	Yes	Yes
	Notes	White translucent viscous liquid	White translucent viscous liquid	White opaque more viscous liquid	White, opaque homogeneous deformable gel.	White opaque homogeneous gel. Self-supporting.
	Trend	Increasing gel stiffness and opacity →				
0.10	Gel at 37 °C?	No	No	Partial	Yes	Yes
	Notes	White translucent viscous liquid	White opaque, more viscous liquid	White opaque partially gelled liquid	White, opaque homogeneous deformable gel. Low stiffness.	White opaque homogeneous gel. Self-supporting. Deformable.
	Trend	Increasing gel stiffness and opacity →				
0.15	Gel at 37 °C?	No	No	No	No	No
	Notes	White translucent heterogeneous low-viscosity fluid	White opaque heterogeneous low-viscosity fluid.	White opaque heterogeneous low-viscosity fluid.	White, opaque, heterogeneous low-viscosity fluid.	White, opaque, heterogeneous low-viscosity fluid.
	Trend	Increasing heterogeneity and opacity →				

Table 5-8: Summary of results of agarose and HMP combined in various concentrations at pH 7.0 after 12 hours at 37°C

[HMP] (M)		Agarose Concentration (% w/v)				
		0.5	**1.0**	**1.5**	**2.0**	**2.5**
0.05	Gel at 37 °C?	Yes	Yes	Yes	Yes	Yes
	Notes	Translucent homogeneous gel	Translucent homogeneous gel	Translucent homogeneous gel	White opaque homogeneous gel	White opaque homogenous gel
	Trend	Increasing gel stiffness and homogeneity →				
0.10	Gel at 37 °C?	Yes	Yes	Yes	Yes	Yes
	Notes	Translucent homogeneous gel	Translucent homogeneous gel	White opaque homogeneous gel	White opaque homogeneous gel	White opaque homogeneous gel
	Trend	Increasing gel stiffness and homogeneity →				
0.15	Gel at 37 °C?	No	No	No	No	No
	Notes	Translucent viscous fluid	White opaque viscous fluid	White opaque viscous fluid	White opaque viscous fluid	White opaque viscous fluid
	Trend	Increasing gel stiffness and homogeneity →				

5.3.3 Injectability

Mild filter pressing occurred with the agarose gels, but all of the contents could be expelled and there was no blockage of the needles. The contents of the syringes were “chopped” as they were injected, forming multiple small pieces. Post-injection, these formed a mass of chopped gel that would, for example, adhere to an upturned surface. The post-injection agarose gels exhibited moderate syneresis.

Gellan was easier to inject than agarose. There was no filter pressing. The gel did not chop as it was injected but extruded smoothly and then coalesced into a single mass that appeared no different to pre-injection gel. The injected gel was also able to adhere to an upturned surface.

5.3.4 Rheology

Frequency sweep results for post-injection 1.25% high acyl gellan and 2.5% agarose loaded with 0.1 M HMP are shown in Figure 5-4 and Figure 5-5. Under low and intermediate shear rates, G' is dominant. At very high shear rates (approaching 500 radians/s) the trend changes with G' starting to diminish and G" to increase. In the case of high acyl gellan, the G" and G' cross. With agarose, they values do not cross but the trend is that they are converging. As with the strain sweeps, the absolute values of G' and G" for agarose are approximately 20 times greater than those for gellan.

5.3.5 Release Assay

Release assay results are shown in Figures 5-6 and Figure 5-7.

5.3.6 Biological Apatite-Dissolving Ability of HMP Loaded Gels

3-Dimensional reconstructions of the mineralised volumes of the samples pre- and post-incubation are shown in Figure 5-8. Mineralised volumes are given in Table 5-9.

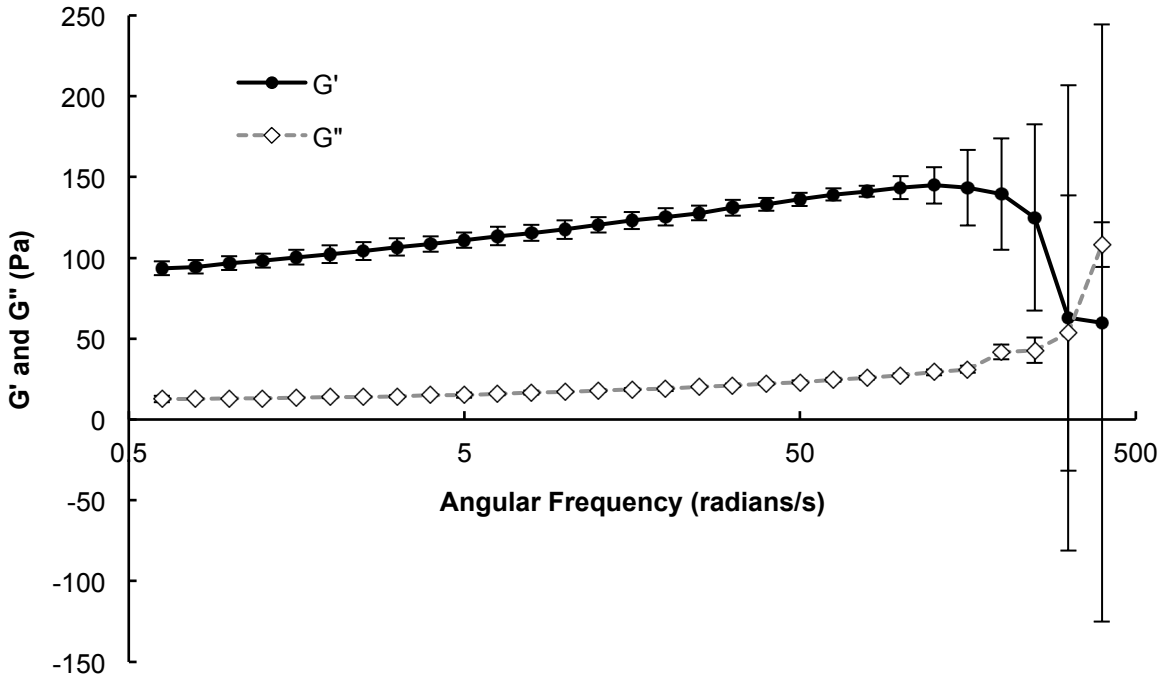

Figure 5-4: Frequency sweep for post-injection 1.25% high acyl gellan containing 0.1 M HMP. G' (storage modulus) predominates until high angular frequency indicating that an elastic, rather than viscous physical character is dominant except under high shear conditions. Error bars are +/- SD.

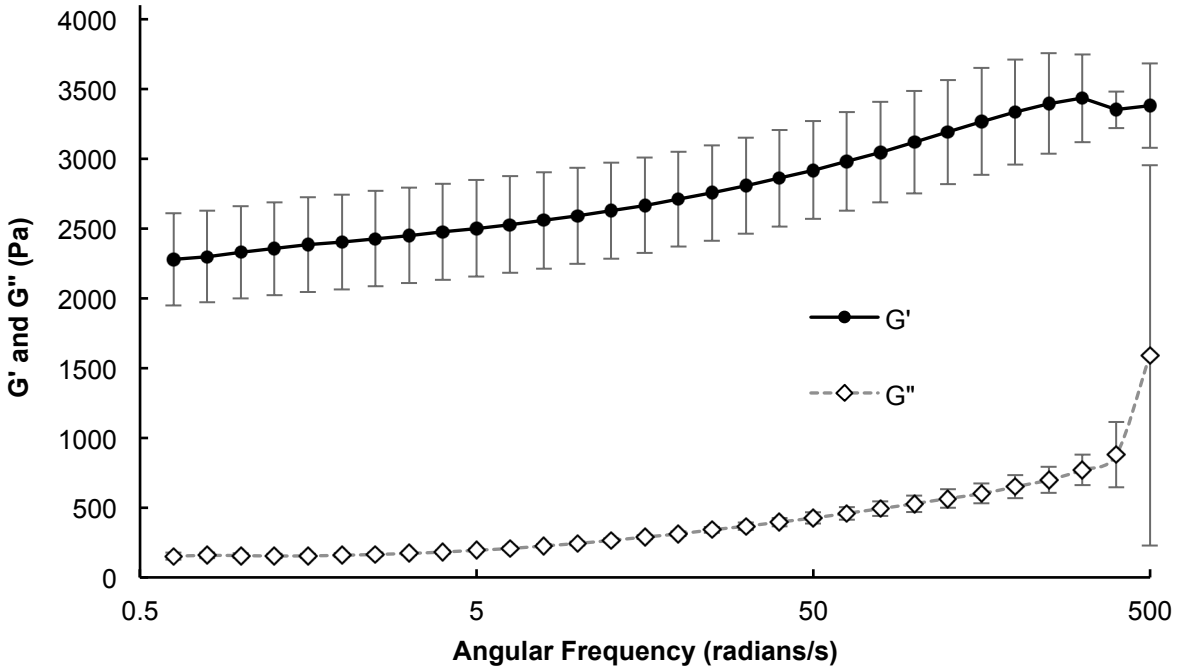

Figure 5-5: Frequency sweep for post-injection 2.5% agarose containing 0.1 M HMP. G' (storage modulus) predominates indicating that an elastic, rather than viscous physical character is dominant except under high shear conditions. Error bars are +/- SD.

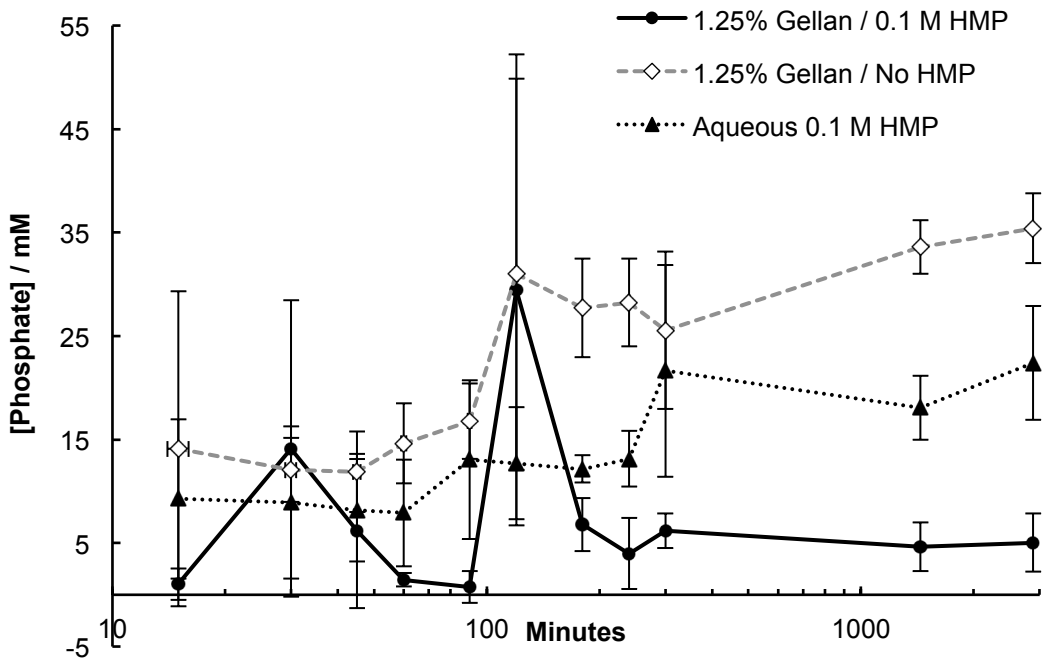

Figure 5-6: Phosphate release as a surrogate indicator of HMP release from 1.25 % high acyl gellan control containing no HMP (grey dashed line), aqueous solution of 0.1 M HMP (black dotted line), and 1.25% high acyl gellan loaded with 0.1 M HMP (black solid line). Error bars = SD.

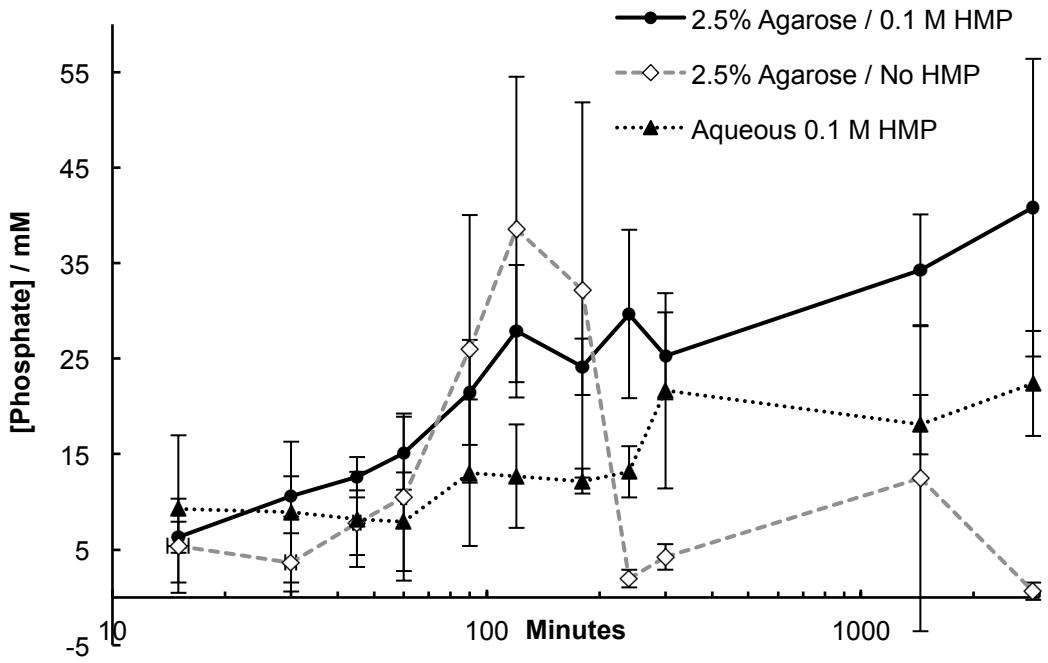

Figure 5-7: Phosphate release as a surrogate indicator of HMP release from 2.5 % agarose control containing no HMP (grey dashed line), aqueous solution of 0.1 M HMP (black dotted line), and 2.5% agarose loaded with 0.1 M HMP (black solid line). Error bars = SD.

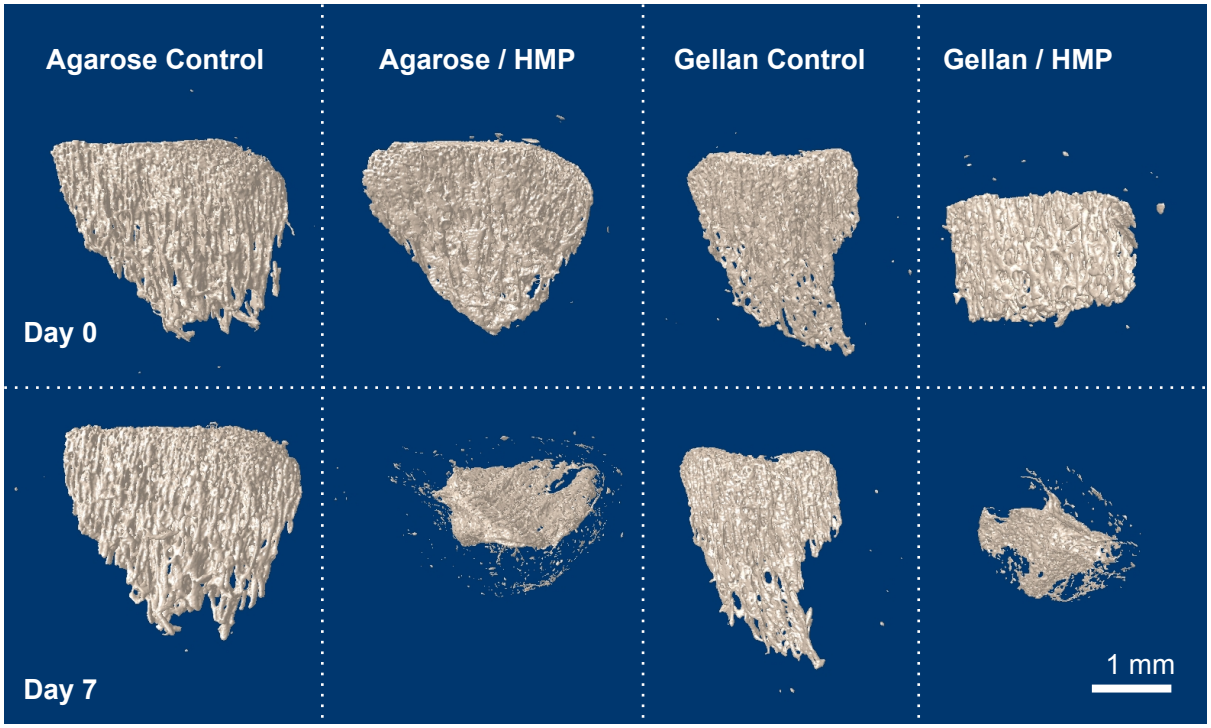

Figure 5-8: 3-Dimensional reconstructions of microCT scans of trabecular rat bone samples. It is clear that the samples incubated in gels containing HMP were highly attenuated compared to controls. Agarose control = 2.5 % agarose, no HMP. Agarose / HMP = 2.5% agarose containing 0.1 M HMP. Gellan control = 1.25% high acyl gellan, no HMP. Gellan / HMP = 1.25% high acyl gellan containing 0.1M HMP.

Table 5-9: Mineralised volumes of samples of rat tibia before and after incubation in gels. Agarose control = 2.5 % agarose, no HMP. Agarose / HMP = 2.5% agarose containing 0.1 M HMP. Gellan control = 1.25% high acyl gellan, no HMP. Gellan / HMP = 1.25% high acyl gellan containing 0.1M HMP.

	Agarose Control	Agarose / HMP	Gellan Control	Gellan / HMP
Day 0	2.85	4.37	2.04	1.79
Day 7	3.17	2.25	1.89	0.47
% Change	+11.1	-48.6	-7.35	-73.7

5.4 Discussion

5.4.1 Hexametaphosphate Compatibility Screening

The purpose of this screening experiment was to assess whether or not commonly used natural hydrogels could be synthesised in the presence of 0.1 M HMP and the absence of crosslinking agents. Pectin and alginate could not form gels under the experimental conditions outlined above. Agarose and gellan (both high and low acyl) formed gels in the presence of HMP. Interestingly, low acyl gellan (1% w/v) did not form a gel in isolation but did so in the presence of HMP. Thus HMP acted as a crosslinking agent. This is surprising because the literature reports that divalent cations are required to crosslink low acyl gellan and it is unclear how HMP, an intensely anionic molecule that actively chelates divalent cations, can act as a crosslinker. Low acyl gellan (1% w/v) was rejected because it formed a brittle gel in the presence of HMP meaning that it would not be suitable for injection. Thus, having rejected the other candidates, agarose and high acyl gellan were selected for further testing as they were able to form set, but non-brittle, gels containing 0.1 M HMP in the absence of divalent cationic crosslinking agents.

The key limitations of this experiment were that each gel was tested at only a single concentration, HMP concentration was also fixed at a single value, and the pH was not controlled. These limitations were a consequence of keeping this step as simple as possible. Despite the simplicity of this screening step, it was successful in providing sufficient justification to reject all but two of the gels, which was important because time and resources did not allow for more detailed investigation of a greater number of candidate vehicles.

5.4.2 Varying HMP and Gel Concentration Under Temperature and pH Control

Both high acyl gellan and agarose demonstrated similar behaviour with respect to increasing polymer and HMP concentration. Neither were able to form gels in the presence of the highest HMP concentration (0.15 M). Both formed stiffer and more opaque gels at higher polymer concentrations but this is not surprising. A higher polymer concentration would provide more opportunities for crosslinks and thus a stiffer gel. What is encouraging about these data is that both polymers can form gels in the presence of 0.1 M HMP at 37^{o}C at pH 7.0 and this means that these materials could be stable *in vivo* when loaded with HMP. 0.1M HMP has been shown to be a sufficiently high concentration to dissolve solid sintered pellets of HA so it is likely to be sufficient to dissolve unsintered biological apatite.

Of the gellan samples, a combination of 0.1 M HMP and 1.25% high acyl gellan was the most suitable to take forward for injectability testing. This is because it demonstrated qualitatively optimised mechanical properties with a high HMP concentration. The optimal agarose combination was 0.1 M HMP and 2.5% agarose. This not only represented an optimised combination of HMP concentration and qualitative mechanical properties but also demonstrated the best homogeneity of the agarose samples, as determined by macroscopic observation. See Figure 5-3 for an example of an homogeneous agarose gel. Homogeneity is important, as it is desirable that any one unit of volume of the vehicle should carry the same dose of active ingredient as another.

5.4.3 Injectability

Both agarose (2.5%) and high acyl gellan (1.25%) gels containing 0.1 M HMP could be injected through a 19G needle. High acyl gellan performed better than agarose as it was easier to inject and the post-injection material had remarkable self-healing properties. Despite being a firm deformable gel, it was able to be injected and then return to a single cohesive mass with the same appearance. Whether the chopping phenomenon demonstrated by agarose is clinically significant is not clear from this experiment. However, the filter pressing and “weeping” of the injected gel could lead to burst release of the HMP, which is in the aqueous phase.

As this experiment was subjective, it was decided that external validation of the findings would add rigor. As such, a surgeon (not the author) was recruited to repeat the injections and give their observations. They were blind to the contents of the syringes but understood the potential application of this system for the treatment and prevention of HO. The surgeon provided comments that support the above observations in that they preferred the handling properties of gellan/HMP and was concerned about the chopping and syneresis demonstrated by the agarose/HMP.

5.4.4 Rheology

The frequency sweeps provide information on the behaviour of the materials under different shear-rates, which correspond to different mechanical environments in use. Both gels demonstrated a dominantly elastic, rather than viscous, property over almost the entire frequency range. The values of G’ and G” for high acyl gellan are approximately 20 times lower at each shear rate than the values for agarose. This means that its stiffness is much lower than agarose, which matches the qualitative

findings above. The conclusion from the relationship between G' and G" for both gels is that they will not demonstrate viscous flow except under a high shear load. This is ideal as this was one of the desired properties of a delivery vehicle for this application.

These rheology data do have significant limitations however. First, the agarose samples demonstrated some syneresis upon being compressed by the cone and plate geometry of the rheometer. This would cause the gel to have a higher polymer-to-water ratio and may go some way to explain why the values for G' and G" were so much higher than for high acyl gellan. The second limitation of this technique is slip. The moist surface of the gels may provide a fluid layer between the main bulk and the cone or plate of the rheometer. As such, the rotational oscillations of the cone will not be fully transferred to the gel. As the rheometer calculates the results based on an assumption of perfect transfer of shear from the cone to the material under test, this may lead to erroneous results. However, it is important to note that the aim of this experiment was not to provide a perfect characterisation of the rheological properties of the gels; it was to establish whether the gels displayed broadly viscous or elastic behaviour under a range of shear conditions. To that end, these experiments have been successful.

5.4.5 Release Assay

It is challenging to draw conclusions from the release assay data for a number of reasons. First, there appears to be a significant experimental artefact affecting all results between 100 – 240 minutes. Results during this period are elevated and then return to lower values. Whilst this may be due to the release and then reabsorption of

free phosphate for this time period, it is more probable that it is an artefact due to the sampling process or the colourimetric phosphate assay. Second, some of the results are nonsensical. For example, Figure 5-6 shows that at the 1440 and 2880 minute timepoints, free phosphate in the no-HMP group was higher than in either the aqueous HMP or gellan HMP groups. Confidence in these data is, therefore, low. It is suspected that the noisiness of these data and the likely experimental artefacts are due to the following factors. First, the number of individual physical operations required to make each measurement from start to finish is exceptionally high. Accumulations of errors at each stage can reinforce or counteract each other unpredictably. This probably accounts for the high variability in the values and error bars. Second, unhydrolysed HMP was found to interfere with the phosphate assay (unpublished data). No method was used to confirm the completeness of hydrolysis of HMP so it is possible that some remained intact and interfered with the assay. Third, while the use of laboratory glassware was limited to essential items only (with disposable plastic ware being used in its place as far as possible), it was not possible to eliminate its use completely. It is recognised that glassware may have residual phosphate residue on its surface due to routine washing. No steps were taken to remove this residue and there is a risk that this may have interfered with the result.

In conclusion, the release study experiment has not provided data of sufficient reliability to draw any meaningful conclusions. However, reporting this finding here is of value because it suggests that the methods described here are flawed and that an alternative method should be sought by those who seek to measure HMP release from hydrogels in future studies.

5.4.6 Biological Apatite-Dissolving Ability of HMP Loaded Gels

The dissolution of samples of trabecular rat tibiae using HMP-loaded gels was a simple test of effectiveness. With n = 1 for each experimental condition, the intention was not to characterise the effect fully, but simply to check that the gels don't abolish the HA-dissolving ability of HMP. Given the dramatic reduction in mineralised volume of the samples exposed to HMP-loaded gels after 7 days, the conclusion is that the gels do not abolish this ability. Control gels, without HMP loading, were included to gain an indication of the effect of incubating the samples in a gel in the absence of HMP. The small measured change in mineralised volume (+/- ~10%) is probably within the bounds of experimental error for this method and probably does not indicate a real effect. Multiple repetitions of each experimental condition would be required to investigate this effect further but this was of secondary importance to the main aim of this experiment, which was satisfied with a single sample per condition.

5.5 Discussion

Hydrogels seem ideal candidates for delivery of HMP into the soft tissues to prevent and treat HO. They meet many of the required criteria for drug delivery in general and this application in particular (Table 5-1 and Table 5-2). However, attempting to synthesise these gels in the presence of HMP revealed significant problems with compatibility. One of the key problems was that many of the gels require crosslinking with divalent cations such as calcium. HMP chelates calcium with very high affinity, which means that its presence prevents gelation in crosslink-dependent gels. Interestingly, HMP appeared to act as a crosslinking agent itself for both high and low acyl gellan. The mechanism for this observation is unclear as, under these

conditions, HMP is highly negatively charged whereas the usual crosslinkers are positively charged.

Agarose and high acyl gellan were identified, through screening steps, to be compatible with HMP at a range of concentrations. Further steps identified optimal gel concentrations and these combinations of gel / HMP were taken forward for mechanical testing including injectability and rheology. Subsequently, an attempt was made to quantify the HMP-release characteristics of the gels but this did not generate meaningful results. Finally, it was shown that high acyl gellan and agarose loaded with HMP were able to dissolve the mineralised portion of samples of rat bone. This test was a surrogate for using these loaded gels on human HO, as these samples were too precious.

The results of this formulation engineering work show that 1.25% gellan is preferable to 2.5% agarose. This is because agarose required a subjectively large amount of force to inject and demonstrated significant filter pressing and syneresis. Also, some of the agarose / HMP preparations demonstrated a tendency to separate into two phases over time (although this was not studied in detail).

In terms of further work, sterilisation is one of the critical steps that will need to be studied and optimised if these gels are to be translated into clinical practice. Another important consideration for a delivery vehicle that has not been addressed with this research is degradation. There is a notable lack of studies that provide information on the breakdown and ultimate fate of hydrogels. As such, translation of a hydrogel

delivery vehicle into the clinic would require detailed analysis of how the vehicle is degraded and how the components are excreted from the body.

5.6 Conclusions

It is possible to formulate injectable hydrogels containing HMP. Gellan and agarose are promising candidates for further development in future but significant issues remain unresolved. These include a greater understanding of the mechanism of degradation of the vehicle, means of sterilisation, and optimisation of an assay for HMP activity that would allow release characteristics to be measured.

Finally, it is important to note that this work was performed concurrently with the *in vivo* testing described in detail in the next chapter. The results of this formulation engineering work were, therefore, not available at the start of the animal model work.

6 ANIMAL MODEL OF HETEROTOPIC OSSIFICATION

6.1 Animal Models of HO

While mathematical modelling of HO is currently in development, animal modelling remains the mainstay of research in this area.[242] A variety of different models have been developed that vary by their fidelity, reliability, welfare severity, logistical burden, and relevance to different forms of HO. Each model type is suited for a particular purpose or type of research and choosing an appropriate model requires an understanding of the advantages and disadvantages of each.

6.1.1 Types of Model

6.1.1.1 Injury

Trauma models are considered to be the most representative of acquired heterotopic ossification as they can reproduce the condition without the need for genetic modification or administration of osteogenic agents. An early and well-known study by Michelsson *et al.*[243] used repeated cycles of manipulation followed by immobilisation of rabbit knee joints as the traumatic stimulus. This method reliably produced ectopic ossification but it is difficult to see how this relates to acute trauma and the welfare considerations are significant. Also, whether or not the ectopic bone is excessive fracture callus or true heterotopic bone is unclear, a fact the authors concede in a follow-up paper.[244]

In order to develop a more clinically relevant model, Schneider *et al.*[245] performed hip surgery on rabbits with and without additional muscle injury to study the prophylactic effects of radiotherapy on HO. One criticism of the Schneider method is that bone

reaming debris was left *in situ* whereas in hip surgery in humans, care is taken to wash any debris away. The concern is that these reamings may seed the local soft tissue with bone-forming cells and that this may be the cause of the observed ectopic bone formation. This is theoretically possible in traumatic or post-operative HO, where injuries to bone could lead to this seeding. However, the consensus (see Chapter 1) is that most types of HO, including traumatic and post-operative, form through recruitment or induction of bone forming cells rather than direct seeding of tissues.

6.1.1.2 Implantation / Injection

In these models, a foreign material or structure is implanted into an animal in an ectopic site to induce bone formation. This foreign material most often consists of bone morphogenic protein (BMP) infiltrated into some form of scaffold.[54,246] There are many variations of this model including implantation of inert microporous calcium phosphate particles,[247] osteogenic cells,[248] or BMP-encoding genetic material.[249] Criticism of the implantation models includes the artificially high local levels of BMP, which brings into question the validity of the system. Further, local trauma caused by the implantation of the materials could induce HO at the site anyway, or even stimulate an inflammatory response, which is known to promote HO formation.

6.1.1.3 Genetic

Genetic models rely on creating animals with modified BMP production or signalling. A key example is the mutation in the ACVR1 gene that codes for a BMP receptor, leading to constitutive activation and a fibrodysplasia ossificans phenotype.[250] Other examples of genetic mutations being used to attempt to induce ectopic bone

formation include BMP inhibitor knockouts,[251] BMP overexpression,[252] and BMP downstream signalling modification.[253] Genetic modification of animal models has been described as having little relevance to human acquired heterotopic ossification.[254] Even when the intention is to study genetic forms of HO, only one of the genetic models phenotypically resembles the human version of the disease even remotely.[252]

6.1.1.4 Blast

A trauma model with clear clinical relevance is the application of blast injury to rats. The first published example of this came from Tannous *et al.*[90] who used explosive charges to induce hind or forelimb amputations in Sprague-Dawley rats. The main criticisms of this method are that the blast injury caused a high mortality rate amongst the animals, and reliability in generating HO was low. A refined version of this model was developed by Polfer *et al.*[255] whereby the blast was delivered by a pneumatic shock tube rather than explosive. This study showed that while blast exposure alone is not enough to produce HO, it potentiates the disease in the context of superadded muscle injury and surgical amputation. This model was particularly well designed in that it allowed the relative contribution of blast and amputation to be elucidated.

6.1.1.5 Achilles Tenotomy

The Achilles tenotomy model has grown in favour as a means of generating HO due to its simplicity, reliability, and the fact that no genetic manipulation or exogenous osteogenic factors are required. The development of ectopic bone formation at the site of Achilles tenotomy was first described in rats by Buck in 1953 in a study on tendon healing.[256] It was subsequently shown to occur in mice also, and the model's

reputation for reliability was advanced by McClure in 1983, who showed that 100% of the mouse models in a study had developed HO after 10 weeks.[257] Interestingly, this study was investigating the effect of bisphosphonates on HO and concluded that they had no effect. Also, the study noted that after 5 weeks, only 60% of the models had developed HO. More recently, Lin *et al.* used the Achilles tenotomy in rats to show that it develops via an endochondral ossification mechanism.[258] This study demonstrated the same temporal progression of HO as McClure, with 60% of the models having radiographic evidence of HO at 5 weeks and 100% at 10 weeks. Thus it has been demonstrated in several studies over several decades that this model behaves reliably.

In terms of simplicity, this model compares favourably with many other models. The only intervention required is the tenotomy operation itself, which takes only a few minutes and requires only basic surgical and anaesthetic equipment that is found in most animal research laboratories. This is in stark contrast to the blast models, for example, which require large amounts of highly specialised equipment, engineering support, and attract a significant health and safety burden.

Finally, from an animal welfare point of view, the Achilles tenotomy model is also favourable when compared to other techniques. The papers mentioned above describe the animal models as tolerating the tenotomy well, with no discernable impact on function after recovery from the operation. Again, this is in contrast to some of the other methods such as the Michelsson manipulation model.[243]

Interestingly, it has been shown that the addition of a burn injury increases the speed and magnitude of HO development in the murine model.[47,81] This is interesting in that it shows that inflammation can potentiate HO. However, it was felt by the author that the addition of burn would cause excessive animal welfare issues and was unnecessary for the requirements of this project given the reliability of the tenotomy-only method.

It is clear from published studies that the Achilles tenotomy model is the simplest, most reliable, and best tolerated method of generating ectopic bone formation. Whether or not it produces HO through the same biological and biochemical networks as human post-traumatic HO is irrelevant to this study. This is because, as discussed in previous chapters, the novel therapeutic approach that underpins this work is the direct dissolution and inhibition of formation of HA. Thus, in order to test the efficacy of such a treatment, it is irrelevant what pathways were involved in creating the ectopic bone. What is important is that the model is reliable, so that if no HO is detected, it must be due to an effective treatment rather than an ineffective model.

6.2 Aims

These animal experiments were performed with two main aims. The first aim was to set up the Achilles tenotomy HO model in our institution in order to have a reliable means of producing HO *in vivo.* The second aim was to use this model to prove the concept that HMP can be used to inhibit the formation of HO *in vivo.* Secondary aims included: quantitative evaluation of the effect of HMP on orthotopic bone, basic

evaluation of toxicity of HMP when injected parenterally, and evaluation of the suitability of alginate as a delivery vehicle *in vivo.*

6.3 Methods

6.3.1 Animal Licencing and Regulation

In order to gain authorisation to perform the required animal experiments for this project, the author applied for and obtained a personal and project licence as laid out in the Animals (Scientific Procedures) Act 1986. Note that the project licence is held by Dr Zubair Ahmed. Briefly, the personal licence allows the holder to perform specified procedures on specified species. The project licence defines the experimental protocols that can be undertaken on the specific species. Formal University Ethical Committee approval was sought and gained, as was Home Office approval. The University of Birmingham biomedical services unit (BMSU) already has an establishment licence to allow animal experimentation to be carried out. The design and conduct of all experiments were undertaken with full regard for the principles codified by the National Centre for the Replacement, Refinement, and Reduction of Animals in Research (NC3Rs). All animal work was conducted within the BMSU in accordance within the terms of the granted licences, ethical approvals, and the law.

6.3.2 Achilles Tendon Model Development

At the time of performing these experiments, no animal model of HO was being undertaken in the UK so the author set up the model *de novo* using information from the literature.[48,81,258] In total, nine adult male Sprague-Dawley rats (Charles River UK, Ltd., Margate, UK) were used to establish the model. The aim was to determine the

reliability of the model and quantify the baseline burden of HO after Achilles tenotomy at various timepoints. This would allow comparison with subsequent batches of animals that would receive either control or active injections of the novel HO-dispersing agent.

This model development stage was performed as three sequential batches of three rats. The rationale was that, if the tenotomy or subsequent HO were found to be excessively distressing, only a small number of animals would be affected and modifications to the protocols could be made for future experiments. All animals underwent unilateral right-sided Achilles tenotomy (see below). The first batch of three animals were killed 5 weeks after the procedure. The second and third batches were killed at 10 weeks after the procedure.

Right-sided unilateral Achilles tenotomy was performed on all animals as follows. Preoperatively, the rats were weighed and received 0.2 ml of buprenorphine subcutaneously. Induction and maintenance of general anaesthesia was achieved through inhaled isoflurane. The animals were placed prone on a warmed operating table and hair was removed from the dorsum of the right hind limbs using electric clippers. After confirmation of adequate depth of anaesthesia and application of sterile drapes, a 5 mm longitudinal midline incision was made over the distal Achilles tendon using surgical scissors. Blunt dissection was performed to deliver the Achilles tendon into the wound. This was cut transversely using a scalpel blade. After confirmation that the tendon had been completely sectioned, the wound was closed with two interrupted sutures of 4-0 undyed vicryl rapide (dissolvable co-polymer containing 90% glycolide / 10% L-lactide, Ethicon, New Jersey, USA). To prevent

wound dehiscence, surgical wound adhesive was used to augment the wound closure (see Figure 6-1 for operative photographs).

Post-operatively, the animals were housed individually for 24 hours and allowed access to food, water, and oral opioid analgesia as required. After this time, the animals were group-housed in batches of three with *ad libitum* access to food, water, and environmental enrichment. No animals were given any form of non-steroidal anti-inflammatory medication at any stage throughout the study.

At the appropriate time-point (5 weeks or 10 weeks after tenotomy), the animals were killed using the approved schedule-one method of inhaled rising CO_2 concentration. The right and left hind limbs were harvested through sharp dissection and disarticulation at the femoro-acetabular joint (hip). Subsequently, the hind limbs were disarticulated at the tibio-femoral joint (knee). Care was taken to preserve the soft tissue distal to the tibio-femoral joint.

Harvested limbs were placed into 60 ml sample pots and stored at -80 ^{o}C until needed for microCT analysis. Limbs were fully defrosted and allowed to equilibrate to room temperature before scanning.

All limbs were scanned using a Bruker Skyscan 1172 microCT scanner (Bruker, Coventry, United Kingdom). The scan settings used were as follows: near camera

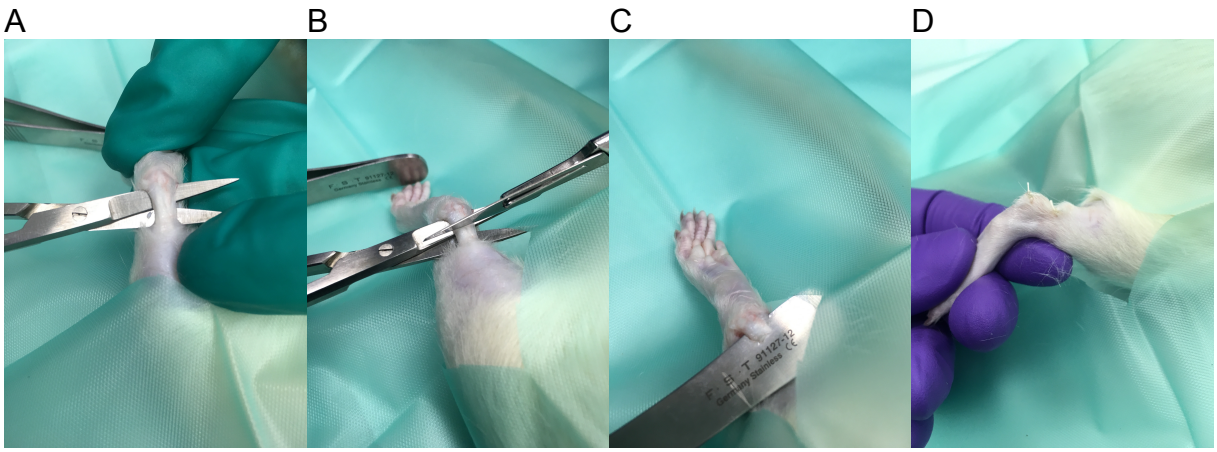

Figure 6-1: Photographs of unilateral Achilles tenotomy operation. A: blunt dissection underneath the Achilles tendon. B: Sharp sectioning of the tendon using a scalpel. C: Confirmation that the tendon has been completely divided. D: Two sutures to close the surgical wound.

position, tube voltage 75 kV, tube current 100 μA, 180° rotation, rotation step 0.6°, 2 frame averaging, exposure time 400 ms, pixel size 21.5 μm, camera size 1000 x 666 pixels. Each sample scan was double width and lasted for approximately 90 minutes. Scans were reconstructed using NRecon (software version 1.6.10.2, Bruker microCT) with the following settings: beam hardening correction 50, smoothing 3, ring artefact reduction 4. Reconstructed datasets were processed (adaptive thresholding followed by despeckling) and analysed using the 3D object tool in CTan (version 1.15.4.0, Bruker microCT). All scanning and reconstruction parameters were kept constant across all samples except for the movement artefact compensation, which was manually adjusted to optimise the data for each sample.

Scan datasets were processed to remove normal bone and scanning artefacts in order to quantify the volume of extra-skeletal mineralised tissue (HO) in the limbs. Reconstructed datasets were processed and analysed using the CTan software (version 1.15.4.0, Bruker microCT). First, a volume of interest was hand-drawn

around the HO leaving a margin of normal soft tissue. Subsequently, the processing steps and parameters were as follows: adaptive thresholding (median-C) in 3D space using round kernel radius 3 pixels (70 < threshold < 255), 2D white despeckle < 9 pixels, 3D white despeckle < 300 voxels, 3D analysis.

6.3.3 Testing Hexametaphosphate *in vivo*

As discussed in the concluding remarks of the last chapter, the formulation engineering work was performed concurrently with these animal experiments. Ideally, the formulation work would have been concluded before the animal experiments were started but limitation of time and resources precluded these circumstances. Decisions had to be made about the nature of the carrier vehicle, dose of HMP, and frequency of injections based on what limited objective information was available and certain obvious limitations. The first limitation was that the project licence stipulated a maximum frequency of injection of once per week. Given the length of time that the animal models would be run for, a pragmatic decision was made to perform the injections once every two weeks. Second, there is a limit to the volume that an adult male Sprague-Dawley rat can tolerate having injected into its hind limb. Experimentation on cadaveric models suggested that approximately 400 μl could be injected into the site of the Achilles tenotomy before feeling any significant resistance. Therefore, in order to introduce a significant margin for error, the volume of injection was limited to 200 μl. As the volume and frequency of administration were limited, it was decided to use an HMP concentration of 0.2 M rather than the 0.1 M that had been used for the majority of the *in vitro* work. This was to increase the chance of the animal model showing a positive result, which would reduce the total

number of animals required in the course of proving this concept. Finally, 1% uncrosslinked alginate was chosen as the delivery vehicle because, out of the choice of hydrogels, alginate has the most substantial evidence of use *in vivo*.[224,259,260] 1% uncrosslinked alginate is a viscous liquid rather than a gel. This was a deliberate choice as it represented a compromise between being viscous enough to limit its spread away from the target area while still being able to pass through a 0.2 μm filter for sterilisation. This is in contrast to the agarose and high-acyl gellan vehicles developed in Chapter 5, which could not be passed through such a filter. Sterilisation of these gels remains an unresolved issue.

In total, 12 adult male Sprague-Dawley rats were used for this stage. The experimental protocol was performed on two sequential batches of six animals. In each batch, three of the animals were in the control arm of the protocol and three were in the active treatment arm of the protocol. The experiment was performed in batches so that, should there be adverse effects due to the injections, the number of animals affected at any one time would be limited. Unilateral right-sided Achilles tenotomy was performed on all animals as described above. After 24 hours in individual recovery cages, the animals were housed in two cages with three animals per cage. The online randomisation tool random.org was used to determine which cages would receive the control (200 μl of 1% alginate) or treatment (200 μl of 1% alginate / 0.2 M HMP). Subcutaneous injections were administered at 2, 4, 6, and 8 weeks post Achilles tenotomy. All animals were killed at 10 weeks post tenotomy. Harvesting of hind limbs, MicroCT scanning, and data processing were carried out as described above.

Injections were manufactured no more than 24 hours before each round of administration to avoid any potential problems with shelf stability or bacterial contamination. Disposable sterile tissue culture plastic, autoclave-sterilised glassware, and a cell culture laminar flow hood were used to provide aseptic conditions in which to prepare the control and therapeutic injections. For the control injections of carrier vehicle, 25 ml of sterile water for injections (Gibco Life Technologies, Paisley, UK) was agitated and heated to 60^{o}C then 0.25 g alginate (alginic acid sodium salt from brown algae, Sigma-Aldrich, Darmstadt, Germany) was added and allowed to dissolve fully to produce a 1% alginate solution. The pH of this solution was adjusted to 7.1 < pH < 7.4 using 2 M NaOH solution that had been passed through a 0.2 μm filter (Minisart, Sartorius Stedim Biotech, Göttingen, Germany). This pH-adjusted uncrosslinked 1% alginate was then passed through a 0.2 μm filter and 0.2 ml aliquots were loaded into 1 ml syringes. For the active injections, 1% uncrosslinked alginate was made as above. 3.06 g of SHMP (Sigma-Aldrich) was then dissolved in this solution during heating and agitation. This was pH adjusted, passed through a 0.2 μm filter, and loaded into 1 ml syringes in the same manner as the control solution. All syringes were stored at 4^{o}C in a laboratory refrigerator until 1 hour before use.

Injections were administered at 2, 4, 6, and 8 weeks after Achilles tenotomy. All animals were given 0.2 ml buprenorphine subcutaneously 30 minutes before administration of the experimental preparations. The author gave the injections to all animals and was blind as to whether the animal was from the control group or the

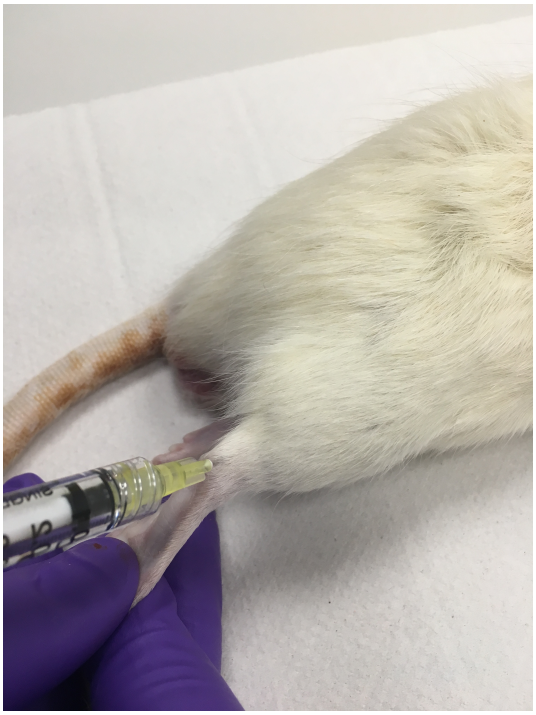

Figure 6-2: Injections of control or HMP-loaded gel into the site of HO formation.

therapeutic group. The author was also blind as to whether the syringes contained the blank carrier vehicle (200 μl of 1% alginate) or the active therapeutic load (200 μl of 1% alginate / 0.2 M HMP). The injections were administered via 30-gauge needles (HSW Fine-Ject, Sigma-Aldrich) into the right hind limbs at the site of the Achilles tenotomy (Figure 6-2).

6.3.4 Bone and Tissue Mineral Density of Orthotopic Bone

Bone mineral density (BMD) of trabecular bone and tissue mineral density (TMD) of cortical bone adjacent to the site of injections were quantified in order to determine

whether the injections had any effect on orthotopic bone. The reconstructed microCT datasets that had been collected to quantify the HO volume were reused for this purpose but the post-reconstruction processing differed. For BMD, the vertical limits of the volume of interest was defined as being from 30 to 130 slices (641 to 3418 μm) above the distal tibial physeal scar and the horizontal limits were hand-drawn at intervals with interpolation to select only trabecular bone. For TMD, the vertical limits were defined as being from 130 to 230 slices (3418 to 4914 μm) above the distal tibial physeal scar and the horizontal limits were hand-drawn at intervals with interpolation to select only cortical bone. These vertical limits were derived by examining the datasets and determining the distribution of cortical and cancellous bone in the distal tibiae of the experimental models. Figure 6-3 summarises these volumes of interest schematically.

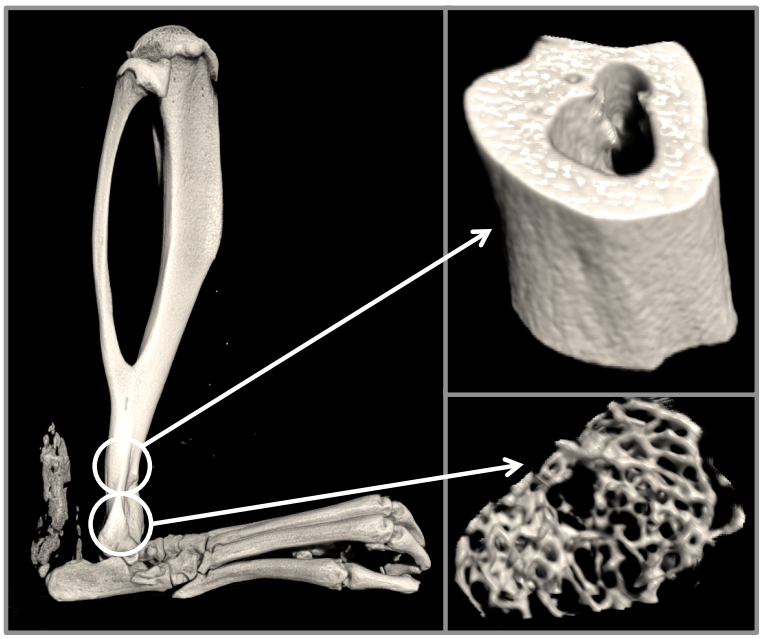

Figure 6-3: Schematic representation of volumes of interest for bone mineral density (bottom right) and tissue mineral density (top right) quantification.

6.3.5 Statistical Analysis

All statistical analysis was performed using R (version 3.2.4).[261] Normalised HO volume, TMD, and BMD of the control and active groups were compared using a Welch t-test.

6.4 Results

6.4.1 Achilles Tenotomy Model Development

One animal developed a minor subcutaneous haematoma. This did not lead to wound dehiscence and did not become infected. It is likely that this haematoma was the result of imperfect haemostasis at the time of surgery. Subsequent to this complication, meticulous operative haemostasis was achieved in all animals using swabs, cotton buds, and pressure. This haematoma resolved spontaneously over 2 weeks. There were no other adverse events during the model development phase.

All animals were able to bear weight on the operated limbs within 24 hours of operation. Weight gain, social interaction, and behaviour were normal for the duration of the post-operative period. There were no observable negative consequences due to the tenotomy or subsequent development of HO.

No heterotopic ossification was detected in the contralateral (non operative) limbs of any of the rats (reconstructions not shown).

Table 6-1: Model development results. Weight and microCT measurement of volume of HO for each animal model. Absolute and normalised figures are given.

Animal ID	Weight At Death (g)	Elapsed Time After Achilles Tenotomy	Volume Of HO (mm^3)	HO volume normalised to bodyweight (mm^3 / g)
1.1.1	Not Recorded	5 Weeks	0.0	N/A
1.1.2	Not Recorded	5 Weeks	2.41	N/A
1.1.3	Not Recorded	5 Weeks	0.20	N/A
Mean (SD)	**-**	**-**	***0.87 (1.34)***	**-**
1.1.4	566	10 Weeks	13.3	0.024
1.1.5	485	10 Weeks	8.62	0.018
1.1.6	545	10 Weeks	14.6	0.027
1.2.4	474	10 Weeks	13.9	0.029
1.2.5	494	10 Weeks	22.2	0.045
1.2.6	494	10 Weeks	14.4	0.029
Mean (SD)	***510 (36.9)***	**-**	***14.5 (4.37)***	***0.029 (0.009)***

Figure 6-4: 3-D microCT reconstructions of the mineralised tissue (HO and bone) in the right hind limb of rats that have undergone Achilles tenotomy. Scale bar = 5 mm.

6.4.2 Testing Hexametaphosphate *in vivo*

Achilles tenotomy surgery was performed without any adverse events (zero incidence of haematoma, wound breakdown, and wound infection). During the second round of injections, one animal developed a haematoma at the site of the injection. This was possibly due to the tip of the needle causing damage to a vein or artery in the track of the injection. This had resolved spontaneously by the time of the next injection 2 weeks later. Animals injected with the blank carrier gel control were reluctant to bear weight on the injected limb for up to one hour post injection. Animals injected with the active therapeutic agent were observed to be in more discomfort than the control animals and were unwilling to bear weight for 2 – 4 hours post-injection. After this time the animals were observed to behave normally. At no point did the discomfort of the animals exceed the terms of the animal licence.

One of the animals in the second batch of the therapeutic group died as a result of the injection at week 6 after Achilles tenotomy. Death occurred within five seconds of administration of the injection of 1% alginate / 0.2 M HMP. After review of the case with the named veterinary surgeon, it was concluded that death had occurred due to inadvertent intravascular injection of the contents of the syringe with embolisation of the contents and immediate cardiorespiratory compromise and death. As a result of this event, the injection technique was modified to include aspiration before injection to check whether the tip of the needle was inside a blood vessel. Flashback of blood into the syringe would indicate this situation and the injection aborted and reattempted. No cases of flashback were observed in any subsequent injections.

The absolute and body weight-normalised volumes of HO in each animal model are shown in Table 6-2. 3-D reconstructions of the hind limbs with HO and close up views of the HO volumes are shown in Figure 6-7 and Figure 6-8.

Table 6-2: Testing hexametaphosphate *in vivo* results. Weight and microCT measurement of volume of HO for each animal model. Absolute and normalised figures are given. Tissue mineral density (TMD) and bone mineral density (BMD) values are included.

Animal ID Code	Weight At Death (g)	Group / Batch	Volume Of HO (mm^3)	HO volume normalised to bodyweight (mm^3 / kg)	TMD (g/cm^3)	BMD (g/cm^3)
2.1.1	555	Control / **1**	26.9	48.5	0.35	1.18
2.1.2	478	Control / **1**	25.0	52.4	0.29	1.18
2.1.3	436	Control / **1**	21.1	48.5	0.31	1.19
2.2.4	569	Control / **2**	21.2	37.3	0.33	1.17
2.2.5	495	Control / **2**	7.50	15.2	0.35	1.13
2.2.6	569	Control / **2**	17.6	30.9	0.28	1.13
Mean (SD)	***517 (56)***	**-**	***19.9 (6.90)***	***38.8 (14.1)***	***0.32 (0.031)***	***1.16 (0.027)***
2.1.7	505	HMP / **1**	15.2	30.0	0.39	1.23
2.1.8	514	HMP / **1**	16.7	32.5	0.29	1.23
2.1.9	476	HMP / **1**	14.6	30.7	0.30	1.20
2.2.1	**Died**	HMP / **2**	N/A	N/A	N/A	N/A
2.2.2	536	HMP / **2**	15.3	28.6	0.29	1.15
2.2.3	491	HMP / **2**	15.7	32.0	0.16	1.08
Mean (SD)	***498 (20)***	**-**	***15.5 (0.77)***	***30.7 (1.54)***	***0.29 (0.081)***	***1.17 (0.058)***

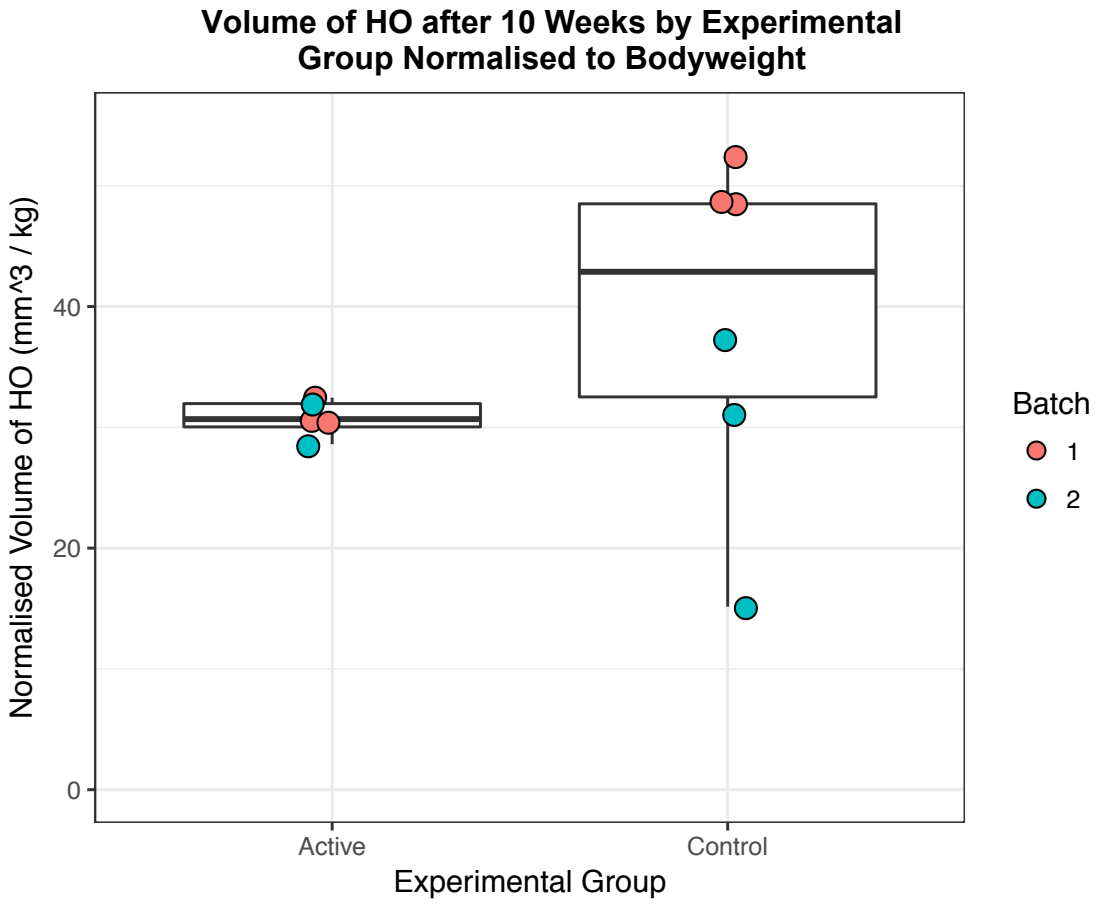

Figure 6-5: Combined dot-plot and box-and-whisker plot for volume of HO in the right hind limb of rats that have undergone right sided Achilles tenotomy and subsequent fortnightly injections of 200 μl of either control (1% alginate) or active (1% alginate / 0.2 M HMP) into the site of formation of HO. n = 5 in the active group. n = 6 in the control group. All available data are shown. Box plot bounds = interquartile range. Box plot horizontal line = median. Whiskers = range. Welch t-test p = 0.22

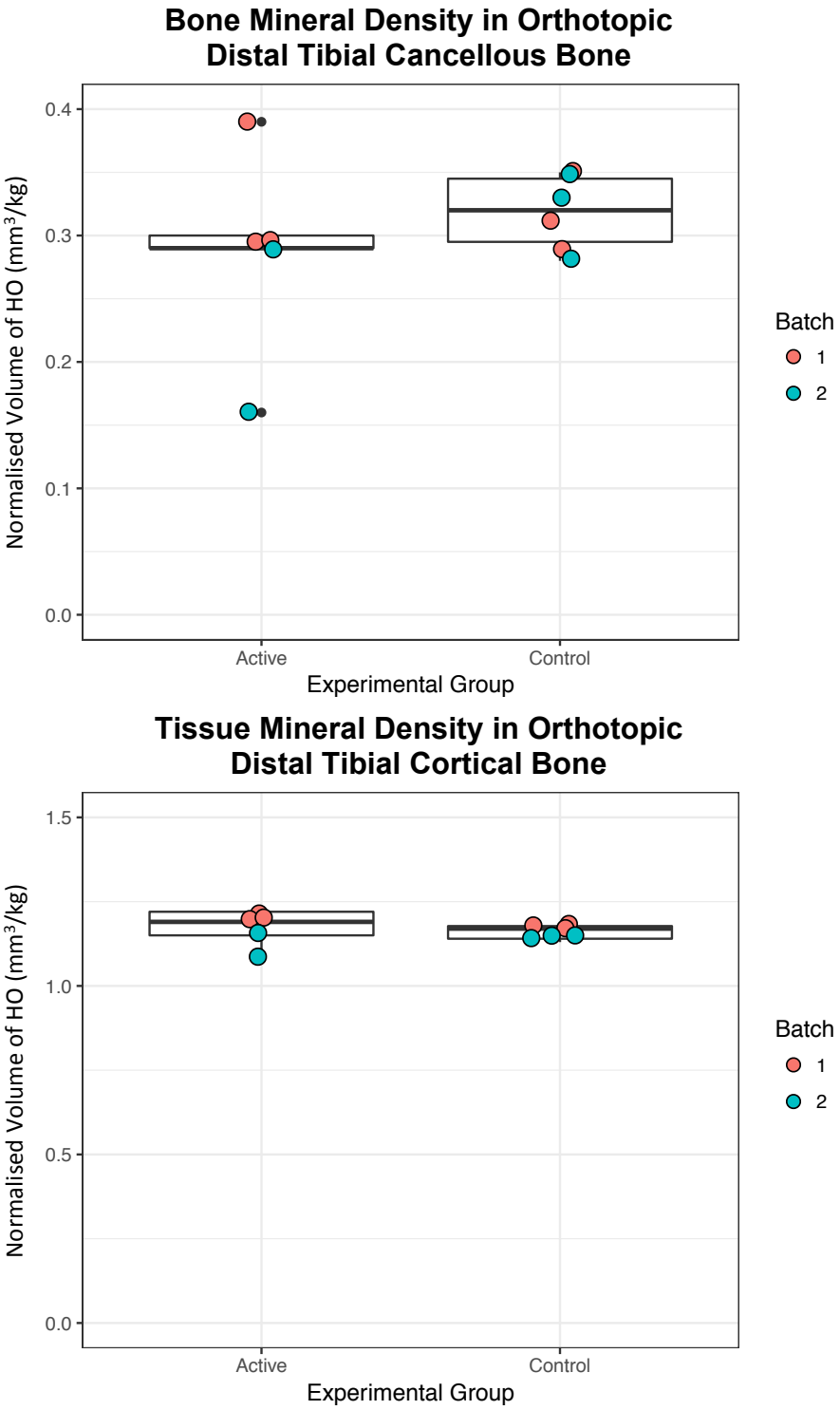

Figure 6-6: Combined dot-plot and box-and-whisker plot for tissue mineral density (TMD) and bone mineral density (BMD) in the right hind limb of rats that have undergone right sided Achilles tenotomy and subsequent fortnightly injections of 200 μl of either control (1% alginate) or active (1% alginate / 0.2 M HMP) into the site of formation of HO. n = 5 in the active group. n = 6 in the control group. All available data are shown. Box plot bounds = interquartile range. Box plot horizontal line = median. Whiskers = range. Black dots = outliers >1.5 interquartile range.

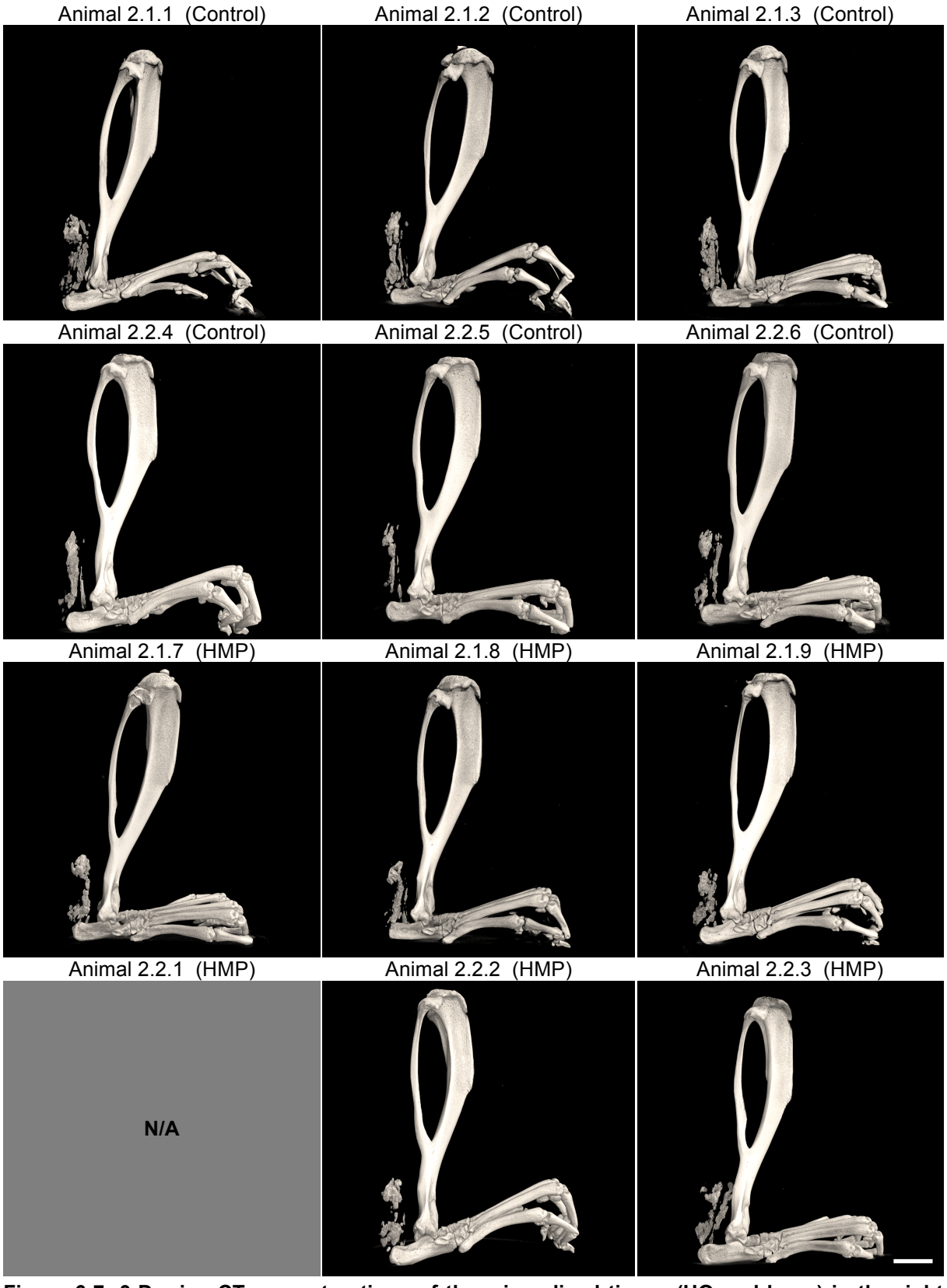

Figure 6-7: 3-D microCT reconstructions of the mineralised tissue (HO and bone) in the right hind limb of rats that have undergone Achilles tenotomy and subsequent fortnightly injections of 200 μl of either control (1% alginate) or active (1% alginate / 0.2 M HMP) into the site of formation of HO. Scale bar = 5 mm.

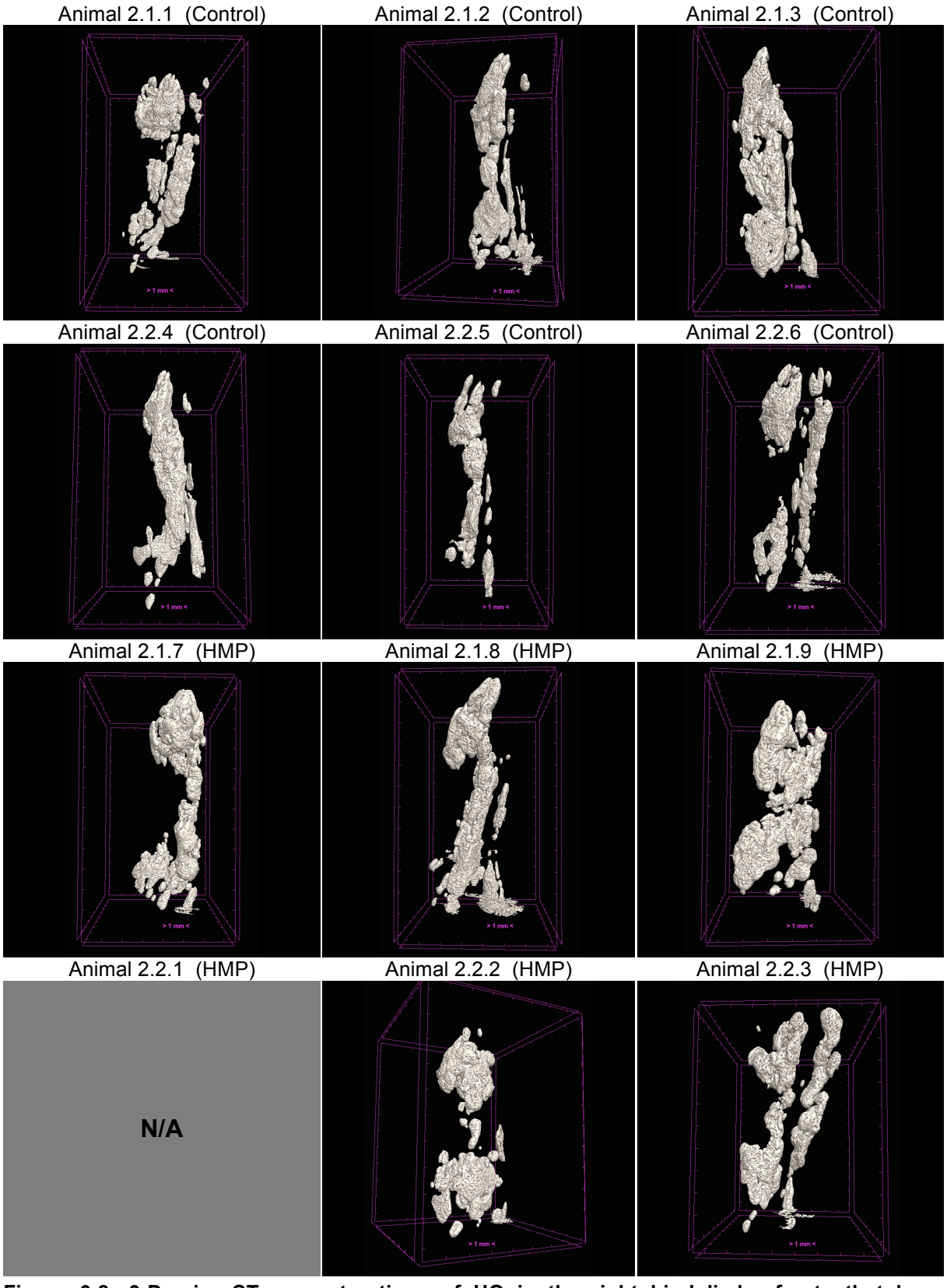

Figure 6-8: 3-D microCT reconstructions of HO in the right hind limb of rats that have undergone Achilles tenotomy and subsequent fortnightly injections 200 μl of either control (1% alginate) or active (1% alginate / 0.2 M HMP) into the site of formation of HO. Ticks on bounding cuboids = 1 mm.

6.5 Discussion

6.5.1 Achilles Tenotomy Model Development

The conclusion from these data is that unilateral Achilles tenotomy followed by 10 weeks of maturation in the adult rat is a simple and highly reliable model of HO. The reason that only three animals were taken to the 5-week time point is that the likelihood of developing HO at this point was shown to be low (only 2 out of three animals had any HO and the amount that did form was variable and small). This was to be expected from the published literature[81] but still provided valuable confirmation that the model was behaving as expected and that our results are therefore generalizable and comparable to previous work. No further useful information could be gained by increasing the number of animals killed at this time point.

HO in the right limbs of these models formed at the site of division of the Achilles tendon. This is interesting because there is very little muscle at this anatomical site. The HO in this model is therefore likely to have formed in the connective and scar tissue that would result from the Achilles tenotomy. Unfortunately, it was not possible to perform histology on these models to establish the exact tissue in which the HO formed. However, the purpose of this model is not to study the mechanism of HO formation but is to provide a simple and reliable platform on which to test the efficacy of a novel HO therapy. Having established that the model is reliable, this aim has been satisfied.

6.5.2 Testing Hexametaphosphate *in vivo*

The most significant result of this work is that a Welch t-test failed to demonstrate a significant difference in the volume of weight-normalised HO between the active and

control groups. However, this does not automatically lead to rejection of the hypothesis that HMP can prevent or treat HO. This is because these experiments were the first time that HMP had been injected into an animal model of HO and the aim was as much about observing the way in which the treatment was tolerated as about expecting to see a statistically significant result at the first attempt. Apart from the unfortunate animal model death as a result of intravenous embolisation of the treatment, it was not shown to cause any lasting harm or any adverse effects on orthotopic bone. Also, the parameters used, including frequency of injection, dose of HMP, and choice of carrier vehicle were chosen with limited information and no *in vivo* data as guidance. This work will prove highly valuable in providing the first benchmark against which alterations in these parameters may be measured. For example, increasing the concentration of HMP per dose or administering the injections more frequently may demonstrate a larger effect. Additionally, once further experiments have been performed to optimise the dose, frequency, and vehicle, a larger number of animals per group will be required to power the statistical analyses appropriately; something that is not appropriate at this early stage of model development and first attempt at treatment.

A further point to make is that there was significant inter-batch variation and this may have contributed to the final result lacking statistical significance. Figure 6-5 has been colour-coded to indicate which batch the animals were in; red for batch 1 and blue for batch 2. In the active group, all animal models generated a very similar normalised volume of HO and there is no discernable difference between the batches. In the control group, however, there is a clear difference between the HO volume generated in the animals in batch 1 and 2. The difference between the

volumes of HO generated in the two batches of control animals is striking, with a mean volume of HO in batch 1 of 49.8 mm^3/kg (SD 2.2) and batch 2 of 27.8 mm^3/kg (SD 11.4). In addition to the mean value of HO in control batch 2 being lower than expected, the distribution of values was much wider than in any other batch from either experimental arm. Indeed, there appears to be an outlier in this batch with only 15.2 mm^3/kg of HO. This is nearly half of the value of the next lowest data point. Careful analysis of the experimental notes does not provide any clue as to why this model should have produced such a small volume of HO (e.g. inadvertent NSAID administration). In fact, it is not clear why control batch 2 produced such a variable and small volume of HO in comparison to batch 1. The animals were all of the same strain, underwent the same operation, received the same control injections at the same frequency, were fed the same diet, and were housed in the same conditions. It is possible that this effect is simply a reflection that variation is an unavoidable characteristic of *in vivo* experimentation. One possible way to avoid this situation in future would be to avoid the batch system by performing the experiment on 6 control and 6 treatment arm animals concurrently. This is now feasible because the work described in this chapter has shown that the tenotomy and injections are well tolerated (as long as care is taken to avoid intravascular injection).

Another important conclusion from this work is that there is no measurable adverse effect on orthotopic cortical or cancellous bone adjacent to the injection site. The most obvious potential problem with injecting a bone-mineral dissolving agent into a limb is that it would attack physiological and pathological bone equally. The data demonstrates that this is not the case, however, and it is worth considering what the explanation for this is. First, it was shown in Chapter 4 that HMP was able to dissolve

both human HO and normal (albeit murine) bone and so the observed specificity for pathological bone is not due to a lack of ability to dissolve it. Second, it was also shown in Chapter 4 that HMP is more potent at dissolving HA in low pH conditions, such as those that predispose to HO. Therefore, it is possible that this effect is acting in a highly localised manner to potentiate the dissolution of HO while preventing dissolution of orthotopic bone. Generating evidence to test this hypothesis would be extremely challenging but might include investigation of local tissue pH at the site of HO formation or perhaps alteration of the pH of the administered treatment. However, the simplest explanation is the most likely; that forming HO mineral has a much higher surface to volume ratio than mature orthotopic bone and would be much more vulnerable to dissolution. Mature orthotopic bone is also covered in a thick periosteal membrane, which would further protect it from dissolution by HMP.

It is significant to note that for hexametaphosphate to be taken further towards translation in the form of human trials, pre-clinical proof of efficacy in an animal model is not currently required by pharmaceutical regulators in the United States or Europe.[262] As such, the failure of this experiment to show a statistically significant effect on the volume of HO is not necessarily a barrier to progress. The current lack of safety data for parentally administered HMP is a more important issue. However, without some evidence of efficacy, it is unlikely that any funding to perform the safety testing would be secured. In summary, both safety and efficacy will need to be demonstrated more compellingly before human trials can begin.

6.6 *In Vivo* Model Conclusions

The Achilles tenotomy method provides a simple model for generating ectopic bone. This makes it ideal as means for testing a hydroxyapatite dissolving and inhibiting treatment for HO. The animal models tolerated the tenotomy operation well and did not show any adverse post-operative effects. Fortnightly injection with 200 μl of either (control) 1% alginate or active (1% alginate / 0.2 M HMP) was found to cause short-term discomfort but no long-term harm. Care must be taken not to deliver the injections into the vascular system. There was no evidence of an adverse effect on orthotopic bone. Finally, while these data did not show a significant difference in the volume of HO in the control and active arms of the protocol, this was not the primary aim of this first attempt at using HMP as a treatment. The primary aims were to set up the model in our institution and to test whether it was possible to inject HMP as a treatment. Both of these aims have been achieved by this work and the conditions have been set for future work to optimise the dose, timing, and carrier vehicle for this treatment in order to show evidence of efficacy in preventing and treating HO.

7 CONCLUSIONS AND FURTHER WORK

7.1 Conclusions

Heterotopic ossification is a disabling condition that can occur as a consequence of many types of injury. It has come to prominence recently due to the increased prevalence in severely blast-injured survivors of the military interventions in Iraq and Afghanistan. HO presents a major barrier to the functional recovery of these patients and there is currently no adequate means of preventing its formation once injury has occurred. This work has attempted to increase our understanding of this condition and develop a new means of preventing and treating it. One of the key problems with studying HO is that there is a great deal of uncertainty in the literature surrounding the cellular and signalling mechanisms involved. There is no consensus that HO due to different aetiologies either forms through the same mechanisms or is even the same disease.

In order to understand HO more fully, human samples were acquired and subjected to advanced physicochemical analysis. This is the first time that HO tissue has been examined using synchrotron nano tomography, mapped synchrotron X-ray diffraction, mapped X-ray fluorescence, or mapped Raman spectroscopy. The results of these investigations have shown that HO displays disordered physical structure above the micron to millimetre length scale, but highly ordered physical and chemical structure below this length scale. Additionally, tantalising evidence of an undescribed “calcium-first” mineralisation mechanism has been revealed by X-ray fluorescence imaging. It was not possible to make firm conclusions about the morphological parameters of HO because of the incredible degree of heterogeneity in the structure

of the samples. This variable morphology was seen both within individual samples over a very short length scale and between different samples. The only valid conclusion that can be made, therefore, is that the tools we currently use to describe normal bone morphology are inappropriate for HO.

The novel treatment discovery and development work found that hexametaphosphate, a cyclical polyphosphate, is a highly promising candidate for development. It was shown to be able to dissolve synthetic and biological hydroxyapatite (the mineral component of bone) under physiological conditions *in vitro.* Encouragingly, this effect was shown to be controllable through the effect of pH and the action of the enzyme alkaline phosphatase, which is found ubiquitously in the body. Also, there is some evidence that hexametaphosphate is able to inhibit the synthesis of hydroxyapatite, which suggests a possible role as a combined prophylaxis and treatment for HO. Developing a delivery vehicle that can allow the targeted application of hexametaphosphate to the site of formation of HO was found to be extremely challenging. The same chemical properties that are thought to make hexametaphosphate effective at dissolving hydroxyapatite also make it challenging to incorporate into injectable hydrogels, which are still likely to prove to be the best method of delivery in the future.

In order to test the feasibility of using hexametaphosphate for preventing and treating HO, an animal model was set up. The rat Achilles tenotomy model was shown to be simple, reliable, and well tolerated by the animal models. Having set up the model, hexametaphosphate injections were compared to controls. This is the first recorded use of hexametaphosphate to inhibit and treat HO in an animal model. This

experiment did not show a statistically significant result but it did show that it is possible to conduct this kind of work and provides a starting point from which further work can be compared.

In summary, this project has increased our understanding of the chemical and physical structure of human post-traumatic HO, has discovered that hexametaphosphate is a promising candidate for further development as both a treatment and prophylaxis against HO, and shown that it is possible to test this in an animal model of HO.

7.2 Further Work

While a few subsamples of human HO investigated in this work have been, necessarily, destroyed by the process of analysis, the majority are intact. This means that there is no barrier to further analysis. In general, it would be of great interest to explore the mineralisation mechanism in more detail. In the first instance, this could be achieved simply through the use of mapped X-ray fluorescence of more sections of the tissue. Further insights may be gained by looking at what other chemical species are associated with the calcium-rich islands discovered in the course of this work. This may require nuclear magnetic resonance spectroscopy and specialised analysis.

Development of new methods of quantifying and classifying the micro and macro scale morphology of HO would also be of great interest. If it could be shown that HO from different aetiologies formed in quantifiably different patterns, this would lend weight to the hypothesis that not all HO is the same disease and could allow

researchers to start describing different types of HO. The morphology is also of great importance to those who seek to investigate the effect of the mechanical environment of the stumps of amputees, which may allow a greater understanding of the effect on HO of topical negative pressure, for example.

One intriguing finding that may benefit from further investigation is the presence of what appear to be calcospherites in the samples of human HO. If the composition of these structures could be analysed, then their function and role in HO formation may be better understood.

In terms of treating and preventing HO using hexametaphosphate, the most pressing challenge is the lack of an optimal delivery system. Viscous uncrosslinked alginate was used for the *in vivo* work out of necessity but a shear-thinning gel may prove to be a better vehicle. Gellan and agarose proved promising but neither was satisfactory for use in the animal model. Further formulation engineering work needs to be carried out looking at a wider array of injectable hydrogels or even more novel approaches such as 3-D printed implantable reservoirs filled with hexametaphosphate. Understanding how to sterilise such a system would be of prime importance and is not an insignificant challenge.

There are extant plans for further animal model experiments. The timing of injections and dose of hexametaphosphate per dose are easily modifiable and will be explored. These experiments have been planned so that any potential batch-effects are minimised. Once the dose and scheduling parameters are optimised, a definitive experiment will be carried out with sufficient numbers of animals in each arm of the

study to test the hypothesis that hexametaphosphate can inhibit and treat HO *in vivo.* If this is shown to be the case, then work towards human trials can begin. An integral part of this phase of work will be establishing what the regulatory requirements are for such a therapy and addressing these. Additionally, formal toxicity testing will need to be undertaken. Finally, safety and efficacy will need to be demonstrated before this concept can be utilised in the human setting.

It is important to note that the funding, personnel, and resolve to continue with this work are already in place and I am confident that further progress will be made in the near future. The last few words of this thesis are reserved for the person who has taken the baton from me and will lead the next phase of this research as part of his PhD project: Mr Tom Robinson, good luck.

8 APPENDIX 1

A version of Chapter 2 has been published in the journal Advanced Healthcare Materials:

Eisenstein NM, Cox SC, Williams RL, Stapley SA, Grover LM. Bedside, Benchtop, and Bioengineering: Physicochemical Imaging Techniques in Biomineralization. *Advanced Healthcare Materials* 2016;5(5):507-28. doi: 10.1002/adhm.201500617

A copy of this publication is included below.

9 APPENDIX 2

A version of Chapter 4 has been published in the Journal of Materials Chemistry B:

Eisenstein N, Williams R, Cox S, Stapley S, Grover L. Enzymatically regulated demineralisation of pathological bone using sodium hexametaphosphate. *Journal of Materials Chemistry B* 2016;4(21):3815-22. doi: 10.1039/c6tb00461j

A copy of this publication is included below.

10 LIST OF REFERENCES

1. Spink MS, Lewis GL. Albucasis: on surgery and instruments: a definitive edition of the Arabic text with English translation and commentary: Wellcome Institute of the History of Medicine 1973.

2. Patin G. Lettres Choisies Defeu. *Guy Patin Coldene* 1692:28.

3. Otis G, Huntington D. Wounds and complications. *The medical and surgical history of the Civil War* 1883;2(pt 3):880.

4. Brackett EG. Care of the amputated in the United States. Washington: US Government Printing Office 1921:713-48.

5. Alfieri KA, Forsberg JA, Potter BK. Blast injuries and heterotopic ossification. *Bone and Joint Research* 2012;1(8):192-7.

6. Cunnane EM, Mulvihill JJE, Barrett HE, Healy DA, Kavanagh EG, Walsh SR, Walsh MT. Mechanical, biological and structural characterization of human atherosclerotic femoral plaque tissue. *Acta Biomaterialia* 2015;11(0):295-303.

7. Katz LD, Lindskog D, Eisen R. Neuritis ossificans of the tibial, common peroneal and lateral sural cutaneous nerves. *Journal of Bone and Joint Surgery (British Volume)* 2011;93-B(7):992-94.

8. Cottignoli V, Cavarretta E, Salvador L, Valfré C, Maras A. Morphological and Chemical Study of Pathological Deposits in Human Aortic and Mitral Valve Stenosis: A Biomineralogical Contribution. *Pathology Research International* 2015;Article ID 342984

9. O'Connor G. Calcific band keratopathy. *Transactions of the American Ophthalmological Society* 1972;70:58.

10. Tam L-S, Gu J, Yu D. Pathogenesis of ankylosing spondylitis. *Nature Reviews Rheumatology* 2010;6(7):399-405.

11. Bleil J, Maier R, Hempfing A, Schlichting U, Appel H, Sieper J, Syrbe U. Histomorphologic and histomorphometric characteristics of zygapophyseal joint remodeling in ankylosing spondylitis. *Arthritis and Rheumatology* 2014;66(7):1745-54.

12. George DH, Scheithauer BW, Spinner RJ, Buchler U, Cronin TE, Reedy MT, Arndt BC. Heterotopic ossification of peripheral nerve ("neuritis ossificans"): report of two cases. *Neurosurgery* 2002;51(1):244-6.

13. Myllylä RM, Haapasaari KM, Palatsi R, Germain-Lee EL, Hägg PM, Ignatius J, Tuukkanen J. Multiple miliary osteoma cutis is a distinct disease entity: four case reports and review of the literature. *British Journal of Dermatology* 2011;164(3):544-52.

14. Burke G, Shah D, MacBean A. Panniculitis ossificans traumatica: an unusual presentation. *British Journal of Oral and Maxillofacial Surgery* 2008;46(7):596-98.

15. Culbert AL, Chakkalakal SA, Convente MR, Lounev VY, Kaplan FS, Shore EM. Chapter 24 - Fibrodysplasia (Myositis) Ossificans Progressiva. In: Igarashi RVTPWAE, ed. Genetics of Bone Biology and Skeletal Disease. San Diego: Academic Press 2013:375-93.

16. Shore EM, Xu M, Feldman GJ, Fenstermacher DA, Cho T-J, Choi IH, Connor JM, Delai P, Glaser DL, LeMerrer M. A recurrent mutation in the BMP type I receptor ACVR1 causes inherited and sporadic fibrodysplasia ossificans progressiva. *Nature Genetics* 2006;38(5):525-27.

17. Fukuda T, Kohda M, Kanomata K, Nojima J, Nakamura A, Kamizono J, Noguchi Y, Iwakiri K, Kondo T, Kurose J. Constitutively activated ALK2 and increased SMAD1/5 cooperatively induce bone morphogenetic protein signaling in fibrodysplasia ossificans progressiva. *Journal of Biological Chemistry* 2009;284(11):7149-56.

18. Urtizberea JA, Testart H, Cartault F, Boccon-Gibod L, Le Merrer M, Kaplan FS. Progressive osseous heteroplasia. *Journal of Bone and Joint Surgery (British Volume)* 1998;80(5):768-71.

19. Kaplan FS, Shore EM. Progressive osseous heteroplasia. *Journal of Bone and Mineral Research* 2000;15(11):2084-94.

20. Pignolo RJ, Ramaswamy G, Fong JT, Shore EM, Kaplan FS. Progressive osseous heteroplasia: diagnosis, treatment, and prognosis. *The application of clinical genetics* 2015;8:37.

21. Forsberg JA, Pepek JM, Wagner S, Wilson K, Flint J, Andersen RC, Tadaki D, Gage FA, Stojadinovic A, Elster EA. Heterotopic ossification in high-energy wartime extremity injuries: prevalence and risk factors. *The Journal of Bone and Joint Surgery (American Volume)* 2009;91(5):1084-91.

22. Potter BK, Burns TC, Lacap AP, Granville RR, Gajewski DA. Heterotopic ossification following traumatic and combat-related amputations. Prevalence, risk factors, and preliminary results of excision. *Journal of Bone and Joint Surgery (American Volume)* 2007;89(3):476-86.

23. Edwards MD, Phillip LCRD, Bosanquet N, Bull AM, Clasper CJC. What is the magnitude and long-term economic cost of care of the British military Afghanistan amputee cohort? *Clinical Orthopaedics and Related Research* 2015;473(9):2848-55.

24. Matsumoto ME, Khan M, Jayabalan P, Ziebarth J, Munin MC. Heterotopic Ossification in Civilians With Lower Limb Amputations. *Archives of Physical Medicine and Rehabilitation* 2014;95(9):1710-13.

25. Dizdar D, Tiftik T, Kara M, Tunc H, Ersoz M, Akkus S. Risk factors for developing heterotopic ossification in patients with traumatic brain injury. *Brain Injury* 2013;27(7-8):807-11.

26. Genêt F, Jourdan C, Schnitzler A, Lautridou C, Guillemot D, Judet T, Poiraudeau S, Denormandie P. Troublesome heterotopic ossification after central nervous system damage: a survey of 570 surgeries. *PloS One* 2011;6(1):e16632.

27. Berstock J, Blom A, Beswick A. A systematic review and meta-analysis of complications following the posterior and lateral surgical approaches to total hip arthroplasty. *Annals of the Royal College of Surgeons of England* 2015;97(1):11-16.

28. Nauth A, McKee MD, Ristevski B, Hall J, Schemitsch EH. Distal humeral fractures in adults. *The Journal of Bone and Joint Surgery (American Volume)* 2011;93(7):686-700.

29. Chen H-C, Yang J-Y, Chuang S-S, Huang C-Y, Yang S-Y. Heterotopic ossification in burns: Our experience and literature reviews. *Burns* 2009;35(6):857-62.

30. Penn-Barwell JG, Roberts SA, Midwinter MJ, Bishop JR. Improved survival in UK combat casualties from Iraq and Afghanistan: 2003–2012. *Journal of Trauma and Acute Care Surgery* 2015;78(5):1014-20.

31. Potter BK, Burns TC, Lacap AP, Granville RR, Gajewski D. Heterotopic ossification in the residual limbs of traumatic and combat-related amputees. *Journal of the American Academy of Orthopaedic Surgeons* 2006;14(10 Spec No.):S191-7.

32. Brown KV, Clasper JC. The changing pattern of amputations. *Journal of the Royal Army Medical Corps* 2013;159(4):300-03.

33. Brown KV, Dharm-Datta S, Potter BK, Etherington J, Mistlin A, Hsu JR, Clasper JC. Comparison of development of heterotopic ossification in injured US and UK Armed Services personnel with combat-related amputations:

preliminary findings and hypotheses regarding causality. *Journal of Trauma and Acute Care Surgery* 2010;69(1):S116-S22.

34. Potter BK, Forsberg JA, Davis TA, Evans KN, Hawksworth JS, Tadaki D, Brown TS, Crane NJ, Burns TC, O'Brien FP, Elster EA. Heterotopic ossification following combat-related trauma. *Journal of Bone and Joint Surgery (American Volume)* 2010;92 Suppl 2:74-89.

35. Evriviades D, Jeffery S, Cubison T, Lawton G, Gill M, Mortiboy D. Shaping the military wound: issues surrounding the reconstruction of injured servicemen at the Royal Centre for Defence Medicine. *Philosophical Transactions of the Royal Society of London Series B: Biological Sciences* 2011;366(1562):219-30.

36. Masini BD, Waterman SM, Wenke JC, Owens BD, Hsu JR, Ficke JR. Resource utilization and disability outcome assessment of combat casualties from Operation Iraqi Freedom and Operation Enduring Freedom. *Journal of Orthopaedic Trauma* 2009;23(4):261-66.

37. Beckmann JT, Wylie JD, Kapron AL, Hanson JA, Maak TG, Aoki SK. The Effect of NSAID Prophylaxis and Operative Variables on Heterotopic Ossification After Hip Arthroscopy. *The American journal of sports medicine* 2014;42(6):1359-64.

38. Burd T, Hughes M, Anglen J. Heterotopic ossification prophylaxis with indomethacin increases the risk of long-bone nonunion. *Journal of Bone and Joint Surgery (British Volume)* 2003;85(5):700-05.

39. de Abreu KLS, Silva Júnior GB, Barreto AGC, Melo FM, Oliveira BB, Mota RMS, Rocha NA, Silva SL, Araújo SMHA, Daher EF. Acute kidney injury after trauma: Prevalence, clinical characteristics and RIFLE classification. *Indian Journal of Critical Care Medicine* 2010;14(3):121-28.

40. Popovic M, Agarwal A, Zhang L, Yip C, Kreder HJ, Nousiainen MT, Jenkinson R, Tsao M, Lam H, Milakovic M, Wong E, Chow E. Radiotherapy for the prophylaxis of heterotopic ossification: A systematic review and meta-analysis of published data. *Radiotherapy and Oncology* 2014;113(1):10-17.

41. Pakos EE, Pitouli EJ, Tsekeris PG, Papathanasopoulou V, Stafilas K, Xenakis TH. Prevention of heterotopic ossification in high-risk patients with total hip arthroplasty: the experience of a combined therapeutic protocol. *International Orthopaedics* 2006;30(2):79-83.

42. Haran M, Bhuta T, Lee B. Pharmacological interventions for treating acute heterotopic ossification. *Cochrane Database of Systematic Reviews* 2004;4(4):CD003321.

43. Shafer DM, Bay C, Caruso DM, Foster KN. The use of eidronate disodium in the prevention of heterotopic ossification in burn patients. *Burns* 2008;34(3):355-60.

44. Prabhu RKR, Swaminathan N, Harvey LA. Passive movements for the treatment and prevention of contractures. *Cochrane Database of Systematic Reviews* 2013; (12).

45. Shimono K, Tung W-E, Macolino C, Chi AH-T, Didizian JH, Mundy C, Chandraratna RA, Mishina Y, Enomoto-Iwamoto M, Pacifici M. Potent inhibition of heterotopic ossification by nuclear retinoic acid receptor-[gamma] agonists. *Nature Medicine* 2011;17(4):454-60.

46. Johnson RW, Sims NA. Embedded in bone, but looking beyond: osteocalcin, epigenetics and ectopic bone formation (ASBMR 2014). *IBMS BoneKEy* 2014;11

47. Peterson JR, De La Rosa S, Eboda O, Cilwa KE, Agarwal S, Buchman SR, Cederna PS, Xi C, Morris MD, Herndon DN. Treatment of heterotopic ossification through remote ATP hydrolysis. *Science Translational Medicine* 2014;6(255):255ra132.

48. Zimmermann SM, Wurgler-Hauri CC, Wanner GA, Simmen HP, Werner CM. Echinomycin in the prevention of heterotopic ossification - an experimental antibiotic agent shows promising results in a murine model. *Injury* 2013;44(4):570-5.

49. Chalidis B, Stengel D, Giannoudis PV. Early excision and late excision of heterotopic ossification after traumatic brain injury are equivalent: a systematic review of the literature. *Journal of Neurotrauma* 2007;24(11):1675-86.

50. Ranganathan K, Loder S, Agarwal S, Wong VC, Forsberg J, Davis TA, Wang S, James AW, Levi B. Heterotopic Ossification: Basic-Science Principles and Clinical Correlates. *Journal of Bone and Joint Surgery (American Volume)* 2015;97(13):1101-11.

51. Reichel LM, Salisbury E, Moustoukas MJ, Davis AR, Olmsted-Davis E. Molecular mechanisms of heterotopic ossification. *Journal of Hand Surgery* 2014;39(3):563-6.

52. Ramirez DM, Ramirez MR, Reginato AM, Medici D. Molecular and cellular mechanisms of heterotopic ossification. *Histology and Histopathology* 2014;29(10):1281-5.

53. Downey J, Lauzier D, Kloen P, Klarskov K, Richter M, Hamdy R, Faucheux N, Scimè A, Balg F, Grenier G. Prospective heterotopic ossification progenitors in adult human skeletal muscle. *Bone* 2015;71:164-70.

54. Lounev VY, Ramachandran R, Wosczyna MN, Yamamoto M, Maidment AD, Shore EM, Glaser DL, Goldhamer DJ, Kaplan FS. Identification of progenitor cells that contribute to heterotopic skeletogenesis. *Journal of Bone and Joint Surgery (American Volume)* 2009;91(3):652-63.

55. Davies OG, Grover LM, Eisenstein N, Lewis MP, Liu Y. Identifying the Cellular Mechanisms Leading to Heterotopic Ossification. *Calcified Tissue International* 2015;97(5):432-44.

56. Jackson WM, Aragon AB, Bulken-Hoover JD, Nesti LJ, Tuan RS. Putative heterotopic ossification progenitor cells derived from traumatized muscle. *Journal of Orthopaedic Research* 2009;27(12):1645-51.

57. Olmsted-Davis E, Gannon FH, Ozen M, Ittmann MM, Gugala Z, Hipp JA, Moran KM, Fouletier-Dilling CM, Schumara-Martin S, Lindsey RW, Heggeness MH, Brenner MK, Davis AR. Hypoxic adipocytes pattern early heterotopic bone formation. *American Journal of Pathology* 2007;170(2):620-32.

58. Dey D, Bagarova J, Hatsell SJ, Armstrong KA, Huang L, Ermann J, Vonner AJ, Shen Y, Mohedas AH, Lee A, Eekhoff EM, van Schie A, Demay MB, Keller C, Wagers AJ, Economides AN, Yu PB. Two tissue-resident progenitor lineages drive distinct phenotypes of heterotopic ossification. *Science Translational Medicine* 2016;8(366):366ra163.

59. Forsberg JA, Potter BK, Polfer EM, Safford SD, Elster EA. Do inflammatory markers portend heterotopic ossification and wound failure in combat wounds? *Clinical Orthopaedics and Related Research* 2014;472(9):2845-54.

60. Evans KN, Forsberg JA, Potter BK, Hawksworth JS, Brown TS, Andersen R, Dunne JR, Tadaki D, Elster EA. Inflammatory cytokine and chemokine expression is associated with heterotopic ossification in high-energy penetrating war injuries. *Journal of Orthopaedic Trauma* 2012;26(11):e204-13.

61. Peterson JR, De La Rosa S, Sun H, Eboda O, Cilwa KE, Donneys A, Morris M, Buchman SR, Cederna PS, Krebsbach PH, Wang SC, Levi B. Burn injury enhances bone formation in heterotopic ossification model. *Annals of Surgery* 2014;259(5):993-8.

62. Giannoudis PV. Current concepts of the inflammatory response after major trauma: an update. *Injury* 2003;34(6):397-404.

63. Vanzant EL, Lopez CM, Ozrazgat-Baslanti T, Ungaro R, Davis R, Cuenca AG, Gentile LF, Nacionales DC, Cuenca AL, Bihorac A, Leeuwenburgh C, Lanz J, Baker HV, McKinley B, Moldawer LL, Moore FA, Efron PA. Persistent Inflammation, Immunosuppression and Catabolism Syndrome after Severe Blunt Trauma. *The Journal of Trauma and Acute Care Surgery* 2014;76(1):21-30.

64. Nauth A, Giles E, Potter BK, Nesti LJ, O'Brien FP, Bosse MJ, Anglen JO, Mehta S, Ahn J, Miclau T, Schemitsch EH. Heterotopic Ossification in Orthopaedic Trauma. *Journal of Orthopaedic Trauma* 2012;26(12):684-88.

65. Evans KN, Potter BK, Brown TS, Davis TA, Elster EA, Forsberg JA. Osteogenic gene expression correlates with development of heterotopic ossification in war wounds. *Clinical Orthopaedics and Related Research* 2014;472(2):396-404.

66. Tannous O, Stall AC, Griffith C, Donaldson CT, Castellani RJ, Jr., Pellegrini VD, Jr. Heterotopic bone formation about the hip undergoes endochondral ossification: a rabbit model. *Clinical Orthopaedics and Related Research* 2013;471(5):1584-92.

67. Medici D, Olsen BR. The role of endothelial-mesenchymal transition in heterotopic ossification. *Journal of Bone and Mineral Research* 2012;27(8):1619-22.

68. Dharm-Datta S, Etherington J, Mistlin A, Rees J, Clasper J. The outcome of British combat amputees in relation to military service. *Injury* 2011;42(11):1362-7.

69. Ladlow P, Phillip R, Etherington J, Coppack R, Bilzon J, McGuigan MP, Bennett AN. Functional and Mental Health Status of United Kingdom Military Amputees Postrehabilitation. *Archives of Physical Medicine and Rehabilitation* 2015;96(11):2048-54.

70. Eisenstein NM, Cox SC, Williams RL, Stapley SA, Grover LM. Bedside, Benchtop, and Bioengineering: Physicochemical Imaging Techniques in Biomineralization. *Adv Healthc Mater* 2016;5(5):507-28.

71. Murphy DB, Davidson MW. Fundamentals of Light Microscopy and Electronic Imaging: John Wiley & Sons 2012.

72. Allen MR, Burr DB. Chapter 7 - Techniques in Histomorphometry. In: Allen MR, Burr DB, eds. Basic and Applied Bone Biology. San Diego: Academic Press 2014:131-48.

73. von Kossa J. Concerning artificially produced calcification in organs. *Beitrage zur Pathologischen Anatomie und zur Allgemeinen Pathologie* 1901;29(2):163-202.

74. Oishi T, Uezumi A, Kanaji A, Yamamoto N, Yamaguchi A, Yamada H, Tsuchida K. Osteogenic differentiation capacity of human skeletal muscle-derived progenitor cells. *PloS One* 2013;8(2):e56641.

75. Peterson JR, Okagbare PI, De La Rosa S, Cilwa KE, Perosky JE, Eboda ON, Donneys A, Su GL, Buchman SR, Cederna PS, Wang SC, Kozloff KM, Morris MD, Levi B. Early detection of burn induced heterotopic ossification using transcutaneous Raman spectroscopy. *Bone* 2013;54(1):28-34.

76. Wang L, Zhang B, Bao C, Habibovic P, Hu J, Zhang X. Ectopic Osteoid and Bone Formation by Three Calcium-Phosphate Ceramics in Rats, Rabbits and Dogs. *PloS One* 2014;9(9):e107044.

77. Davis TA, Lazdun Y, Potter BK, Forsberg JA. Ectopic bone formation in severely combat-injured orthopedic patients -- a hematopoietic niche. *Bone* 2013;56(1):119-26.

78. Isaacson BM, Brown AA, Brunker LB, Higgins TF, Bloebaum RD. Clarifying the structure and bone mineral content of heterotopic ossification. *Journal of Surgical Research* 2011;167(2):e163-70.

79. Sasaki J-I, Matsumoto T, Egusa H, Matsusaki M, Nishiguchi A, Nakano T, Akashi M, Imazato S, Yatani H. In vitro reproduction of endochondral ossification using a 3D mesenchymal stem cell construct. *Integrative Biology* 2012;4(10):1207-14.

80. Becker ST, Bolte H, Schünemann K, Seitz H, Bara JJ, Beck-Broichsitter BE, Russo PAJ, Wiltfang J, Warnke PH. Endocultivation: the influence of delayed vs. simultaneous application of BMP-2 onto individually formed hydroxyapatite matrices for heterotopic bone induction. *International Journal of Oral and Maxillofacial Surgery* 2012;41(9):1153-60.

81. Perosky JE, Peterson JR, Eboda ON, Morris MD, Wang SC, Levi B, Kozloff KM. Early detection of heterotopic ossification using near-infrared optical imaging reveals dynamic turnover and progression of mineralization following Achilles tenotomy and burn injury. *Journal of Orthopaedic Research* 2014;32(11):1416-23.

82. Beniash E, Dey A, Sommerdijk NA. Transmission electron microscopy in biomineralization research: Advances and challenges. In: DiMasi E, Gower L, eds. Biomineralization Sourcebook: Characterization of Biominerals and Biomimetic Materials. Boca Raton: CRC Press 2014:420.

83. Hong SI, Hong SK, Kohn DH. Nanostructural analysis of trabecular bone. *Journal of Materials Science: Materials in Medicine* 2009;20(7):1419-26.

84. Nudelman F, Pieterse K, George A, Bomans PHH, Friedrich H, Brylka LJ, Hilbers PAJ, de With G, Sommerdijk NAJM. The role of collagen in bone apatite formation in the presence of hydroxyapatite nucleation inhibitors. *Nature Materials* 2010;9(12):1004-09.

85. Nudelman F, Bomans PHH, George A, de With G, Sommerdijk NAJM. The role of the amorphous phase on the biomimetic mineralization of collagen. *Faraday Discussions* 2012;159(0):357-70.

86. Weiner S, Traub W, Wagner HD. Lamellar bone: structure-function relations. *Journal of Structural Biology* 1999;126(3):241-55.

87. Vaquette C, Ivanovski S, Hamlet SM, Hutmacher DW. Effect of culture conditions and calcium phosphate coating on ectopic bone formation. *Biomaterials* 2013;34(22):5538-51.

88. Kikkawa N, Ohno T, Nagata Y, Shiozuka M, Kogure T, Matsuda R. Ectopic calcification is caused by elevated levels of serum inorganic phosphate in Mdx mice. *Cell Structure and Function* 2009;34(2):77-88.

89. Orzel JA, Rudd TG. Heterotopic bone formation: clinical, laboratory, and imaging correlation. *Journal of Nuclear Medicine* 1985;26(2):125-32.

90. Tannous O, Griffith C, O'Toole R, Pellegrini VD, Jr. Hetertopic Ossification After Extremity Blast Amputation in a Sprague-Dawley Rat Animal Model. *Journal of Orthopaedic Trauma* 2011;25(8):506-10.

91. Allen MR, Krohn K. Chapter 5 - Skeletal Imaging. In: Allen DBBR, ed. Basic and Applied Bone Biology. San Diego: Academic Press 2014:93-113.

92. Porter BD, Lin AS, Peister A, Hutmacher D, Guldberg RE. Noninvasive image analysis of 3D construct mineralization in a perfusion bioreactor. *Biomaterials* 2007;28(15):2525-33.

93. Saito A, Suzuki Y, Ogata S-I, Ohtsuki C, Tanihara M. Prolonged ectopic calcification induced by BMP-2–derived synthetic peptide. *Journal of Biomedical Materials Research Part A* 2004;70A(1):115-21.

94. Shehab D, Elgazzar AH, Collier BD. Heterotopic ossification. *Journal of Nuclear Medicine* 2002;43(3):346-53.

95. Frangioni JV. In vivo near-infrared fluorescence imaging. *Current Opinion in Chemical Biology* 2003;7(5):626-34.

96. Zaheer A, Lenkinski RE, Mahmood A, Jones AG, Cantley LC, Frangioni JV. In vivo near-infrared fluorescence imaging of osteoblastic activity. *Nature Biotechnology* 2001;19(12):1148-54.

97. Xu H, Othman SF, Magin RL. Monitoring tissue engineering using magnetic resonance imaging. *Journal of Bioscience and Bioengineering* 2008;106(6):515-27.

98. Wick L, Berger M, Knecht H, Glücker T, Ledermann HP. Magnetic resonance signal alterations in the acute onset of heterotopic ossification in patients with spinal cord injury. *European Radiology* 2005;15(9):1867-75.

99. Ledermann HP, Schweitzer ME, Morrison WB. Pelvic heterotopic ossification: MR imaging characteristics. *Radiology* 2002;222(1):189-95.

100. Shirkhoda A, Armin AR, Bis KG, Makris J, Irwin RB, Shetty AN. MR imaging of myositis ossificans: variable patterns at different stages. *Journal of Magnetic Resonance Imaging* 1995;5(3):287-92.

101. De Smet AA, Norris MA, Fisher DR. Magnetic resonance imaging of myositis ossificans: analysis of seven cases. *Skeletal Radiology* 1992;21(8):503-7.

102. Ehara S, Shiraishi H, Abe M, Mizutani H. Reactive heterotopic ossification. Its patterns on MRI. *Clinical Imaging* 1998;22(4):292-6.

103. Washburn NR, Weir M, Anderson P, Potter K. Bone formation in polymeric scaffolds evaluated by proton magnetic resonance microscopy and X-ray microtomography. *Journal of Biomedical Materials Research, Part A* 2004;69(4):738-47.

104. Xu H, Othman SF, Hong L, Peptan IA, Magin RL. Magnetic resonance microscopy for monitoring osteogenesis in tissue-engineered construct in vitro. *Physics in Medicine and Biology* 2006;51(3):719-32.

105. Adzamli IK, Gries H, Johnson D, Blau M. Development of phosphonate derivatives of gadolinium chelates for NMR imaging of calcified soft tissues. *Journal of Medicinal Chemistry* 1989;32(1):139-44.

106. Chesnick IE, Fowler CB, Mason JT, Potter K. Novel mineral contrast agent for magnetic resonance studies of bone implants grown on a chick chorioallantoic membrane. *Magnetic Resonance Imaging* 2011;29(9):1244-54.

107. Othman SF, Xu H, Royston TJ, Magin RL. Microscopic magnetic resonance elastography (microMRE). *Magnetic Resonance in Medicine* 2005;54(3):605-15.

108. Hartman EH, Pikkemaat JA, Vehof JW, Heerschap A, Jansen JA, Spauwen PH. In vivo magnetic resonance imaging explorative study of ectopic bone formation in the rat. *Tissue Engineering* 2002;8(6):1029-36.

109. Hartman EH, Pikkemaat JA, Van Asten JJ, Vehof JW, Heerschap A, Oyen WJ, Spauwen PH, Jansen JA. Demineralized bone matrix-induced ectopic bone formation in rats: in vivo study with follow-up by magnetic resonance imaging, magnetic resonance angiography, and dual-energy X-ray absorptiometry. *Tissue Engineering* 2004;10(5-6):747-54.

110. McDicken WN, Anderson T. CHAPTER 1 - Basic physics of medical ultrasound. In: Weston PLAMBJ, ed. Clinical Ultrasound (Third Edition). Edinburgh: Churchill Livingstone 2011:3-15.

111. Bodley R, Jamous A, Short D. Ultrasound in the early diagnosis of heterotopic ossification in patients with spinal injuries. *Paraplegia* 1993;31(8):500-6.

112. Thomas EA, Cassar-Pullicino VN, McCall IW. The role of ultrasound in the early diagnosis and management of heterotopic bone formation. *Clinical Radiology* 1991;43(3):190-6.

113. Cassar-Pullicino VN, McClelland M, Badwan DA, McCall IW, Pringle RG, el Masry W. Sonographic diagnosis of heterotopic bone formation in spinal injury patients. *Paraplegia* 1993;31(1):40-50.

114. Youssefian T, Sapena R, Carlier R, Bos C, Denormandie A, Denys P, Cormier A, Bandelier M. Nodular osteochondrogenic activity in soft tissue surrounding osteoma in neurogenic para osteo-arthropathy: morphological and immunohistochemical study. *BMC Musculoskeletal Disorders* 2004;5:46.

115. Cho K-H, Lee Y-H, Lee S-M, Shahid MU, Suh KJ, Choi JH. Sonography of bone and bone-related diseases of the extremities. *Journal of Clinical Ultrasound* 2004;32(9):511-21.

116. Falsetti P, Acciai C, Palilla R, Carpinteri F, Patrizio C, Lenzi L. Bedside ultrasound in early diagnosis of neurogenic heterotopic ossification in patients with acquired brain injury. *Clinical Neurology and Neurosurgery* 2011;113(1):22-7.

117. Gudur M, Rao RR, Hsiao YS, Peterson AW, Deng CX, Stegemann JP. Noninvasive, Quantitative, Spatiotemporal Characterization of Mineralization in Three-Dimensional Collagen Hydrogels Using High-Resolution Spectral Ultrasound Imaging. *Tissue Engineering Part C-Methods* 2012;18(12):935-46.

118. Chen Y, Yan Y, Li X, Li H, Tan H, Li H, Zhu Y, Niemeyer P, Yaega M, Yu B. Application of Ultrasound on Monitoring the Evolution of the Collagen Fiber Reinforced nHAC/CS Composites In Vivo. *BioMed research international* 2014;2014

119. Hayashi T, Kobayashi S, Asakura M, Kawase M, Ueno A, Uematsu Y, Kawai T. Immature muscular tissue differentiation into bone-like tissue by bone morphogenetic proteins in vitro, with ossification potential in vivo. *Journal of Biomedical Materials Research Part A* 2014;102(9):3112-21.

120. Misof B, Roschger P, Fratzl P. Imaging Mineralized Tissues in Vertebrates. In: Ducheyne P, ed. Comprehensive Biomaterials. Oxford: Elsevier 2011:407-26.

121. Stahler AC, Monahan JL, Dagher JM, Baker JD, Markopoulos MM, Iragena DB, NeJame BM, Slaughter R, Felker D, Burggraf LW, Isaac LAC, Grossie D, Gagnon ZE, Sizemore IEP. Evaluating the abnormal ossification in tibiotarsi of developing chick embryos exposed to 1.0 ppm doses of platinum group metals by spectroscopic techniques. *Bone* 2013;53(2):421-29.

122. Boskey A, Pleshko Camacho N. FT-IR imaging of native and tissue-engineered bone and cartilage. *Biomaterials* 2007;28(15):2465-78.

123. Boyan B, Bonewald L, Paschalis E, Lohmann C, Rosser J, Cochran D, Dean D, Schwartz Z, Boskey A. Osteoblast-mediated mineral deposition in culture is dependent on surface microtopography. *Calcified Tissue International* 2002;71(6):519-29.

124. Boskey A, Paschalis E, Binderman I, Doty S. BMP‐6 accelerates both chondrogenesis and mineral maturation in differentiating chick limb‐bud mesenchymal cell cultures. *Journal of Cellular Biochemistry* 2002;84(3):509-19.

125. Heyma D, Touchais S, Bohic S, Rohanizadeh R, Coquard C, Passuti N, Daculsi G. Heterotopic implantation of mouse bone-marrow cells: an in vivo model allowing analysis of mineral phases during mineralization processes. *Connective Tissue Research* 1998;37(3-4):219-31.

126. Amer M. Raman spectroscopy for soft matter applications. New Jersey: John Wiley & Sons 2009.

127. Colomban P. Raman analyses and "smart" imaging of nanophases and nanosized materials. *Spectroscopy Europe* 2003;15(6):8-16.

128. Crane NJ, Polfer E, Elster EA, Potter BK, Forsberg JA. Raman spectroscopic analysis of combat-related heterotopic ossification development. *Bone* 2013;57(2):335-42.

129. Ghita A, Pascut FC, Sottile V, Notingher I. Monitoring the mineralisation of bone nodules in vitro by space-and time-resolved Raman micro-spectroscopy. *Analyst* 2014;139(1):55-58.

130. Wang Y, Geil PH. X‐Ray Diffraction. First ed. Oxford, UK: Wiley‐Blackwell 2012:163-179.

131. Peyrin F. Investigation of bone with synchrotron radiation imaging: from micro to nano. *Osteoporosis International* 2009;20(6):1057-63.

132. Sabou F, Necula R, Șamota I, Sabou A. The Presence Of Hydroxyapatite Crystal In Heterotopic Ossifications Analyzed By Means Of X-Ray Powder Diffraction Method. *Romanian Journal of Biophysics* 2013;23(4):221-30.

133. Zhang Z-L, Chen X-R, Bian S, Huang J, Zhang T-L, Wang K. Identification of dicalcium phosphate dihydrate deposited during osteoblast mineralization in vitro. *Journal of Inorganic Biochemistry* 2014;131(0):109-14.

134. Zipfel WR, Williams RM, Webb WW. Nonlinear magic: multiphoton microscopy in the biosciences. *Nature Biotechnology* 2003;21(11):1369-77.

135. Helmchen F, Denk W. Deep tissue two-photon microscopy. *Nature Methods* 2005;2(12):932-40.

136. Mansfield J, Yu J, Attenburrow D, Moger J, Tirlapur U, Urban J, Cui Z, Winlove P. The elastin network: its relationship with collagen and cells in articular cartilage as visualized by multiphoton microscopy. *Journal of Anatomy* 2009;215(6):682-91.

137. Downes A, Mouras R, Bagnaninchi P, Elfick A. Raman spectroscopy and CARS microscopy of stem cells and their derivatives. *Journal of Raman Spectroscopy* 2011;42(10):1864-70.

138. Liu E, Treiser MD, Johnson PA, Patel P, Rege A, Kohn J, Moghe PV. Quantitative biorelevant profiling of material microstructure within 3D porous scaffolds via multiphoton fluorescence microscopy. *Journal of Biomedical Materials Research Part B: Applied Biomaterials* 2007;82(2):284-97.

139. Villa MM, Wang L, Huang J, Rowe DW, Wei M. Visualizing Osteogenesis In Vivo Within a Cell–Scaffold Construct for Bone Tissue Engineering Using Two-Photon Microscopy. *Tissue Engineering Part C: Methods* 2013;19(11):839-49.

140. Qureshi AT, Crump EK, Pavey GJ, Hope DN, Forsberg JA, Davis TA. Early Characterization of Blast-related Heterotopic Ossification in a Rat Model. *Clinical Orthopaedics and Related Research* 2015:1-9.

141. Jähn K, Stoddart MJ. Viability assessment of osteocytes using histological lactate dehydrogenase activity staining on human cancellous bone sections. *Mammalian Cell Viability: Methods and Protocols* 2011:141-48.

142. Scaglione S, Giannoni P, Bianchini P, Sandri M, Marotta R, Firpo G, Valbusa U, Tampieri A, Diaspro A, Bianco P, Quarto R. Order versus Disorder: in vivo bone formation within osteoconductive scaffolds. *Scientific Reports* 2012;2:274.

143. Boskey AL, Posner AS. Conversion of amorphous calcium phosphate to microcrystalline hydroxyapatite. A pH-dependent, solution-mediated, solid-solid conversion. *The Journal of Physical Chemistry* 1973;77(19):2313-17.

144. Isaacson B, Potter B, Bloebaum R, Epperson R, Kawaguchi B, Swanson T, Pasquina P. Link between clinical predictors of heterotopic ossification and histological analysis in combat-injured service members. *Journal of Bone and Joint Surgery (American Volume)* 2016;98(8):647-57.

145. Rubin MA, Jasiuk I, Taylor J, Rubin J, Ganey T, Apkarian RP. TEM analysis of the nanostructure of normal and osteoporotic human trabecular bone. *Bone* 2003;33(3):270-82.

146. Zimmermann SM, Schwitter LW, Scheyerer MJ, Jentzsch T, Simmen H-P, Werner CM. Prevention of heterotopic ossification: an experimental study using a plasma expander in a murine model. *BMC Surgery* 2016;16(1):1.

147. Arduini M, Mancini F, Farsetti P, Piperno A, Ippolito E. A new classification of peri-articular heterotopic ossification of the hip associated with neurological injury: 3D CT scan assessment and intra-operative findings. *Bone & Joint Journal* 2015;97-B(7):899-904.

148. Jones AC, Arns CH, Sheppard AP, Hutmacher DW, Milthorpe BK, Knackstedt MA. Assessment of bone ingrowth into porous biomaterials using MICRO-CT. *Biomaterials* 2007;28(15):2491-504.

149. Langer M, Peyrin F. 3D X-ray ultra-microscopy of bone tissue. *Osteoporosis International* 2016;27(2):441-55.

150. Langer M, Pacureanu A, Suhonen H, Grimal Q, Cloetens P, Peyrin F. X-ray phase nanotomography resolves the 3D human bone ultrastructure. *PloS One* 2012;7(8):e35691.

151. A new quantitative approach for estimating bone cell connections from nano-CT images. Engineering in Medicine and Biology Society (EMBC), 2013 35th Annual International Conference of the IEEE; 2013. IEEE.

152. Hesse B, Varga P, Langer M, Pacureanu A, Schrof S, Männicke N, Suhonen H, Maurer P, Cloetens P, Peyrin F. Canalicular Network Morphology Is the Major Determinant of the Spatial Distribution of Mass Density in Human Bone Tissue: Evidence by Means of Synchrotron Radiation Phase‐Contrast nano‐CT. *Journal of Bone and Mineral Research* 2015;30(2):346-56.

153. Orzel JA, Rudd TG, Nelp WB. Heterotopic bone formation (myositis ossificans) and lower-extremity swelling mimicking deep-venous disease. *Journal of Nuclear Medicine* 1984;25(10):1105-7.

154. Potter K, Sweet DE, Anderson P, Davis GR, Isogai N, Asamura S, Kusuhara H, Landis WJ. Non-destructive studies of tissue-engineered phalanges by magnetic resonance microscopy and X-ray microtomography. *Bone* 2006;38(3):350-8.

155. Sampath Kumar TS. Chapter 2 - Physical and Chemical Characterization of Biomaterials. In: Bose AB, ed. Characterization of Biomaterials. Oxford: Academic Press 2013:11-47.

156. De Aza PN, Luklinska ZB, Santos C, Guitian F, De Aza S. Mechanism of bone-like formation on a bioactive implant in vivo. *Biomaterials* 2003;24(8):1437-45.

157. Thula TT, Svedlund F, Rodriguez DE, Podschun J, Pendi L, Gower LB. Mimicking the nanostructure of bone: Comparison of polymeric process-directing agents. *Polymers* 2011;3(1):10-35.

158. Koburger S, Bannerman A, Grover LM, Müller FA, Bowen J, Paxton JZ. A novel method for monitoring mineralisation in hydrogels at the engineered hard–soft tissue interface. *Biomaterials Science* 2014;2(1):41.

159. Spence G, Phillips S, Campion C, Brooks R, Rushton N. Bone formation in a carbonate-substituted hydroxyapatite implant is inhibited by zoledronate: the importance of bioresorption to osteoconduction. *The Journal of Bone and Joint Surgery (British Volume)* 2008;90(12):1635-40.

160. Cruz ACCd, Pochapski MT, Daher JB, Silva JCZd, Pilatti GL, Santos FA. Physico-chemical characterization and biocompatibility evaluation of hydroxyapatites. *Journal of Oral Science* 2006;48(4):219-26.

161. Calasans-Maia M, Calasans-Maia J, Santos S, Mavropoulos E, Farina M, Lima I, Lopes RT, Rossi A, Granjeiro JM. Short-term in vivo evaluation of zinc-containing calcium phosphate using a normalized procedure. *Materials Science and Engineering: C* 2014;41:309-19.

162. Kazarian SG, Andrew Chan KL, Maquet V, Boccaccini AR. Characterisation of bioactive and resorbable polylactide/Bioglass composites by FTIR spectroscopic imaging. *Biomaterials* 2004;25(18):3931-38.

163. Harris M, Cilwa K, Elster EA, Potter BK, Forsberg JA, Crane NJ. Pilot study for detection of early changes in tissue associated with heterotopic ossification: moving toward clinical use of Raman spectroscopy. *Connective Tissue Research* 2015;56(2):144-52.

164. Patterson AL. The Scherrer Formula for X-Ray Particle Size Determination. *Physical Review* 1939;56(10):978-82.

165. Omelon S, Georgiou J, Henneman ZJ, Wise LM, Sukhu B, Hunt T, Wynnyckyj C, Holmyard D, Bielecki R, Grynpas MD. Control of Vertebrate Skeletal Mineralization by Polyphosphates. *PloS One* 2009;4(5):e5634.

166. Engler AJ, Sen S, Sweeney HL, Discher DE. Matrix Elasticity Directs Stem Cell Lineage Specification. *Cell* 2006;126(4):677-89.

167. Discher DE, Janmey P, Wang Y-l. Tissue Cells Feel and Respond to the Stiffness of Their Substrate. *Science* 2005;310(5751):1139-43.

168. Jermyn M, Mok K, Mercier J, Desroches J, Pichette J, Saint-Arnaud K, Bernstein L, Guiot M-C, Petrecca K, Leblond F. Intraoperative brain cancer detection with Raman spectroscopy in humans. *Science Translational Medicine* 2015;7(274):274ra19-74ra19.

169. Betts F, Blumenthal NC, Posner AS. Bone mineralization. *Journal of Crystal Growth* 1981;53(1):63-73.

170. Eppell SJ, Tong W, Katz JL, Kuhn L, Glimcher MJ. Shape and size of isolated bone mineralites measured using atomic force microscopy. *Journal of Orthopaedic Research* 2001;19(6):1027-34.

171. Iyengar G, Tandon L. Minor and trace elements in human bones and teeth: International Atomic Energy Agency, Section of Nutritional and Health-Related Environmental Studies, Vienna (Austria), 1999.

172. Grynpas MD, Omelon S. Transient precursor strategy or very small biological apatite crystals? *Bone* 2007;41(2):162-64.

173. Nudelman F, Lausch AJ, Sommerdijk NAJM, Sone ED. In vitro models of collagen biomineralization. *Journal of Structural Biology* 2013;183(2):258-69.

174. Viguet-Carrin S, Garnero P, Delmas P. The role of collagen in bone strength. *Osteoporosis International* 2006;17(3):319-36.

175. George A, Veis A. Phosphorylated Proteins and Control over Apatite Nucleation, Crystal Growth, and Inhibition. *Chemical Reviews* 2008;108(11):4670-93.

176. Burr DB, Akkus O. Chapter 1 - Bone Morphology and Organization. In: Allen MR, Burr DB, eds. Basic and Applied Bone Biology. San Diego: Academic Press 2014:3-25.

177. Bellido T, Plotkin LI, Bruzzaniti A. Chapter 2 - Bone Cells. In: Allen MR, Burr DB, eds. Basic and Applied Bone Biology. San Diego: Academic Press 2014:27-45.

178. Henriksen K, Neutzsky-Wulff AV, Bonewald LF, Karsdal MA. Local communication on and within bone controls bone remodeling. *Bone* 2009;44(6):1026-33.

179. Kamioka H, Honjo T, Takano-Yamamoto T. A three-dimensional distribution of osteocyte processes revealed by the combination of confocal laser scanning microscopy and differential interference contrast microscopy. *Bone* 2001;28(2):145-49.

180. Olszta MJ, Cheng XG, Jee SS, Kumar R, Kim YY, Kaufman MJ, Douglas EP, Gower LB. Bone structure and formation: A new perspective. *Materials Science and Engineering Reports* 2007;58(3-5):77-116.

181. Huiskes R, Ruimerman R, Van Lenthe GH, Janssen JD. Effects of mechanical forces on maintenance and adaptation of form in trabecular bone. *Nature* 2000;405(6787):704-06.

182. Xiong J, O'Brien CA. Osteocyte RANKL: New insights into the control of bone remodeling. *Journal of Bone and Mineral Research* 2012;27(3):499-505.

183. Wallace JM. Chapter 6 - Skeletal Hard Tissue Biomechanics. In: Allen MR, Burr DB, eds. Basic and Applied Bone Biology. San Diego: Academic Press 2014:115-30.

184. Fukumoto S, Martin TJ. Bone as an endocrine organ. *Trends in Endocrinology and Metabolism* 2009;20(5):230-36.

185. Seipel R, Langner S, Platz T, Lippa M, Kuehn JP, Hosten N. Neurogenic heterotopic ossification: epidemiology and morphology on conventional radiographs in an early neurological rehabilitation population. *Skeletal Radiology* 2012;41(1):61-66.

186. Isaacson BM, Stinstra JG, MacLeod RS, Pasquina PF, Bloebaum RD. Developing a quantitative measurement system for assessing heterotopic ossification and monitoring the bioelectric metrics from electrically induced osseointegration in the residual limb of service members. *Annals of Biomedical Engineering* 2010;38(9):2968-78.

187. Damanski M. Heterotopic ossification in paraplegia. *The Journal of Bone and Joint Surgery (British Volume)* 1961;43(2):286-99.

188. Brooker AF, Bowerman JW, Robinson RA, Riley LH. Ectopic ossification following total hip replacement. *Journal of Bone and Joint Surgery (American Volume)* 1973;55(8):1629-32.

189. Chantraine A, Nusgens B, Lapiere CM. Biochemical analysis of heterotopic ossification in spinal cord injury patients. *Paraplegia* 1995;33(7):398-401.

190. Basham M, Filik J, Wharmby MT, Chang PC, El Kassaby B, Gerring M, Aishima J, Levik K, Pulford BC, Sikharulidze I. Data Analysis WorkbeNch (DAWN). *Journal of synchrotron radiation* 2015;22(3):853-58.

191. Méheust Y, Knudsen KD, Fossum JO. Inferring orientation distributions in anisotropic powders of nano-layered crystallites from a single two-dimensional WAXS image. *Journal of Applied Crystallography* 2006;39(5):661-70.

192. Zhang Z-M, Chen S, Liang Y-Z. Baseline correction using adaptive iteratively reweighted penalized least squares. *Analyst* 2010;135(5):1138-46.

193. Cloetens P, Ludwig W, Baruchel J, Van Dyck D, Van Landuyt J, Guigay J, Schlenker M. Holotomography: Quantitative phase tomography with micrometer resolution using hard synchrotron radiation x rays. *Applied Physics Letters* 1999;75(19):2912-14.

194. Reznikov N, Shahar R, Weiner S. Bone hierarchical structure in three dimensions. *Acta Biomaterialia* 2014;10(9):3815-26.

195. Hillier ML, Bell LS. Differentiating human bone from animal bone: a review of histological methods. *Journal of Forensic Sciences* 2007;52(2):249-63.

196. Boyde A, Jones SJ. Scanning electron microscopy of bone: instrument, specimen, and issues. *Microscopy Research and Technique* 1996;33(2):92-120.

197. Crane NJ, Popescu V, Morris MD, Steenhuis P, Ignelzi MA. Raman spectroscopic evidence for octacalcium phosphate and other transient mineral species deposited during intramembranous mineralization. *Bone* 2006;39(3):434-42.

198. Weiner S. Transient precursor strategy in mineral formation of bone. *Bone* 2006;39(3):431-33.

199. Spencer J, Missen G. Pseudomalignant heterotopic ossification ("myositis ossificans"). Recurrence after excision with subsequent resorption. *Bone & Joint Journal* 1989;71(2):317-19.

200. Eisenstein N, Williams R, Cox S, Stapley S, Grover L. Enzymatically regulated demineralisation of pathological bone using sodium hexametaphosphate. *Journal of Materials Chemistry B* 2016;4(21):3815-22.

201. Fleish H, Neuman WF. Mechanisms of calcification: role of collagen, polyphosphates, and phosphatase. *American Journal of Physiology* 1961;200(6):1296-300.

202. Fleisch H, Straumann F, Schenk R, Bisaz S, Allgower M. Effect of condensed phosphates on calcification of chick embryo femurs in tissue culture. *American Jounal of Physiology* 1966;211:821-25.

203. McGaughey C, Stowell EC. Effects of Polyphosphates on the Solubility and Mineralization of HA: Relevance to a Rationale for Anticaries Activity. *Journal of Dental Research* 1977;56(6):579-87.

204. McGaughey C. Binding of polyphosphates and phosphonates to hydroxyapatite, subsequent hydrolysis, phosphate exchange and effects on demineralization, mineralization and microcrystal aggregation. *Caries Research* 1983;17(3):229-41.

205. Rao RR, Kannan TS. Dispersion and slip casting of hydroxyapatite. *Journal of the American Ceramic Society* 2001;84(8):1710-16.

206. Cini R, Chindamo D, Catenaccio M, Lorenzini S, Selvi E, Nerucci F, Picchi MP, Berti G, Marcolongo R. Dissolution of calcium pyrophosphate crystals by polyphosphates: an in vitro and ex vivo study. *Annals of the Rheumatic Diseases* 2001;60(10):962-7.

207. Afshar A, Ghorbani M, Ehsani N, Saeri M, Sorrell C. Some important factors in the wet precipitation process of hydroxyapatite. *Materials & Design* 2003;24(3):197-202.

208. Kura G, Ohashi S, Kura S. Complex formation of cyclic phosphate anions with bivalent cations. *Journal of Inorganic and Nuclear Chemistry* 1974;36(7):1605-09.

209. Andreola F, Castellini E, Manfredini T, Romagnoli M. The role of sodium hexametaphosphate in the dissolution process of kaolinite and kaolin. *Journal of the European Ceramic Society* 2004;24(7):2113-24.

210. Fleisch H, Russell RGG, Straumann F. Effect of Pyrophosphate on Hydroxyapatite and Its Implications in Calcium Homeostasis. *Nature* 1966;212(5065):901-03.

211. Robins JC, Akeno N, Mukherjee A, Dalal RR, Aronow BJ, Koopman P, Clemens TL. Hypoxia induces chondrocyte-specific gene expression in mesenchymal cells in association with transcriptional activation of Sox9. *Bone* 2005;37:313-22.

212. Currey JD. The effect of porosity and mineral content on the Young's modulus of elasticity of compact bone. *Journal of Biomechanics* 1988;21(2):131-39.

213. Landis WJ. The strength of a calcified tissue depends in part on the molecular structure and organization of its constituent mineral crystals in their organic matrix. *Bone* 1995;16(5):533-44.

214. Wang X, Bank RA, TeKoppele JM, Agrawal C. The role of collagen in determining bone mechanical properties. *Journal of Orthopaedic Research* 2001;19(6):1021-26.

215. Hoffman AS. Hydrogels for biomedical applications. *Advanced Drug Delivery Reviews* 2012;64:18-23.

216. Black J. Biological performance of materials: fundamentals of biocompatibility: CRC Press 2005.

217. Peppas NA. Hydrogels and drug delivery. *Current Opinion in Colloid and Interface Science* 1997;2(5):531-37.

218. Qiu Y, Park K. Environment-sensitive hydrogels for drug delivery. *Advanced Drug Delivery Reviews* 2001;53(3):321-39.

219. Bae KH, Wang L-S, Kurisawa M. Injectable biodegradable hydrogels: progress and challenges. *Journal of Materials Chemistry B* 2013;1(40):5371-88.

220. Ito T, Yeo Y, Highley CB, Bellas E, Benitez CA, Kohane DS. The prevention of peritoneal adhesions by in situ cross-linking hydrogels of hyaluronic acid and cellulose derivatives. *Biomaterials* 2007;28(6):975-83.

221. Jin R, Hiemstra C, Zhong Z, Feijen J. Enzyme-mediated fast in situ formation of hydrogels from dextran–tyramine conjugates. *Biomaterials* 2007;28(18):2791-800.

222. Oh JK, Lee DI, Park JM. Biopolymer-based microgels/nanogels for drug delivery applications. *Progress in Polymer Science* 2009;34(12):1261-82.

223. Morris ER, Nishinari K, Rinaudo M. Gelation of gellan – A review. *Food Hydrocolloids* 2012;28(2):373-411.

224. Lee KY, Mooney DJ. Alginate: properties and biomedical applications. *Progress in Polymer Science* 2012;37(1):106-26.

225. Young S, Wong M, Tabata Y, Mikos AG. Gelatin as a delivery vehicle for the controlled release of bioactive molecules. *Journal of Controlled Release* 2005;109(1–3):256-74.

226. Ravi Kumar MNV. A review of chitin and chitosan applications. *Reactive and Functional Polymers* 2000;46(1):1-27.

227. Hoare TR, Kohane DS. Hydrogels in drug delivery: progress and challenges. *Polymer* 2008;49(8):1993-2007.

228. Wang B, Adhikari B, Barrow CJ. Optimisation of the microencapsulation of tuna oil in gelatin–sodium hexametaphosphate using complex coacervation. *Food Chemistry* 2014;158:358-65.

229. Dash R, Foston M, Ragauskas AJ. Improving the mechanical and thermal properties of gelatin hydrogels cross-linked by cellulose nanowhiskers. *Carbohydrate Polymers* 2013;91(2):638-45.

230. Coutinho DF, Sant SV, Shin H, Oliveira JT, Gomes ME, Neves NM, Khademhosseini A, Reis RL. Modified Gellan Gum hydrogels with tunable physical and mechanical properties. *Biomaterials* 2010;31(29):7494-502.

231. Silva-Correia J, Miranda-Gonçalves V, Salgado AJ, Sousa N, Oliveira JM, Reis RM, Reis RL. Angiogenic potential of gellan-gum-based hydrogels for application in nucleus pulposus regeneration: in vivo study. *Tissue Engineering Part A* 2012;18(11-12):1203-12.

232. Silva‐Correia J, Zavan B, Vindigni V, Silva TH, Oliveira JM, Abatangelo G, Reis RL. Biocompatibility Evaluation of Ionic‐and Photo‐Crosslinked Methacrylated Gellan Gum Hydrogels: In Vitro and In Vivo Study. *Advanced Healthcare Materials* 2013;2(4):568-75.

233. El-hefian EA, Yahaya AH. Effects of temperature, shearing time and rate of shear on the viscosity of chitosan/agar-blend solutions. *Maejo International Journal of Science and Technology* 2010;4(2):261-67.

234. Becker TA, Kipke DR. Flow properties of liquid calcium alginate polymer injected through medical microcatheters for endovascular embolization. *Journal of Biomedical Materials Research* 2002;61(4):533-40.

235. Laaman TR. Hydrocolloids: Fifteen Practical Tips. Hydrocolloids in Food Processing. Oxford: Wiley-Blackwell 2010:1-17.

236. Moreira HR, Munarin F, Gentilini R, Visai L, Granja PL, Tanzi MC, Petrini P. Injectable pectin hydrogels produced by internal gelation: pH dependence of gelling and rheological properties. *Carbohydrate Polymers* 2014;103:339-47.

237. Guvendiren M, Lu HD, Burdick JA. Shear-thinning hydrogels for biomedical applications. *Soft Matter* 2012;8(2):260-72.

238. Sánchez‐Díaz JC, Becerra‐Bracamontes F, González‐Álvarez A, Cruz‐Barba LE, Martínez‐Ruvalcaba A. Effect of sodium hexametaphosphate

concentration on the swelling and controlled drug release properties of chitosan hydrogels. *Journal of Applied Polymer Science* 2010;117(6):3595-600.

239. Street D, Bangsbo J, Juel C. Interstitial pH in human skeletal muscle during and after dynamic graded exercise. *The Journal of Physiology* 2001;537(3):993-98.

240. Zuidema JM, Rivet CJ, Gilbert RJ, Morrison FA. A protocol for rheological characterization of hydrogels for tissue engineering strategies. *Journal of Biomedical Materials Research Part B: Applied Biomaterials* 2014;102(5):1063-73.

241. D'Souza S. A review of in vitro drug release test methods for nano-sized dosage forms. *Advances in Pharmaceutics* 2014;2014

242. Ganbat D, Kim K, Jin YJ, Kim YH. Heterotopic ossification in cervical total disk replacement: A finite element analysis. *Proceedings of the Institution of Mechanical Engineers, Part H: Journal of Engineering in Medicine* 2014;228(2):200-05.

243. Michelsson JE, Granroth G, Andersson LC. Myositis ossificans following forcible manipulation of the leg. A rabbit model for the study of heterotopic bone formation. *Journal of Bone and Joint Surgery (American Volume)* 1980;62(5):811-15.

244. Michelsson J-E, Pettilä M, Valtakari T, Leivo I, Aho HJ. Isolation of Bone From Muscles Prevents the Development of Experimental Callus-Like Heterotopic Bone: A Study of the Interaction of Bone and Muscle in New Bone Formation. *Clinical Orthopaedics and Related Research* 1994;302:266-72.

245. Schneider DJ, Moulton MJ, Singapuri K, Chinchilli V, Deol GS, Krenitsky G, Pellegrini Jr VD. Inhibition of Heterotopic Ossification With Radiation Therapy in an Animal Model. *Clinical Orthopaedics and Related Research* 1998;355:35-46.

246. Volek-Smith H, Urist MR. Recombinant human bone morphogenetic protein (rhBMP) induced heterotopic bone development in vivo and in vitro. *Experimental Biology and Medicine* 1996;211(3):265-72.

247. Le Nihouannen D, Daculsi G, Saffarzadeh A, Gauthier O, Delplace S, Pilet P, Layrolle P. Ectopic bone formation by microporous calcium phosphate ceramic particles in sheep muscles. *Bone* 2005;36(6):1086-93.

248. Friedenstein A, Piatetzky-Shapiro I, Petrakova K. Osteogenesis in transplants of bone marrow cells. *Journal of Embryology and Experimental Morphology* 1966;16(3):381-90.

249. Gonda K, Nakaoka T, Yoshimura K, Otawara‐Hamamoto Y, Harrii K. Heterotopic Ossification of Degenerating Rat Skeletal Muscle Induced by Adenovirus‐Mediated Transfer of Bone Morphogenetic Protein‐2 Gene. *Journal of Bone and Mineral Research* 2000;15(6):1056-65.

250. Shen Q, Little SC, Xu M, Haupt J, Ast C, Katagiri T, Mundlos S, Seemann P, Kaplan FS, Mullins MC. The fibrodysplasia ossificans progressiva R206H ACVR1 mutation activates BMP-independent chondrogenesis and zebrafish embryo ventralization. *The Journal of Clinical Investigation* 2009;119(11):3462.

251. Tylzanowski P, Mebis L, Luyten FP. The Noggin null mouse phenotype is strain dependent and haploinsufficiency leads to skeletal defects. *Developmental Dynamics* 2006;235(6):1599-607.

252. Kan L, Hu M, Gomes WA, Kessler JA. Transgenic mice overexpressing BMP4 develop a fibrodysplasia ossificans progressiva (FOP)-like phenotype. *The American Journal of Pathology* 2004;165(4):1107-15.

253. Ueta C, Iwamoto M, Kanatani N, Yoshida C, Liu Y, Enomoto-Iwamoto M, Ohmori T, Enomoto H, Nakata K, Takada K. Skeletal malformations caused by overexpression of Cbfa1 or its dominant negative form in chondrocytes. *The Journal of Cell Biology* 2001;153(1):87-100.

254. Kan L, Kessler JA. Animal models of typical heterotopic ossification. *Journal of Biomedicine and Biotechnology* 2011;2011:309287.

255. Polfer E, Hope D, Elster E, Qureshi A, Davis T, Golden D, Potter B, Forsberg J. The development of a rat model to investigate the formation of blast-related post-traumatic heterotopic ossification. *Bone & Joint Journal* 2015;97(4):572-76.

256. Buck R. Regeneration of tendon. *The Journal of Pathology and Bacteriology* 1953;66(1):1-18.

257. McClure J. The effect of diphosphonates on heterotopic ossification in regenerating Achilles tendon of the mouse. *The Journal of Pathology* 1983;139(4):419-30.

258. Lin L, Shen Q, Xue T, Yu C. Heterotopic ossification induced by Achilles tenotomy via endochondral bone formation: expression of bone and cartilage related genes. *Bone* 2010;46(2):425-31.

259. Tønnesen HH, Karlsen J. Alginate in drug delivery systems. *Drug Development and Industrial Pharmacy* 2002;28(6):621-30.

260. Augst AD, Kong HJ, Mooney DJ. Alginate hydrogels as biomaterials. *Macromolecular Bioscience* 2006;6(8):623-33.

261. Team RC. R: A language and environment for statistical computing. R Foundation for Statistical Computing, Vienna, Austria., 2014.

262. Kimmelman J, Federico C. Consider drug efficacy before first-in-human trials. *Nature* 2017;542(7639):25.